Dynamics of Cellular Flame Propagation

for Hydrogen, Methane, and Propane

Jeong Do Kim

BEng, MEng

Submitted in accordance with the requirements for the degree of

Doctor of Philosophy

The University of Leeds

Institute of Thermofluids

School of Mechanical Engineering

Aug 2019

Intellectual Property and Publication Statements

The candidate confirms that the work submitted is his/her own, except where work which has formed part of jointly-authored publications has been included. The contribution of the candidate and the other authors to this work has been explicitly indicated below. The candidate confirms that appropriate credit has been given within the thesis where reference has been made to the work of others.

In the following two papers, the candidate completed all experimental studies, evaluation of data, and preparation of publications. All authors contributed to proof reading of the articles prior to publication.

Part of Chapter 3, 4, and 5 of the thesis is based on a jointly-authorised conference extended abstract paper: Jeongdo Kim, Alexey Burluka, Junfeng Yang, Experimental Study of Flame Instability of Hydrogen/Air Mixtures under Laminar Flow Conditions in an Optical SI Engine, Advanced Combustion Methods, 5 April 2018

Part of Chapter 3, 4, and 5 of the thesis is based on a jointly-authorised conference extended abstract paper; Jeongdo Kim, Alexey Burluka, Junfeng Yang, An Experimental Study on the Laminar Flame Dynamics of H_2, CH_4, and C_3H_8/Air Mixtures in an Optical SI Combustion Engine, 37th International Symposium on Combustion, 29 Jul - 3 Aug 2018

Acknowledgements

This thesis would not be completed if there were not the help and support of many people. They always encouraged me to proceed the present research. I would like to express my sincere mind to them.

First of all, I appreciate the guidance and suggestions of my supervisors, Prof. Alexey Burluka, Dr. Junfeng Yang, and Prof. Harvey Thompson. They provided me with new ideas and a lot of advice through the entire period of my PhD study.

I would like to thank the former technical staff in the Institute of Thermofluids laboratory: Mark Batchelor, Paul Banks, and Brian Leach. During the preparation of the experiment, they helped me set up the experiment equipment with kindness.

My gratitude should be given to my PhD colleagues: Dr. Zhengyang Ling, Dr. Nini Chen, Dr. Wangkang Zhang, Aaron Mifflin, and Dr. Jamie Smith. They helped me settle in Leeds, and provided me with beneficial ideas and the pleasure of working together.

I also appreciate the encouragement of Prof. Jaesung Choi and Prof. Kwonhae Cho at Korea Maritime and Ocean University. If I did not learn fundamental knowledge and skills from them, my PhD course would not be started.

At last, I am grateful to my family and siblings: Jongsu Kim, Jongji Lee, Minseong Kim, Yuji Kimoto, Taeseok Cho, Kyoungtae Gum, Seonyoung Cho, and Jaeho Cho. And I thank my lovely wife and twins, Jiyoung Cho, Yunseo Kim, and Huiseo Kim. I could proceed my PhD study with their dedicated love and encouragement.

Abstract

Since the outbreak of the economic crisis in 2009 and the explosion of the nuclear power plant in Japan in 2011, the price and needs of fossil fuel have gradually decreased, and environmental problems, e.g. greenhouse gas, have directed the world's attention to other energy resources, so-called green energy. However, not only are oil reserves many in the world, but also a boom of shale gas, which the US has triggered, plays an important role in developing relevant technologies and has the possibility of making tectonic shifts in energy initiative. Moreover, although many kinds of electric cars have been released by major companies, a massive number of vehicles are still equipped with internal combustion engines, and power plants involving the combustion of fossil fuels are also used to produce electricity. It is certain that the technologies relevant to the combustion of fossil fuels are still essential and should exist for a fairly long time. The ultimate goal of combustion research is enhancing the understanding of the mechanism of combustion, fuel efficiency, and so forth, of which practical results end up helping us control combustion process safely and efficiently. Among such research subjects, the measurement of burning velocities about laminar and turbulent flames have been studied and discussed in the last decades. Regrettably, there is still doubt on how a variety of factors affect the burning rate. Especially, cellular flame structures that appear in a certain condition require more considerable observation and research to investigate their characteristics.

The aim of this research is to examine the characteristics of cellular flame. In order to observe the flame, LUPOE-2D, Leeds University Ported Optical Engine version 2 with Disc-head, was used and an optical-accessible engine. In order to measure flame propagation speed, unburned gas velocity, burning velocity, and others, the research engine was modified, and the appropriate diagnostic system was installed. Hydrogen, methane, and propane were employed as fuels in this research. In the case of hydrogen, many researchers and major companies have paid much attention to it as a clean energy source to alleviate the global warming. And methane and propane have been widely used in the industrial fields. Using these three fuels, the experiment was carried out, and it was investigated how their cellular flames were locally changed.

.

Table of Contents

List of Figures

List of Tables

Nomenclature

Roman and Greek symbols

Symbol	Unit	Description
a	km/s^2	Fluid acceleration
A	mm^2	Surface area
		Cross section area between the float and tapered tube
c	-	Progress variable
C	-	Cross correlation
C_k	1/mm	Curvature
C_{km}	-	Curvature of a circle having the identical dimension to the burned area in a binary flame image
c_p	J/kgK	Specific heat of product
d_p	Mm	Diameter of particle
D	cm^2/s	Molecular mass diffusivity
D_F	cm^2/s	Fuel molecular mass diffusivity
		Molecular diffusivity of deficient reactant
D_o, D_{ox}	cm^2/s	Oxidant molecular mass diffusivity
		Molecular diffusivity of excess reactant
F	-	Factor
		Forward Fourier transform
F^{-1}	-	Inverse Fourier transform
G, g	m/s^2	Gravity of acceleration
h	mm	Height of float
		Height
I	-	Intensity
k	-	Proportional constant

		Wavenumber
k_c	-	Cut-off wavenumber
k_d	-	Drag coefficient
k_m	-	Maximum wavenumber
k_1	-	Proportional constant $1/k$
k_2	-	Constant, $k_d {k_1}^2$
k_3	-	Constant, $\sqrt{\frac{V_s g}{k_2}}$
m	kg	Mass
M	kg/mol	Molecular weight per mole
n	mol	Amount of gas
		Differential coefficient
L_t	mm	Length scale
Le	-	Lewis number
P	bar	Pressure
P_{abs}	bar	Pressure measured by absolute transducer
$\bar{P}_{abs}$	bar	Average pressure measured by absolute transducer
P_{cyl}	bar	In-cylinder pressure
P_{dyn}	bar	Pressure measured by dynamic transducer
$\bar{P}_{dyn}$	bar	Average pressure measured by dynamic transducer
P_o	bar	Reference pressure; atmospheric pressure
		Initial pressure at the start of ignition
P_u	bar	Initial pressure of unburnt gas
Q	J	Heat released by chemical reaction
	kg/min	Flow rate
	ml/min	Volumetric flow rate
r	-	Ratio of specific heats
	mm	Flame radius
r_m	mm	Mean flame radius

R	J/K·mol	Universal gas constant, 8.314 [J/K·mol]
R_e	mm	Mean entrainment radius
$\dot{s}$	s^{-1}	Stretch rate
S	m/s	Flame speed, flame propagation speed
$\bar{S}$	m/s	Local mean flame propagation speed
S_L	m/s	Perturbed laminar flame speed
S_L^0, S_n	m/s	Unperturbed laminar flame speed
$S_{L,b}$	m/s	Perturbed laminar flame speed in the burned gas side
$S_{L,b}^0$	m/s	Unperturbed laminar flame speed in the burned gas side
T	K	Temperature
T_0	K	Temperature of unburnt gas
		Reference temperature; 298 K
		Initial temperature at the start of ignition
T_{ad}	K	Adiabatic temperature
T_b	K	Product temperature
T_u	K	Fresh or unburnt gas temperature
		Initial temperature of unburnt gas
t	ms	Time
	-	Point index along a flame contour line
t_{ign}	°	Ignition timing
u, u_u	m/s	Fresh or unburned gas velocity
u'	m/s	Fluctuating velocity in an instantaneous turbulent velocity
u_b	m/s	Burned gas velocity
u_c	kg/m^2s	Consumption speed, consumption velocity, consumption rate, burning rate
u_l	m/s	perturbed laminar premixed flame speed
		laminar burning velocity

u_n	m/s	Normal flame speed
		Unperturbed laminar premixed flame speed
		Burning velocity
U	m/s	Velocity
		Linear velocity passing through an area between the float and tapered tube
$\overline{U}$	m/s	Local mean burning velocity
U_f	m/s	Fluid velocity
U_{lag}	m/s	Lag velocity
U_p	m/s	Particle velocity
v	m/s	Tangential velocity
V	m^3	Volume
V_s	m^3	Volume of float
V_g	m/s	Unburned gas velocity or fresh gas velocity
V_n	m/s	Normal unburned gas velocity to each point of the flame front
$\overline{V_n}$	m/s	Local mean normal unburned gas velocity
W	kg/cm^3	Reaction rate
x	mm	Direction of flame propagation or distance
Y	g/s	Mass fraction
Y_F	g/s	Mass fraction of fuel
Y_F^0	g/s	Initial mass fraction of fuel
α	-	Flame strain rate, rate of strain,
		Mixing ratio
κ	m^2/s	Molecular thermal diffusivity
μ_f	kg/ms	Fluid absolute or dynamic viscosity
ν		Source or sink of mass fraction
ρ	kg/m^3	Density

ρ_u	kg/m^3	Density of unburned mixture, density of fresh mixture
ρ_b	kg/m^3	Density of burned mixture, density of product
ρ_f	kg/m^3	Density of fluid
ρ_p	kg/m^3	Density of particle
ρ_s	kg/m^3	Density of float
σ	-	Density ratio, ρ_u/ρ_b
ζ	mm	New variable for coordinate framework, $\zeta = x - u_n t$
ζ_F	mm	Boundary of reaction and pre-heat zones
Σ_u	mm^2	Surface area in the unburned side
Σ_r	mm^2	Surface area in the reaction side
θ	º	Crank angle (degree)
θ_{EPC}	º	Crank angle at exhaust port closure
λ	-	wavelength
ϕ	-	Equivalence ratio

Abbreviation

abs		absolute
aTDC		After top dead centre
BDC		Bottom dead centre
bTDC		Before top dead centre
CA		Crank angle
CW		Continuous wave
CCD		Semiconductor charge-coupled device
CMOS		Complementary metal oxide semiconductor
DFT		Discrete Fourier transform
EXP		Experimental condition
FFT		Fast Fourier transform
LHS		Left hand side
LHV	MJ/kg	Lower heating value

LUSIE	Leeds University spark ignition engine
LUSIEDA	Leeds University spark ignition engine data analysis
Nd:YLF	Neodymium-doped: yttrium lithium fluoride
PIV	Particle image velocimetry
RMS	Root-mean-square
RHS	Right hand side
SLPM	Standard litre per minute
STD	Standard condition
TDC	Top dead centre

Subscript

ref	Reference flowmeter
rtm	Rotameter

Chapter 1 Introduction and scope of research

1.1 Research motivation

As the world population has been increased and the quality of people's lives has been improved, a demand for energy has been increased continuously, with the relevant technologies advanced. It is predicted that the usage of energy will increase by 35 % in the next 20 years (Mobil 2013). According to Mobil's report (2013), the usage of electricity will continue to rise and be the main reason for the increasing demand for energy. In order to meet the increasing demand for energy, the usage of natural gas will gradually increase from 16 to 29 %, whereas the usage of coal will decrease from 46 to 32 %. Additionally, the proportion of renewable energy such as solar energy, geothermal energy, and so forth, will increase, with environmental problems receiving more attention.

Since the use of fossil fuels causes various environmental problems such as global warming and air pollutant emissions, the proportion of fossil fuels in energy production will gradually be reduced. Although it is true that the usage of renewable energy will increase to mitigate environmental problems, fossil fuels will still be used for the production of the future energy for a fairly long time (EEA 2008, Birol 2010). The main issues are how to reduce the amount of air pollutant emissions and how to improve the efficiency of combustors in which fossil fuels are used.

In order to solve the challenging problems, it is essential to enhance the understanding of a combustion process, and the relevant researches have been carried out for many years. Among the various researches, the studies of laminar and turbulent flames have been important topics, and many researchers have made significant efforts to investigate the characteristics of the flames. Flame stability has also been thought of as an important subject in combustion research. Initially stable flame can become unstable because of the imbalance between flame propagation speed and unburned mixture flow velocity or the imbalance between the molecular diffusivity of an unburned mixture and the thermal diffusivity of the burned product: they are named hydrodynamic instability and molecular-thermal diffusive instability respectively. Unstable flame appears as a cellular structure, and it has been thought that the instability of a flame surface can make the flame turbulent and improve the flame propagation speed (Groff 1982, Hertzberg 1989).

The measurement of the laminar burning velocity, which is defined for an unstrained and steady laminar flame, has been one of the most important topics. The laminar burning velocity is the unique characteristic of a combustible mixture. It has been used for laminar and turbulent combustion modelling and to validate the relevant chemical mechanisms. For these reasons, many researchers have measured the laminar burning velocity. However, most of the laminar burning velocities have been measured as an average value, which is almost impossible to give the information on the local change of the burning velocity (Andrews and Bradley 1972, Rallis and Garforth 1980). Although the local and instantaneous burning velocity of propagating flame has been measured (Zhou and Garner 1996, Balusamy et al. 2011), there have been the very few measurements of the burning velocity under the occurrence of cellular flame structures.

The current research concentrated on measuring flame propagation speed, the velocity of unburned gas at a flame front, and burning velocity where cellular flame appeared. Hydrogen, methane, and propane were used as fuels in this experiment. This is because hydrogen receives attention as a clean energy source to alleviate the global warming and methane and propane are widely used in the industrial fields. The appropriate research engine and particle image velocimetry system were adopted for the measurements of flame propagation speed, unburned gas velocity, and burning velocity. Using the experimental apparatus, the characteristics of cellular flame were investigated.

1.2 Scope of research

The aim of this research is to analyse the local and instantaneous change of a cellular flame structure as the flame develops. The change of a flame structure is accompanied by the variations of the flame propagation speed, unburned gas velocity, and burning velocity. In order to measure the speed and velocities, an appropriate experimental apparatus is required.

The first objective of the current work was to develop the relevant experimental equipment. LUPOE-2D, Leeds University Ported Optical Engine version 2 with Disc-head, was employed in this research. LUPOE-2D has been used by the Leeds combustion research group (Dawood 2011, Hussin 2012, Chen 2016). For this research, the engine was modified by the author.

The LUPOE-2D used in the current work consists of a single cylinder, and is a two stroke engine. It is ignited by spark and supplied with hydrogen, methane, and propane separately. The engine speed ranges between 10 and 200, and is controlled easily. Since top and side quartz windows are installed in the cylinder head of the research engine, it is possible to observe the combustion process inside the cylinder. To visualize the flow of a combustible mixture, the appropriate PIV, particle image velocimetry, system was installed.

In order to measure local flame propagation speed, it was necessary to obtain a flame contour image from the raw PIV flame image. Since the intensities of pixels of a flame image that was obtained through the PIV technique were fluctuated, appropriate image processing was needed to gain a desirable flame contour image. Hence, the proper image processing algorithms were configured, and the code of the appropriate image binarization was developed.

For the measurement of local unburned gas velocity at the flame front, the proper code was also developed. Since seeding particles in the PIV system are burned at the flame front, it is difficult to measure the unburned gas velocity at that region directly. Therefore, the unburned gas velocity at the flame front was calculated by extrapolation. The data of unburned gas velocity ahead of the flame front were used for the extrapolation. Through the measurement of flame propagation speed and unburned gas velocity at each point of the flame front, local burning velocity was calculated.

Lastly, the correlation between the change of an unburned gas flow and a flame structure was investigated. After the vorticity data of unburned gas ahead of the flame front were obtained, it was examined how a cellular structure was changed. The change of vorticity data of unburned gas was represented as a histogram, and the variation of a flame structure was expressed as wavenumber: the wavenumber was calculated with the curvature of a flame surface.

1.3 Thesis outline

This thesis is comprised of six chapters. Each chapter is described briefly as follows:

- Chapter 1 explains the motivation and scope of this research, and then outlines this thesis.

- Chapter 2 describes the fundamental concepts and notions of laminar and turbulent flames which are relevant to this research. The theory of laminar premixed flame is reviewed, and then the flame instabilities is illustrated. After describing the condition where a cellular structure appears, the theory of turbulent premixed flame is explained.

- Chapter 3 presents the detailed description of the experimental equipment that was used in this research. The geometric specification of the LUPOE-2D is described, and the fuel and air supply system are illustrated. The PIV and imaging system that was used to visualize the flow of a combustible mixture is explained in detail. And then the description of the engine control and data acquisition system is given, and the experimental procedure is mentioned.

- Chapter 4 describes the procedure of image processing and the methodology for analysis. The image processing consists of image pre-processing and image binarization. And then, it is explained in detail how to measure and calculate flame propagation speed, unburned gas velocity, burning velocities, and other relevant derivatives.

- Chapter 5 presents the experimental results of cellular flames which were obtained by the experimental equipment. After explaining the experimental condition, the results of hydrogen-, methane-, propane-air mixture are presented. In each mixture, three representative sections were chosen: they are a convex, concave, smoothly-curved section respectively. In each section, it is explained how flame propagation speed, unburned gas velocity, and burning velocity are locally changed with respect to time. The relationship between flame propagation speed and wavenumber is also investigated. Lastly, the relationship between local mean wavenumber and unburned gas vorticity is examined.

- Chapter 6 summarizes the findings of this research, and presents the recommendations for the future study.

Chapter 2 Background to premixed flame

In this chapter, laminar premixed flame is first described. In order to investigate the premixed flame, its theoretical background is introduced, and then, the factors in having the main influence on the unperturbed laminar premixed flame speed are explained. Going beyond the assumptions that are used to derive the equation of the laminar premixed flame speed, the reasons why flame is disturbed or perturbed are mentioned, introducing hydrodynamic and molecular-thermal diffusive instability. While flame develops, the conditions where the cellular flame occurs are illustrated. After that, how much effect the pressure, temperature, and mixture composition in combustion process have on the disturbance of the flame is mentioned. Lastly, the theoretical background of turbulent premixed flame and main factors in affecting it are introduced.

2.1 Laminar premixed flame

Before the combustion process, when fuel and oxidizer are perfectly well mixed, the combustion takes place within a self-sustained propagating flame wave, and the speed is constant under a certain condition (Burluka 2014). One of the most important and fundamental notions in combustion theory is unperturbed laminar premixed flame speed or normal flame speed, u_n. The flame speed is an idealized model, and, in reality, a practical laminar premixed flame is always perturbed owing to heat losses, flame curvature, and so forth. It is certain that the speed of a practical flame is different from that of the unperturbed laminar premixed flame. However, since the difference between the unperturbed laminar premixed speed and practical one is not too large, it is obvious that a study on the normal flame speed is the key physical-chemical characteristic of a combustible mixture.

In order to derive the equation of the unperturbed laminar premixed speed in a planar flame, the following assumptions are required:

- The fuel and oxidant are perfectly mixed before the start of combustion process and the combustible mixture occupies an unburned space.

- The density of the fuel-oxidant mixture, ρ, is constant, that is, there is no motion that is induced by the thermal expansion.

- Combustion wave is planar and one dimensional. x is the location and direction of the flame propagation.

- The molecular mass diffusivities for fuel and oxidant and the thermal diffusivity are equal, $D_F = D_{ox} = \kappa$. They are not dependent on temperature.

- The molecular transport is described with Fourier and Fick's laws.

- Chemical reactions occur in one step and are irreversible. The fuel is the deficient reactant.

Under the assumptions above, the transport equations for temperature T and concentration Y_F can be written as:

$$\rho c_p \frac{\partial T}{\partial t} + \rho u c_p \frac{\partial T}{\partial x} = \rho c_p \kappa \frac{\partial^2 T}{\partial x^2} + \rho Q W \qquad \textbf{Eq.} (2.1)$$

$$\frac{\partial Y_F}{\partial t} + \rho u \frac{\partial Y_F}{\partial x} = \rho D_F \frac{\partial^2 Y_F}{\partial x^2} + \rho \nu W \qquad \textbf{Eq.} (2.2)$$

ρ: density c_p: specific heat of product T: temperature
t: time of flame u: unburned gas velocity x: position of flame
κ: molecular mass or thermal diffusivity W: reaction rate
Q: heat released by chemical reaction
Y_F: mass fraction of fuel D_F: fuel molecular mass diffusivity
ν: source of mass fraction

And the followings are their boundary conditions:

$$T(-\infty) = T_{ad}, \qquad T(\infty) = T_0 \qquad \textbf{Eq.} (2.3)$$

$$Y_F(-\infty) = 0, \qquad Y_F(\infty) = Y_F^0 \qquad \textbf{Eq.} (2.4)$$

$$\frac{\partial T}{\partial x}(-\infty) = 0, \qquad \frac{\partial T}{\partial x}(\infty) = 0 \qquad \textbf{Eq.}\ (2.5)$$

$$\frac{\partial Y_F}{\partial x}(-\infty) = 0, \qquad \frac{\partial Y_F}{\partial x}(\infty) = 0 \qquad \textbf{Eq.}\ (2.6)$$

$$\frac{T(x,t) - T(\infty)}{T(-\infty) - T(\infty)} = \frac{Y_F(\infty) - Y_F(x,t)}{Y_F(\infty) - Y_F(-\infty)} \qquad \textbf{Eq.}\ (2.7)$$

T: temperature
T_0: T at the start of combustion
Y_F^0: Y_F at the start of combustion
T_{ad}: T at the end of combustion
Y_F: mass fraction of fuel

In the equations of the boundary conditions, while ∞ means the position and time before the start of the combustion, $-\infty$ refers to those after the end of combustion. Eq. (2.1) and Eq. (2.2) are similar, and the results are also analogous.

Where the progress variable, $c(x,t)$, which is dependent on the position x and time t of flame, is introduced, the simple sketch of a premixed planar laminar flame may be drawn as Figure 2.1.

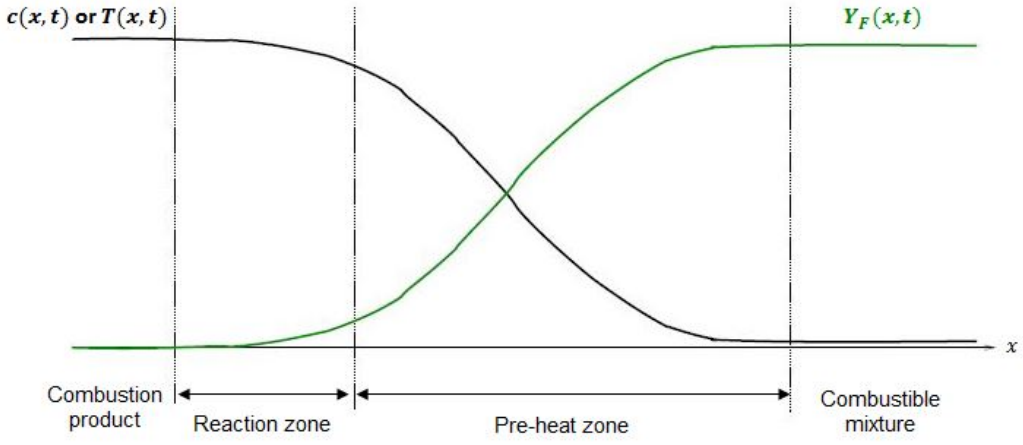

Figure 2.1 A simple sketch of planar laminar unperturbed flame (Burluka 2014)

As is common in combustion model, Eq. (2.1) and (2.2) can be expressed below, using the progress variable $c(x,t)$:

$$\frac{\partial c(x,t)}{\partial t} + \vec{u}\frac{\partial c(x,t)}{\partial x} = \kappa\frac{\partial^2 c(x,t)}{\partial x^2} + W(c(x,t))$$ **Eq.** (2.8)

c: progress variable x: position of flame t: time of flame
$\vec{u}$: unburned gas velocity in one dimension
κ: molecular mass or thermal diffusivity W: reaction rate

The solution of Eq. (2.8) describes the progress of combustion that depends on the location and time, which represents the structure of planar laminar unperturbed flame. By introducing the new variable, ζ, to use the coordinate framework attached to a flame, the number of parameters for the progress variable $c(x,t)$ can be reduced, which means that the flame profile does not depend on time any more. The following equation represents the relation between ζ, x, and t.

$$\zeta = x - u_n t$$ **Eq.** (2.9)

ζ: new variable x: position of flame u_n: burning velocity
t: time of flame

Therefore, Eq. (2.8) can be re-written as follows:

$$-u_n\frac{dc(\zeta)}{d\zeta} = \kappa\frac{d^2 c(\zeta)}{d\zeta^2} + W(c(\zeta))$$ **Eq.** (2.10)

u_n: burning velocity c: progress variable ζ: new variable
κ: molecular mass or thermal diffusivity W: reaction rate

Since the chemical source term, $W(c(\zeta))$, is non-linear, it is impossible to integrate Eq. (2.10) directly. However, it is possible to estimate the value of the unperturbed laminar premixed flame speed u_n through the practical approach.

As seen in Figure 2.1, the flame can generally be separated into the two regions. One of them is referred to as the pre-heat zone, and the other is the reaction zone (Irvin and Richard 2008). The reaction zone, including the luminous zone that we can see, is relatively very thin in real flame, whereas the pre-heat zone is thicker than it. Depending on the zone, the term which mainly affects the transport equation should selectively be considered. In Eq. (2.10), $-u_n\frac{dc(\zeta)}{d\zeta}$, $\kappa\frac{d^2 c(\zeta)}{d\zeta^2}$, and $W(c(\zeta))$ represents the convection, diffusion, and chemical term respectively. Figure 2.2 shows a simple sketch of flame

profile. It may be useful in realizing which terms have significant influences on Eq. (2.10) in each zone.

The whole flame thickness is divided into two zones, which are separated at the boundary, ζ_F. In the pre-heat zone, while the convection and diffusion term are the main factors in having much effect on the transport equation, the chemical term can be neglected because its effect is relatively very small. In the reaction zone, the chemical and diffusion term should be considered to be the most important component for the transport equation, whereas the effect of the convection term is relatively very small. Therefore, the following Eq. (2.11) and (2.12) can be derived.

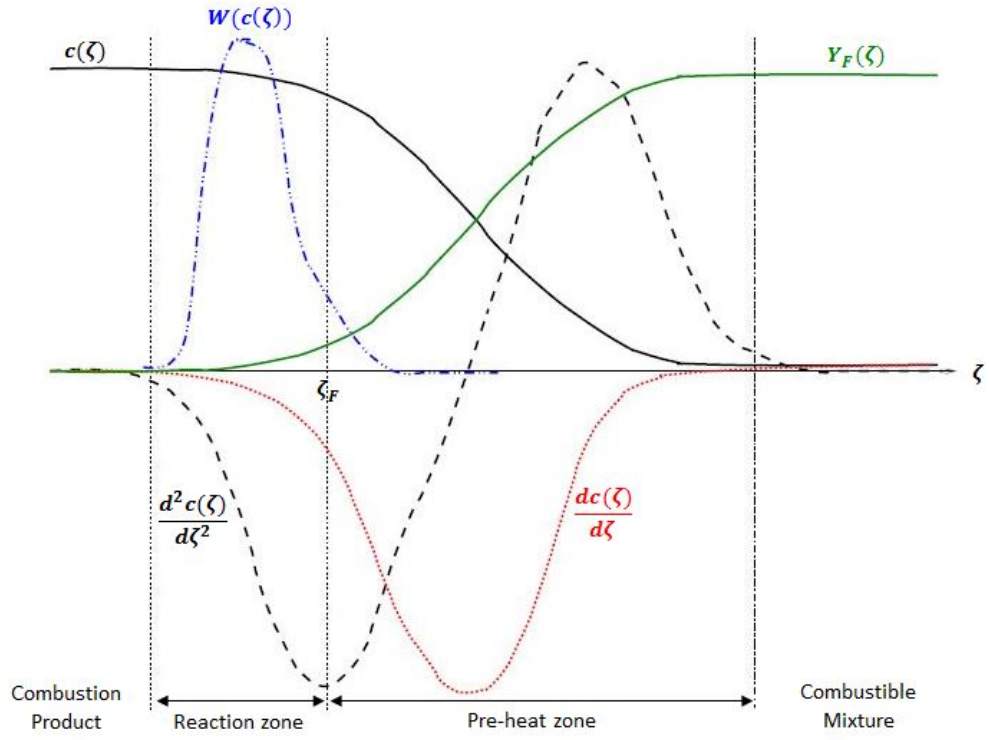

Figure 2.2 A simple sketch of flame profile through a flame front (Burluka 2014)

pre-heat zone: from ∞ to ζ_F

$$-u_n \frac{dc(\zeta)}{d\zeta} = \kappa \frac{d^2c(\zeta)}{d\zeta^2} \qquad \textbf{Eq.} (2.11)$$

u_n: burning velocity c: progress variable ζ: new variable
κ: molecular mass or thermal diffusivity

reaction zone: from ζ_F to $-\infty$

$$\kappa \frac{d^2 c(\zeta)}{d\zeta^2} + W\big(c(\zeta)\big) = 0 \qquad \textbf{Eq.}\ (2.12)$$

κ: molecular mass or thermal diffusivity c: progress variable
ζ: new variable W: reaction rate

These equations have the boundary conditions as follows:

$$c(\zeta \to -\infty) = 1 \qquad c(\zeta \to \infty) = 0 \qquad c(\zeta \to \zeta_F) = 1 \qquad \textbf{Eq.}\ (2.13)$$

$$\frac{dc(\zeta \to -\infty)}{d\zeta} = 0 \quad \frac{dc(\zeta \to \infty)}{d\zeta} = 0 \qquad \textbf{Eq.}\ (2.14)$$

c: progress variable ζ: new variable
ζ_F: ζ at the boundary of reaction and pre-heat zones

Considering the boundary conditions above, Eq. (2.11) may be integrated as follows:

$$\kappa\, d\left(\frac{dc(\zeta)}{d\zeta}\right) = -u_n\, dc(\zeta) \qquad \textbf{Eq.}\ (2.15)$$

$$\kappa \int_{\zeta_F}^{\infty} d\left(\frac{dc(\zeta)}{d\zeta}\right) = -u_n \int_{\zeta_F}^{\infty} dc(\zeta) \qquad \textbf{Eq.}\ (2.16)$$

$$\kappa \left[\frac{dc(\zeta)}{d\zeta}\right]_{\zeta_F}^{\infty} = -u_n [c(\zeta)]_{\zeta_F}^{\infty} \qquad \textbf{Eq.}\ (2.17)$$

$$\left.\frac{dc(\zeta)}{d\zeta}\right|_{\zeta=\zeta_F} = -\frac{u_n}{\kappa} \qquad \textbf{Eq.}\ (2.18)$$

κ: molecular mass or thermal diffusivity c: progress variable
ζ: new variable u_n: burning velocity
ζ_F: ζ at the boundary of reaction and pre-heat zones

In the region from ζ_F to $-\infty$, by introducing the new variable c' instead of $c(\zeta)$ to avoid confusion, Eq.(2.12) may be integrated in the following way that:

$$\kappa \frac{d}{d\zeta}\frac{dc(\zeta)}{d\zeta}\frac{dc(\zeta)}{dc'} = -W(c') \qquad \textbf{Eq.}\ (2.19)$$

$$\kappa \frac{d}{d\zeta}\frac{dc(\zeta)}{d\zeta}dc(\zeta) = -W(c')dc' \qquad \textbf{Eq.}\ (2.20)$$

$$\kappa \frac{dc(\zeta)}{d\zeta}d\frac{dc(\zeta)}{d\zeta} = -W(c')dc' \qquad \textbf{Eq.}\ (2.21)$$

$$\kappa \frac{1}{2}d\left(\frac{dc(\zeta)}{d\zeta}\right)^2 = -W(c')dc' \qquad \textbf{Eq.}\ (2.22)$$

$$\frac{\kappa}{2}\int_{-\infty}^{\zeta_F} d\left(\frac{dc(\zeta)}{d\zeta}\right)^2 = -\int_{1}^{c'_{\zeta_F}} W(c')dc' \qquad \textbf{Eq.}\ (2.23)$$

$$\frac{\kappa}{2}\left[\left(\frac{dc(\zeta)}{d\zeta}\right)^2\right]_{-\infty}^{\zeta_F} = \int_{c'_{\zeta_F}}^{1} W(c')dc' \qquad \textbf{Eq.}\ (2.24)$$

κ: molecular mass or thermal diffusivity ζ: new variable
c: progress variable c': new progress variable W: reaction rate
ζ_F: ζ at the boundary of reaction and pre-heat zones
c'_{ζ_F}: c' at the boundary of reaction and pre-heat zones

In Figure 2.2, the value of $\frac{dc(\zeta)}{d\zeta}$ is always negative. And since the zone where the chemical term mainly affects the transport equation is the reaction zone, its integration may be expanded from c'_{ζ_F} to zero. That is, the region for the integration may be from $\zeta = -\infty$ to $\zeta = \infty$. Hence, Eq. (2.24) can be written as follows:

$$\left.\frac{dc(\zeta)}{d\zeta}\right|_{\zeta=\zeta_F} = -\left[\frac{2}{\kappa}\int_0^1 W(c')dc'\right]^{\frac{1}{2}} \qquad \textbf{Eq.}\ (2.25)$$

c: progress variable c': new progress variable ζ: new variable
κ: molecular mass or thermal diffusivity W: reaction rate

It is certain that the values of $\frac{dc(\zeta)}{d\zeta}$ that are calculated in Eq. (2.18) and Eq.(2.25) have to be identical at the position where $\zeta = \zeta_F$. Therefore, the unperturbed laminar premixed flame speed u_n can be derived as follows:

$$\left.\frac{dc(\zeta)}{d\zeta}\right|_{\zeta=\zeta_F} = -\frac{u_n}{\kappa} = -\left[\frac{2}{\kappa}\int_0^1 W(c')dc'\right]^{\frac{1}{2}} \qquad \textbf{Eq.} (2.26)$$

$$u_n = \left[2\kappa\int_0^1 W(c')dc'\right]^{\frac{1}{2}} \qquad \textbf{Eq.} (2.27)$$

c: progress variable c': new progress variable ζ: new variable
κ: molecular mass or thermal diffusivity u_n: burning velocity
W: reaction rate

This is the main result of the theory that was suggested by Zeldovich, Semenov, and Frank-Kamenetsky (Irvin and Richard 2008). The aim of this theory, so-called activation energy asymptotic theory, is to determine the speed of an unperturbed laminar premixed flame (Lipatnikov 2012). It is worth stressing that the laminar premixed flame speed u_n depends only on the thermal diffusivity κ or molecular diffusivity D according to the assumption and the integral of the reaction rate profile. It is also remarkable that the flame speed does not depend on a particular characteristic of the reaction rate dependency on the temperature and concentration.

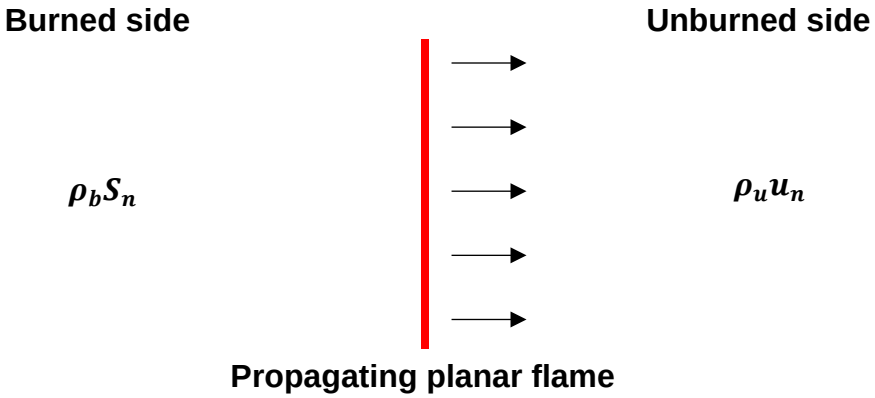

Figure 2.3 A sketch of planar unperturbed laminar premixed flame reproduced from Burluka (2015)

The laminar premixed flame is considered to be a discontinuity between the two flow fields, as depicted in Figure 2.3, which splits into the unburned side consisting of the fuel-oxidant mixture and the burned area that is comprised of combustion product. The density ahead or behind the flame is ρ_u or ρ_b respectively. The assumptions that are made in this case are that the thickness of the flame is infinitely thin and it propagates at a constant speed u_n, which is called burning velocity. It is also assumed that the conditions before and after the flame surface dramatically change: the properties such as pressure, volume, density, and so on vary drastically. As shown in Figure 2.3, where the thin flame is ideally one-dimensional planar laminar premixed flame and the unburned gas is stationary, the direction at which the flame propagates towards the unburned side is normal to the infinitely thin flame front. Since this chemical reaction obeys the law of conservation of mass for the cross section, the following equation can be derived.

$$\rho_u u_n = \rho_b S_n \qquad \textbf{Eq.} (2.28)$$

ρ_u: density of fuel-oxidant mixture
ρ_b: density of combustion product
u_n: burning velocity
S_n: flame propagation speed

After obtaining the values of the densities of the unburned gas and the combustion product through chemical equilibrium programs such as Gaseq (Morley 2005), in turn, the flame propagation speed S_n is measured through appropriate methods, the burning velocity u_n can be calculated. In the process of the combustion, the effect of the thermal expansion on the flame that is induced by the burned gas also has to be noted, which has an influence on the movement of the unburned gas. It can be said that the unburned gas pushes the flame, which is shown in Figure 2.4.

The flame propagation speed S_n, which is relative to the burned gas, consists of two components. One of them is the burning velocity u_n in the figure, and the other is the unburned gas velocity V_g (Balusamy et al. 2011, Long and Hargrave 2011, Burluka 2015). This relationship can be written as follows:

$$S_n = u_n + V_g \qquad \textbf{Eq.} (2.29)$$

S_n: flame propagation speed
V_g: unburned gas velocity
u_n: burning velocity

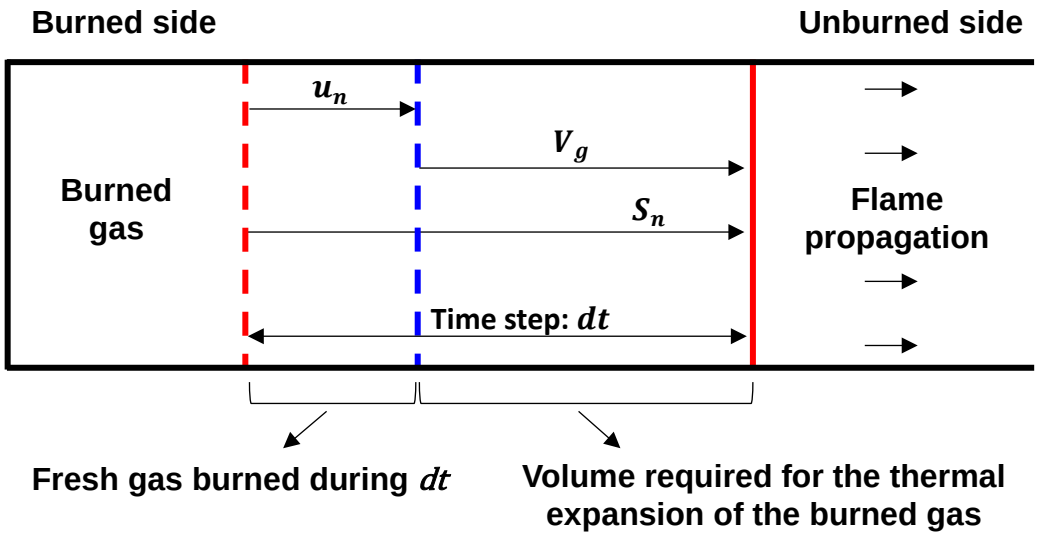

Figure 2.4 Illustration of flame propagation considering the effect of the thermal expansion of the burned gas (Burluka 2015)

The attempts to measure laminar burning velocity have been made theoretically and experimentally over many years by many researchers (Bradley et al. 1996, Zhou and Garner 1996, Balusamy et al. 2011). The methodology can be divided into two categories in the sense that stationary or propagating flame is dealt with. When investigating the former, burner methods and flat-flame methods have been widely employed. In the case of propagating flame, cylindrical tube methods, flame kernel method, soap-bubble method, spherical constant-volume vessel method, and outwardly cylindrical flame method have been adopted (Rallis and Garforth 1980).

The experimental methodology that was adopted in this research is an outwardly cylindrical flame method. Using the research engine, the flame that propagated outwardly towards the wall of the cylinder was observed, with the use of three kinds of gaseous fuels, hydrogen, methane, and propane: the detailed description of the experimental equipment is introduced in Chapter 3, and the methodology to analyse the result of the experiment is described in detail in Chapter 4.

Figure 2.5 shows a simple sketch of outwardly propagating flame in the cylinder of the research engine. In the experiment of this research, the spark plug to ignite flame was located in the centre of the cylinder. It was assumed that the height of flame in the cylinder was equal to that of the combustion chamber while the flame was recorded: the flame radius ranged from 6 to 20 mm, which is introduced in Sec. 4.2. The assumption is reasonable in the sense that the surface of the flame front reaches the upper side of the

combustion chamber and the top side of the piston crown of the research engine after the flame radius is 4 mm (Burluka 2015, Chen 2016). Therefore, where flame propagates outwardly in the cylinder, the flame propagation speed S_n can written as follows:

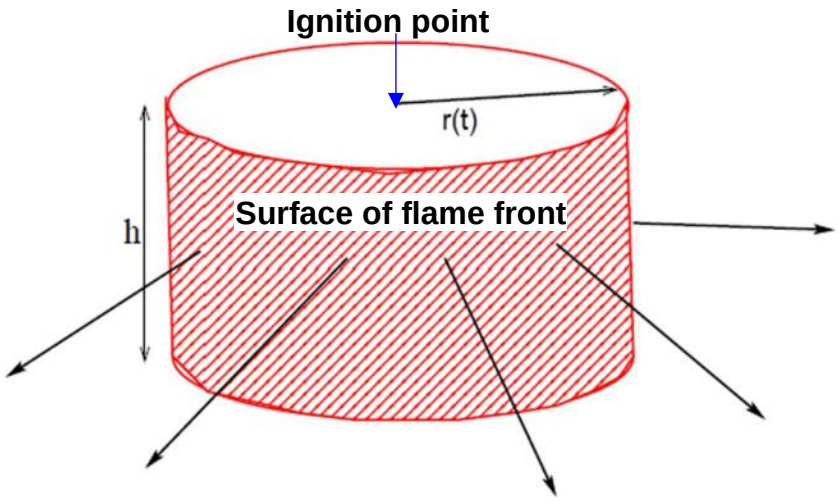

Figure 2.5 A schematic illustration of outwardly propagating flame in the cylinder of the research engine reproduced from Burluka (2015)

$$S_n = \frac{dr}{dt} \qquad \textbf{Eq.}\ (2.30)$$

S_n: flame propagation speed r: flame radius t: time

The way of calculating flame propagation speed at each point of the flame front is described in detail in Sec. 4.2.2. And the measurement of the unburned gas velocity was taken, using the PIV system, which is explained in Sec. 3.4. The calculation of unburned gas velocity at each point of the flame front, which was made through extrapolation, is also explained in Sec. 4.2.2.

2.2 Instability of laminar premixed flame and onset of cellularity

Laminar premixed flame that is initially stable tends to become unstable as the flame proceeds (Markstein 1951, Irvin and Richard 2008, Lipatnikov 2012). One of the reasons for the instability is the imbalance between flame speed and the velocity of a combustible mixture, which is named hydrodynamic

instability (Petersen and Emmons 1961). Another reason is the difference between the molecular diffusivity of a combustible mixture and the thermal diffusivity, which is called molecular-thermal diffusive instability (Hertzberg 1989). In this section, hydrodynamic instability is first described, and then molecular-thermal diffusive instability is explained. After that, it is illustrated where a cellular structure appears, and the factors in having effect on the occurrence of cellular flame are explained.

2.2.1 Hydrodynamic instability

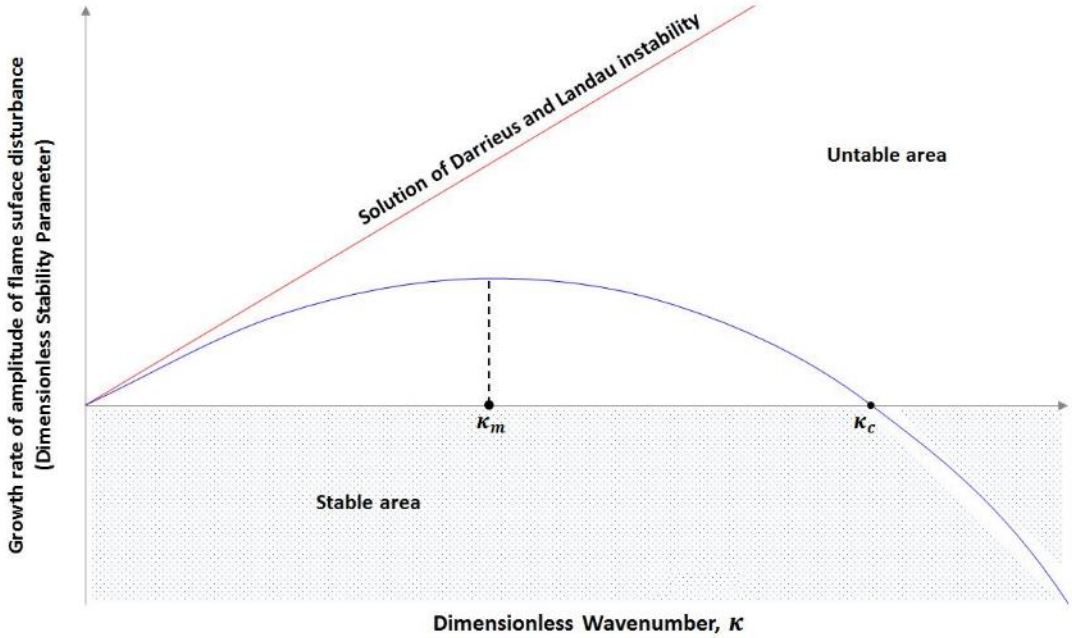

Figure 2.6 Growth rate of amplitude of flame surface disturbance *vs* dimensionless wavenumber reproduced from Petersen and Emmons (1961)

As explained by Lipatnikov (2012), two great researchers, Darrieus in 1938 and Landau in 1944, first independently examined the hydrodynamic instability of laminar premixed flame. Their theoretical work dealt with the following issue.

Their analysis for flame instability is that the flame becomes unstable to infinitesimal perturbations of all wavenumbers κ, with the growth rate of the amplitude of a flame surface disturbance being linearly increased with respect

to the wavenumber (Lipatnikov 2012): refer to the red line, the solution of Darrieus and Landau instability, in Figure 2.6.

Figure 2.6 shows that the growth rate of amplitude of a flame disturbance rises, with the increase of wavenumber until its value reaches the certain one κ_m when the growth rate is maximum. After the crest, the growth rate gradually decreases, and then becomes the cut-off value at the wavenumber κ_c. According to Markstein's investigation (1951), in the range where the value of the growth rate is negative, the flame becomes stable because the wave decays. In other words, flames are unstable only up to a certain wavenumber (Petersen and Emmons 1961).

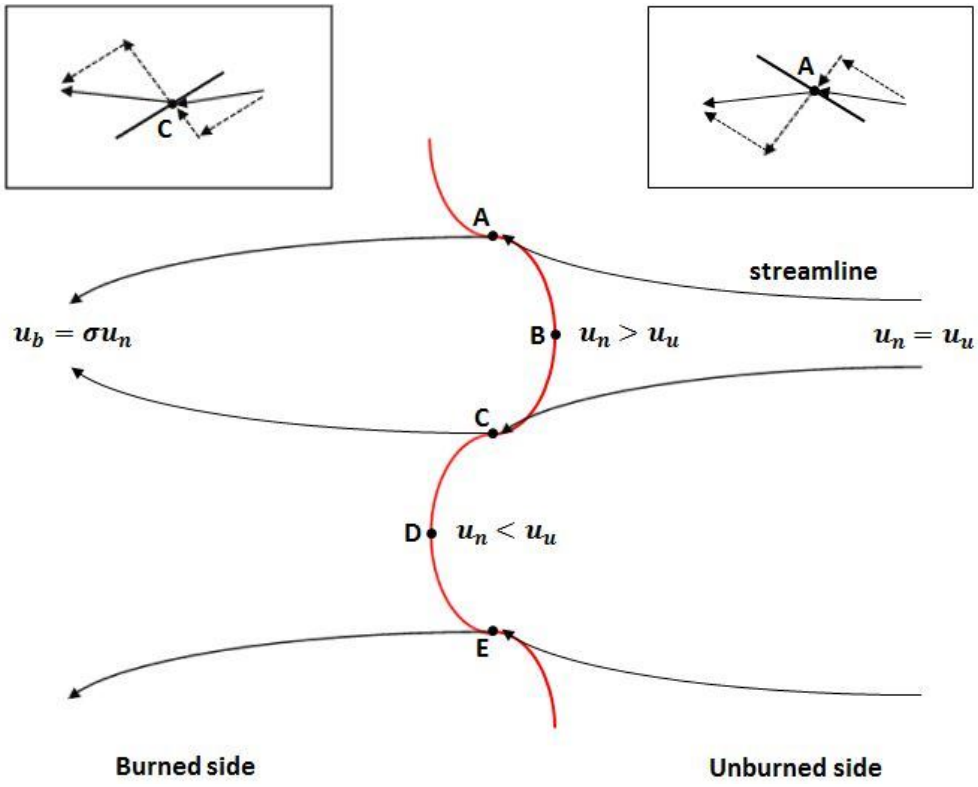

Figure 2.7 A sketch of a hydrodynamically unstable flame reproduced from Lipatnikov (2012)

Figure 2.7 shows an example of the hydrodynamic instability of flame. In the figure, the red line represents the flame surface, and the fuel-oxidant mixture moves from the right to left. Where the flame becomes hydrodynamically unstable, the physical mechanism is that the velocity of the fuel-oxidant mixture u_u in the vicinity of the point D at the flame surface increases because the mixture flow converges with the flame perturbation, whereas the flame speed u_n still keeps constant. On the contrary, owing to the divergence of the

unburned gas flow, the velocity of the fresh mixture nearby the point B becomes slower than the flame speed, $u_n > u_u$.

Since the difference between the flame speed and unburned gas velocity takes place, the growth of the convex and concave part toward the fuel-oxidant mixture gradually proceeds in the vicinity of the point D and B respectively. Therefore, the amplitude of the disturbance also gradually increases, which has more effects on the perturbation of the flame speed.

As mentioned by Lipatnikov (2012), it should be noted that the flame can have an influence on the variation of the unburned gas velocity only when the ratio of the fresh gas mixture density to the combustion product density σ varies through a cause like the expansion of the combustion product gas. As shown in Figure 2.7, the flow of the fresh gas mixture passing through the segment AC changes into the combustion product, and then converges again in the burned side, which is due to the decrease of the density that is caused by an increase in the temperature. As depicted in the insets in Figure 2.7, the variation of the density ahead and behind the flame surface makes it possible for the normal component of the flow vector to increase after the surface. The variation of the gas flow ahead and behind the flame surface can also have an effect on the pressure in the unburned side. The pressure perturbation in the area of the fresh gas mixture that is caused by the flame disturbs the unburned gas flow further.

The theoretical research of Darrieus and Landau was examined further with a variety of experiment by Markstein (1953). He assumed that flame speed is not a constant quantity but is affected by the local curvature along with the flame surface (Lipatnikov 2012). With the assumption, he could predict the stability of flame with respect to wavenumbers. If Lewis number, which represents the ratio of thermal diffusivity to mass diffusivity (Irvin and Richard, 2008) and is described in Sec. 2.2.3, is one, the flame speed in the point D increases. In contrast, the flame speed in the convex part B toward the unburned side decreases in the same condition.

If the local curvature of the flame surface is large, which means that the disturbed wavelength is short and the wavenumber is large, it has more influences on the flame speed because the effect of the curvature exceeds that of the changes in the unburned gas velocity that are caused by the flame perturbation. Therefore, the flame in the vicinity of the point D becomes stable again as the wavenumber goes beyond the certain value. The assumption that was made by Markstein has been studied theoretically, and many kinds of

experiment has also been carried out by various researchers (Truffaut and Searby 1999, Lipatnikov and Chomiak 2005). As explained Lipatnikov (2012), the outcomes of the experiment show a good agreement with the results of the theoretical investigation.

2.2.2 Molecular-thermal diffusive instability

Where laminar premixed flame is initially planar and stable, if the imbalance between the molecular and thermal diffusivities takes place along the flame surface, the flame will start becoming curved and unstable (Law 2006b). The molecular-thermal diffusive instability can be seen in unburned gas mixtures with high molecular diffusivity of the deficient reactant and low molecular diffusivity of the excess reactant. And it can make the local flame speed increases or decreases depending on the shape of the flame surface. The local variation of enthalpy, mixture composition, reaction rate, and consumption velocity, causes a local change in flame speed (Lipatnikov 2012).

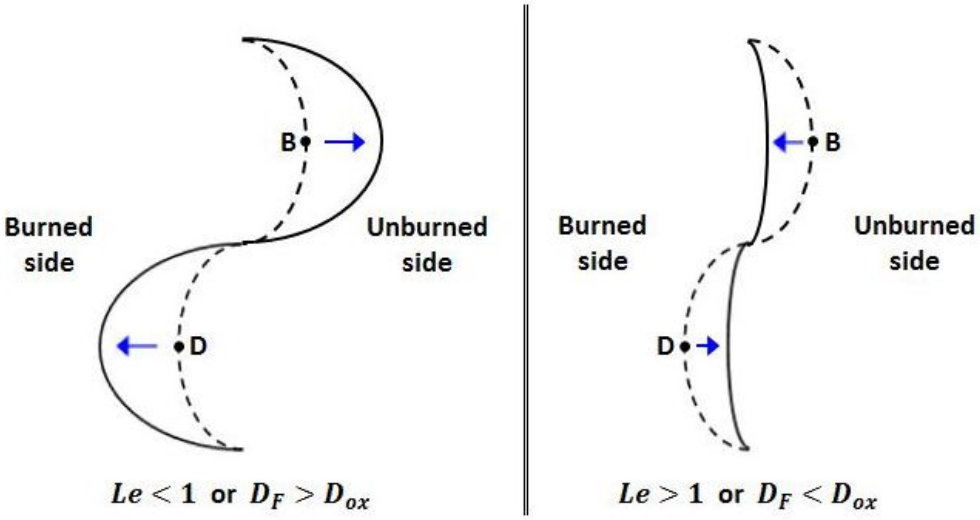

Figure 2.8 A sketch of molecular-thermal diffusive instability reproduced from Lipatnikov (2012)

Figure 2.8 shows how flame front is changed by the molecular-thermal diffusive instability. In the figure, the black dashed and solid lines represent the flame fronts before and after the molecular-thermal diffusive instability proceeds.

Where Lewis number *Le* is smaller than one, the chemical energy which is provided in the vicinity of the point B by the molecular diffusivity is more than

the heat loss through molecular conductivity. In the case that the molecular diffusivity of the deficient reactant D_F is larger than that of the excess reactant D_{ox}, the equivalence ratio near the point B locally changes toward the stoichiometric condition because the diffusion of the deficient reactant becomes more active than that of the excess reactant. In the two cases $Le < 1$ or $D_F > D_{ox}$, a local increase in flame speed takes place in the vicinity of the point B. However, the diametrically opposite phenomenon in the vicinity of the point D appears under $Le < 1$ or $D_F > D_{ox}$. That is, with the chemical energy and the effect of the diffusion of the deficient reactant, a local decrease in flame speed rather occurs.

On the contrary, where $Le > 1$, the chemical energy that is supplied in the vicinity of the point B is less than the amount of the heat loss, which causes the decrease of the flame speed in the local area. And where $D_F < D_{ox}$, the equivalence ratio in the vicinity of the point B becomes lean. Hence, the flame speed in the vicinity of the point B locally decreases. On the other hand, a local increase in flame speed in the point D takes place under the same condition. The changes at the point B and D enable the magnitude of flame disturbance caused by hydrodynamic instability, which is mentioned Sec. 2.2.1, to become stable with respect to the weak perturbation of the flow velocity (Lipatnikov 2012).

2.2.3 Cellularity: onset and development for growing flames

Many researches have been carried out to understand hydrodynamic and molecular-thermal diffusive instability, and the scholars have done many experiments to prescribe the characteristics of laminar flame in various experimental conditions. A cellular structure is observed when a flame surface becomes wrinkled irregularly, and cellular flame sometimes splits into a small size of the structures. The condition where a cellular structure appeared on a flame surface was described by Zeldovich (1949). He analysed the diffusion phenomena which occurred in the combustion process, using the combustible mixtures with various molecular properties. Cellular structures on a flame surface can be seen in the condition where the molecular diffusivity of a fuel-oxidant mixture is greater than the thermal diffusivity. The imbalance between the molecular and thermal diffusivities brings about a local diffusion enrichment of the perturbed surface element at a greater rate than the heat which is lost by thermal conductivity (Zeldovich 1949).

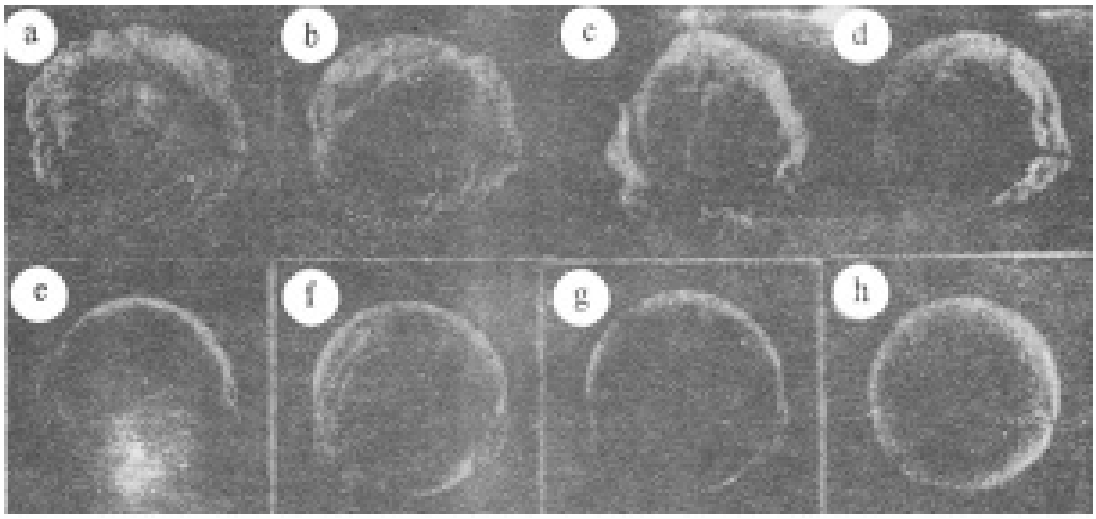

	a	b	c	d	e	f	g	h
α	12	6	4	2	1.5	1.2	1.1	1.0
n	4.5	10	15	15	15	15	15	15
u_n [m/s]	0.27	0.29	0.15	0.2	0.17	0.13-0.14	0.12	0.10-0.12

Figure 2.9 Change in the structure of laminar flames of $2H_2 + \alpha O_2 + nN_2$ (Karpov 1982)

Figure 2.9 shows the schlieren photographs of laminar flames of hydrogen where $2H_2 + \alpha O_2 + nN_2$ at $\alpha + n = constant$ and the product temperature is fixed within 20℃ (Karpov 1982). As seen in the figure, it is obvious that the leaner the combustible mixture becomes, the more pieces the flame surface break into: refer to the inset a to d. On the other hand, the size of the cells gradually becomes large as α decreases: refer to the inset d to h. In the case that α is larger than four, the change of the flame structure can hardly be identified because the flame surface is broken up too much.

Figure 2.10 shows the photographs of the flame of the mixture $2H_2 + 6O_2 + nN_2$ with respect to the change in the amount of nitrogen. As the concentration of the nitrogen diminishes, the flame surface breaks into more pieces and the size of the cell decreases (Karpov 1982). According to the relevant researches (Karpov and Severin 1980, Hertzberg 1989), laminar flames in combustible mixtures where Lewis number is smaller than one, that is, the molecular diffusivity of the deficient reactant is greater than its thermal diffusivity, are usually developed as cellular structures. Through a variety of experiment by

many researchers, it was concluded that flames should become stable if the fuel-oxidant mixture that consists of heavy hydrocarbon is lean. In the case of hydrogen, the flame should also become stable if the combustible mixture is rich.

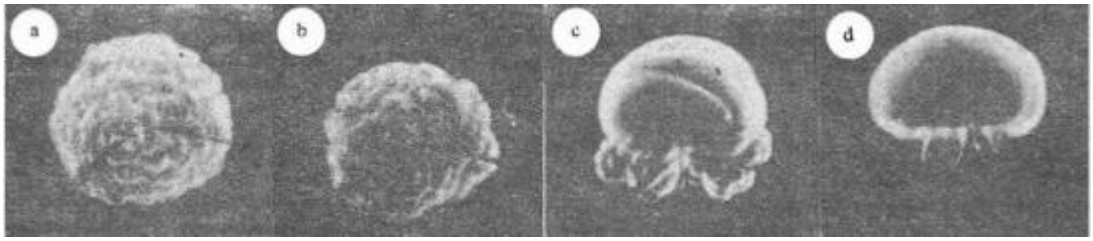

	a	b	c	d
n	6	10	14	16
T_b [K]	1430	1200	1050	970
u_n [m/s]	0.45	0.29	0.13	0.07
$\frac{\kappa}{u_n}$ [cm^3]	0.0045	0.0070	0.018	0.0285

Figure 2.10: Effect of parameter $\frac{\kappa}{u_n}$ on laminar flame structure in the mixture *2H₂ + 6O₂ + nN₂* (Karpov 1982)

Figure 2.11 illustrates the effect of selective or preferential diffusion of fuel and oxygen into the flame zone depending on the composition of a fuel-air mixture. When laminar flame propagates towards the combustible mixture, which is assumed that the mixture is perfectly well mixed and homogeneous, a radical change in the concentration of the reactants is generated: refer to the solid green line in Figure 2.12. It involves the large diffusion of the fuel-air molecules that comes from the unburned gas. Where one reactant of the combustible mixture, the fuel or oxidant molecules, is more diffusive, it will be dominant over the other. Hence, the selective diffusion of the dominant molecules will occur.

In the case of a light hydrocarbon-air mixture, which is shown in Figure 2.11 (A), the fuel molecules diffuses selectively into the propagating flame, and the composition of the mixture becomes richer than the initial composition. The change brings about the change in the burning velocity. As seen in Figure 2.11 (B), this phenomenon can be seen in a heavy hydrocarbon-air mixture.

The difference is that the selectively diffusing reactant is oxygen molecules and the mixture behave as though the composition becomes leaner than the initial composition.

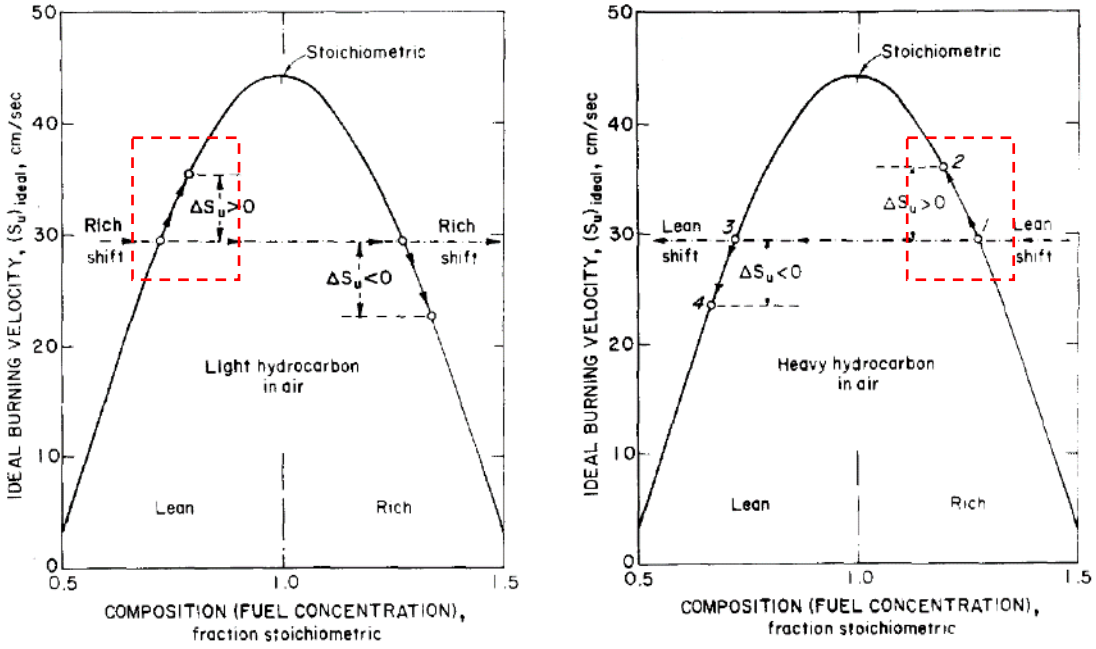

Figure 2.11 The effect of selective diffusion of fuel (A) and oxygen (B) into the flame zone cited from Hertzberg (1989)

Because of the selective diffusion, the variation in the burning velocity also takes place in the case of the light and heavy hydrocarbon-air mixture. In relation to the red dashed boxes of Figure 2.11 (A) and (B), it should be noted that the selective diffusions caused by the fuel and oxygen molecules results in an increase in burning velocity in the lean and rich condition respectively, compared with the burning velocities in the initial composition. Cellular flame structures mainly have a tendency to show up in the region where the increase of burning velocity in light and heavy hydrocarbon-air mixtures takes place (Hertzberg 1989, Lipatnikov 2012).

The reason is that as mentioned in Sec. 2.2.2, since the molecular diffusivity of light hydrocarbon is larger than that of oxygen, the equivalence ratio at the local area of the flame front increases towards the stoichiometric condition. In the case of a heavy hydrocarbon-air mixture, the deficient reactant, oxygen, diffuses selectively towards the local area of the flame front, which causes the equivalence ratio to decrease towards the stoichiometric condition. Therefore, a part of the flame front is curved or wrinkled, and even cellular structures can

be observed. Based on this, the experiment of the hydrogen- and methane-air mixture in this research was carried out in the lean condition, which was close to their flammability limits. Regarding the propane-air mixture, the experiment was conducted in the rich condition, which is mentioned in detail in Chapter 3.

However, it should be mentioned that, as described by Konnov (2005), the cellular structures were observed where propane-air mixtures were in the stoichiometric range. And in the case of hydrogen-oxygen-nitrogen mixtures, where they were in the rich condition, cellular structures were observed (Botha and Spalding 1954, Mitani and Willimas 1980). Since there is still doubt on when a cellular structure can be observed, it is required to investigate the conditions of occurrence of cellular flame in detail with respect to combustible mixtures.

Lewis number, *Le*, which is already mentioned in Sec. 2.2.1 and 2.2.2, is defined the ratio of thermal diffusivity to molecular or mass diffusivity and a dimensionless number (Hewitt, Shire et al. 1998). In the assumption to derive the equation of unperturbed laminar premixed speed or normal flame speed u_n in Sec. 2.1, the molecular diffusivity for fuel and oxidant and the thermal diffusivity are equal $D_F = D_{ox} = \kappa$, that is, Lewis number is unity.

Let us assume that Lewis number is not one. Where the temperature profile T, which is the black solid line in Figure 2.12, is kept and the laminar flame speed is unchanged, if the molecular diffusivity of the deficient reactant D_F is increased, that is, *Le* < 1, the mass fraction profile Y_F would become wider than before: this means in Figure 2.12 that the green solid line changes into the green dashed line.

Comparing the fuel-oxidant mass fraction of the solid and dashed green profiles in the reaction zone, the amount of the mass fraction in the green dashed profile is smaller than that of the mass fraction in the green solid profile. Hence, the reaction rate would progressively decrease, and the flame speed would also become slower than before (Lipatnikov 2012). Where Lewis number is less than unity, the flame speed becomes proportional to the value of the number.

On the contrary, when the thermal diffusivity is equal to or larger than the molecular diffusivity, i.e. $Le \geq 1$, the flame that propagates at a constant speed becomes unstable, and the flame speed oscillates. As already mentioned in Eq**.** (2.27) in Sec. 2.1, an unperturbed laminar premixed flame speed depends strongly on the molecular and thermal diffusivities.

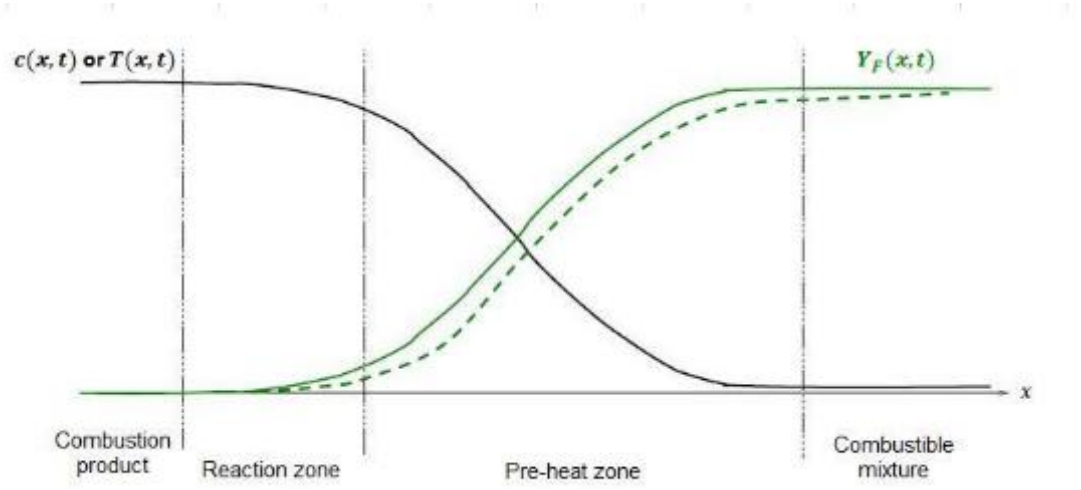

Figure 2.12: A simple sketch of the effect of Lewis number on the structure of an unperturbed laminar premixed flame (Burluka 2014)

2.2.4 Effects of pressure, temperature, and mixture composition

When combustion starts, the initial pressure and temperature have an influence on the variations of flame propagation speed, burning velocity, and other properties in great way. The investigation on the effects of the initial pressure and temperature at the start of combustion has been carried out for many years. Through a variety of the experiments on hydrocarbon combustion, the correlation between pressure, temperature, and laminar premixed flame speed was derived. The relevant equation could be represented as follows (Dugger and Graab 1953, Metghalchi and Keck 1980, Burluka 2014):

$$u_l = u_n \left(\frac{T_u}{T_o}\right)^{\alpha} \left(\frac{P_u}{P_o}\right)^{\beta} (1 - x_b^{0.77}) \qquad \textbf{Eq.} (2.31)$$

u_l: laminar burning velocity
u_n: unperturbed laminar burning velocity
T_u: initial temperature
T_o: reference temperature
P_u: initial pressure
P_o: reference pressure
α: temperature index
β: pressure index
x_b: mole fraction of the residual burned gas

In Eq**.** (2.31), u_l and u_n are laminar burning velocity and unperturbed laminar burning velocity respectively. T_o and P_o represent the reference temperature and pressure and are regarded as 298 K and atmospheric pressure. T_u and

P_u indicate the initial temperature and pressure of unburned gas respectively when combustion starts. x_b is the mole fraction of the residual burned gas. Many researchers have carried out the relevant experiments to measure flame speed and calculate unperturbed laminar premixed flame speed u_n, with the use of various hydrocarbon-air mixtures (Metghalchi and Keck 1980, Gu et al. 2000, Law et al. 2005, Konnov 2015). In relation to the combustion of hydrocarbon gases, it is typical that the values of the index α and β are positive and negative respectively. In the case of the methane-air mixture where its equivalence ratio is stoichiometric, the α and β are approximately 1.6 and -0.4 respectively.

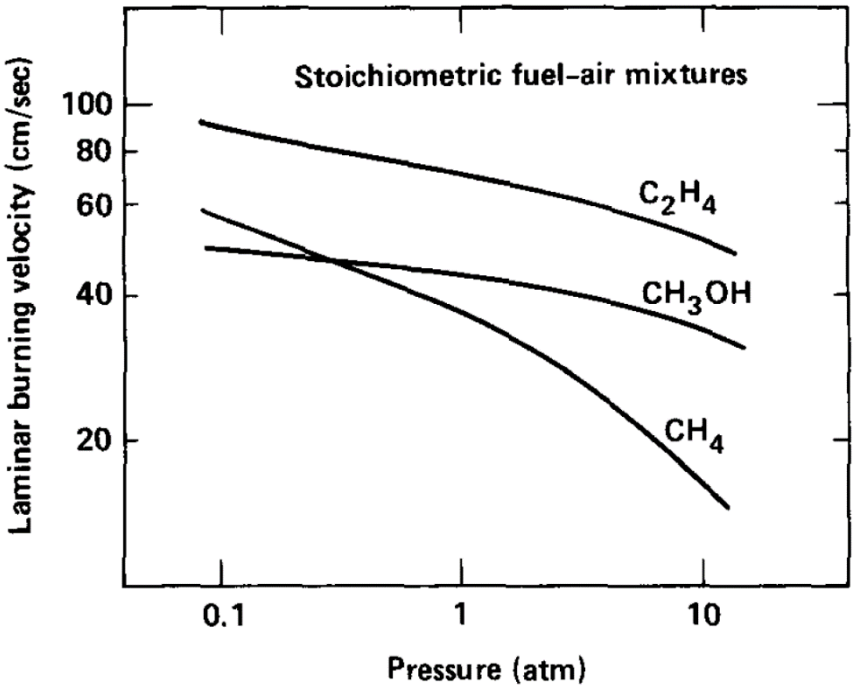

Figure 2.13 Variation in laminar burning velocity with respect to pressure for stoichiometric fuel-air mixtures (Westbrook and Dryer 1984)

Figure 2.13 shows the variation in laminar burning velocity as a function of pressure. As expected through Eq**.** (2.31), as the initial pressure increases, the laminar burning velocities of the fuel-air mixtures gradually decreases. Figure 2.14 shows the relationship between the laminar burning velocity and the initial temperature of unburned gas. The laminar burning velocity rises, with an increases in the initial temperature of the unburned gas. Compared with the declined of the laminar burning velocity with respect to the initial pressure, the growth of the burning velocity with respect to the initial temperature is relatively large.

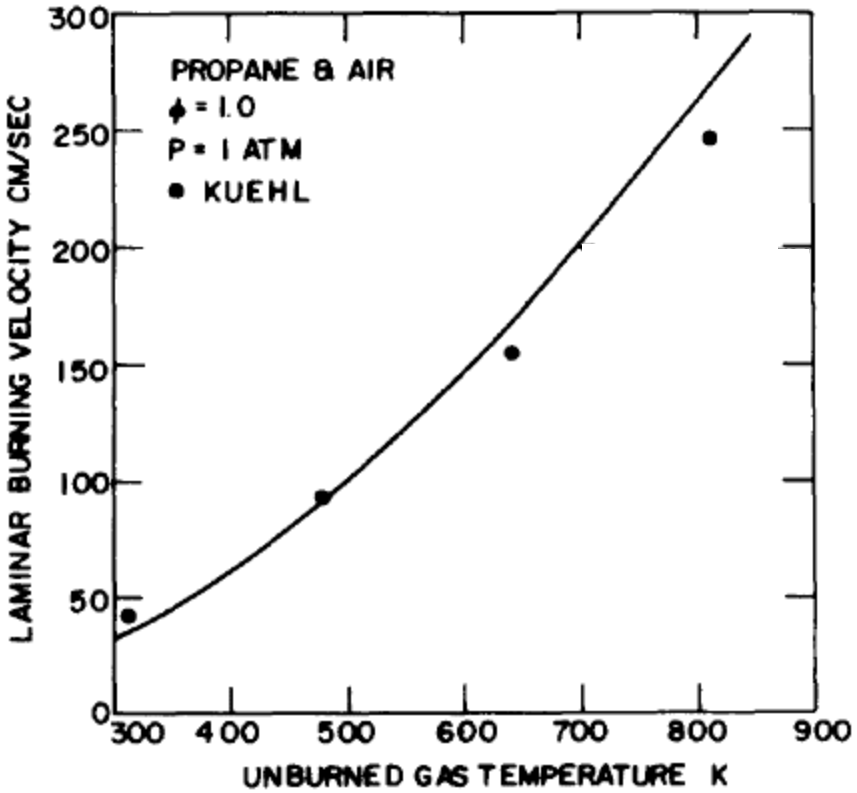

Figure 2.14 Variation in laminar burning velocity for the propane-air mixture (Metghalchi and Keck 1980)

Figure 2.15 shows the schlieren flame images, which were taken using the constant-pressure chamber (Law et al. 2005). The hydrogen-propane-air mixture was adopted as fuel, and its equivalence ratio was 0.6. The proportion of mixing hydrogen with propane α was 0.5: the method of calculating α and other information are described in detail in the reference. As seen in the figure, the flame instability is observed at the elevated pressures. Regardless of a change in the pressure, in the beginning of the combustion, which is the uppermost row of the figure, the flame surfaces are smooth and stable. In all the case of the figure, as the combustions proceed, the flames become wrinkled and unstable in the end. When the pressure is atmospheric, which is the left column of the figure, the flame surface seem to keep at the stable condition although some cracks can be seen at the last stage.

However, as shown in the middle and right columns of the figure, as the pressure rises, the state where the flame becomes unstable shows up more quickly. Moreover, it is certain that the higher the pressure becomes, the more pieces the flame surfaces break into. While the flame surfaces break into

pieces, the size of the cells tend to progressively become smaller. According to the researches that have been carried out over many years (Law et al. 2005, Hu et al. 2009, Far et al. 2010), it is obvious that the surface of flame front becomes destabilised as the initial pressure increases.

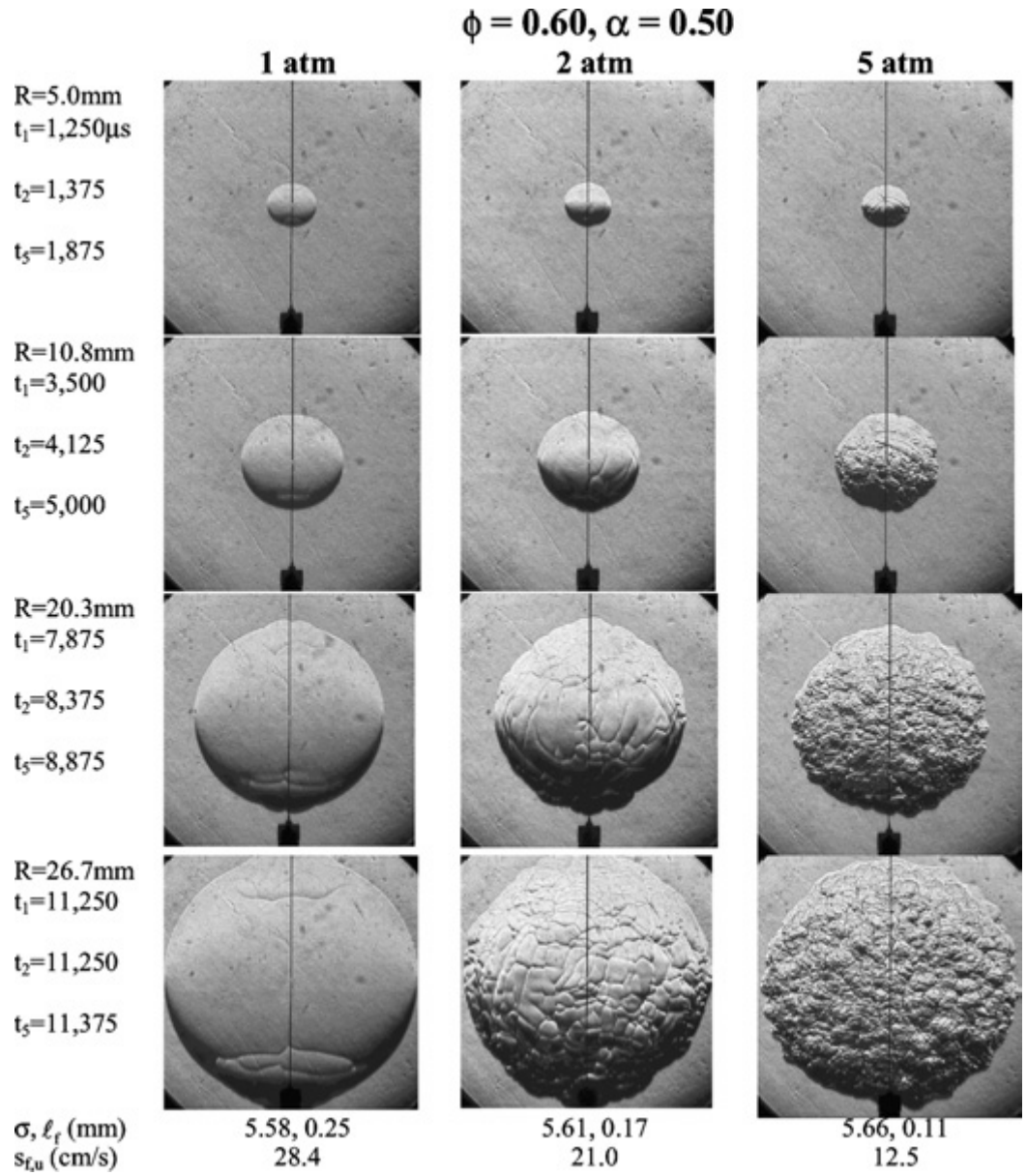

Figure 2.15 Flame instability of hydrogen-propane-air mixtures at 1, 2, and 5 atm. Equivalence ratio: 0.6 / initial temperature: 298 K (Law et al. 2005)

In order to characterize the composition of a fuel-air mixture, there are a number of terms, which are equivalence ratio, relative air-fuel ratio, mixture strength, percentage excess air and so forth. Among the various terms, equivalence ratio is one of the widely used parameters. Its definition is that

the ratio of the amount of fuel available to the one of oxygen that is actually provided is normalized by the ratio of the amount of fuel to the one of air when it is stoichiometric. The stoichiometric ratio of fuel and air means that the theoretically optimum amount of fuel and air is used in chemical reaction where it is assumed that its chemical reaction proceeds to completion (Giunta 2016).

$$Equivalence\ ratio\ \phi = \frac{\left(\frac{Fuel}{Air}\right)_{actual}}{\left(\frac{Fuel}{Air}\right)_{stoichiometric}} \qquad \textbf{Eq.}\ (2.32)$$

Where the equivalence ratio is smaller than one, the fuel-air mixture is said that it is at the lean condition. In contrast, in the case that equivalence ratio is larger than one, the fuel-air mixture implies that it is at the rich condition. The stoichiometric condition means that the equivalence ratio is one.

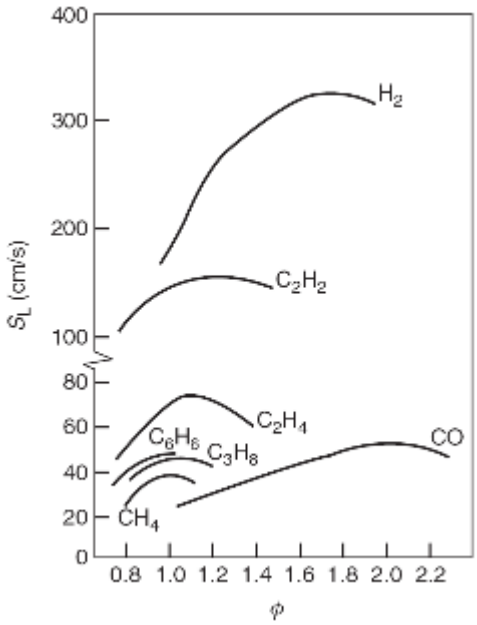

Figure 2.16 General variation in laminar flame speeds with equivalence ratio ϕ for various fuel-air mixtures. Initial pressure: 1 atm / initial temperature 298 K (Irvin and Richard 2008)

Equivalence ratio is also one of the most invaluable factors in affecting the changes of flame propagation speed, burning velocity, and other properties. The ratio is frequently used for prescribing the correlation between itself and

flame speed. Relevant researches have been conducted over many years (Egolfopoulos and Law 1990, (Gu et al., 2000, Park et al., 2011, Burluka et al., 2015).

Figure 2.16 shows the variation in laminar flame speeds with respect to equivalence ratio. Except for the cases of hydrogen and carbon monoxide, the hydrocarbon fuels have the maximum laminar flame speeds when their equivalence ratios are almost stoichiometric or slightly higher than one. As they deviate from the stoichiometric condition, their speeds gradually decrease.

Figure 2.17 shows the schlieren images taken in the constant pressure chamber as the flames develops (Law 2006a). The fuels were the hydrogen-air and propane-air mixtures, and the initial pressure and temperature were 5 atm and 298 K respectively. The main parameter of the experiment was equivalence ratio. In the case of the combustion for the hydrogen-air mixture, where the mixture composition is at the lean condition, which is $\phi = 0.6$ in the figure, the surface of the flame front starts to become unstable at the early stage. As the flame develops, the flame front breaks into more pieces. On the contrary, where the equivalence ratio is 4.0, although some cracks can be seen at the end, the surface of the flame front keep smooth and stable regardless of the development of the flame.

Similarly, such phenomenon is seen in the case of propane-air mixture in the figure. However, the difference between two mixtures is that the propane-air mixture becomes progressively destabilized where its equivalence ratio is rich, which is $\phi = 1.4$. As mentioned in Sec. 2.2.2 and 2.2.3., the diffusivity of the hydrogen molecules dominates over that of the oxygen molecules when the mixture is lean, and thus the flame becomes destabilised. In the case of the rich propane-air mixture, the diffusivity of the oxygen molecules is dominant to that of the propane molecules, which brings about the flame instability.

In this research, three kinds of gaseous fuels, hydrogen, methane, and propane, which have been widely used as energy sources, were adopted to investigate the characteristics of their combustion. This research concentrated mainly on the combustion where the cellular flame of the gaseous fuels took place. Referring to the researches carried out by Hertzberg, Law and others mentioned in Sec. 2.2.3, the equivalence ratios of the fuel-air mixtures were selected. In the case of the hydrogen- and methane-air mixtures, the experiment was carried out at the lean condition, whereas the experiment of the propane-air mixture was conducted at the rich condition. The values of

equivalence ratios of three gaseous fuels were close to their flammability limits. The relevant description is mentioned in detail in Chapter 3.

In this study, the experimental condition where cellular flame was a laminar condition. Hence, turbulent premixed flame is not mentioned in this paper. However, it was confirmed whether a laminar condition in the experiment rig was formulated or not prior to the actual measurement. The relevant theoretical background and result are shown in Appendix A.

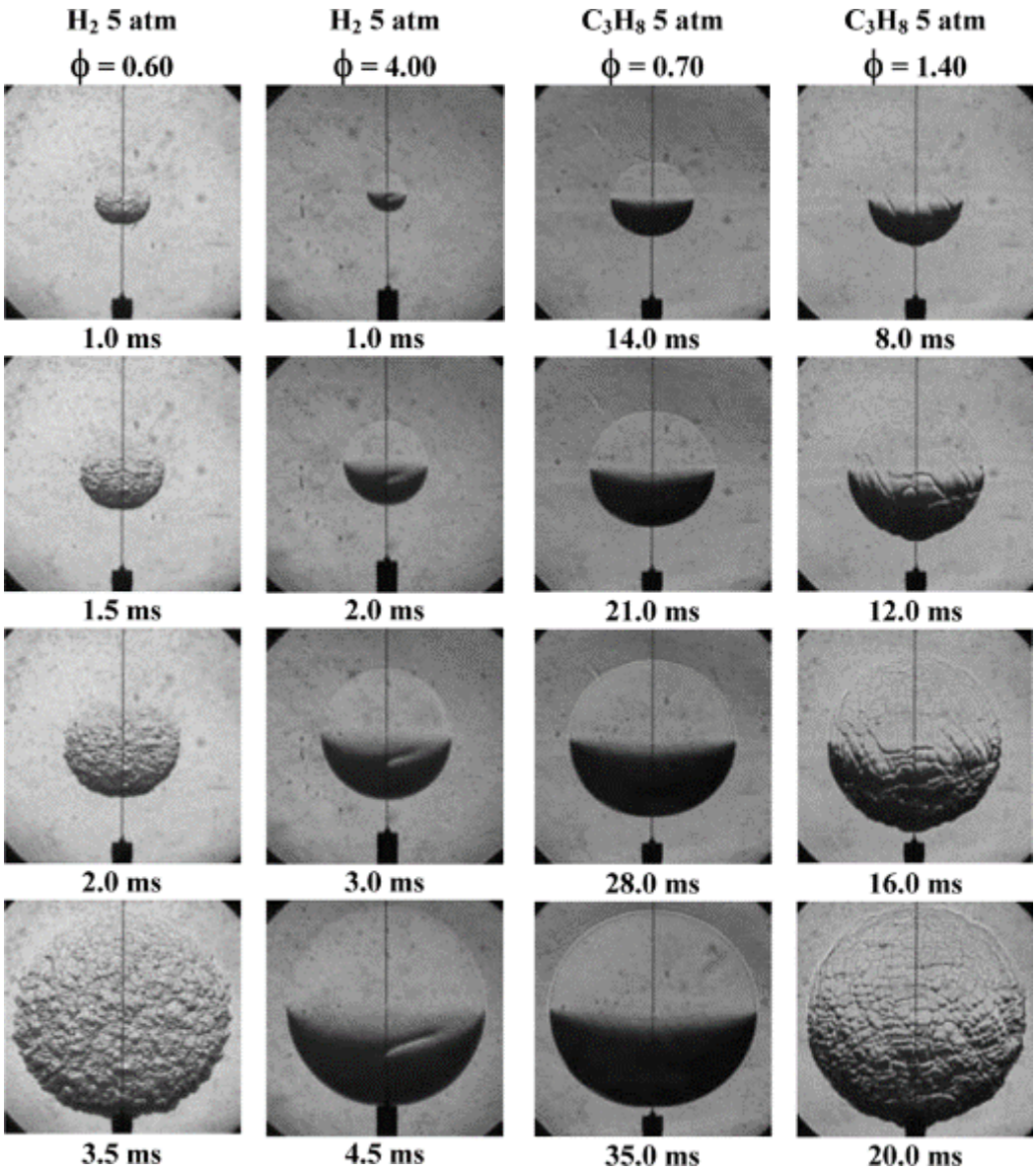

Figure 2.17 Flame instability of hydrogen-air and propane-air mixtures with respect equivalence ratio. Initial pressure: 5 atm / initial temperature 298 K (Law et al. 2006a)

Chapter 3 Experimental equipment

In recent years, using LUPOE-2D, Leeds University Ported Optical Engine-Version 2 with Disc-head, the Leeds combustion research group has carried out excellent and remarkable researches to prescribe a combustion process, with the use of various kinds of liquid and gaseous fuels (Dawood 2011, Hussin 2012, Ling 2014, Chen 2016). Especially, with the use of liquid fuels, most of the studies were conducted at a high speed which of the research engine was operated higher than 750 rpm. These researches focused on investigating the characteristics of flame where the experimental conditions were at turbulent conditions (Hussin 2012, Ling 2014). Except for the case of Chen's research (2016), where the research engine has been operated at a low speed, the investigations into the characteristics of laminar premixed flame with gaseous fuels have rarely been carried out.

In order to investigate laminar combustion inside a cylinder at a low speed, the research engine was modified. The reduction gear and pulley between the prime mover motor and the crank shaft enabled the research engine to be operated at a low speed. For the supply of gaseous fuels, the fuel supply system was also modified, and three kinds of gaseous fuels could be supplied safely and separately at the same time.

The purpose of the current study is to investigate the characteristics of cellular flame inside the cylinder of the engine, including the flow field of unburned gas ahead of the flame front to prescribe the correlation between the movement of the combustible mixture and the flame instability. To achieve the aim, the PIV system, particle image velocimetry system was set up. The system was comprised of the double-pulsed high speed laser, high speed digital camera, and others.

In this chapter, the research engine, LUPOE-2D, is first described in detail, and then the fuel and air supply system is introduced. After that, the description of how to obtain pressure data and the way of calculating the temperature of a fuel-air mixture where it is compressed inside the cylinder of the engine are given. The PIV system is also illustrated, and it is presented whether the research engine can create a laminar condition. Lastly, the engine control and data acquisition system is described, and the experimental procedure is mentioned at the end of this chapter.

3.1 Reciprocating combustion chamber: LUPOE-2D

LUPOE-2D, Leeds University Ported Optical Engine version 2 with Disc-head, is based on a commercial Lister Petter-PH11 diesel engine, which is a single-cylinder engine. The research engine was developed by the Leeds combustion research group. It has been retrofitted continuously corresponding to the objectives of the researches (Hicks 1994, Butler 1999, Abdi Aghdam 2003, Murad 2006).

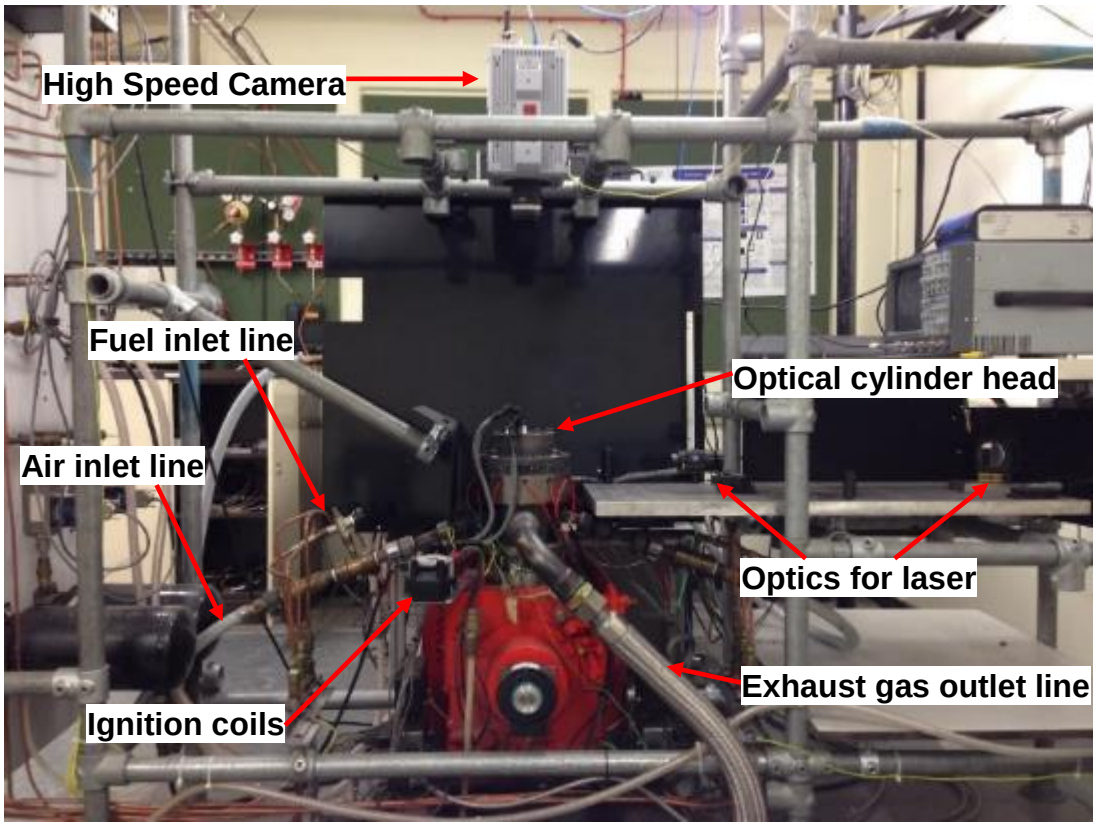

Figure 3.1 Photograph of LUPOE-2D and each instrument

Figure 3.1 shows the photograph of the research engine. The overhead valve which was mounted at the place of the cylinder head was removed to observe the inside of the cylinder easily during the combustion process and to minimize an unnecessary flow of unburnt gas that can be caused by the configuration. And then the optical cylinder head was designed and installed. Three windows of the cylinder head were installed at the top and two diametrically opposite sides respectively. The top window made it possible to have optical access to a combustion phenomenon inside the cylinder of the research engine, and the two opposite side windows enabled the light source of illuminating seeding

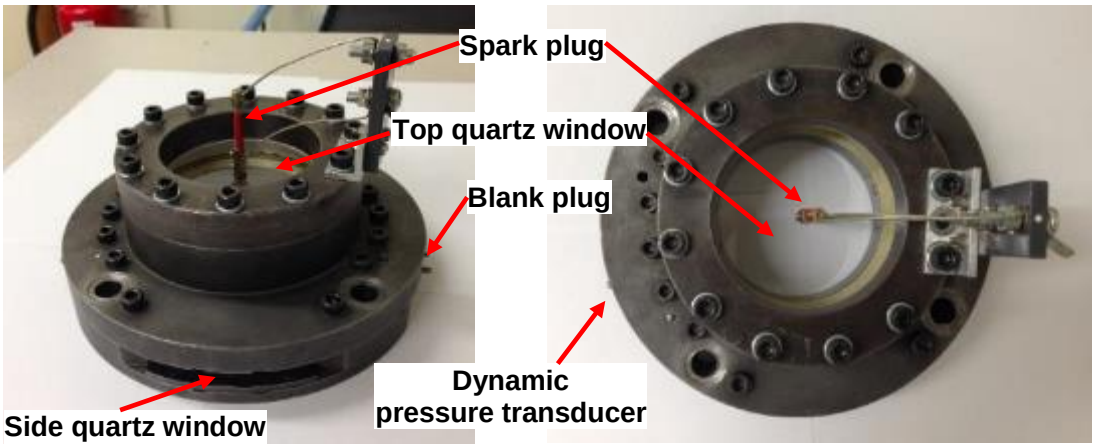

Figure 3.2: Photograph of disc-shaped optical engine head

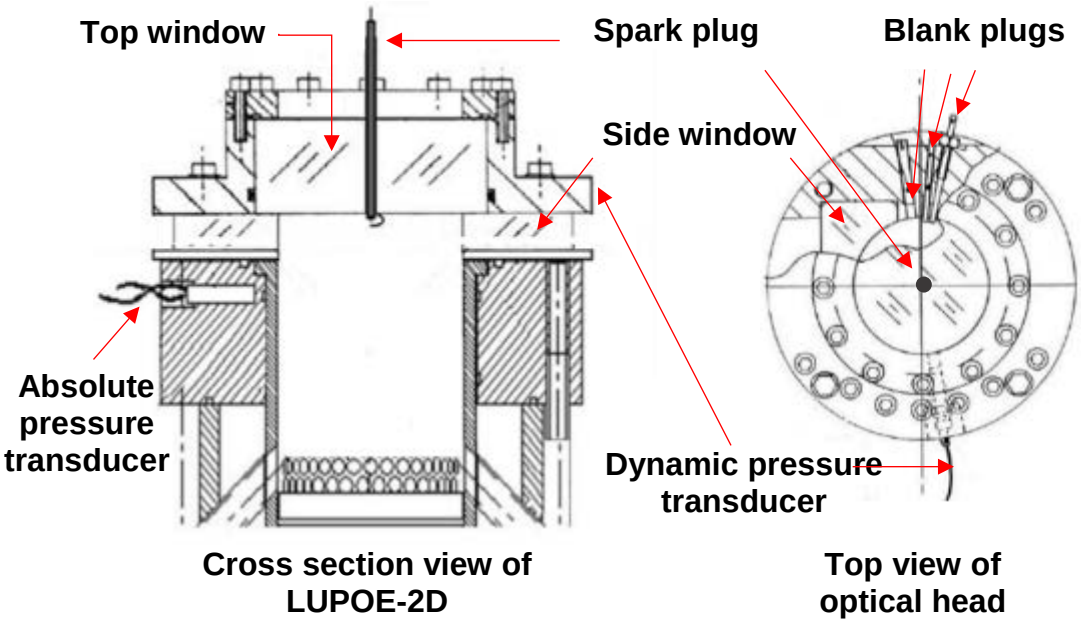

Figure 3.3: LUPOE-2D and optical head plans modified from Ling (2014)

particles, which is a laser sheet in this research, to be provided for the combustion chamber.

The photographs of the optical cylinder head and its plans are shown in Figure 3.2 and Figure 3.3. In order to measure in-cylinder pressure during combustion process, two kinds of pressure transducers were adopted. A dynamic and absolute pressure transducer were fitted in the side of the optical head and the cylinder wall respectively. As seen in Figure 3.3, the location of the absolute pressure transducer is lower than that of the dynamic pressure transducer. The timings when the absolute pressure transducer is opened and

closed by the movement of the piston are presented in Table 3.1. Using two pressure transducers, the variation of the in-cylinder pressure could be measured. In Sec. 3.3, the measurement of in-cylinder pressure is described in detail.

A 12 V double ignition coil transformer and the customized spark plug were used for the ignition system. The ignition coil transformer used in the current research is commonly called double spark ignition coils in the automotive industry. It is typically used in a spark ignition engine with even numbers of cylinders, and provides the electrodes of the spark plug with a proper electrical spark that is enough electrical energy to initialize combustion.

As seen in Figure 3.3, the spark plug was mounted in the centre of the top window in the optical cylinder head. A 0.5 mm diameter of steel wire is used as anode. It is sheathed with a 3.0 mm of alumina tube, which acts as cathode. The length of the steel wire is longer than that of the alumina tube, and a plastic tube is inserted as insulator between the inner steel wire and outer alumina tube. One tip of the inner steel wire is covered with a brass tube that is soldered with a 1.0 mm diameter of steel wire. It is connected to the terminal of the ignition coil transformer. The other tip is the electrode for the occurrence of ignition spark inside the cylinder. Similarly, another brass tube is also used for one end of the alumina tube and is connected to the terminal of the ignition coil transformer through a soldered steel wire. A 0.5 mm diameter of L-shaped steel wire is soldered at the other end of the outer alumina tube. The gap between the ends of the 0.5 mm steel wire and L-shaped steel wire was less than 1.0 mm to avoid misfire by the absence of an electrical spark. And it was confirmed that the occurrence of spark inside the cylinder was in good condition.

In relation to the ignition spark, the electrical interference can give rise to problems for other electrical instruments such as a high speed digital camera, laser, and so on. This is because the instantaneous voltage of ignition spark is very high. Hence, earth cables were used to minimize the effects: the detailed description is presented in Sec. 3.6.4. The length of the protruding part of the spark plug toward the combustion chamber was 4.0 mm, and the entire diameter of the part related to the spark plug was 3.0 mm. A small size of the spark plug enabled to have the maximum full-bore access to a combustion process from the top view when the flame images were recorded. The timing when ignition spark occurred could be controlled through an electrical signal which was generated by the micro-controller in the engine control system, which is mentioned in Sec. 3.5 in detail.

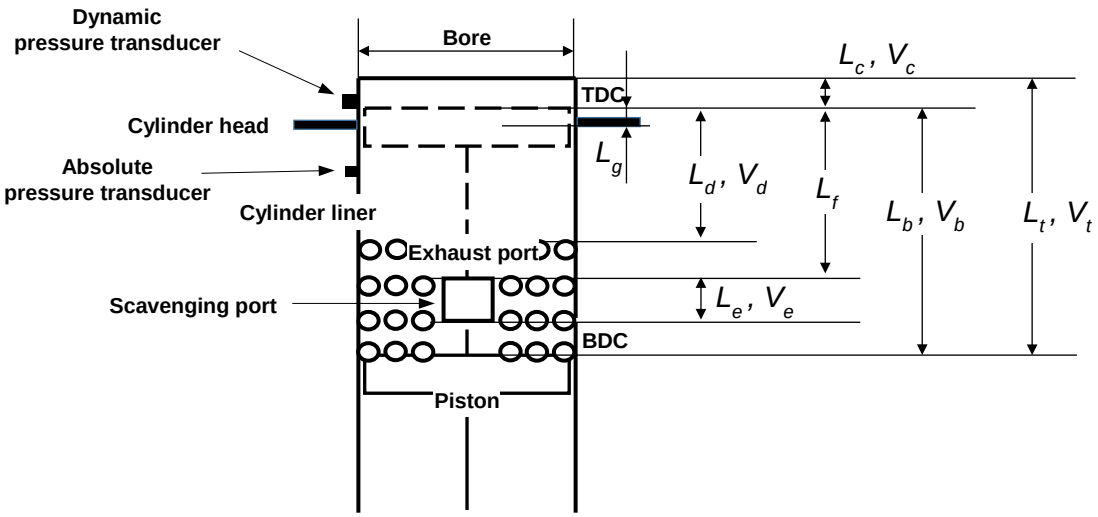

Figure 3.4: Dimension of LUPOE-2D: refer to Table 3.1

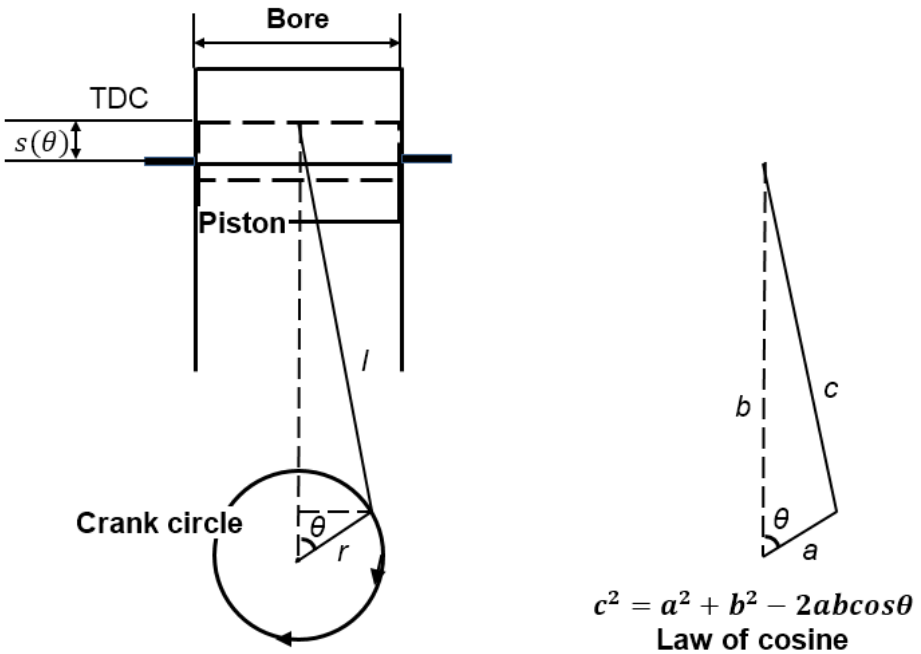

$$s(\theta) = l + r - \left(rcos\theta + \sqrt{l^2 - r^2 sin^2\theta}\right)$$

Figure 3.5: Piston displacement in terms of the variation of crank angle

Table 3.1 Geometrical specification of LUPOE-2D: refer to Figure 3.4

Bore [mm]	80
Clearance [mm], L_c	8
Stroke [mm], L_b	110
Connecting rod [mm]	232
Total length [mm], L_t	118
Effective stroke [mm], L_d (From TDC to the point at which the exhaust ports completely close)	72
Height of scavenging port [mm], L_e	17
Length of the protruding piston part [mm], L_g	12
Loss stroke [mm], L_f-L_d (L_f: 78 mm)	6
Connecting rod [mm]	232
Diameter of an exhaust port [mm], L_j	10
Clearance volume [mm^3], V_c (the volume of the protruding part of the spark plug from the cylinder head to cylinder: 23 mm^3)	40189
Swept volume [mm^3], V_b	552920
Effective swept volume [mm^3], V_d (From TDC to the point at which the exhaust ports completely close)	361911
Total volume [mm^3], V_t	593110
Compression ratio	14.75
Effective compression ratio	10.00
Scavenging port close[° CA bTDC/aTDC]	109.4
Exhaust port close [° CA bTDC/aTDC]	101.2
Absolute pressure transducer close [°CA bTDC/aTDC]	69.8
Diameter of the hole for absolute pressure transducer [mm]	4
Diameter of the hole for dynamic pressure transducer [mm]	5.5
Engine operating speed range [rpm]	10 - 200

Figure 3.4 and Figure 3.5 show the dimension of the research engine and the calculation of the piston displacement with regard to the variation of crank angle. After measuring the position of each part vertically from TDC, each crank angle was calculated. Table 3.1 shows the geometrical specification of LUPOE-2D. As the piston moves from BDC to TDC during the compression stroke, the two scavenging ports are first closed, and then four rows of the exhaust ports are closed by it. The close timings of the scavenging and exhaust ports are 109.4 and 101.2 ºCA bTDC respectively. The stroke where the scavenging ports are blocked by the piston and some of the exhaust ports are open is 7 mm, which is L_f - L_d. Because of this period, the in-cylinder pressure can have the pressure similar to the atmospheric pressure when the effective stroke L_d starts. Considering this condition, the amount of fuel and air supply was calculated: the relevant description is presented in Sec. 3.2.1 and 3.2.2.

The piston starts blocking the port of the absolute pressure transducer when the crank angle is 73.6 ºCA bTDC. The point when the port is completely closed is 69.6 ºCA bTDC. Since the absolute pressure transducer acts as a reference transducer for the dynamic pressure transducer, this is essential information in pressure data measurement. Considering the timing when the absolute pressure transducer is blocked by the piston, the in-cylinder pressure was measured, which is described in detail in Sec. 3.3.

The piston crown is flat, and the shape of the piston is cylindrical. When the piston is at TDC, the length of its protruding part toward the top window of the optical cylinder head L_g is 12 mm. The depth from the end of the cylinder to the bottom of the top window L_c + L_g is 20 mm. Hence, the clearance L_c is 8 mm.

Since the length of a protruding part of the spark plug is 4 mm, the vertical position of a laser sheet that goes through one side window of the optical head should be noted when the PIV system was set up. This is because the spark plug can be an obstacle to the movement of the laser sheet. To avoid the problem, the thickness of the laser sheet was minimized and the vertical position was adjusted properly: the detailed description is given in Sec. 3.4.2 . The piston was painted with black colour to minimize the effect of the reflection that could be caused by the illumination of a laser sheet and to record clear PIV images.

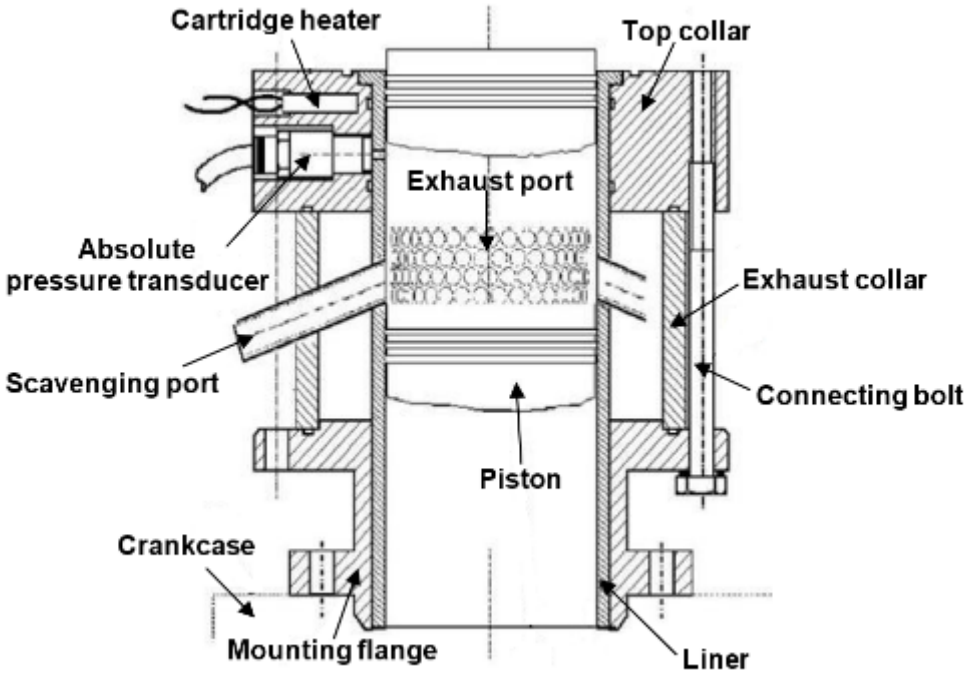

Figure 3.6 A plan of the combustion chamber of LUPOE-2D: the figure is modified from Abdi Aghdam (2003)

The breathing system of the research engine was modified from a typical ported two stroke engine (Hicks 1994, Butler 1999, Abdi Aghdam 2003, Murad 2006, Dawood 2011, Hussin 2012). Figure 3.6 shows a plan of the combustion chamber of LUPOE-2D that was used in the current research. A fresh fuel-air mixture gas is introduced through two rectangular scavenging ports that are horizontally symmetrical. The scavenging ports are connected to two diametrically opposed pipes respectively through which a fuel-air mixture gas is supplied. The fuel-air supply pipes are horizontally inclined at 20 º to help the mixture to flow naturally. The engine exhausts burnt gas through four rows of exhaust holes, of which each diameter is 10 mm. By drilling holes on the cylinder liner, this passage for the exhaust gas was made. The combustion product goes through the space, that is, exhaust collar, between the cylinder and liner. After that, it is expelled through the exhaust pipe that is connected to the ventilation duct. To prevent back pressure that can be caused for the combustion chamber by a stagnation flow in the exhaust pipes, the extract fan that was connected to the ventilation duct was operated whenever the experiment was carried out.

According to the result of Chen's research (2014), where the research engine runs at 50 rpm, the mean velocity of the unburned gas at TDC is less than 0.1

m/s, and the root-mean square velocity is less than 0.4 m/s. In addition, in the different condition where the speed of the engine is 750 rpm, Hussin obtained the values of the mean and root-mean square turbulent velocity at TDC: they were approximately 0.5 and 1.26 m/s respectively (Hussin 2012). It means that the research engine, which is equipped with the bespoke breathing system, enables to make a low turbulent condition inside the combustion chamber as the engine speed decreases. Especially, when the research engine is operated at 50 rpm, a laminar condition can be made, which can be regarded as the condition where a laminar flame appears: the relevant result is shown in Sec. 3.4.3.

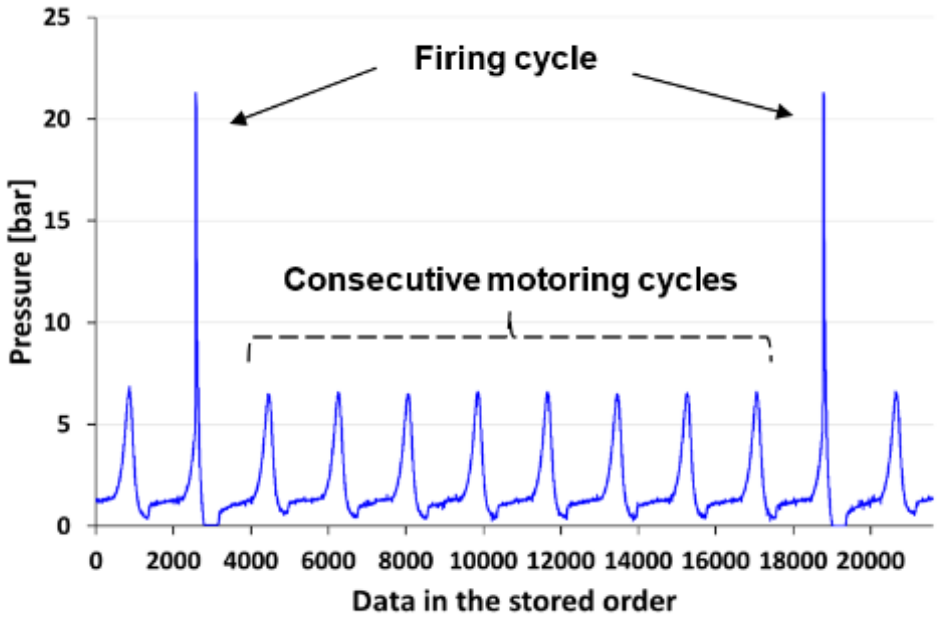

Figure 3.7 Pressure variation in skip fire mode, which consists of eight consecutive motoring cycles and one firing cycle

In order to secure a fresh fuel-air mixture in the combustion chamber without any residual gas that can be caused by the previous firing cycle, when a new combustion process started, the research engine had a firing cycle after consecutive motoring cycles: the motoring cycles are called skip fire mode in this research, and refer to Figure 3.7. By adopting this mode, the residual gas could be removed or minimized, which made it possible to prevent or reduce the problem that could be caused by the trapped gas such as incomplete combustion and cyclic variation (Larsson 2009). The ratio of successive motoring cycles to a firing cycle used in this research was eight to one. The value of the ratio can be changed by manipulating the relevant set value of

the engine control system, which is mentioned in Sec. 3.5. During eight consecutive motoring cycles, a lot of fresh fuel-air mixture was used to purge the residual gas that was caused by the previous combustion. Hence, a new combustion process with fresh fuel-air mixture gas could be realized.

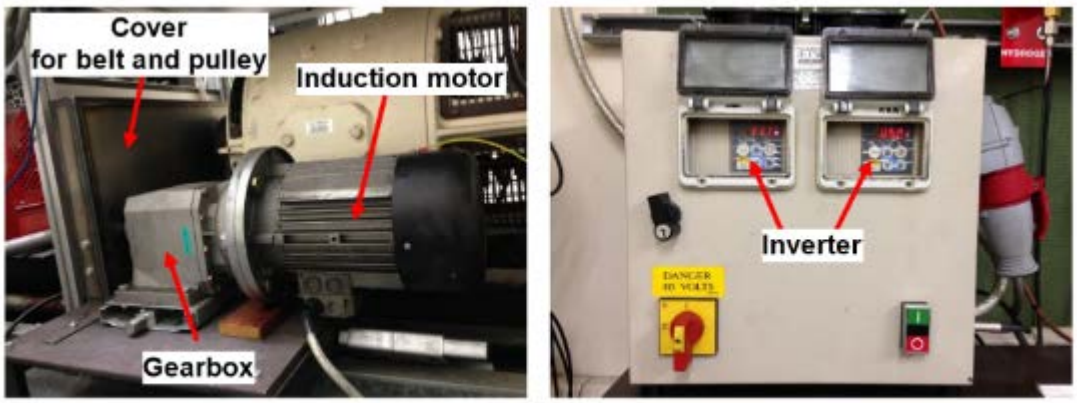

Figure 3.8 Photographs of induction motor for LUPOE-2D and control console

An induction electric motor was used as a prime mover to rotate the research engine. Figure 3.8 shows the relevant equipment. The motor is operated at 2880 rpm where supply voltage is 230 V and frequency 50 Hz. In order to control its speed, an inverter, FARA MOSCON-E5, was adopted (Chen 2016). By adjusting a frequency that is supplied to the motor the speed can be controlled. For a low speed corresponding to the purpose of this research, the motor was connected to the input shaft of the gearbox. A pulley was fitted into the output shaft of the gearbox. Through a timing belt, a torque was transmitted to the pulley of the crankshaft of LUPOE-2D. The reduction ratio of the gearbox was ten to one. The range of the engine operating speed was from 10 to 200 rpm, and the accuracy was ± 1%.

3.2 Fuel and air supply system

The amounts of fuel and air that are supplied into the combustion chamber, that is, equivalence ratio, have the crucial effect on the characteristics of flame such as its burning velocity, molecular and thermal diffusivities, and so forth

(Irvin and Richard 2008). It is essential to provide a combustion chamber with an accurate amount of the fuel-air mixture that is required for the experiment. This section is divided into two subsections. The first subsection describes the fuel supply system including the calibration of the rotameters which were used in this research. In the second subsection, the air supply system is introduced, and then the calibration of the mass flowmeters for this system is explained in detail. Lastly, the temperature control system for a fuel-air mixture is described.

3.2.1 Fuel supply system

Three gaseous fuels, hydrogen, methane, and propane, were used in this study. Methane and propane have been used commonly in industrial fields, and especially, much attention has been paid to hydrogen as it is able to reduce the greenhouse gas emission that causes the global warming. Figure 3.9 shows how the fuel supply system is configured.

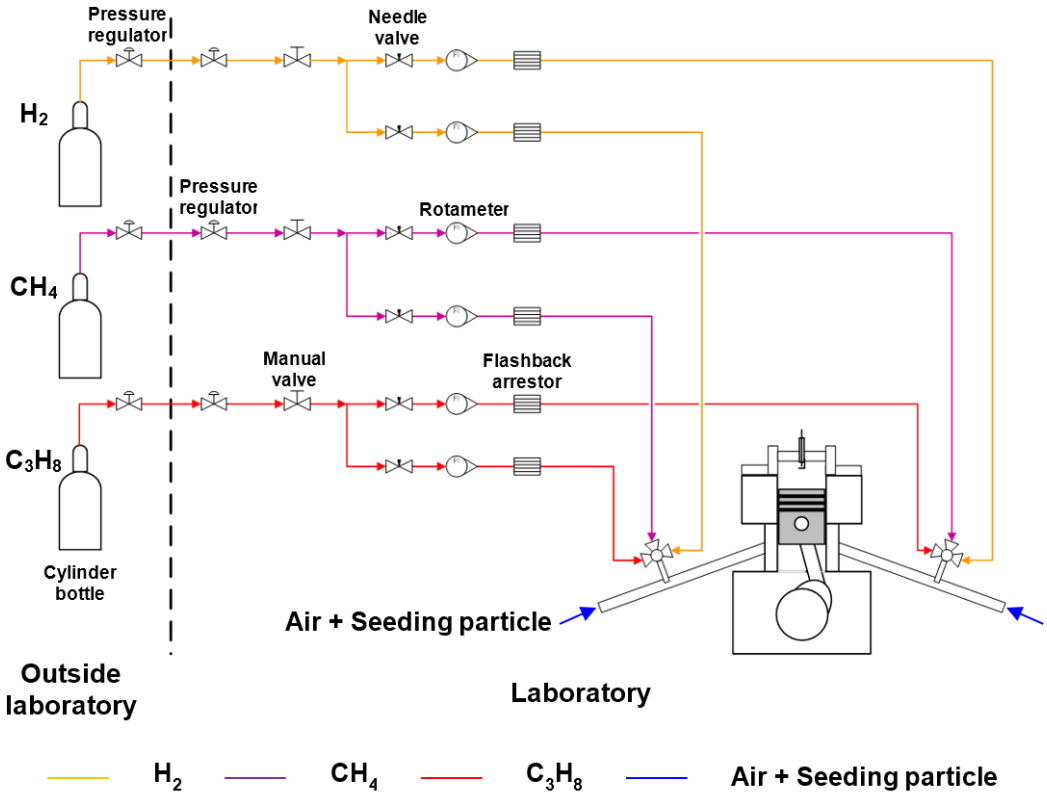

Figure 3.9 Piping and instrumentation diagram of the fuel supply system

The gaseous fuels were supplied from the separate cylinder bottles, and they were stored outside the laboratory building for safety reasons. The outlet pressure of each bottle could be adjusted by each pressure regulator through which the fuel was provided keeping its pressure stable. There was another pressure regulator in the laboratory. This regulator was used to control the fuel supply pressure before the gaseous fuel flows into the combustion chamber of the research engine and also kept the supply pressure stable.

After the regulator, the manual valve was fitted in the line. This valve was a cut-off valve. In the case that an emergency situation would take place, this valve could be used immediately to shut the fuel supply. The fuel supply line branched into two separate lines for two diametrically opposed pipes of the research engine after the cut-off valve. The gaseous fuel of each line went through a rotameter, and the flow rate could be adjusted by the needle valve which was mounted at the inlet of the rotameter. The total number of the rotameters that were used in the experimental equipment was six.

Before the fuel was supplied into the pipe connected to the cylinder of the research engine, a flashback arrestor and three-way connector were installed. The flashback arrestor is a safety device to extinguish flame that can come back from the combustion chamber. Therefore, it prevented the flame from spreading to the gaseous fuel supply line. The gaseous fuels were supplied through the three-way connector. The supplied location was the throat section of the venturi tube in the intake pipe, which is shown in Figure 3.10. Afterward the gaseous fuel mixes with air and seeding particles, the fuel-air mixture is transported into the combustion chamber of the research engine.

Table 3.2 shows the properties of three gaseous fuels that were used in the current research. The purities of hydrogen, methane, and propane were 99.5, 99.995, and 99 % in volume respectively. Hence, it was assumed that the gaseous fuels used in the current work were pure. And according to the assumption, the amount of the supplied fuel was calculated. Although there are many kinds of flowmeters for gas flow measurement such as differential pressure type, displacement, ultrasonic flowmeters, and so forth, a rotameter, which is one of the variable area meters, was adopted in the current research. Even though cutting edge flowmeters are able to provide better performance and guarantee a wider range of measurement, a flow rate measured through a rotameter also shows reasonable performance and good reliability with modest cost. For this reason, the rotameters were mounted in the fuel supply system.

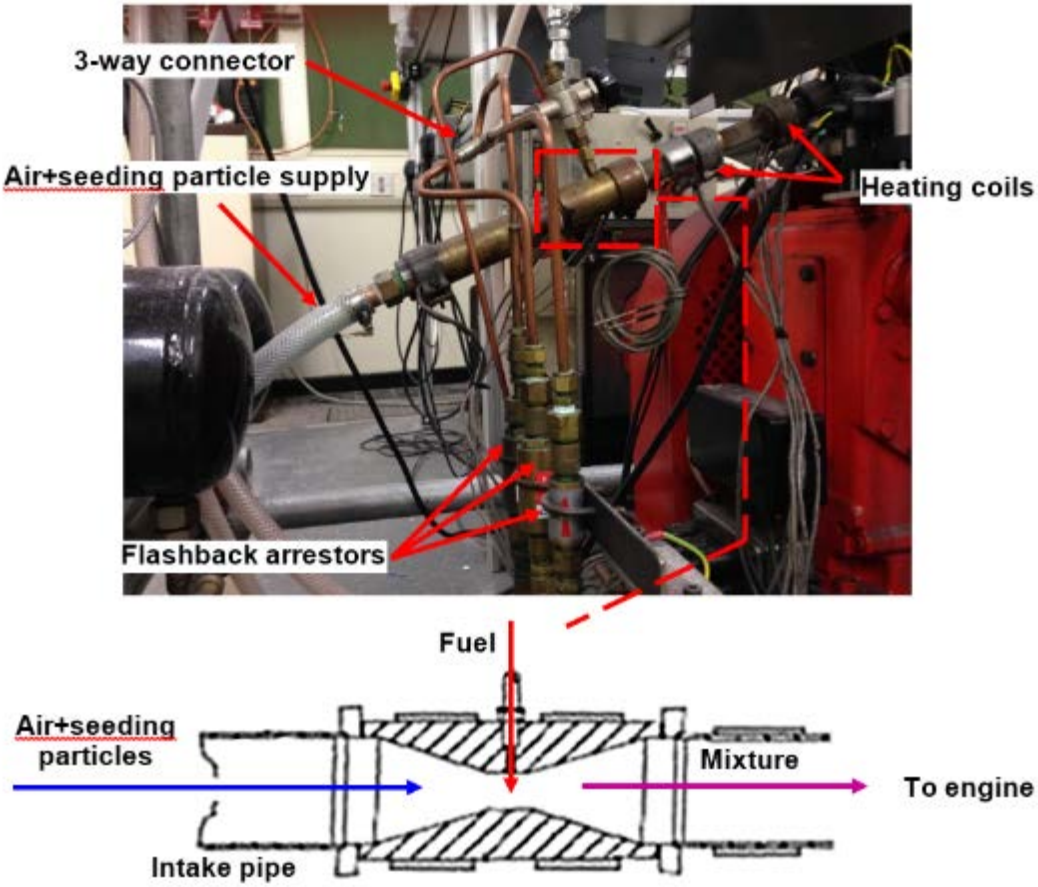

Figure 3.10 Photograph of the intake pipe and a schematic diagram of fuel-air mixing process; the figure is modified and reproduced from Robert (2010)

Table 3.2 Properties of gaseous fuels and air used in the current research (Linstroms and Mallard 2016)

Substance	Density [kg/m^3] at gaseous state				Octane Number (RON)	LHV [MJ/kg]	Purity [%]
	1	2	3	4			
H_2	0.090	0.084	0.166	0.245	>130	119.96	99.5
CH_4	0.716	0.665	1.321	1.950	120	50.00	99.995
C_3H_8	1.967	1.827	3.630	5.360	112	46.35	99
Air	1.292	1.200	2.384	3.569	-	-	-

state1: standard condition, 101.325 Pa / 273.15 K

state2: 101325 Pa / 294.15 K,

state3: 201325 Pa / 294.15 K,

state4: experimental condition, 301325 Pa / 298.15 K,

RON: research octane number

The total number of the rotameters used in the experiment was six, and the models were OMEGA FL-3804ST and FL-3804GT. The accuracy of each model was ± 2 %. The main difference between the two models is the material of the floats which is stainless steel and glass, i.e. its density. Since a float with less density rises higher than the one with more density in the tapered tube, the flow capacity is lower than that of a rotameter having a float with more density. The result of calibration of the flowmeters is shown in Appendix B, and it was confirmed that the rotameters showed a good performance.

3.2.2 Air supply and seeding system

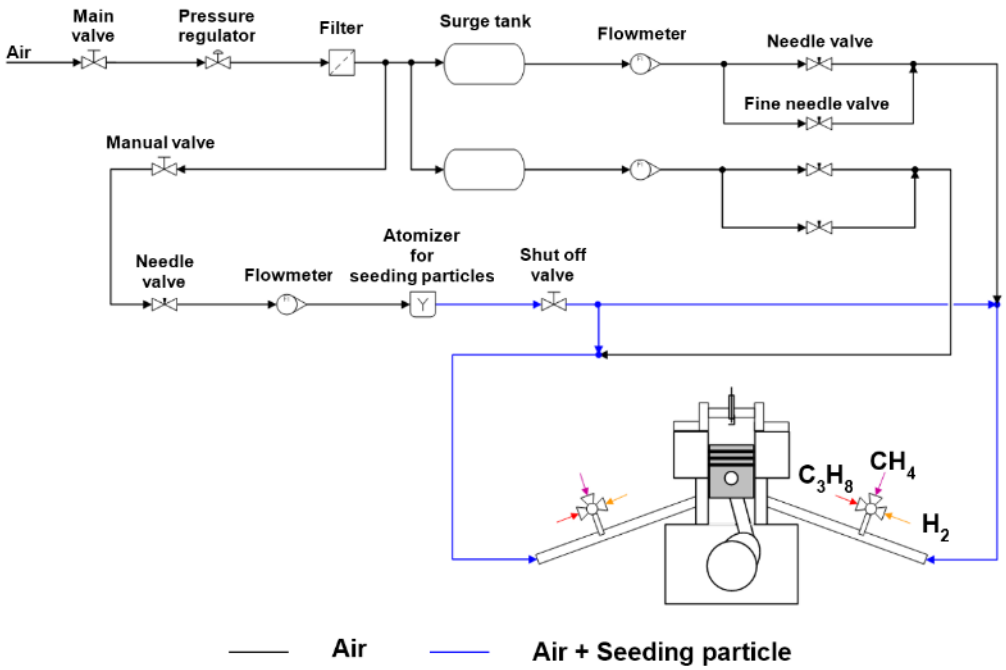

Figure 3.11 Piping and instrumentation diagram of the air supply and seeding system

Figure 3.11 shows the air supply and seeding system. The laboratory compressed air of which the pressure was 7 bar in gauge pressure was used as the source air in the present work. As seen in the figure, the air supplied for the research engine is divided into the two pipelines: the main pipeline supplying pure air, and the secondary pipeline supplying air with seeding particles.

The air supply for the research engine begins with the main valve, and then the air pressure was adjusted and stabilised at 2 bar in gauge pressure through the pressure regulator. Undesirable substances such as oil, dust, and so forth are be filtered through a gas filter. After the filter, the air supply pipeline is divided. The main air supply pipeline, which does not contain seeding particles, splits into two sub-pipelines again. Each sub-pipeline is connected to one of the two diametrically opposed intake pipes in the research engine. A surge tank, of which the capacity is five litre, is mounted in each sub-pipeline of the main pipeline. It reduced the fluctuation of the supply pressure that might be caused by the piston movement or undesirable pressure drop owing to external reasons. A thermal mass flowmeter, TELEDYNE HASTING HFM-301, was installed after the surge tank. The flow rate in the intake pipe can be monitored by the display device, Chell microprocessor display CMD100. The full range of the device is 200 SLPM with an accuracy of ± 1 % of the full scale (TELEDYNE HASTINGS INSTRUMENT 2010). Two needle values were installed on each sub-pipeline to adjust the air flow rate. The needle values are a fine needle valve, which enables to adjust a small amount of flow rate. By throttling the two needle valves, the flow rate of each sub-pipeline was adjusted during the experiment.

The secondary pipeline where seeding particles are mixed with the pure air can be shut off by a manual valve. After it, a needle valve was employed to adjust the flow rate accurately. Brooks 5863S thermal mass flowmeter was used to measure the flow rate in this supply pipeline. Its range is 400 SLPM with an accuracy of ± 1 % of the full scale (Brooks Instrument 1992). The display unit to read the flow rate was Chell 5875.

To feed seeding particles in the air supply line, the atomizer was used. Figure 3.12 shows a schematic drawing of the atomizer, TSI Six-Jet Atomizer Model 9306A, which was adopted in this experiment to provide the supplied air with seeding particles. Olive oil was employed as a seeding material. The pressured air branched from the main air supply pipeline was supplied for the atomizer jet. Through the orifice with which the end of the atomizer jet is equipped, the high-velocity flow can be made, which makes the pressure drop. Olive oil is naturally drawn up through the narrow tube owing to the pressure drop. With the oil and high-velocity air that collide with the spherical impactor, a small size of oil droplets are made as aerosol, and then mix with the pressured air again for dilution. Afterward, the fine oil droplets and air exits from the atomizer through the outlet tube.

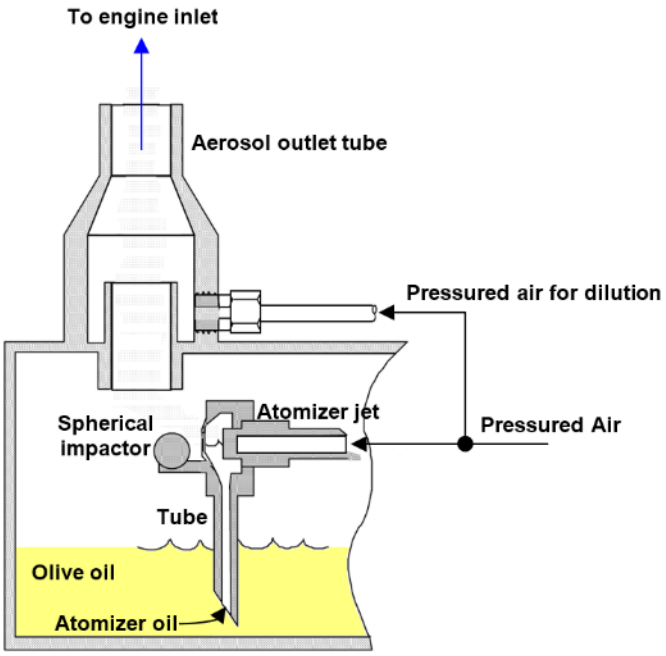

Figure 3.12 A schematic drawing of the atomizer; the figure is reproduced from the manufacturer instruction manual (TSI 2003)

The total number of the atomizer jet in this device is six, and the number of used atomizer jets can be adjusted by the control valves. Two atomizer jets were used in this experiment, and the amount of the air supply through the atomizer was about 10 % of the total air flow rate. Depending on the flow rate of air with seeding particles, the concentration of seeding particles varies and affects the brightness of flame images. Excessive seeding particles can have a bad influence on vector calculation in the PIV system and make the top and side windows of the optical cylinder dirty. This can decrease the reliability of experiment. On the other hand, a small number of seeding particles make it impossible to calculate vector calculation because of a lack of the brightness by the particles: further description is presented in detail in Sec. 3.4.2. It was observed through the experiment that 10 to 12 % of the total air flow was appropriate for the optimal imaging measurement. The result of calibration of three thermal mass flowmeters is shown in Appendix B, and it was confirmed that the flowmeters were in good condition.

It was essential to calculate the supply amount of fuel and air accurately depending on a change in their equivalence ratio. In this research, three gaseous fuels, hydrogen, methane, and propane, were used, and the speed of the research engine was 50 rpm. When the piston is at BDC, the total volume of the combustion chamber is 593110 mm^3. Hence, the volume is

29655500 mm^3 per minute: refer to Table 3.1. It was confirmed that the pressure in the cylinder of the research engine was approximately 120000 Pa when the piston was at BDC. As mentioned in Sec. 3.1, the scavenging ports and exhaust ports are opened at BDC, and the exhaust pipe is connected to the ventilation system at which the extract fan runs. Since the pressure was kept higher than the atmospheric pressure, it was presumed that the volumetric efficiency of the cylinder was 100% in calculating the supply amount of fuel and air. Given a complete combustion of stoichiometric methane-air mixture in which combustion products are only CO_2, H_2O, and N_2, the global reaction can be simply written as follows:

$$CH_4 + 2(O_2 + 3.76N_2) \rightarrow CO_2 + 2H_2O + 7.52N_2 \quad \textbf{Eq.} (3.1)$$

The amounts of methane and air per minute supplied for each intake pipe can be represented as Eq**.** (3.2) and Eq**.** (3.3).

$$CH_4 = \frac{1}{1 + 2 \times (1 + 3.76)} \times 29655500 \times \frac{1}{2} \; [mm^3/min] \quad \textbf{Eq.} (3.2)$$

$$Air = \frac{2 \times (1 + 3.76)}{1 + 2 \times (1 + 3.76)} \times 29655500 \times \frac{1}{2} \; [mm^3/min] \quad \textbf{Eq.} (3.3)$$

For non-stoichiometric cases, the above equations can be re-formulated as:

$$CH_4 = \frac{A_{CH_4}}{A_{CH_4} + 2 \times (1 + 3.76)} \times 29655500 \times \frac{1}{2} \; [mm^3/min] \quad \textbf{Eq.} (3.4)$$

$$Air = \frac{2 \times (1 + 3.76)}{A_{CH_4} + 2 \times (1 + 3.76)} \times 29655500 \times \frac{1}{2} \; [mm^3/min] \quad \textbf{Eq.} (3.5)$$

where A is the coefficient of CH_4. The amounts of fuel and air which are calculated from Eq**.** (3.4) and Eq**.** (3.5) are applied in the experimental condition of which the absolute pressure and temperature are 301325 Pa and 298.15 K. As seen in Sec. 3.2.1, the flow rate data that were obtained the calibrations of the rotameters are applied at 201325 Pa and 294.15 K. And the

unit of three flowmeters for the air supply and seeding system is SLPM, that is, 101325 Pa and 273.15 K. Considering the flow rates of the rotameters and flowmeters that were mounted in the fuel and air systems, Eq**.** (3.4) and Eq**.** (3.5) can be represented as Eq**.** (3.6) and Eq**.** (3.7).

$$CH_4 = \frac{A_{CH_4}}{A_{CH_4} + 2 \times (1 + 3.76)} \times 29655500 \times \frac{1}{2} \times \frac{301325 \times 294.15}{201325 \times 298.15}$$ **Eq.** (3.6)

$[mm^3/min]$

$$Air = \frac{2 \times (1 + 3.76)}{A_{CH_4} + 2 \times (1 + 3.76)} \times 29655500 \times \frac{1}{2} \times \frac{301325 \times 273.15}{101325 \times 298.15}$$ **Eq.** (3.7)

$[mm^3/min]$

To cover the flow rates for all three gaseous fuels, the flow rate table in which the supply amounts of fuel and air depend on the change of equivalence ratio and experimental condition such as the pressure and temperature of fuel and air was constructed using the commercial software, Excel, see Figure 3.13.

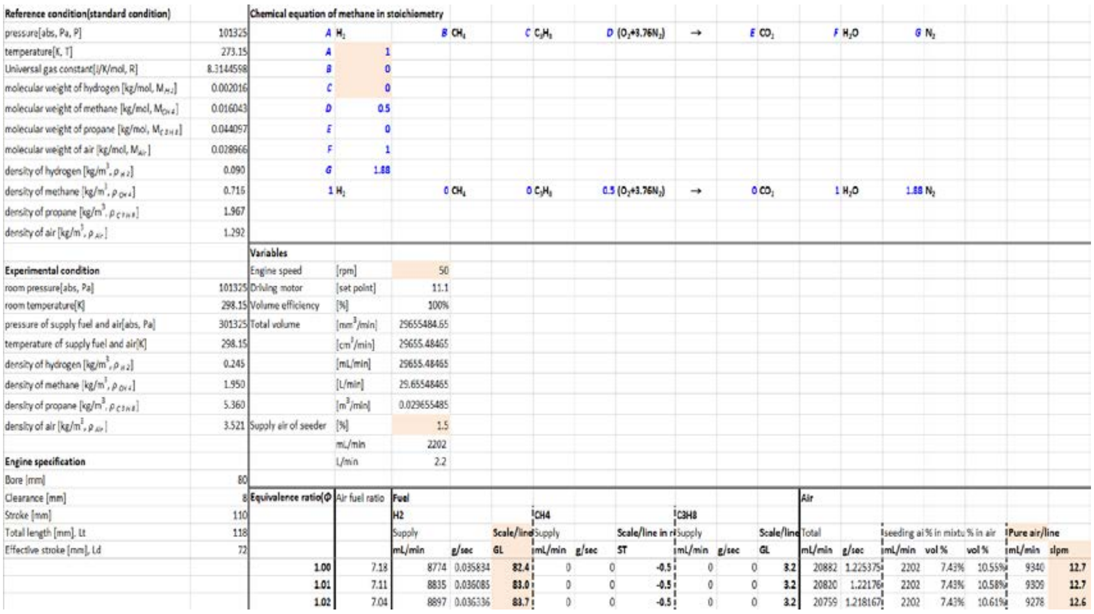

Reference condition(standard condition)	
pressure[abs, Pa, P]	101325
temperature[K, T]	273.15
Universal gas constant[J/K/mol, R]	8.3144598
molecular weight of hydrogen [kg/mol, M_{H2}]	0.002016
molecular weight of methane [kg/mol, M_{CH4}]	0.016043
molecular weight of propane [kg/mol, M_{C3H8}]	0.044097
molecular weight of air [kg/mol, M_{Air}]	0.028966
density of hydrogen [kg/m^3, ρ_{H2}]	0.090
density of methane [kg/m^3, ρ_{CH4}]	0.716
density of propane [kg/m^3, ρ_{C3H8}]	1.967
density of air [kg/m^3, ρ_{Air}]	1.292
Experimental condition	
room pressure[abs, Pa]	101325
room temperature[K]	298.15
pressure of supply fuel and air[abs, Pa]	301325
temperature of supply fuel and air[K]	298.15
density of hydrogen [kg/m^3, ρ_{H2}]	0.245
density of methane [kg/m^3, ρ_{CH4}]	1.950
density of propane [kg/m^3, ρ_{C3H8}]	5.360
density of air [kg/m^3, ρ_{Air}]	3.521
Engine specification	
Bore [mm]	80
Clearance [mm]	8
Stroke [mm]	110
Total length [mm], Lt	118
Effective stroke [mm], Ld	72

Chemical equation of methane in stoichiometry

A H_2	B CH_4	C C_3H_8	D $(O_2+3.76N_2)$	→	E CO_2	F H_2O	G N_2
A	1						
B	0						
C	0						
D	0.5						
E	0						
F	1						
G	1.88						
1 H_2	0 CH_4	0 C_3H_8	0.5 $(O_2+3.76N_2)$	→	0 CO_2	1 H_2O	1.88 N_2

Variables		
Engine speed	[rpm]	50
Driving motor	[set point]	11.1
Volume efficiency	[%]	100%
Total volume	[mm^3/min]	29655484.65
	[cm^3/min]	29655.48465
	[mL/min]	29655.48465
	[L/min]	29.65548465
	[m^3/min]	0.029655485
Supply air of seeder	[%]	1.5
	mL/min	2202
	L/min	2.2

Equivalence ratio(Φ	Air fuel ratio	Fuel									Air						
		H2			CH4			C3H8									
		Supply		Scale/line	Supply		Scale/line in r	Supply		Scale/line	Total		seeding ai	% in mixtu	% in air	Pure air/line	
		mL/min	g/sec	GL	mL/min	g/sec	ST	mL/min	g/sec	GL	mL/min	g/sec	mL/min	vol %	vol %	mL/min	slpm
1.00	7.18	8774	0.035834	**82.4**	0	0	-0.5	0	0	**3.2**	20882	1.225375	2202	7.43%	10.55%	9340	**12.7**
1.01	7.11	8835	0.036085	**83.0**	0	0	-0.5	0	0	**3.2**	20820	1.22176	2202	7.43%	10.58%	9309	**12.7**
1.02	7.04	8897	0.036336	**83.7**	0	0	-0.5	0	0	**3.2**	20759	1.218167	2202	7.43%	10.61%	9278	**12.6**

Figure 3.13 Table for calculating the supply amounts of fuel and air with respect to equivalence ratio, temperature, and pressure

3.2.3 Temperature control system

In order to control the temperature of the supplied fuel-air mixture, the clamp band and cartridge heaters were installed. Figure 3.14 shows a schematic diagram of the temperature control system. A set of five 200 W and 125 W clamp band heaters was mounted on each intake pipe. A set of twelve 20 W cartridge heaters was equidistantly inserted along the cylinder wall. The sets of the heaters were controlled by the temperature control unit. The control unit consisted of three Digitron 4801 temperature controllers of which each was connected to a type-K thermocouple. Each controller displays the temperature of each part, and can set a desirable value.

The heaters keep running till the temperature of each part reaches its set point. Once the temperature is below the set point, the heater starts working automatically when the relay of the controller is reset. The set point was 25°C in this experiment, and depending on the experimental circumstance the temperature control system was switched on or off.

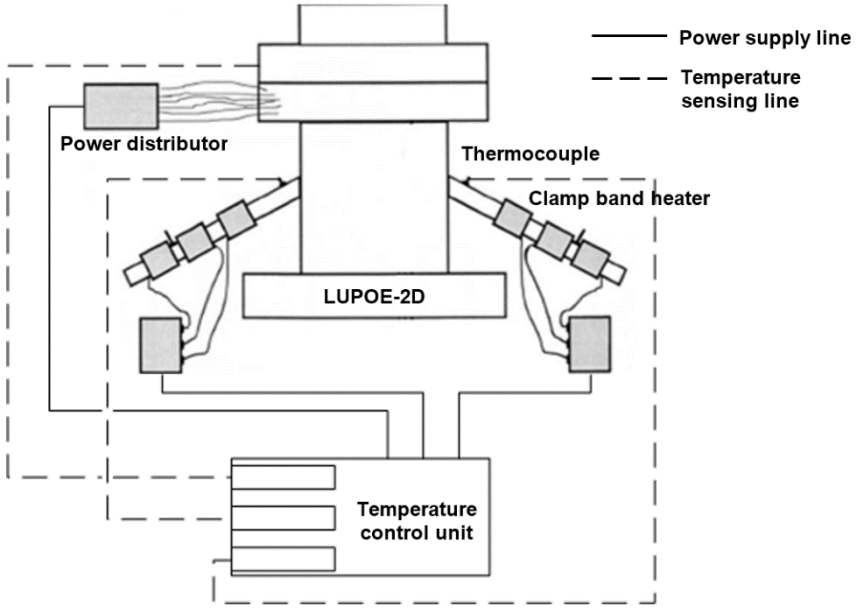

Figure 3.14 A schematic diagram of the temperature control system in the research engine; the figure is modified from Abdi Aghdam (2003)

3.3 Pressure data measurement and temperature calculation

To clarify the experimental condition and compare the result of experiment with the relevant data that other researchers have published, it is crucial to measure the pressure and temperature when combustion starts. Moreover, such pressure data can be used for thermodynamic analysis. For example, the Leeds combustion group has employed pressure data as the input data for LUSIEDA, Leeds university spark ignition engine data analysis. It has enabled to obtain more information on the combustion process such as simulated in-cylinder pressure, unburned and burned gas temperature, rate of heat release, and others (Langridge 1995, Abdi Aghdam 2003, Hattrell 2007, Ling 2014).

In order to measure instantaneous pressure in the cylinder of the research engine, two kinds of pressure transducers were adopted. The first pressure transducer was a piezoresistive transducer, Kistler type 4045 A5, which is named absolute pressure transducer in this research. The measurement range is 0-0.5 MPa. It is typically mounted on an intake or exhaust manifold in internal combustion engines, and is suitable for measuring static and quasi-static pressure (KISTLER 2013). The other transducer was a quartz piezoelectric transducer, Kistler type 601A, which is also called dynamic pressure transducer in the current work. The measurement range is 0-25 MPa. This pressure transducer is commonly installed at a cylinder head in the combustion engines, and is used to measure dynamic and quasi-static pressure (KISTLER 2010).

As shown in Figure 3.3 in Sec. 3.1, the absolute pressure transducer was mounted on the side of the cylinder wall and connected to an amplifier, Kistler piezoresistive amplifier type 4601A, of which the amplified signal range is 0-10 V and was set to be 0.5 bar per voltage in this experiment. The place where the absolute pressure transducer is located on the cylinder wall is higher than the one where the uppermost exhaust ports are located. The hole of the cylinder for the absolute pressure transducer is fully closed by the piston when the crank angle is between 69.6º CA bTDC and aTDC. And the pressure data measured by the absolute pressure transducer is valid only when the hole is open.

The dynamic pressure transducer was installed on the side of the optical cylinder head: refer to Figure 3.3. It has a high response rate. Its electrical signal was amplified with Kistler charge amplifier type 5011, of which the range is 0-10 V and was set to be 10 bar per voltage in the experiment. The

pressure data that are measured by the absolute pressure transducer just before it is blocked by the piston acts as reference data to correct the pressure data that the dynamic pressure transducer measures. Through the correction, the in-cylinder pressure could be acquired. Figure 3.15 shows the dynamic pressure re-alignment. During the engine expansion process, the mis-alignment is observed and might be caused by a thermal shock (Ling 2014). The electrical signals that the absolute and dynamic pressure transducers generated in the experiment were stored through the data acquisition system, which is introduced in Sec. 3.5. To check whether both pressure transducers showed a good performance, the calibration were conducted regularly using a Budenberg dead weight tester and the relevant software. It was confirmed that both of them were in good condition, and the result is shown in Appendix C.

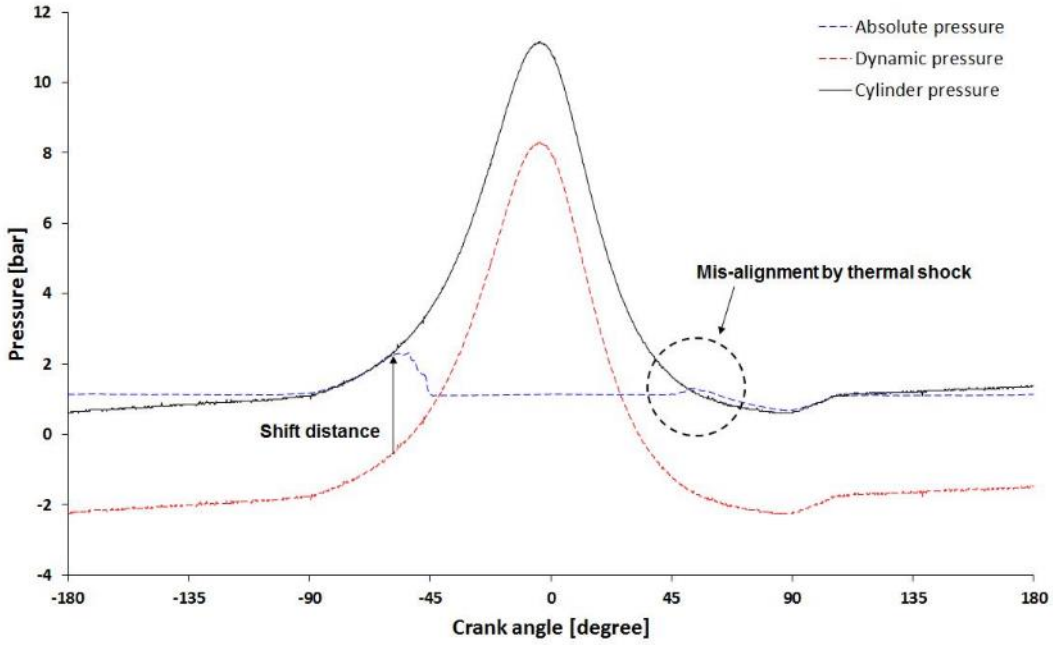

Figure 3.15 Dynamic pressure referencing to the absolute pressure: the engine speed 100 rpm

In this experiment, assuming that the compression stroke was an isentropic process, which is both adiabatic and reversible, the temperature of the mixture was simply calculated from the first law of thermodynamics for an ideal gas (Spalding and Cole 1973). A thermocouple for the temperature measurement was not installed because its response time was not short enough to synchronise the sampling timings of pressure data. And the limitation of the

space at the cylinder head existed. The equation that was used for the temperature calculation of a fuel-air mixture is as follows:

$$T_{i+1} = \left(\frac{P_{i+1}}{P_i}\right)^{\frac{r-1}{r}} \times T_i$$ **Eq.** (3.8)

T: temperature P: pressure r: 1.35, ratio of specific heat

3.4 PIV and imaging system

Over decades, the attempts to image flame and prescribe the flow field of a combustible mixture in the cylinders of spark ignition engines have been made to investigate its characteristics such as flame speed, burning velocity and others for broadening the understanding of combustion phenomenon. A variety of techniques to image flame have been developed, including shadowgraph, particle image velocimetry, the schlieren photography, and so forth.

The schlieren photography uses the variation of refraction index originating from the density gradients between a combustible mixture and the combustion product for a developing flame front to be detected, and natural light photography, which literally employs light luminosity that is emitted by the combustion for a flame front to be displayed, were mainly adopted in the early stage to closely examine the combustion process in a cylinder (Gatowski, Heywood et al. 1984). In the case of shadowgraph and schlieren photograph, it is not easy to arrange a light source, optical lens, and mirror in a research engine with an optical cylinder head. Especially, the mirror that is mounted on the top of the piston crown could cause error in the measurement owing to the vibration when the engine is operated.

In natural light photography, since it uses the light as a light source that the combustion accompanies, how much brightly and clearly the image can be recorded is affected in many ways by the property of a combustible mixture. In the case of lean flame, the luminosity may not be enough to discriminate the burned area from the unburned area in the flame image (Dawood 2011). Through the appearance of a digital camera and its evolutions, a typical high speed camera which is currently used for research makes it possible to detect natural light stemming from the flame very sensitively. However, just because

the high sensitivity is guaranteed does not mean the photography can always materialize images without any problem. Since using electrical device means that it is mostly exposed to unwanted external factors just as electrical noise, it can be not easy to ensure a high quality of a flame image without any electrical noise from a high sensitivity of a high speed camera in the circumstance where a various kinds of electric device is used much at the same time like this research (Hattrell 2007). In relation to the schlieren and natural light imaging, according to the research carried out by Murad (2006), it was said that the difference between the flame images recorded by the two photographic techniques was not much.

Not only does the optical methods mentioned above have been improved, but also there has been a big step in the particle tracer method, which is one of the optical techniques, with an advance in the laser technology. Laser Doppler Velocimetry, LDV, also named as Laser Doppler Anemometry, LDA, also uses a laser to measure the velocity of a fluid flow. This method uses the Doppler effect of a laser beam, which means that the correlation between the variation in frequency or wavelength of the laser for the moving fluid at a fixed, very small zone, practically a point, to realize the information on the flow field of a fluid (Finnemore and Franzini 2002, Serway and Vuille 2014). This feature of concentrating on a single point enables one to closely examine the fluid flow with a very high temporal resolution. Many researches have been carried out with this nonintrusive technique to learn the information on the flow field in engines (Nomura, Takahashi et al. 2004, Turner and Zhang 2011).

Another technique is Laser Induced Fluorescence, LIF, or Laser Stimulated Fluorescence, LSF. It is one of spectroscopic methods. After a molecule in the fluid flow that absorbs the energy from laser light is excited in a high level of energy, it is recorded by a high speed camera when its energy level drops to the ground level spontaneously, radiating the light (Zare 2012). This technique has been used for detecting selective species just as OH*, CH* or seeding particles in a fluid, and employed in internal spark ignition engines to discriminate the flame front between an unburned and burned area (Neij, Johansson et al. 1994, Hult, Richter et al. 2002).

Particle Image Velocimetry, PIV, is widely employed to prescribe how fluid moves. It can be named as Particle Tracking Velocimetry, PTV, or Laser Speckle Velocimetry, LSV, depending on the concentration of particles in a fluid flow (Adrian and Westerweel 2011). By changing the number of a camera and laser and altering the arrangement of experimental equipment, it is possible to embody a three-dimensional flow field. Compared with LDV and

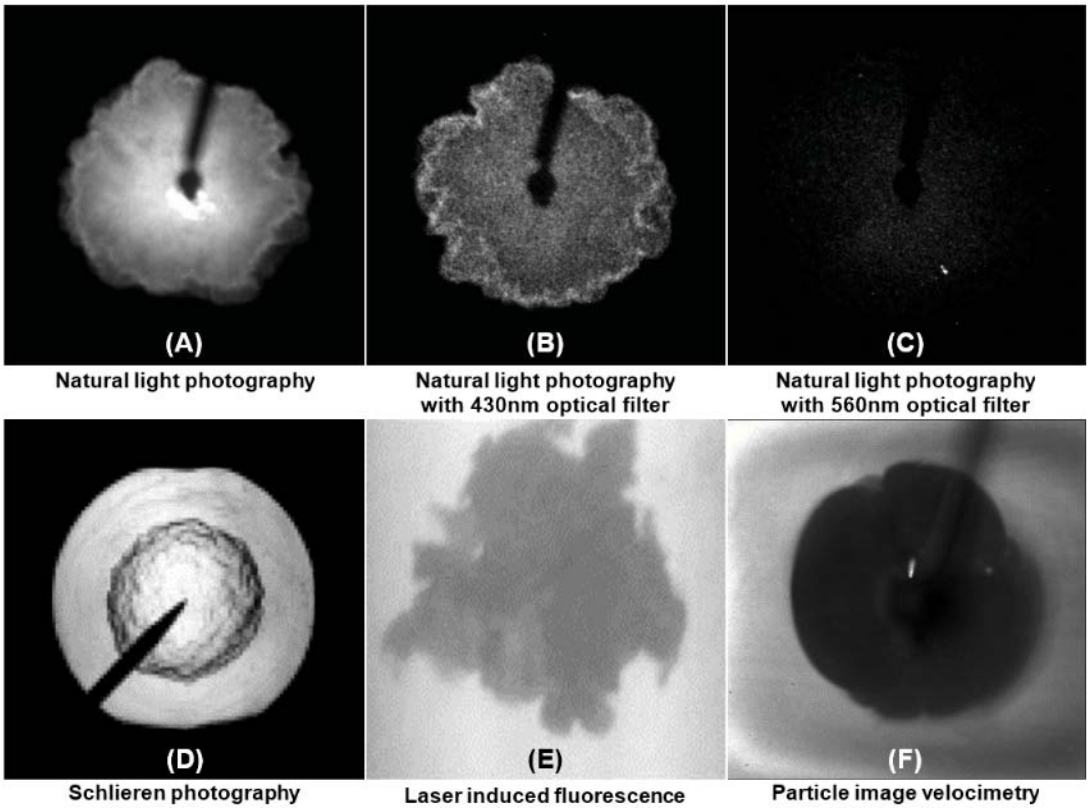

Figure 3.16 Image examples of different flame image techniques: (A), (B), and (C) are cited from Ling's research (2014). (D) is taken by Burluka, Hussin et al. (2011), and (E) is reproduced from the research of Deschamps, Smallwood et al. (1996). (F) was recorded from LUPOE-2D by the author. The engine speed was 50 rpm, and spark timing 2 ^{o}CA bTDC, using the stoichiometric methane-air mixture.

LIF, the main advantage of PIV is to obtain information on the flow field of a much larger area, ensuring an appropriate temporal resolution with a high speed camera and laser. Except for the techniques mentioned so far, there are other methods like Hot Wire Anemometry, HWA, and Doppler Global Velocimetry, DGV, also named Planar Doppler Velocimetry, PDV, which is suitable for investigating a high speed gas flow. More detailed description about the other techniques can be found in the relevant references (Merzkirch 1984, Bruun 1995, Finnemore and Franzini 2002, Nieuwstadt 2012).

There were the two main purposes of this research in using PIV images. The first objective was to derive flame contour images from the developing flame images in the reciprocating combustion chamber. The flame contour images were used to measure their flame propagation speeds. The second objective was to obtain the information on the flow field of the fuel-air mixture ahead of each flame front with high spatial resolution and appropriately high temporal

resolution. The flow fields were used to measure unburned gas velocity at each flame front. In order to achieve both goals simultaneously, the PIV system was adopted in this research.

3.4.1 Principle of PIV

Although the advance of technology always has the bright and dark side like a coin, it is obvious that it has contributed to a rise in the reliability of results of scientific experiment. Solid mechanics is the first academic field where laser speckle, which is followed by the present PIV technique, was originally used for the measurement of flow velocity. Several research groups tried to use the technique to realise whether it could be adopted to prescribe a fluid flow field in 1970s (Adrian 2005). As illumination, recording, evaluation techniques, and computer technology had advanced consistently, the interest in the PIV technique gradually increased. Having secured the reliability of the techniques and improved the relevant theories, nowadays, the measurement of a fluid flow velocity and its evaluation through this method are widely carried out (Adrian and Westerweel 2011).

Currently, a typical PIV system consists of three components, a light source, recording device, and seeder or atomizer, which produces a fluid flow with tracing particles. In most of the laboratory flow measurements, the tracers are supplied in the fluid flow, and are illuminated by using the lighting system which is comprised of several optical lenses and a light source passing through the arrangement. The number of times to illuminate the seeding particles within a very short time is typically at least twice, and the scattered light of the tracking particles in the time is stored by recording device as a type of image files. Depending on the type of recording device, the images that are taken within the short time can be saved either as a single image by superimposing them or two separate images, which is referred to as single frame or single exposure and double frame or double exposure respectively. According to how the image of the tracer particles is recorded, the way of evaluating the image is also different. It is a statistical method including auto correlation and cross correlation. By evaluating the recording, the displacement of the particles between the separate illuminating time is measured (Raffel, Willert et al. 2007, LaVision 2010).

Figure 3.17 briefly shows the typical configuration of a two-dimensional PIV system. A tiny size of tracing particles are supplied in a fluid flow. In the PIV

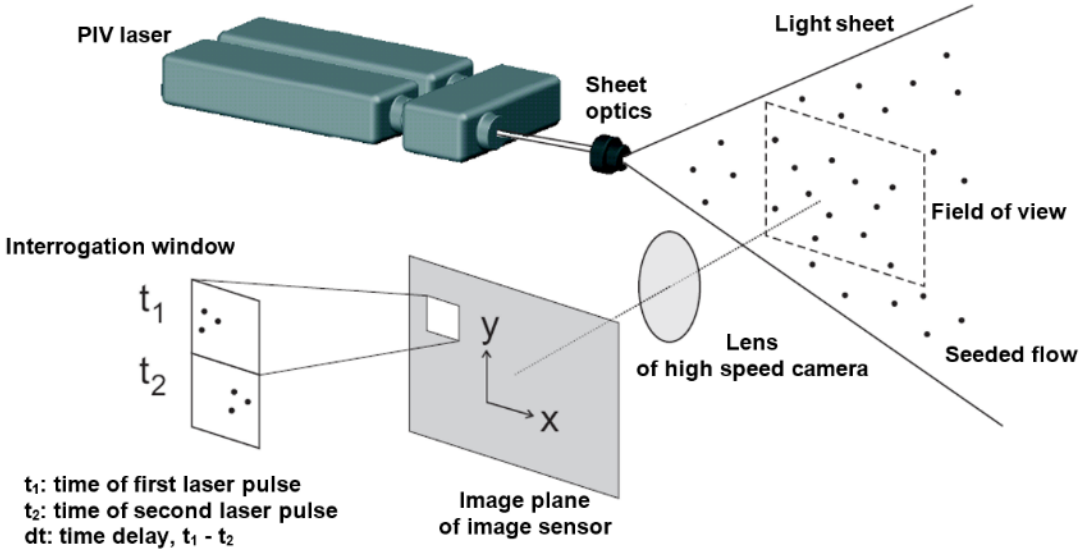

Figure 3.17 General arrangement of a two-dimensional PIV system; the figure is reproduced from the manufacturer manual (LaVision 2010)

technique, it is assumed that the tracing particles follows the movement of the fluid and all of them move homogeneously in the flow field (Raffel, Willert et al. 2007). During a short time, the PIV laser sheet illuminates a plane in the fluid flow twice, which is made up of the fluid and seeding particles. The time delay, *dt*, between the first and second illumination, t_1 and t_2, has to be adjusted to find out the optimal point, considering the average speed of the flow and the size of an interesting area, which is shown in Figure 3.17 as Field of view. The image that contains the scattered light of the seeding particles is captured by a high speed digital camera, of which the position is typically perpendicular to the plane of the laser sheet. Depending on the selection of single or double frame mode, the scattered light image can be saved on the image sensor of the camera as a single or double frame. Subsequently, the images are directly saved in real time in a computer.

Each digital PIV image is divided into a small size of area, which is referred to as interrogation area or interrogation window. The local displacement of the tracer particles in the interrogation window between two illuminations is measured through statistical methods, which are auto correlation and cross correlation. And then it is scaled according to the image magnification, which requires the process of carrying out calibration before the actual experiment. Subsequently, the local displacement is divided by the time between two illumination pulses. Through these steps, one flow vector at the relevant

interrogation window is calculated. The process of obtaining the flow vector of each interrogation window is proceeded to the entire field of view of all the stored images.

Although a PIV system can be equipped with a cutting-edge laser, high speed camera, seeder and other necessary components, the PIV technique would be disregarded by many researchers if the fundamental assumptions were far away from the practical application. Especially, the key of the assumptions is whether tracking particles would be able to follow a fluid well in the allowable margin of error. A small size of particles are advantageous in tracing the fluid due to its size against fluid friction for sure, whereas it is difficult to be said that they are good in terms of how well their lights can be scattered because of the same reason. In the case of a relatively large size of particles, the situation is directly opposite. The relationship between a particle size and its scattered light seems to be trade-off. The size of tracking particles and the light-scattering efficiency should be compromised to some point. In order to ensure that tracing particles move with the local flow, the choice of a tracing particle material should be careful.

$$U_g = d_p^2 \frac{(\rho_p - \rho_f)}{18\mu_f} g \qquad \textbf{Eq.} (3.9)$$

$$U_{lag} = U_p - U_f = d_p^2 \frac{(\rho_p - \rho_f)}{18\mu_f} a_f \qquad \textbf{Eq.} (3.10)$$

$$\tau = d_p^2 \frac{\rho_p}{18\mu_f} \qquad \textbf{Eq.} (3.11)$$

U_g: gravitationally induced velocity
d_p: diameter of particle
ρ_p: particle density velocity
ρ_f: fluid density
μ_f: fluid dynamic viscosity
g: acceleration of gravity
U_{lag}: lag velocity
U_p: particle velocity
U_f: fluid velocity
a_f: fluid acceleration
τ: relaxation time

Through the equations above, the lag that occurs between the fluid velocity and particle velocity and the relaxation time can be estimated. Based on Eq**.** (3.9) of which the velocity U_g is caused by gravity, which is known as Stokes drag law, Eq. (3.10) is derived (Finnemore and Franzini 2002). This can be applied under the assumption that the Reynolds number of particles in the fluid is very low (Raffel et al. 2007).

In this research, olive oil was adopted as a seeding particle material. As described in Sec.3.2.2, the air containing olive oil particles was supplied to the separate air supply pipeline, and the olive oil was added to the pipeline in aerosol state where the liquid was divided finely and uniformly by air in the atomizer. According to the relevant researches (Melling 1997, Raffel et al. 2007, Adrian and Westerweel 2011), the diameter of a seeding particle of olive oil is about 1 μm, and may vary depending on an experimental condition.

In order to calculate the lag velocity U_{lag} and relaxation time τ in Eq. (3.10) and Eq. (3.11), it is presumed that the fluid is air and obeys the ideal gas law, and the density of olive oil is constant, i.e. there is no the variation of the volume with respect to the change of temperature at constant pressure where its phase keeps the same and the diameter of a seeding particle of olive oil is 1 μm. Where the pressure and temperature is 101325 Pa and 293.15 K, which is atmospheric pressure and 20℃, the density of air and olive oil is 1.204 and 920 kg/m^3 respectively. In the same condition, the dynamic viscosity of the tracking particle is 18 x 10^{-6} N·s/m^3 (Finnemore and Franzini 2002). Where the acceleration of the fluid is 1000 m/s^2, provided that the enormous acceleration takes place in the fluid, it can bring about such the acceleration in reality (Adrian and Westerweel 2011). In this condition, the lag velocity and relaxation time is 2.836 mm/s and 2.840 μs. Hence, since the acceleration of the fuel-air mixture in the experimental condition of this research was even smaller than the one in the condition of this assumption, the lag velocity and relaxation time could be neglected. Evidently, it is meant that olive oil in the current research performs its duty of tracing the fluid to show the information on the fluid flow field.

However, it should be noted that the relaxation time τ should also be considered to be important information when the time delay dt between two separate illuminations in Figure 3.17 is adjusted to find out the optimal value. The time delay between the double pulses in the current work was 100 μs. This means that at least 3 % of error existed in calculating the velocity vectors of the fuel-air mixtures even though the seeding particles in this experiment ideally traced the unburned gas.

3.4.2 Used set-up

In this research, a continuous wave neodymium-doped yttrium lithium fluoride laser, which is referred to as a Nd-YLF laser, was used as a light source. The

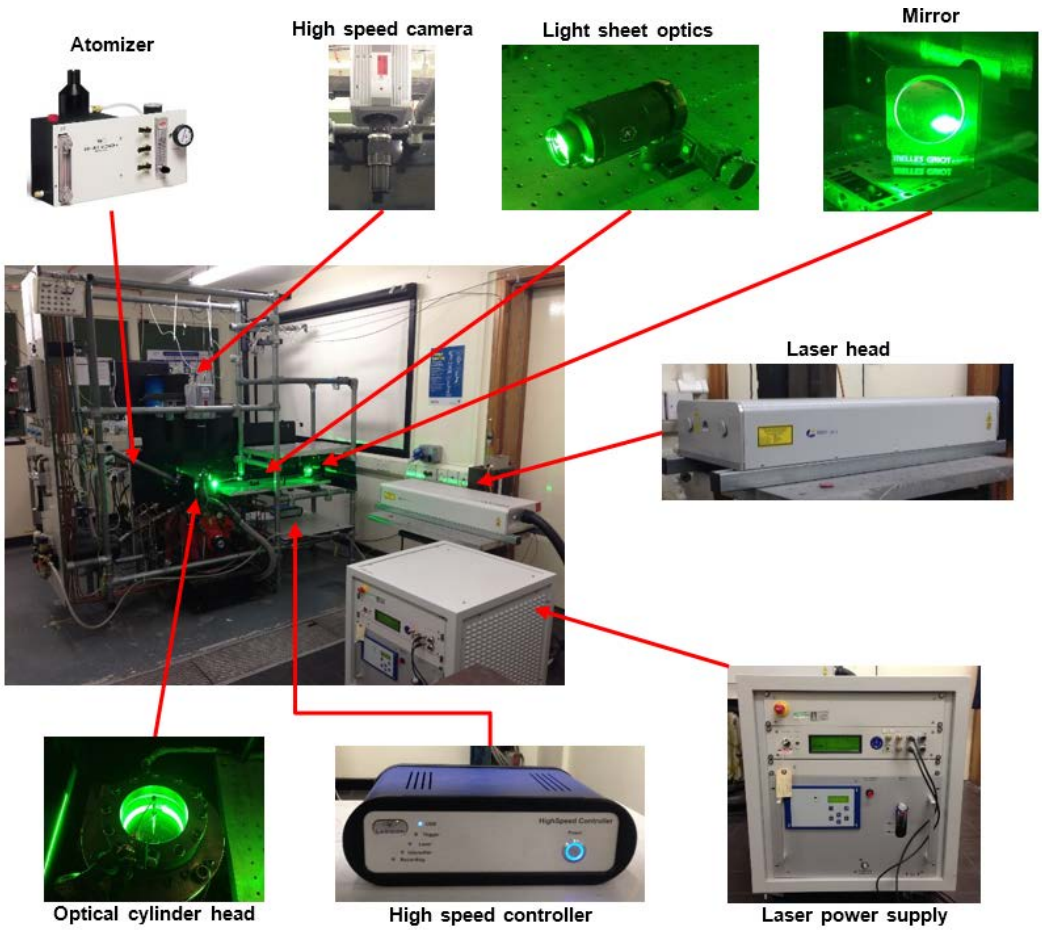

Figure 3.18 Photograph of each component in the PIV system used in this research

maximum power of the laser at 1 kHz is 10 mJ, and the maximum repetition rate is 10 kHz. Its wavelength and pulse duration are 527 *n*m and 100 *n*s respectively. HighSpeedStar6 HSS6 775K-M1 mode was employed as a high speed digital camera. The sensor type of the camera is complementary metal-oxide semiconductor, CMOS. Each pixel in an image which is taken by the high speed digital camera is read individually (Holst and Lomheim 2007). Where the image rate is 2.5 kHz, the maximum resolution is 1024 x 1024 pixels. The image rate can be adjusted up to 20 kHz when the resolution is 512 x 512 pixels. When the high speed camera is used in the double frame mode, the minimum inter-frame time is less than 1 μs. Its sensor pixel size is 20 x 20 μm. One pixel in an image that is captured by this camera is represented in 12 bit, that is, the range of the intensity of one pixel is from 0 to 4095. In the current research, the repetition rate of the laser and the image rate of the high speed camera was 2.5 kHz, and the resolution was 1024 x 1024 to secure high spatial resolution in the given experimental condition.

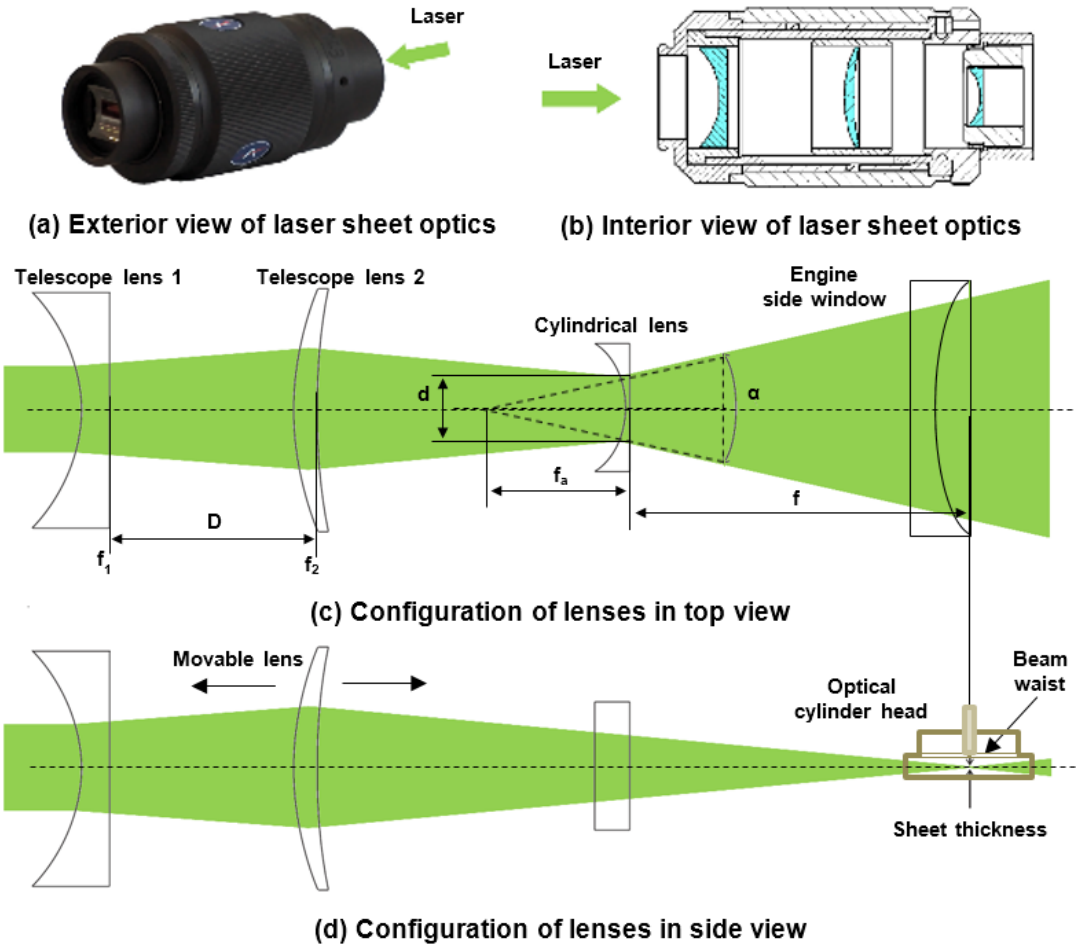

α: aperture angle of light sheet
d: laser beam diameter
$f_α$: focal length of cylindrical lens
f: focal length of light sheet optics
f_1: focal length of telescope 1
f_2: focal length of telescope 2
D: length between two telescope lenses

Figure 3.19 Photograph and configuration of light sheet optics: the figure is reproduced and modified from the manufacturer manual (LaVision 2013)

Although the trigger signal to operate the PIV system was transmitted from the engine control system, which is described in Sec. 3.5, the Nd:YLF laser and high speed camera were operated by the internal signals of the separate controller, which is called high speed controller. After receiving the trigger signal from the engine control system, the high speed controller transmits trigger signals to the laser and camera, and each time resolution is 10 *n*s. TSI Six-Jet-Atomizer Model 9306A was used as an atomizer to add the tracing particles to the air supply system.

In order to convert a laser beam into a type of sheet to illuminate tracking particles homogenously and broadly dispersed inside the optical cylinder head of the research engine, it is essential to arrange a set of lenses properly. In

this experiment, the LaVision light sheet optics, which is comprised of a series of lenses, was adopted: see the configuration of the light sheet optics in Figure 3.19. The light sheet optics is composed of one cylindrical lens and two telescope lenses. The focal length of the cylindrical lens f_a was -20 mm, and the laser beam diameter was approximately 5 mm. The aperture angle of the light sheet α was 14.3 º, which was calculated with Eq. (3.12) and Eq. (3.13) that show the relationship between the focal lengths of lenses of the light sheet optics (LaVision 2014).

$$\alpha = 2arctan\frac{d}{2f_a} \qquad \textbf{Eq.} (3.12)$$

$$f = \frac{f_1 \times f_2}{f_1 + f_2 - D} \qquad \textbf{Eq.} (3.13)$$

α: aperture angle of light sheet
d: laser beam diameter
f_a: focal length of cylindrical lens
f: focal length of light sheet optics
f_1: focal length of telescope 1
f_2: focal length of telescope 2
D: length between two telescope lenses

The focal length of the light sheet optics was 390 mm, which is the length between the centre of the piston crown and the cylindrical lens front. In order for the beam waist to be closest to the centre of the piston crown of the research engine, the location of the light sheet optics and its moveable lens, telescope lens 2 in Figure 3.19, were adjusted, checking that the thickness of the laser sheet at the centre was minimum. By burning black paper that was perpendicular to the laser sheet optics and located at the centre of the piston crown, the thickness of the laser sheet was checked. It was crucial to minimize the thickness of a laser sheet because the undesirable scattered light of tracing particles that could stem from other vertical layers, not the interest plane, could be captured in a PIV image. This would cause false vector data in the process of calculating the flow field. Hence, the thickness of the laser sheet was checked, and was almost 1 mm. Note that the invasion of undesirable scattered light of the tracer particles from other vertical layers is unavoidable unless the thickness of the laser sheet is thin enough.

It was also important to adjust the vertical position of the laser sheet. As mentioned in Sec. 3.1, the gap between the tip of the spark plug and the top of the piston crown when it was at TDC was approximately 4 mm. In order for the laser sheet to pass through the narrow space without any obstacle, the

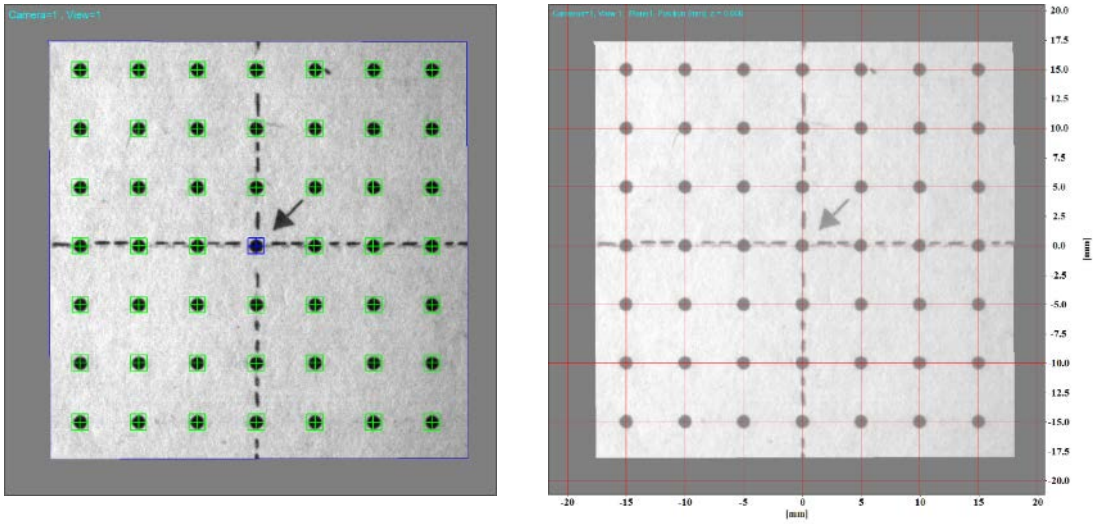

(A) Detection of dot marks **(B) New coordinate system**

Figure 3.20 Calibration result of the high speed camera

proper position of the laser head were located vertically, and the inclination degree of the mirror was adjusted.

After arranging each component properly, the calibration of the high speed digital camera was carried out using the commercial software, DaVis, to correct an image due to the position of the camera, which was not accurately perpendicular to the plane of interest and to make the desirable coordinate system for a PIV image. For the calibration, a 1.5 mm thickness of the calibration plate with dot marks was used. The distance between dots was 5 mm, and the diameter of the dot was 1 mm. The vertical focal point of the camera was about 1.5 mm higher than the top of the piston crown when it was at TDC. The result of the calibration is shown in Figure 3.20. The blue square in Figure 3.20 (A) is the centre of the calibration plate and piston crown. To align the centre of the calibration plate with that of the piston vertically, the separate cast was made and used. The dimension of the interest area was 40 x 40 mm^2, and the distance between pixels was 0.0409 mm.

Figure 3.21 shows the example of the device offset setting. The device offset represents the time delay between the timing when the high speed controller gives a signal to the laser and the one when the laser pulse is emitted. It is obvious that each pulse of the laser has to align with each frame of an image. As seen in Figure 3.21 (b), the pulse A has to be emitted at the1st frame in the i_{th} image, and the pulse B also has to be emitted at the 2nd frame. If undesirable device offset were set up, seeding particles would not appear in

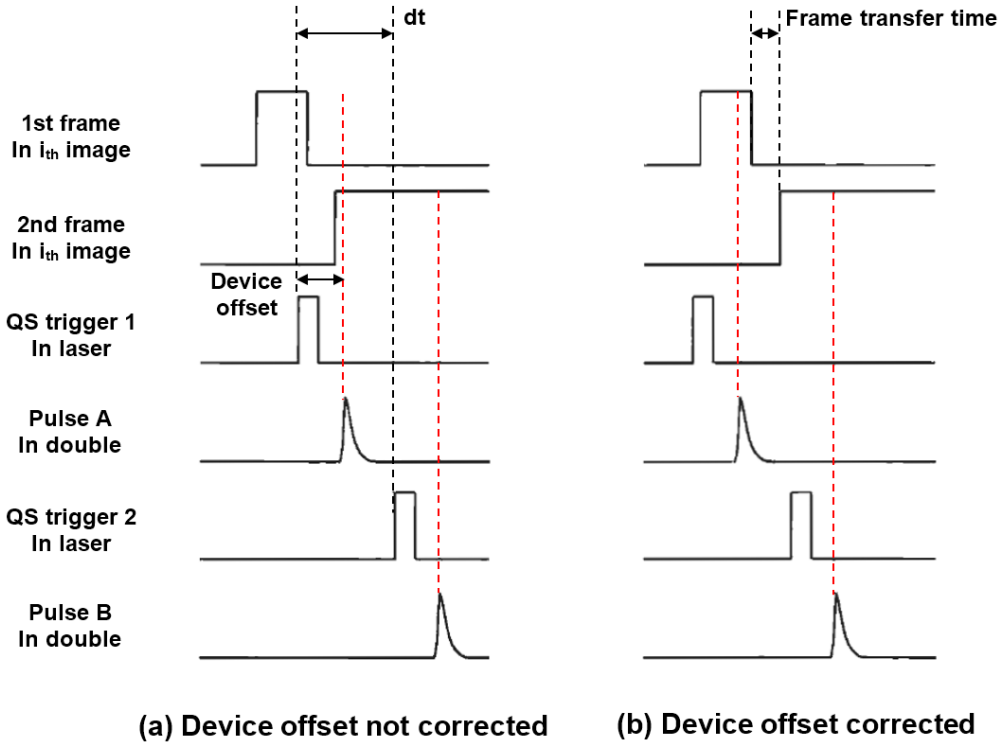

Figure 3.21 Adjustment of the device offset: the figure is reproduced and modified from the manufacturer manual (LaVision 2012)

one of two frames because they are not illuminated when the image is taken: refer to Figure 3.21 (a).

Before the start of the experiment, the device offset was checked, and the values were adjusted: one of two pulses was emitted, and then it was confirmed whether the PIV image was recorded in the corresponding frame. The device offset values are represented in Table 3.3. The high speed controller that transmitted trigger signals to the laser and high speed camera was checked in order to realise whether it provided the sub-components with the signals accurately after it received the trigger signal from the engine control system, which is shown in Figure 3.41 in Sec. 3.5. It was confirmed that the high speed controller was in good condition. Table 3.3 shows the specification of each component of the PIV system and its setting values that were used in the current experiment. Of the items in the table, the items not mentioned so far such as interrogation window size, overlap, shape, and others are described in Sec. 3.4.3.

Table 3.3 Specification of the PIV system and setting values which was used in the experiment

Item	Value
Laser	
Type	Nd:YLF
Maximum power	10 mJ at 1 kHz
Maximum repetition rate	10 kHz
Wavelength	527 nm
Pulse duration	100 ns
Camera	
Type	CMOS
Maximum resolution	1024 x 1024 pixels at 2.5 kHz
Maximum image rate	10 kHz at 512 x 512 pixels
Minimum frame transfer time	< 1 μs
Minimum exposure time	1 μs
Sensor pixel size	20 μm x 20 μm
Digital output	12 bit (0 - 4095)
Lens focal length	105 mm
Lens maximum aperture and scale	f/4.5, f/4.5 – f/32
High speed controller	
Output signal	TTL
Time resolution	10 ns
Trigger source	Internal generator / external TTL input
Image trigger	Internal / external
Atomizer for seeding	
Number of jets	6
Mean droplet diameter	0.35 μm for water 1 – 5 μm for olive oil
Particle concentration	> 10^6 particles/cm^3
Particle material	olive oil, PSL(polystyrene latex), and others
Flow rate per jet	6.5 L/min at 170 kPa 12 L/min at 380 kPa
Maximum in-outlet pressure	550 / 102 kPa
Set values at the current research	
Laser-repetition rate	2.5 kHz
Camera image rate	2.5 kHz
image mode	Double frame
image resolution	1024 x 1024 pixels
Lens focal length	105 mm
Lens aperture	f/4.5
High speed controller-trigger source	External TTL input
image trigger	internal
Atomizer particle material	Olive oil

Item	Value
Number of used jets	6
supply amount of air+seeding particle	10-15 % of the total fuel-air mixture [vol]
Area of interest	40 x 40 mm^2
Inter-frame time (dt)	100 μs
Interrogation window size	32 x 32 pixels
Interrogation window overlap	75 %
Interrogation window shape	adaptive
Particle size	1 - 2 pixels
Device offset	
Laser	Pulse A 0 μs Pulse B -5 μs
camera	1st frame 0 μs 2nd frame 0 μs

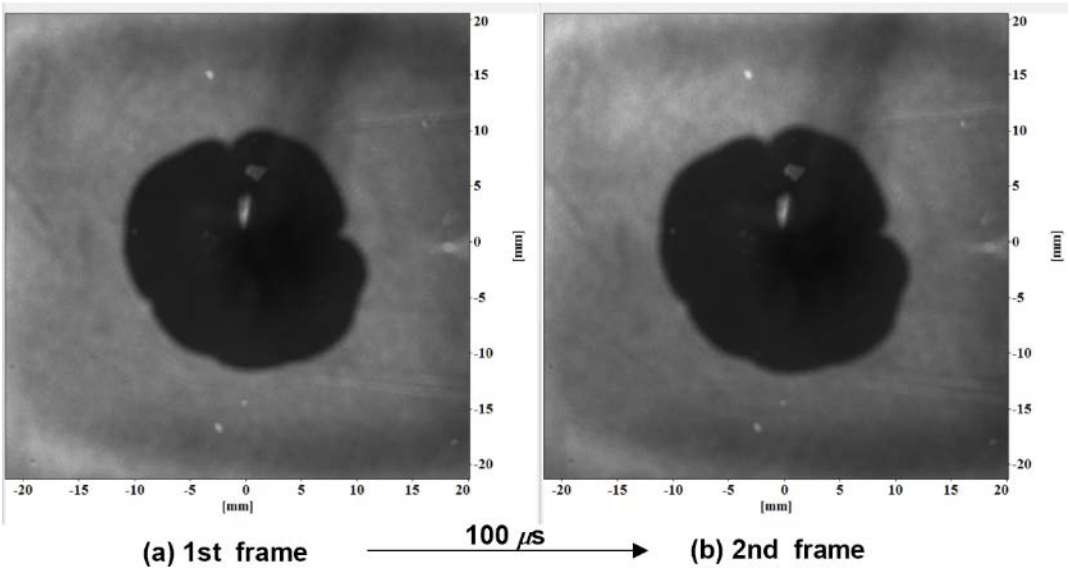

Figure 3.22 Double-frames flame propagation image which was taken 4 ms after the start of the ignition: the experimental condition is that CH_4-air mixture, equivalence ratio 1.0, engine speed 50 rpm, ignition timing 22.0 bTDC, initial pressure and temperature at the start of ignition 6 bar abs / 460 K. Refer to the set values in Table 3.3.

3.4.3 Derivation of the flow field from the PIV images

The primary research objective is to measure flame propagation speed, unburned gas velocity, and burning velocity. To do so, it is essential to obtain the desirable flow field of unburned gas from PIV flame images. This section presents how to calculate the flow velocity vectors of unburned gas. The imaging mode that was used in the current work was double frame mode, i.e.

one image consists of two separate sub-images. Each of them is named 1st and 2nd frame in this paper respectively, and as mentioned in Sec. 3.4.1, cross correlation was carried out.

After PIV images are taken by the high speed CMOS camera, each frame in the image is divided into a certain size of area, which is the interrogation window. Most of the commercial software programs conduct the correlation computation in the frequency domain using fast Fourier transform, FFT. The intensities of pixels in an interrogation window are transformed into frequency, and the location where the maximum frequency appears is found. Subsequently, inverse fast Fourier transform, IFFT, is conducted (Raffel, Willert et al. 2007). Correlation plane of which the interrogation window is located at image position x_0, y_0 can be represented as follows (LaVision 2010):

$$C(x_0, y_0) = \overline{I_1}(x_0, y_0, t) \cdot \overline{I_2}(x_0, y_0, t + dt) \quad \textbf{Eq.} (3.14)$$

where $\overline{I_1}$ and $\overline{I_2}$ are the values into which the functions of I_1 and I_2 are converted through the Fourier transform respectively. The change of the position of the maximum correlation peak in the correlation plane from time t to $t+dt$ is almost in accordance with the displacement of the particles in the interrogation window. By dividing the displacement by the inter-frame time dt, the velocity vector at image position x_0, y_0 can be calculated. Eq. (3.15) represents the calculation.

$$V_x(x_0, y_0), V_y(x_0, y_0) = \frac{Peak\ position\ in\ C(x_0, y_0, t + dt) - Peak\ position\ in\ C(x_0, y_0, t)}{dt} \quad \textbf{Eq.} (3.15)$$

By applying the correlation computation that is mentioned in Eq. (3.14) and Eq. (3.15) to the entire area of a PIV image, its flow field can be obtained.

Figure 3.23 shows a series of steps to process PIV images for the calculation of velocity vectors of a flow field. There are several commercial software programs that are used for a PIV system. Of them, the commercial software that was used in the current research was DaVis, which was made by LaVision. Of the features with which this software is equipped, several functions and the setting values used in this experiment are described below.

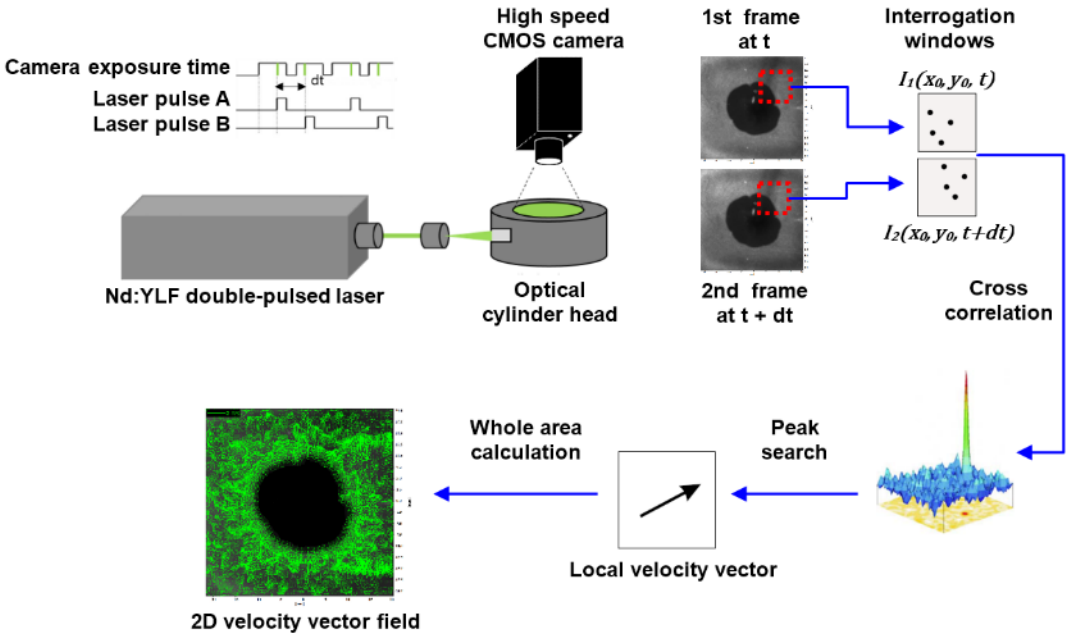

Figure 3.23 2D flow field calculation with the use of cross correlation

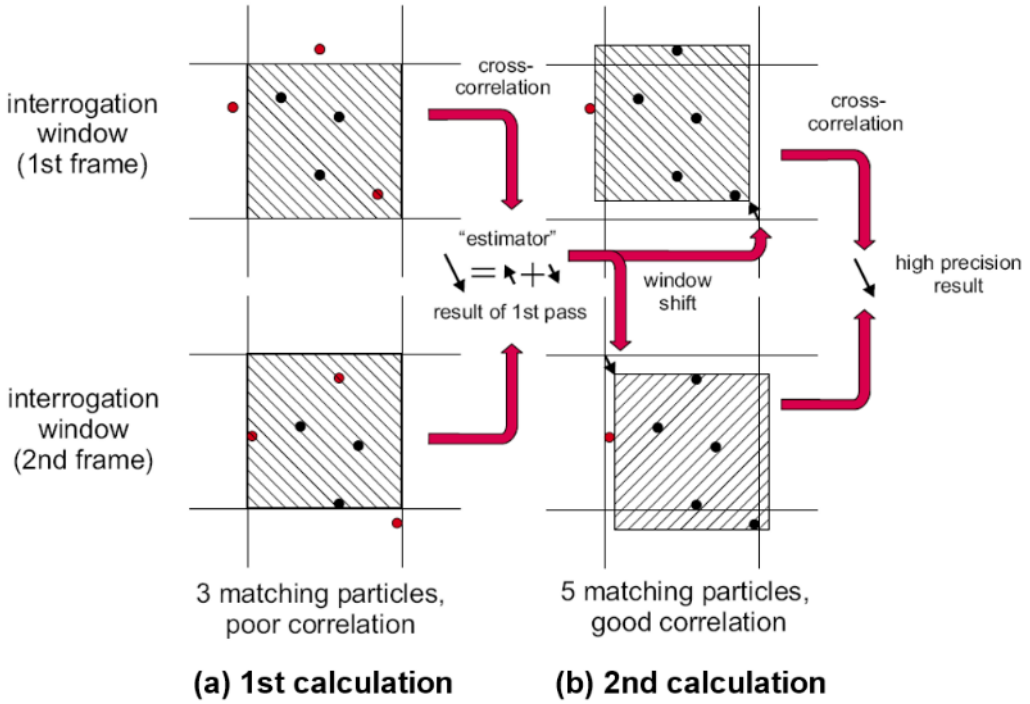

Figure 3.24 Iteration of calculation of an interrogation window reflecting the flow gradient that is obtained from the previous calculation: the figure is cited from the manufacturer manual (LaVision 2010)

The iteration function was used, which repeats the process of calculating the velocity vectors of a flow field as many times as the setting value. During the iteration, which is sometimes called another term “multi pass”, the position of the interrogation window can be shifted, considering the flow gradient that is calculated in the initial or previous calculation. This makes it possible to reduce the number of particles that ran out of the interrogation window in the second frame. Figure 3.24 shows the comparison of the cases that the iteration function is activated (a) and not (b). By applying this feature to the processing, the reliability of the calculation result could be enhanced (Keane and Adrian 1990).

The main factors in the determination of the separation time dt between two frames are the flow gradients and interrogation window size of PIV images. For the accurate calculation of a velocity field, the tracking particles that are taken in the interrogation window of the first frame do not have to deviate from the one of the second frame. According to Keane and Adrian (1990), the displacement of particles in an interrogation window should be smaller than a quarter of the entire interrogation window size. For example, where the interrogation window size is 32 x 32 pixels and dt is 100 μs, the displacement should be smaller than 8 pixels, of which the calculated velocity is 3.2 m/s in a horizontal or vertical direction.

Figure 3.25 shows the velocity vector maps in motoring cycles. The PIV images were taken at 36.2, 27.6, 22.0 º CA bTDC, and TDC. The speed of the research engine was 50 rpm, and the fluid consisted of air and olive droplets. The velocity vector maps were plotted where the separation time dt between two frames was 100 μs, the size of the interrogation window was 32 x 32 pixels, and the overlap percent between two adjacent interrogation windows was 75 %. The mean velocities in (A), (B), (C), and (D) are the spatially-averaged values in each flow field: refer to Appendix A. As the recorded timing approached TDC, the mean velocity gradually increased.

When combustion proceeds, the velocity of unburned gas in the vicinity of a flame front is changed by the effect of the thermal expansion that the burned gas causes (Balusamy et al. 2011, Long and Hargrave 2011, Burluka 2015). Since seeding particles nearby the flame front do not deviate from an interrogation window, it is essential to set up an interrogation window size, overlap percent between two adjacent interrogation windows, and the shape of an interrogation window properly. The set values were adjusted appropriately with trial and error, and Figure 3.26 shows the results.

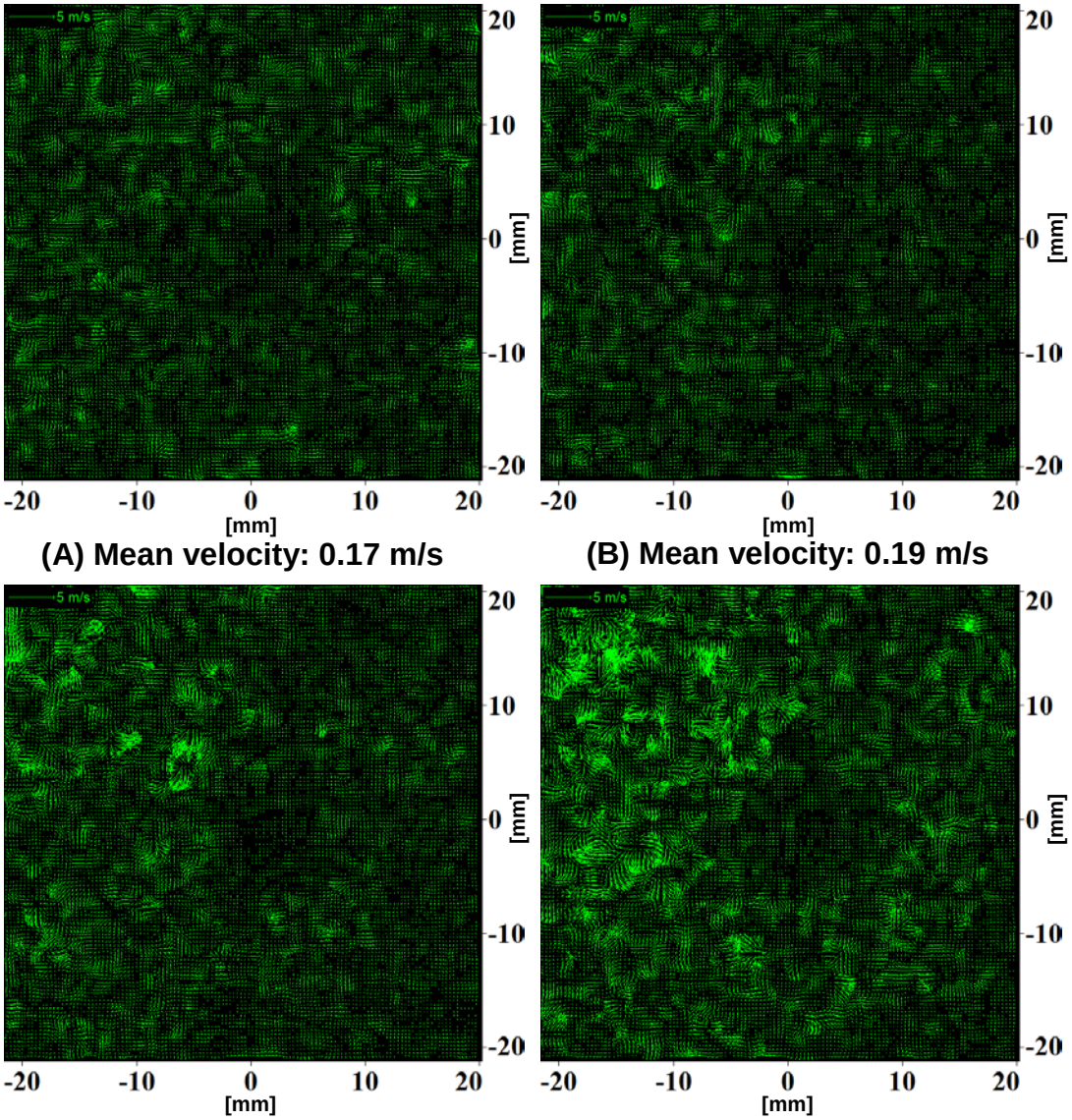

(A) Mean velocity: 0.17 m/s **(B) Mean velocity: 0.19 m/s**

(C) Mean velocity: 0.27 m/s **(D) Mean velocity: 0.37 m/s**

Figure 3.25 Flow fields of the velocity vectors at motoring cycles: recorded timing: 36.2 (A), 27.6 (B), 22.0º CA bTDC (C), and TDC (D)

As seen in Figure 3.26 (a), depending on an interrogation window size, a lot of false velocity data can be calculated. Especially, when an interrogation window size was smaller than 32 x 32 pixels, the velocity data were not reliable. On the other hand, where an interrogation window size was 64 x 64 pixels, although the false velocity did not occur and the velocity data was credible, the number of the data was small to be analysed. Similarly, as shown in Figure 3.36 (b), where the overlap percent between two adjacent interrogation windows was 25 and 50 %, the number of the velocity data in the entire flow field was relatively small. And a lot of the false velocity vectors took place at 87.5 %.

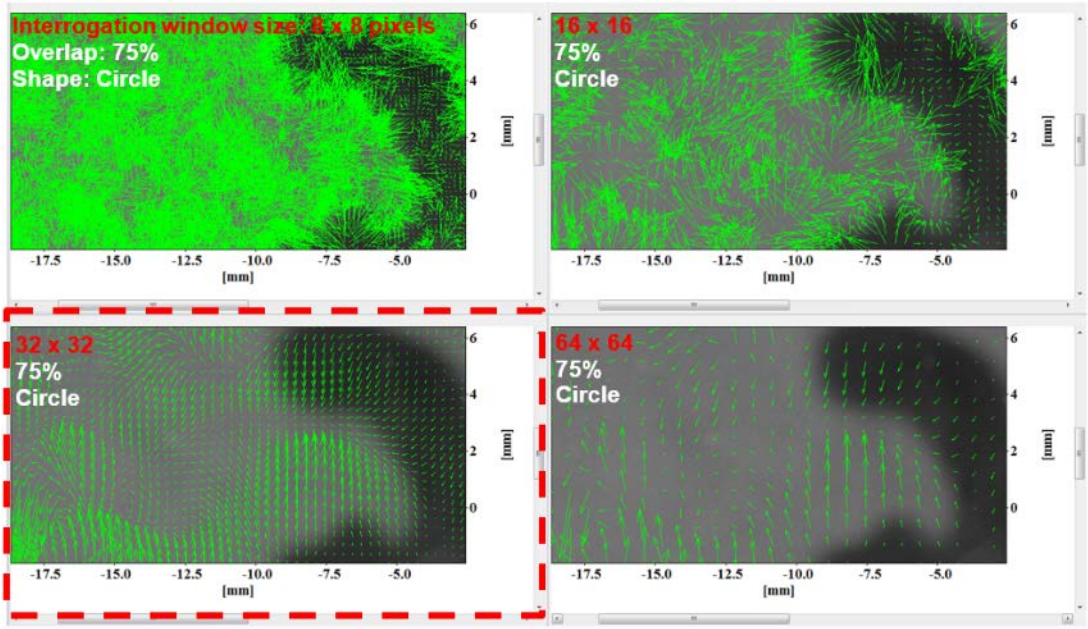

(a) Variation of flow field in terms of interrogation window size

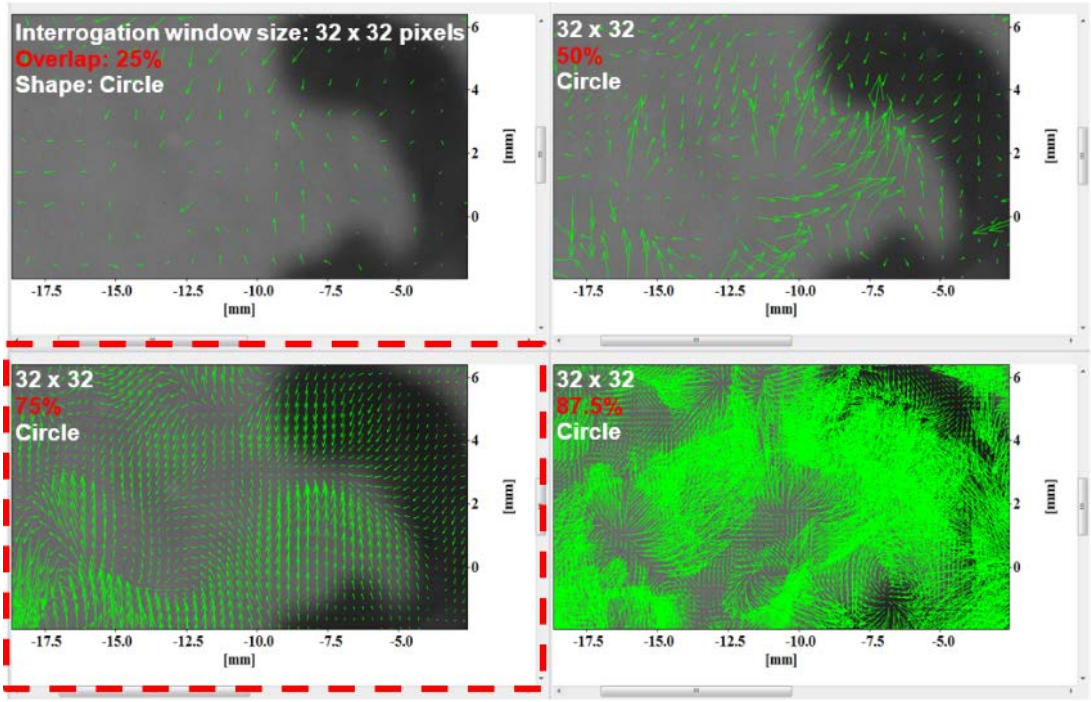

(b) Variation of flow field in terms of overlap percent between two adjacent interrogation windows

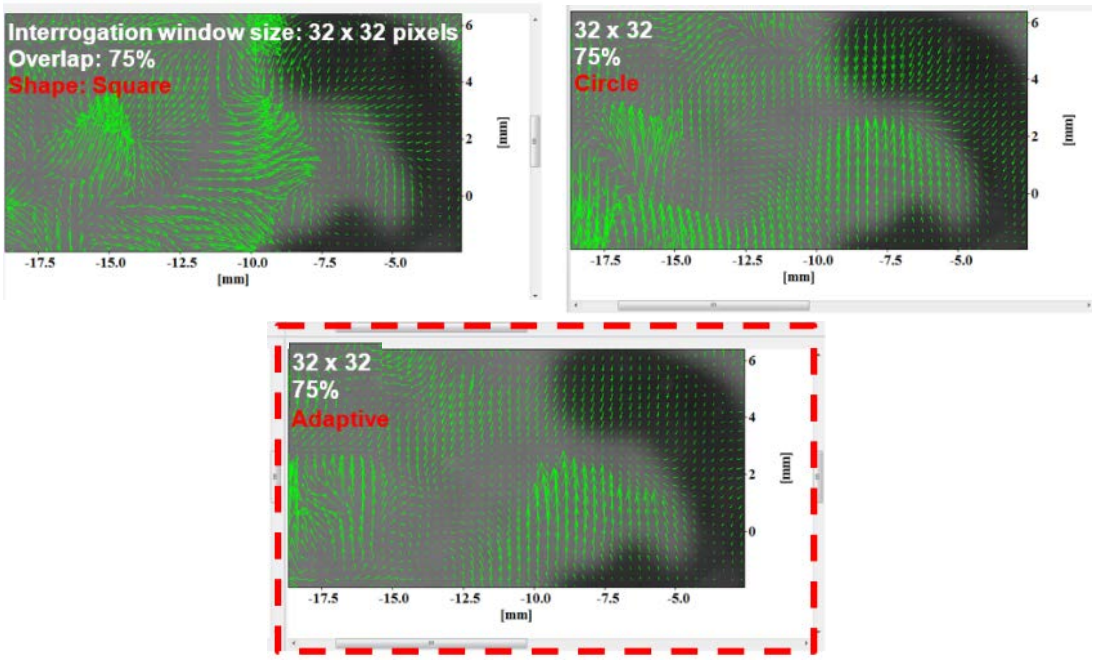

(c) Variation of flow field in terms of interrogation window shape

Figure 3.26 Variation of a flow field in terms of the changes of an interrogation window size, overlap percent between two adjacent interrogation windows, and the shape of an interrogation window: the experimental condition was H_2-air mixture, equivalence ratio: 0.4, the time when the images were taken at 26.4 ms after ignition / the start of ignition 27.6 bTDC / engine speed 50 rpm.

To achieve the more accurate result of local flow field calculation, the shape of an interrogation window was also be adjusted using the internal function, adaptive interrogation window. This function is usually used to find out the optimum shape of an interrogation window, considering the quality of a PIV image and the flow gradient that is calculated from the initial or previous result. And this function works with the iteration function mentioned above. Hence, the interrogation window size and shape are adjusted referring to the result of the previous evaluation (Wieneke[1] and Pfeiffer[1] 2010). In summary, the set values of the separation time, interrogation window size, overlap percent, and shape that were adopted in the current work were 100 μs, 32 x 32 pixels, 75 %, and adaptive mode respectively.

When a digital image is dealt with, it should be noted that peak locking effect, which is usually referred to as spatial aliasing in signal processing, might take place when velocity vectors are calculated. The effect means that velocity data in the flow field have a bias toward the nearest integer velocity value (Overmars, Warncke et al. 2010). For example, although the value of a real flow velocity is 0.4 or 1.6, the calculation may be made of 0 or 2. The pheno-

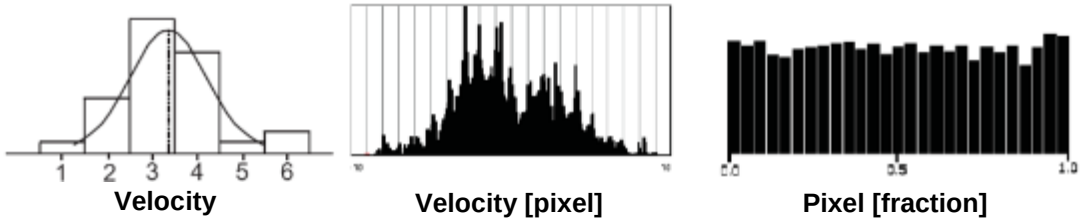

(a) Graph of probability density function in the case of a proper particle image size

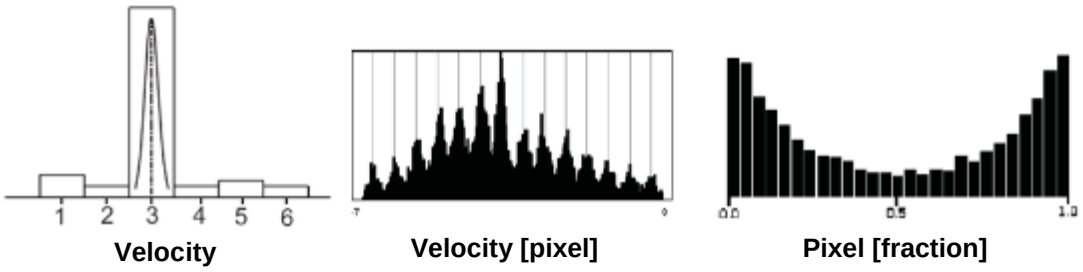

(b) Graph of probability density function in the case of an improper particle image size

Figure 3.27 Peak locking effect for small and big particle image size; the figure was reproduced from the manufacturer manual (LaVision 2010)

-menon may occur when the size of tracking particles is too small, compared with the pixel size of an image. Or where a pixel size is much larger than the size of a seeding particle, peak locking effect may be observed. The reason why peak locking effect occurs is that the spatial resolution is not sufficient for the image to be processed (Raffel, Willert et al. 2007). Prior to the actual measurement, whether the peak locking effect took place or not was checked by investigating the distribution of the flow velocity vectors using the probability density function (LaVision 2010).

Figure 3.27 shows the examples of the probability density function of flow velocity vectors. If peak locking effect does not take place or the effect is very small, pixels in fraction are evenly distributed, which is seen Figure 3.27 (a). On the contrary, where peak locking effect occurs because the inappropriate resolution of an image is selected or the pixel size of a seeding particle is too small, the distribution of pixel in fraction becomes similar to the rightmost graph of Figure 3.27(b). The occurrence of peak locking effect means that the reliability of velocity data that are calculated from PIV images should be doubtful. When peak locking effect happens, it is essential to change image resolution or the material of a seeding particle.

Figure 3.28 shows the result of peak locking effect in the present work. The combustible mixture was the hydrogen-air mixture, and its equivalence ratio was 1.0. The research engine was operated at 50 rpm, the timing when the PIV image started to be recorded was 27.6 º CA before TDC, and the material of a seeding particle was olive oil. Figure 3.28 (a-2) and (b-2) are the histograms of the first decimal place that is relevant to a velocity vector in the x- and y- direction, which means that the integer value of a velocity is cut. For example, if the value of a velocity in x-direction, V_x, is 1.234 in pixels, the value in the histogram will be 0.234 in pixel. Although the histogram (a-3) and (b-3) are also the histograms of the first decimal place which corresponds to a velocity vector, the range of interest in the first decimal place is from 0 to 0.5 in pixel.

Changing the resolution of a PIV image, it was investigated whether peak locking effect occurred or not. As shown in histogram (a-2) and (a-3) in Figure 3.28, in the case that the resolution of the PIV image was 512 x 512 pixels, the values of the velocity vectors in x- and y- direction were biased toward the both side. The mode in histogram (a-2) appeared at zero or near one, and the mode in histogram (a-3) did also the highest at zero. This means that the peak locking effect occurred. The graph (b-1), (b-2), and (b-3) are the result where the resolution of the PIV image was 1024 x 1024 pixels. Except for the change of the resolution, other experimental conditions were not altered. As seen in the histogram (b-2) and (b-3), the values of the velocity vector data were evenly distributed without the bias toward zero or one, and it was confirmed that 1024 x 1024 pixels was a desirable resolution in obtaining trustworthy velocity data. The peak locking effect value, which is shown in Figure 3.28 (a-3) and (b-3), is an index to estimate how much peak locking effect is caused. It is calculated as follows (LaVision 2010):

$$Peak\ locking\ effect\ value = 4 \times (0.25 - center\ of\ mass\ of\ histogram) \quad \textbf{Eq.}\ (3.16)$$

The calculation was made from the centre of mass of the histogram (a-3), and the value was 0.7613. Where the value is zero, it is meant that there is no peak locking effect in velocity data. In contrast, when the value is one, it means that a strong peak locking effect occurs. In the case that the peak locking effect value is less than 0.1, the reliability of the velocity vector data is acceptable (LaVision 2010).

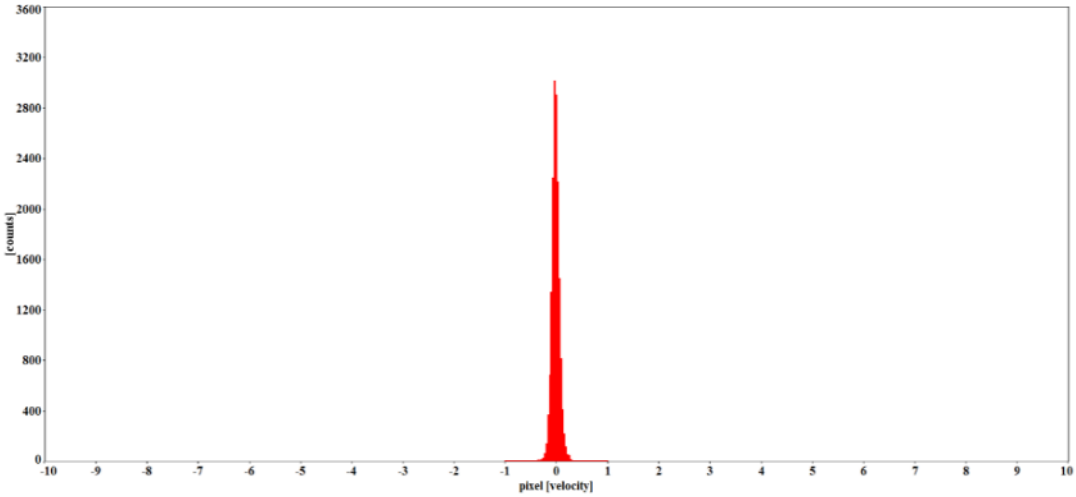

(a-1) Distribution of velocity vectors derived from 512 x 512 pixels of a PIV image

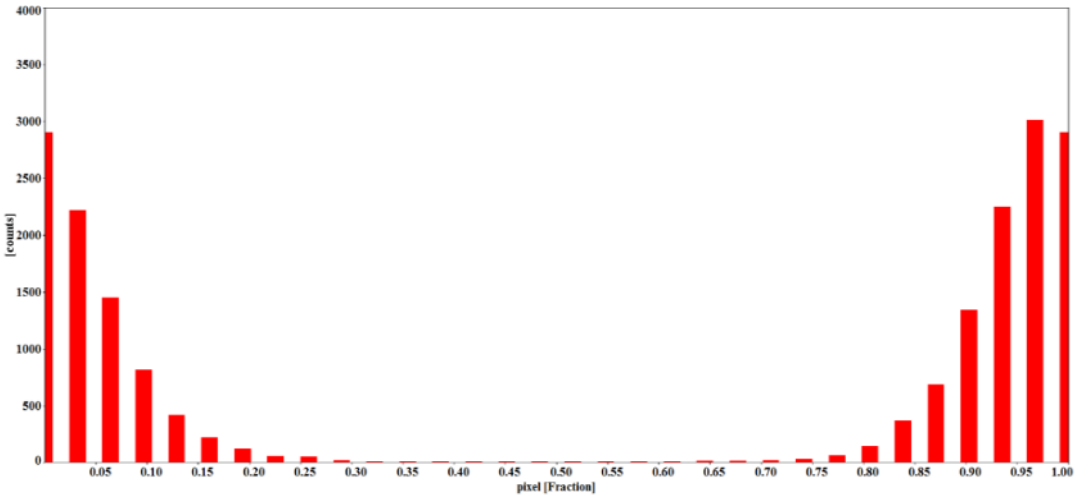

(a-2) Distribution of values in the first decimal place of velocities in a 512 x 512 pixels of a PIV image

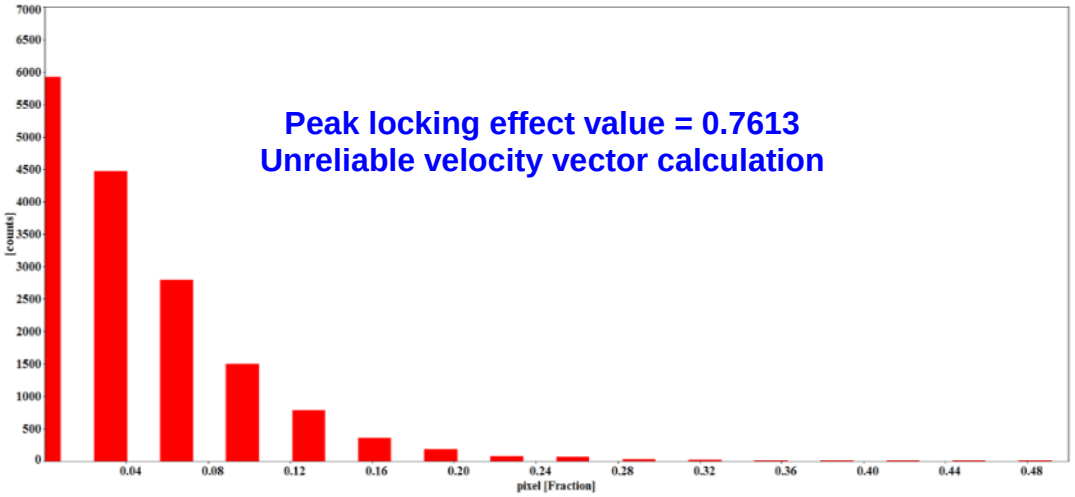

(a-3) Distribution of values equal to or less than 0.5 in the first decimal place of velocities in a 512 x 512 pixels of a PIV image

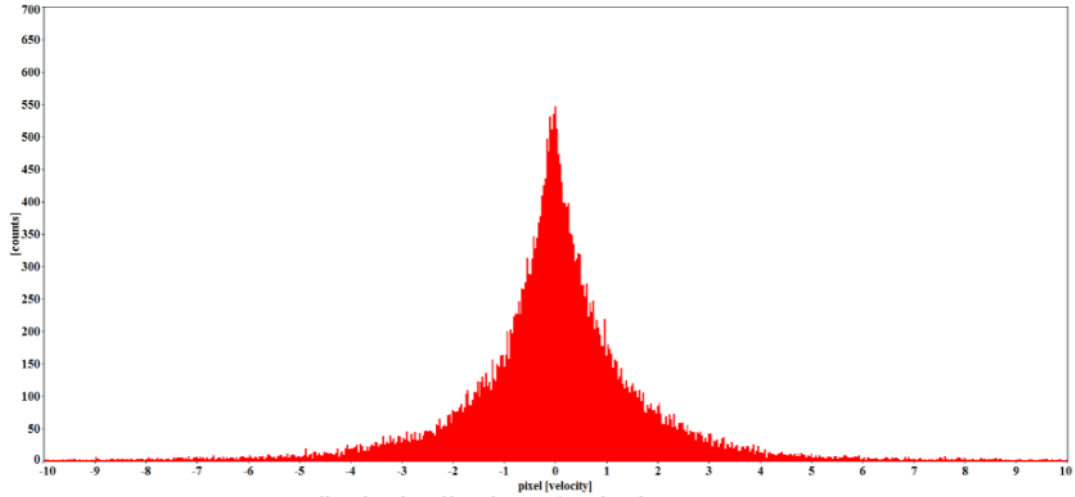

(b-1) Distribution of velocity vectors derived from 1024 x 1024 pixels of a PIV image

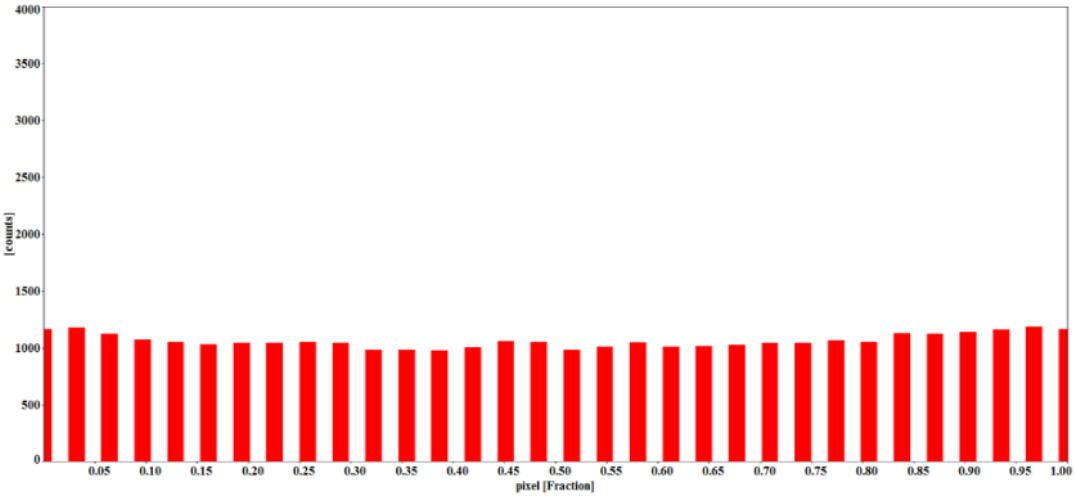

(b-2) Distribution of values in the first decimal place of velocities in a 1024 x 1024 pixels of a PIV image

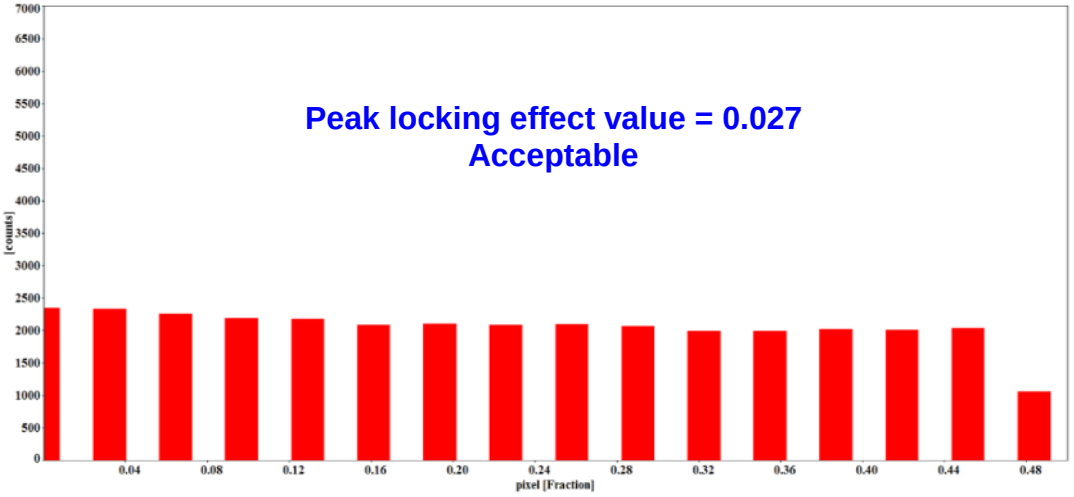

(b-3) Distribution of values equal to or less than 0.5 in the first decimal place of velocities in a 1024 x 1024 pixels of a PIV image

Figure 3.28 Results of checking the occurrence of peak lock effect: fuel H_2-air mixture / equivalence ratio 1.0 / data collected at 4 ms after the start ignition / data collection timing: 27.6 ° bTDC / engine speed 50 rpm

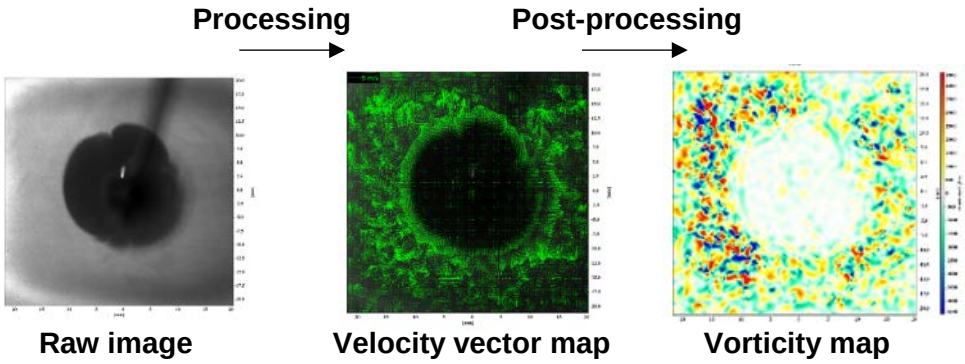

Figure 3.29 An example of processing and post-processing of a PIV image. Fuel: H_2-air mixture / equivalence ratio 1.0 / data collected at 4 ms after ignition / ignition timing: 27.6 ºbTDC / engine speed: 50 rpm

One of the strengths in adopting PIV technique is that the flow field data that are obtained through the process mentioned above can be used repeatedly for their derivatives. In this research, using velocity vector data, additional useful calculation was conducted to obtain the vorticity in a flow field to investigate the correlation between how much wrinkled a flame front was and the flow field ahead of the flame front. Figure 3.29 shows an example of calculation of the velocity data. The combustion mixture in the figure was the stoichiometric hydrogen-air mixture. The timing when the flame image was taken was at 4 ms after ignition, and the ignition timing was 27.6 º CA before TDC. The speed of the research engine was 50 rpm. And the equation for the calculation of the vorticity is shown in Eq. (3.17).

$$Vorticity = \frac{\partial V_x}{\partial y} - \frac{\partial V_y}{\partial x} \qquad \textbf{Eq.}\ (3.17)$$

Prior to the actual experiment, it was essential to make sure whether the combustion condition inside the cylinder of the research engine was laminar or not when the combustion started. Hence, the ensemble-average mean velocity that is mentioned in Appendix A was measured.

From Figure 3.30 to Figure 3.33, the velocity vectors in each flow field and the corresponding scalar maps are shown. The size of the area of interest was 40 x 40 mm^2, and the resolution of the raw PIV images was 1024 x 1024. When the flow fields were recorded, the speed of the research engine was 50 rpm. The flow field were obtained with respect to the recorded timing. The

distinguishable colour in the scalar maps in Figure 3.30 to Figure 3.33 represents the absolute value of the corresponding velocity vectors: see Eq. (3.18)

$$\left|V_g(x,y)\right| = \sqrt{V_{g_x}(x,y)^2 + V_{g_y}(x,y)^2} \qquad \textbf{Eq.}\ (3.18)$$

where V_{gx} and V_{gy} are the velocity vector in the horizontal and vertical direction respectively.

Figure 3.34 shows the change of the mean velocities that are related to the scalar maps in Figure 3.30 to Figure 3.33. When the speed of the research engine was run at 50 rpm, the values of the mean velocities were 0.11, 0.12, 0.18, and 0.24 m/s at 36.2, 27.6, 22.0º CA before TDC, and TDC respectively. As the piston approached the TDC, the mean velocity had a tendency to rise. The most of the velocities in the four scalar maps in Figure 3.30 to Figure 3.33 were less than 0.3 m/s.

Figure 3.35 shows the scalar maps of the velocity vectors in the flow fields with respect to the speed of the research engine, and the timing to record the corresponding images was when the piston was at TDC. The change of the mean velocities of the maps is seen in Figure 3.36. The values of the mean velocities were 0.24, 0.40, 0.42, and 0.47 m/s at an engine speed of 50, 100, 150, and 200 rpm respectively. As the engine speed rose, the mean velocity progressively increased. Considering the simplified geometry of the research engine through the elimination of the undesirable components mentioned in Sec. 3.1, the engine speed seems to be the main factor in the rise of the mean velocity, and the relevant results can found in the other literature (Hall and Bracco 1987, Ling 2014).

In this research, the experiments were carried out at 36.2º CA before the TDC when the research engine was run at 50 rpm. In the same condition, the experiment was conducted at least 100 times using each combustible mixture. The results of the experiment were very similar. The results discussed in Chapter 5 are representatives of many experiments. According to the result of the experiments which were conducted in the similar condition (Chen 2016), the values of the mean velocity are similar to the result of this research, and the root-mean-square velocity is 0.23 m/s when the piston was at 22º CA before the TDC. In addition, as seen in Figure 3.30 to Figure 3.33, it seems difficult to find out a bulk flow that can cause intense turbulence inside the

cylinder. Therefore, it was assumed that the combustion condition in this research was laminar.

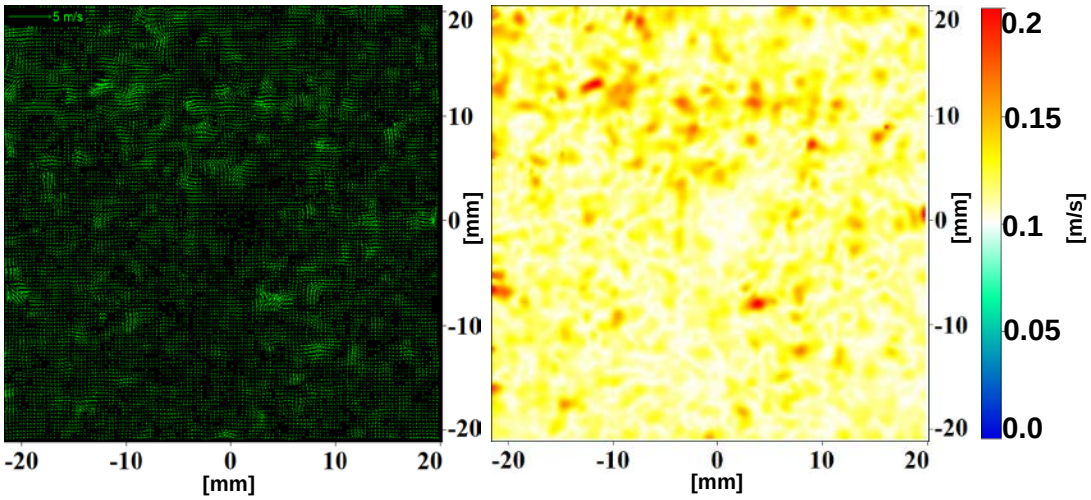

Figure 3.30 Velocity vectors in the flow field (A) and its scalar map (B): engine speed 50 rpm, recorded timing 36.2 º CA before TDC

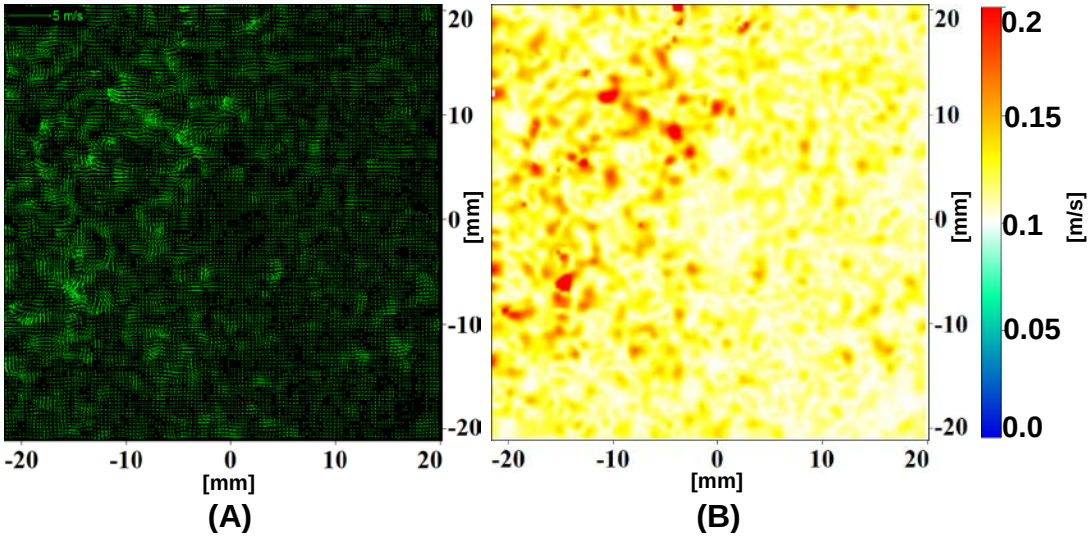

Figure 3.31 Velocity vectors in the flow field (A) and its scalar map (B): engine speed 50 rpm, recorded timing 27.6 º CA before TDC

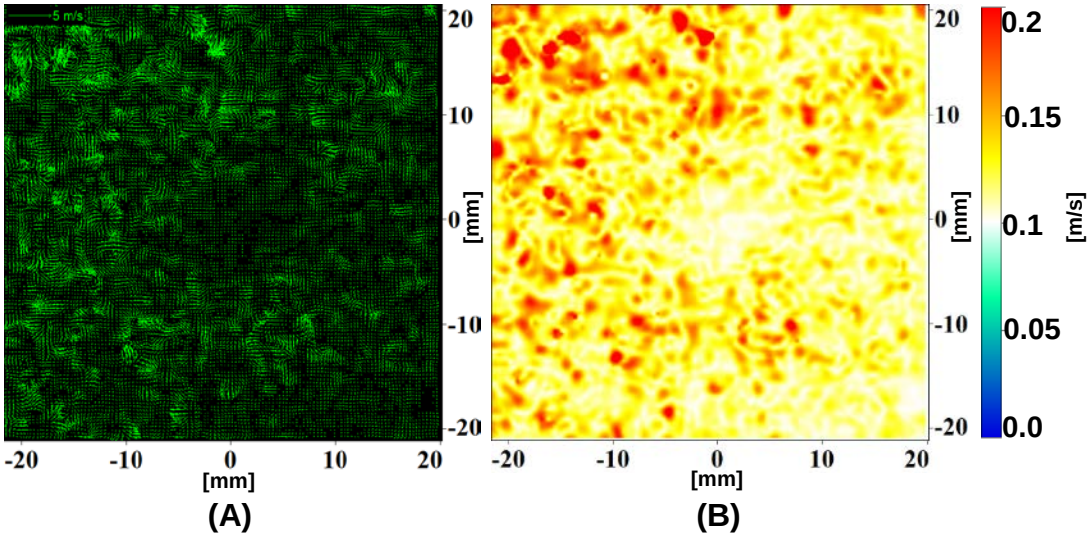

Figure 3.32 Velocity vectors in the flow field (A) and its scalar map (B): engine speed 50 rpm, recorded timing 22.0 ° CA before TDC

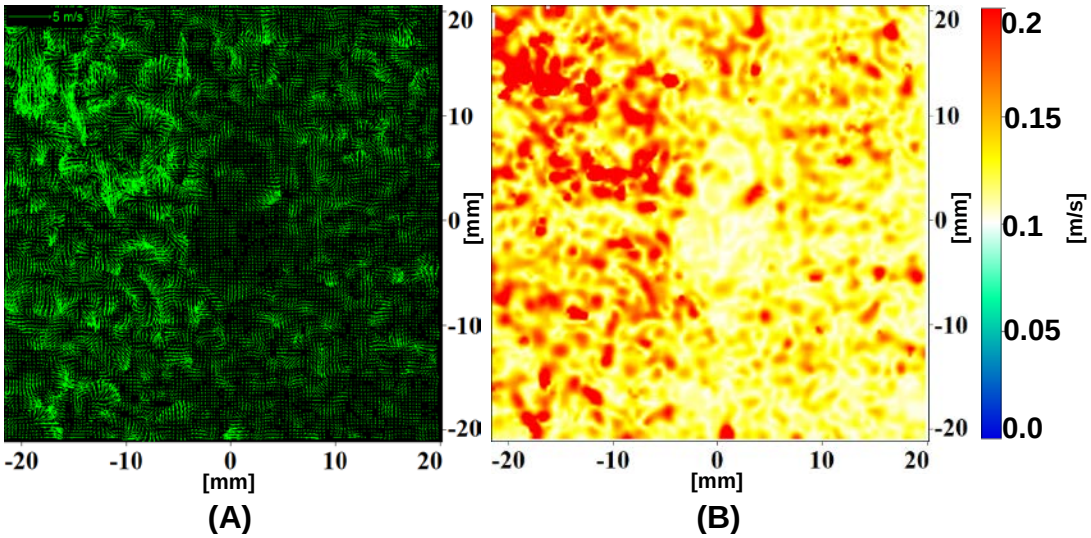

Figure 3.33 Velocity vectors in the flow field (A) and its scalar map (B): engine speed 50 rpm, recorded timing TDC

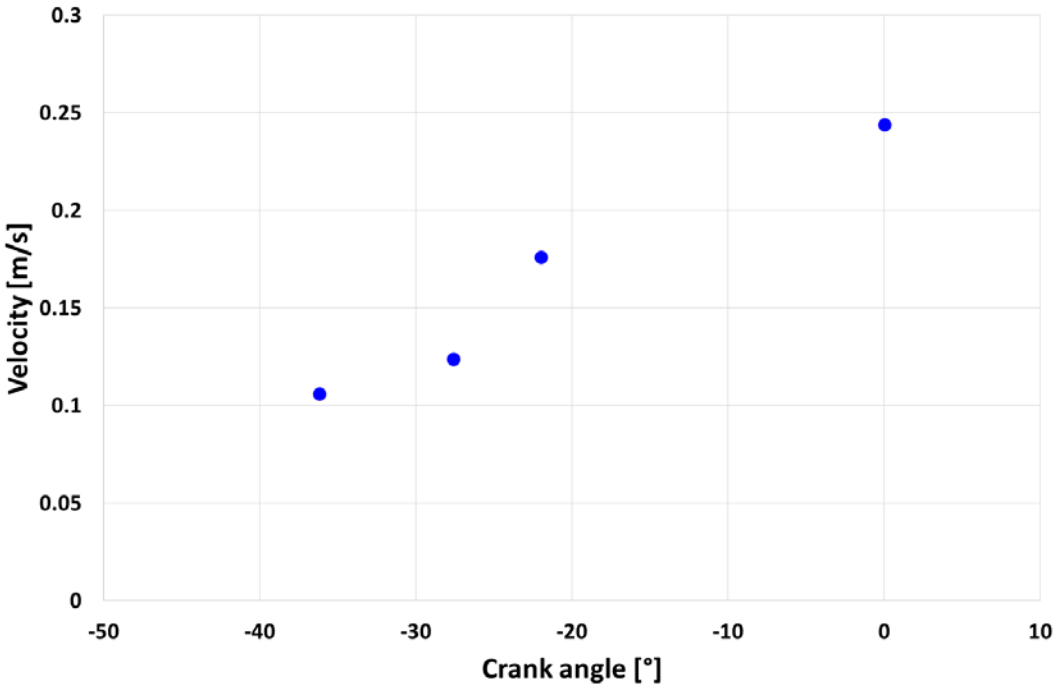

Figure 3.34 A change in the mean velocity of the scalar maps with respect to the crank angle where the research engine was operated at 50 rpm

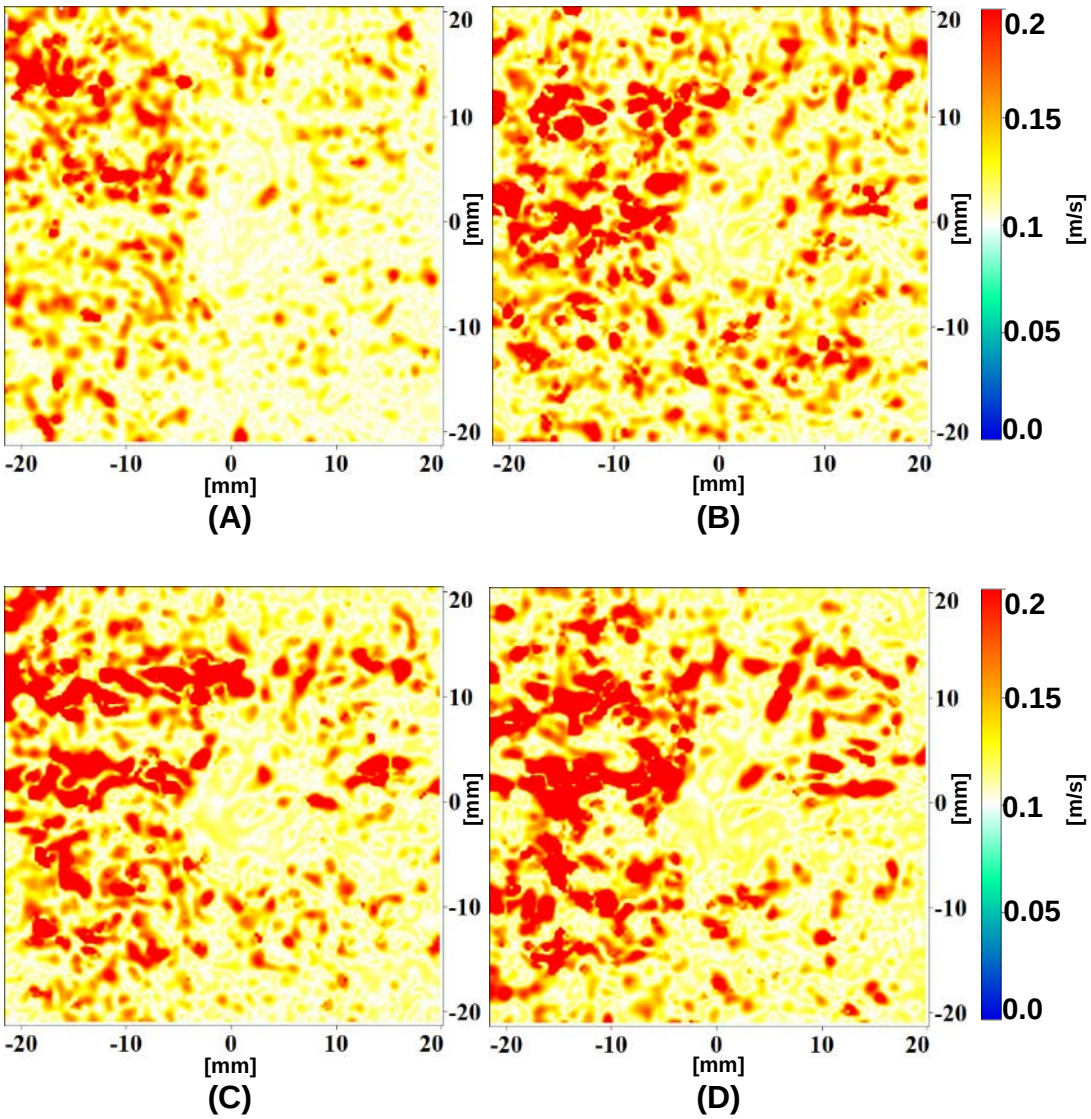

Figure 3.35 Scalar maps of the velocity vectors in the flow fields: recorded timing TDC, engine speed 50 (A), 100 (B), 150 (C), 200 (D) rpm

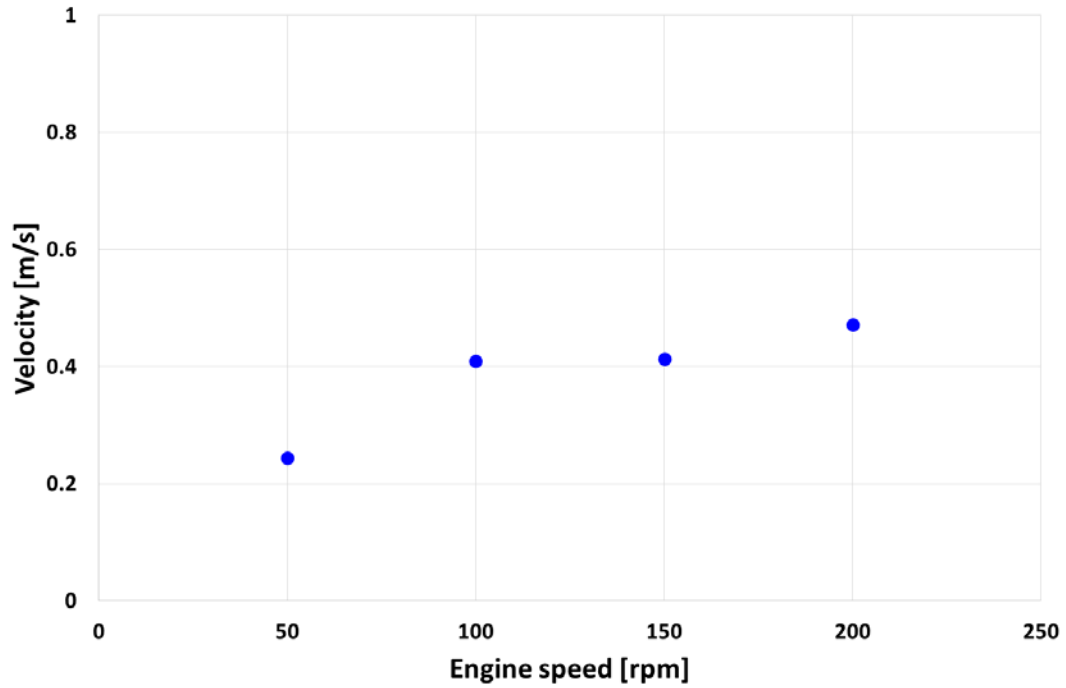

Figure 3.36 A change in the mean velocity of the scalar maps with respect to the speed of the research engine where the recorded timing was TDC

3.5 Engine control and data acquisition system

The engine control panel, Timing Rack, designed by the Leeds university combustion group, was used to control the timings of trigger signals for operating the experimental equipment (Hussin 2012). It was a complex logical circuits system. On top of it, trigger signals to control the ignition unit, camera, and other device could be retarded and advanced in steps of 1º CA. In order to enhance the reliability of a control system for the research engine and to obtain more convenient and a compact control unit, the design of a bespoke control system was implemented by the combustion group (Ling 2014, Chen 2016). The engine control system that was used in this research was based on the research of Ling and Chen. A part of the engine control code and wiring system was revised considering the experimental condition of this research.

The components that comprised the engine control system were a microchip, I/O expansion board, and personal computer. The hardware structure of a microchip, microcontroller Dspic 6014A, is simple, and the coding in the software MPLAB ICE that is provided by the manufacturer is convenient. By

connecting it to the I/O expansion board that provides more numbers of terminals, the control system could be made easy and convenient, ensuring more ports to connect coaxial cables for the input and output signals.

The main function of the microcontroller is to receive input signals, and then send out each output signal to the device on accurate timing. The purpose of its existence was to operate each component of the experimental equipment to collect desirable data at the accurate timing. The input signals for running the microcontroller are the control system trigger, TDC, and clock signal.

The input signal for running the microcontroller is the control system trigger. The trigger signal is generated by pushing the manual button. The TDC and clock signal are also the input signals for the microcontroller. They come from an encoder, Horner 3202 shaft encoder. The shaft encoder produces 1800 pulses per crank shaft revolution, that is, a single pulse is generated per 0.2 ºCA. Additionally, it sends out a separate single pulse when the piston is at TDC position. In relation to the shaft encoder, one of the most important jobs when it is installed is accurately to align it with the crank shaft when the piston position is at TDC. Before starting experiment, it was essential to make sure whether the TDC signal was accurately produced when the piston was at TDC. Using a capacitive proximity meter sensor which was mounted above the piston, the comparison of its signal with the one that shaft encoder generated was carried out to find out the proper location of the encoder. When the two electrical signals were compared, the LabVIEW script that was used for the calibration of the absolute and dynamic pressure transducers in Sec. 3.3 to record the both pressure signals was employed.

An example of encoder alignment is shown in Figure 3.37. Depending on the distance between the proximity meter sensor and the piston, the voltage of its signal varies. The signal curve of the proximity meter sensor represents the piston movement while it goes up and down at 50 rpm. If the shaft encoder were installed well at the free end of crank shaft when the piston position was at TDC, the signal curve of the proximity meter sensor should be divided equally at the point when the TDC signal of the encoder occurs (Hattrell 2007). As seen in Figure 3.37, it was confirmed that the alignment of the shaft encoder with the crank shaft when the piston was at TDC was in good condition and its TDC signal was reliable enough to indicate the position of the piston. Using the control system trigger, TDC, and clock signals, the code that runs the microcontroller produces output signals.

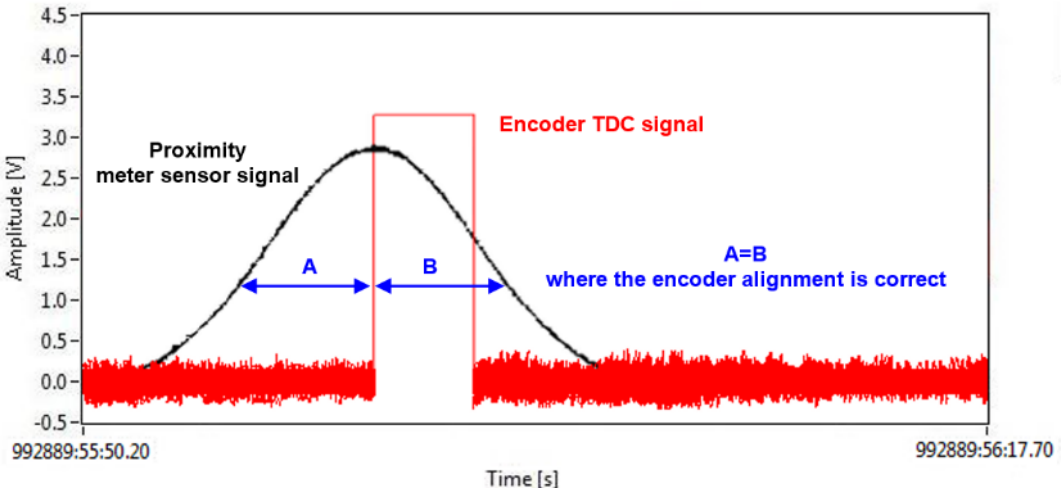

Figure 3.37 Encoder alignment, using the TDC signal from the shaft encoder and the signal from the proximity meter sensor

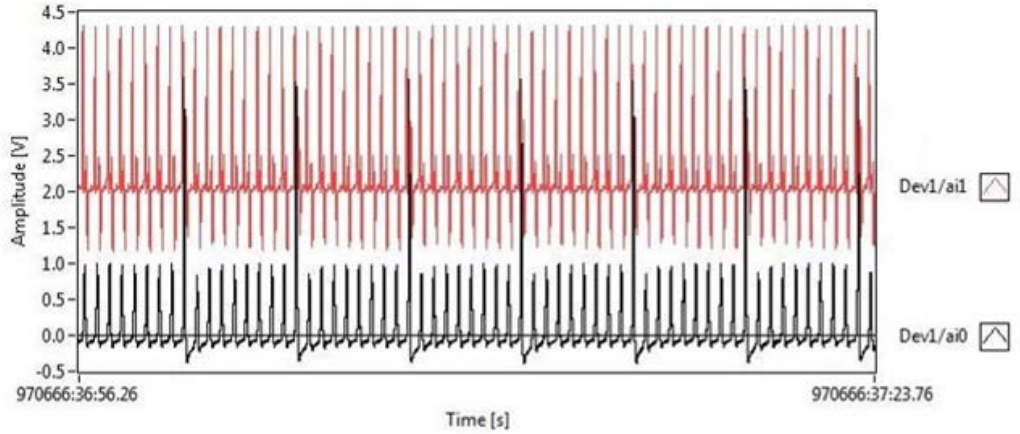

(a) Pressure signals

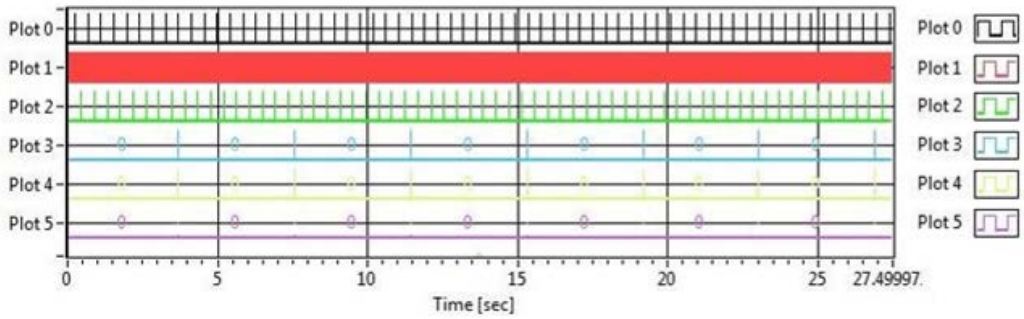

(b) Output signals

Figure 3.38 pressure signal and other output signals recorded by the data acquisition system

The output signals can be categorized into two parts. The first is the signals to be used to count the number of cycles and to indicate the position of the piston. Through a TDC signal from the shaft encoder, the microcontroller counts the number of a cycle. As mentioned in Sec. 3.1, the information on the number of cycles is essential in conducting skip fire mode. By setting the value for the mode in the engine control code, the number of a motoring cycle could be adjusted to secure the time for expelling residual gas and charging fresh fuel-air mixture until the next combustion cycle. When the number of the motoring cycles is the set value, the microcontroller starts calculating a crank angle, counting a clock signal, which means that the user can realize the position of the piston in a crank angle.

The second part is the output signals that are used to operate each component of the experimental rig such as the spark ignition coil, high speed controller for the PIV system, and so forth. When the number of the counted clock signals reaches the number corresponding to the position where the piston is at BDC, the microcontroller generates a BDC signal. Since the microcontroller recognises the number of motoring cycles and the position of the piston through a TDC and clock signal, it can send out a trigger signal on the accurate timing that the user sets up in advance. The timings at which the output signals are sent out to operate each device could be adjusted readily by changing the set values in the author's code. The step of changing the timings was 0.2 ºCA, and the range of the setting value was from 179.8 ºCA bTDC to 179.8 ºCA aTDC.

Figure 3.39 shows how the microcontroller sends out trigger signals to operate the ignition unit and PIV system. After the control code starts, the microcontroller reads a control system trigger signal. Once the trigger signal is received by the microcontroller, it counts the number of cycles through a TDC signal. When the number of cycles becomes the set value, the clock signal is read for counting crank angle. Provided that the crank angle counted through the clock signal is the same as the set values for operating the ignition unit and the PIV system respectively, the microcontroller sends out the separate output signals for them to be operated. This loop in the control code continues until the microcontroller receives the signal for stopping the code.

The data produced through experiment were stored in the computer. Figure 3.40 shows the composition of the engine control and data acquisition system. The data that are saved in the computer can be divided into three kinds. The first data are the signal data that the microcontroller produces. This is crucial in identifying the timings when different kinds of data are obtained because

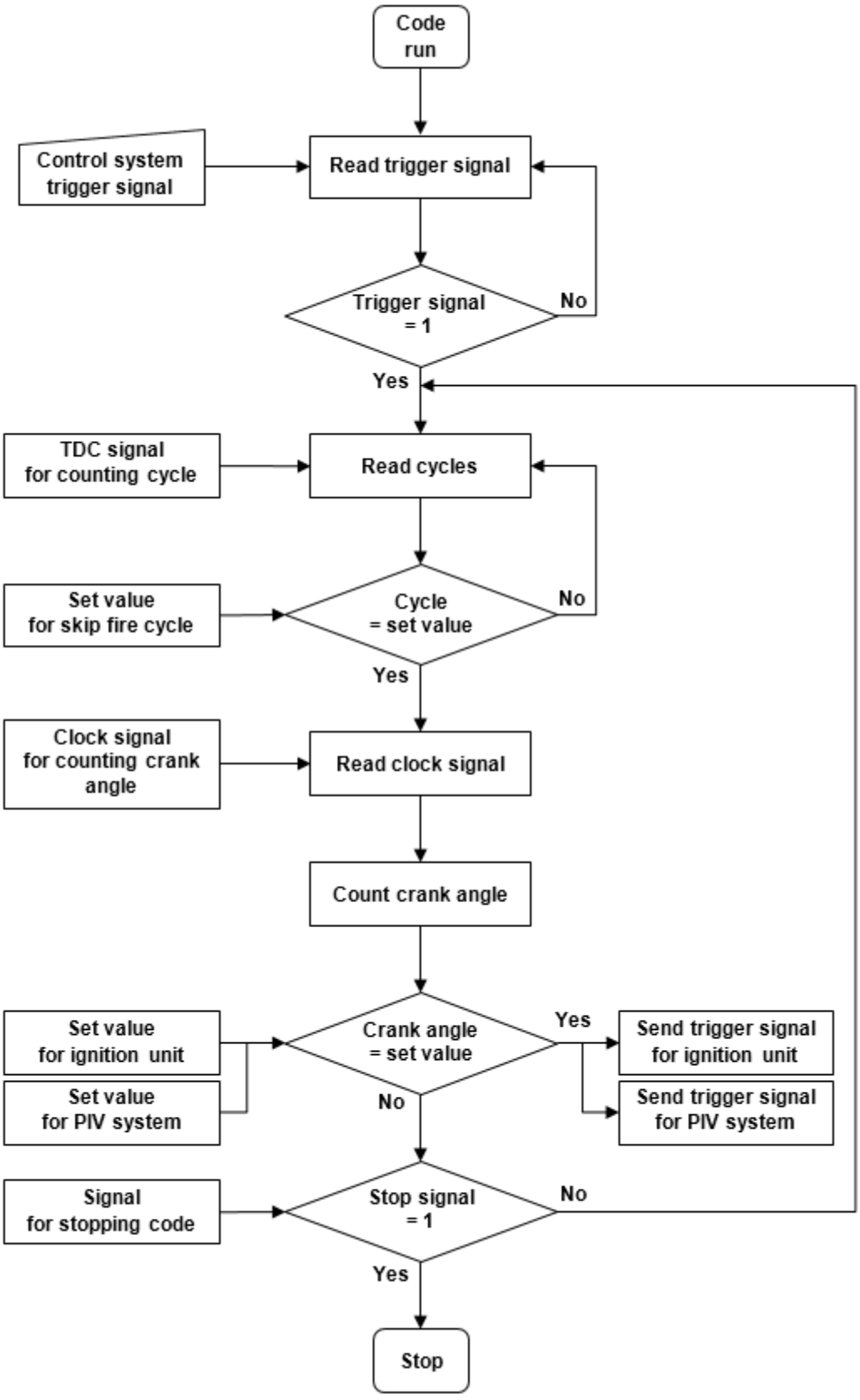

Figure 3.39 Flow chart of the microcontroller code for operating the ignition unit and PIV

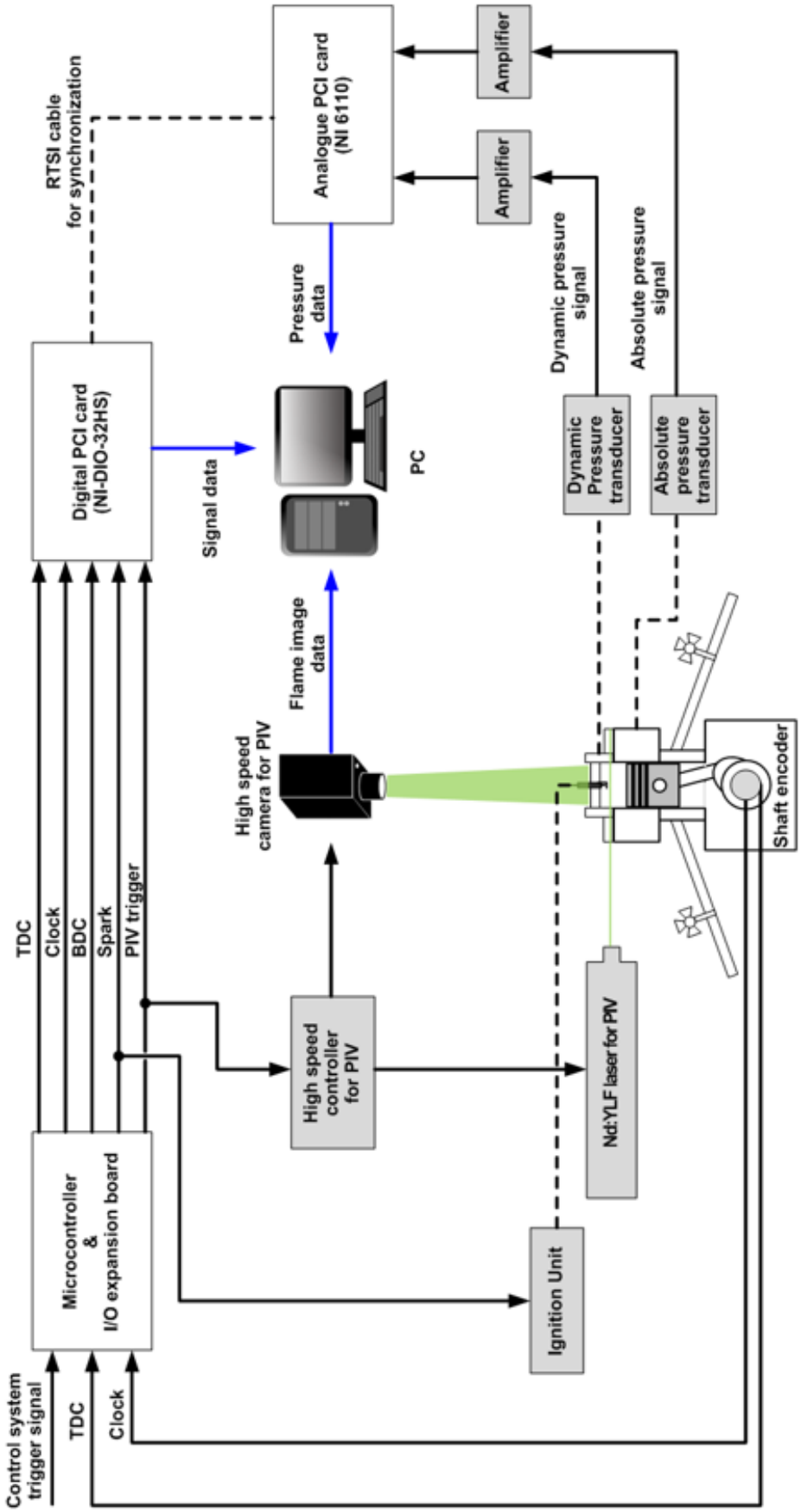

Figure 3.40 Engine control and data acquisition system for LUPOE-2D

the signal data represents the number of cycles, crank angle, and timings for operating other experimental components. In this experiment, the data, TDC, clock, BDC, spark ignition trigger, and PIV trigger signal, were recorded through a PCI card, which is a National Instruments DIO-32HS digital PCI card. The second is the pressure data. As mentioned in Sec. 3.3, the pressure signals sensed by the absolute and dynamic pressure transducers were amplified by two amplifiers respectively, and then were saved in the computer through another PCI card, a National Instruments 6110 analogue PCI card. The analogue PCI card converts the pressure signals to digital forms with accuracy of 12 bits, and the number of the channel through which data can be collected at the same time is four.

Since the datum transmitted from each PCI card has to be stored in correct order, it is essential to synchronise the data of two PIC cards. In order to achieve the synchronisation, a RTSI bus cable, a National Instruments real-time system integration bus cable, was used to connect two PCI cards. This cable enables the data of the analogue PCI card to be synchronised with those of the digital PCI card in the way of a master-slave type configuration (National Instruments 2016). The synchronised data were saved through the LabVIEW script, which was based on Hattrell's work (2007) and modified considering the condition of this research. The sampling rate of the LabVIEW program was 40 kHz, which collected 65 cycles of the data when the research engine speed was at 50 rpm, including seven firing cycles with the ratio of a motoring cycle to a firing cycle being eight and one.

The last data are image data. As aforementioned in Sec. 3.4, the flame images that were taken with the high speed camera were stored in the computer through the commercial software. The image recording rate and the laser repetition rate could be adjusted in this software. Beginning with receiving the trigger signal from the microcontroller, the high speed camera and the laser started working. The working timings of those components were controlled by the high speed controller, which is referred to as a programmable timing unit (LaVision 2010). Although the synchronisation between the high speed camera and laser was made by adjusting the set value in the software, as mentioned in Sec. 3.4.2, it is essential to synchronise the flame image data with the other data. Hence, the image feedback signal representing the time of capturing each flame was checked. The LabVIEW script for the calibration of the absolute and dynamic pressure transducers used in Sec. 3.3 was employed. Figure 3.41 shows whether the synchronisation was achieved or not. After the high speed controller received the PIV trigger signal, the flame

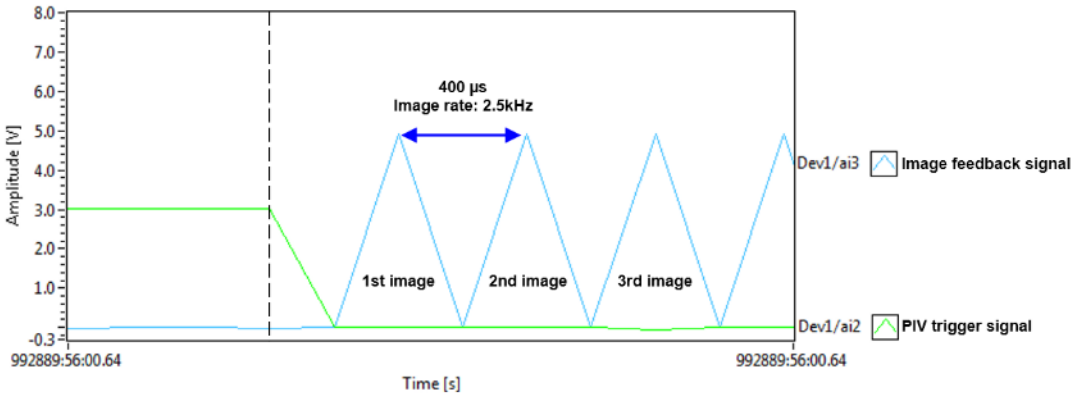

Figure 3.41 An example of the trigger signal for the operation of the PIV system and the image feedback signal

imaging started at the accurate time. Therefore, it was confirmed that all three kinds of the data in this research were synchronised and were kept in good condition. In summary, the below data were collected through the data acquisition system.

- Absolute pressure transducer
- Dynamic pressure transducer
- TDC signal
- Shaft encoder clock signal
- BDC signal
- Spark ignition signal
- PIV trigger signal
- Flame image

3.6 Experimental procedure

The experimental procedure was written to minimize any change in parameters which might have an effect on the consistency of experimental condition. For each experiment, 65 cycles of data were measured and collected through the data acquisition system. In the case that any combustion did not fail in the total cycles, the number of the firing cycles was seven, and the ratio of a motoring cycle to a firing cycle was eight to one. Before the

experiment, the temperature of the fuel and air in the inlet pipeline and the optical cylinder head of the research engine were kept at 25℃ ± 1. The laboratory room pressure and temperature was atmosphere and 22℃ ± 2.

3.6.1 Hardware preparation

Before engaging in experiment, the induction motor that drove the research engine and other components were turned on. They took time to warm up for their condition to be stable, which was at least 30 minutes. It was preferred to switch on the computer first because it was experienced that the probability of occurrence of electrical interference became low. The electrical interference sometimes made electrical noise in flame images, and even stopped the laser or other components in spite of the good insulation of each component: this is mentioned in detail in Sec. 3.6.4. While all the experimental equipment and relevant device were warmed up, the visual and performance check were made. Before the research engine was operated, a series of events that were related to the process of warming up were carried out in turn as follows.

- The computer was turned on, and then the peripherals were switched on: the flowmeter with the display unit for the supply of air, the power supply unit for the ignition unit, the temperature control unit for the intake pipes and cylinder, the flowmeter with the display unit for the supply of air containing seeding particles, the microcontroller, the charge and piezoresistive amplifier for the absolute and dynamic pressure transducer.

- The ventilation fan for the laboratory room and the laboratory exhaust extraction fan were turned on. The extraction fan kept the pressure of the exhaust pipe in the research engine lower than atmospheric pressure, which helps remove residual gas in the cylinder and enhance the scavenging.

- The high speed controller for the PIV system was turned on first, and the Nd-YLF laser and the high speed digital camera were switched on subsequently: it should be noted that error might take place in the

software of the PIV system where the order of turning the components on was changed.

- After checking the level of cooling water of the laser power unit, the cooling pump was run, and then the Nd-YLF laser had to take at least half an hour to warm up (Litron Lasers 2010). The temperature of the cooling water was set to 19 ℃.

- Check the interlock lists that can stop the laser from working and clear them.

- The condition of the absolute pressure transducer reading was checked: after the optical cylinder head was removed, its voltage signal was compared with the atmospheric pressure that was measured by a mercury barometer.

- The positions of the high speed digital camera and laser were checked: by taking the picture of the calibration plate on the piston when it was at TDC, the comparison of the image with the already captured image in the calibration process was carried out. In the case of the laser, the laser beam was emitted to burn a paper plate placed at the location where the partially-burned paper plate by the laser beam after finishing the PIV system setup had been located. And then they were compared.

- The laboratory air supply line was connected and the air was supplied. The supply pressure was set to 2 bar in gauge pressure: the blowing time was taken for 10-15 minutes to eliminate dust and others despite the filter being used.

- The manual valve for the air with seeding particles was opened, and the air with seeding particles was supplied. The supply condition was visually checked with a torch when the light of the laboratory room was turned off. And then the manual valve was shut off.

- The engine flywheel was turned by hand to check whether the piston moved smoothly. During the rotation, the piston crown was checked for the condition of the black paint that was applied on it: it was painted on the piston crown to minimize the reflection of the laser sheet. The piston crown was cleaned, and then the piston was put at BDC.

- The control console for the induction motor for the research engine was turned on and the set value for the desirable engine speed was input.

- After checking the top and side windows of the optical head visually, it was assembled on the cylinder with four 12 mm bolts. The torque to fasten them was set to 100 Nm. When cleaning the top and side windows of the optical head, it should be noted that the gap between the electrodes of the spark plug does not have to be changed and undesirable materials in it and they have to be eliminated to secure reliable spark ignition.

- The manual valves for the gaseous fuels supply were opened and the supply pressure of each was set to 2 bar in gauge pressure by adjusting each pressure regulator: when adjusting the regulator, the pressure drop was considered. It was noted to check the supply pressure whenever the amount of the fuel supply varied.

- The temperature control unit for the intake pipelines and cylinder was turned on. It should be noted that the time to heat up the cylinder was taken relatively longer than the one for the heating cartridges for the intake pipelines. This is because the capacity of the heating cartridges for the cylinder was smaller than that of the cartridge for the intake pipelines: refer to Sec. 3.2.3. The temperature was set to 25 ℃: as the laser starts, the heat from the laser control unit was much enough to raise up the laboratory room. Considering the room temperature, the temperature control unit and the ventilation system were intermittently used.

3.6.2 Software preparation

After setting up the hardware part, the program and software that are used in the engine control, data acquisition, and PIV system were prepared. The experimental parameters such as spark timing, data acquisition sampling rate, and others could be set conveniently before starting experiment.

- The engine control code was browsed and the desirable set values were input, and then the code was complied.
  - Ratio of a motoring cycle to a firing cycle: 8:1
  - Crank angle value for the spark trigger signal: variable
  - Crank angle value for the PIV trigger signal: variable

- The LabVIEW script for the data acquisition was started and the desirable set values were input.
  - Sampling rate of data: 40 kHz
  - Total number of collected data: 3510000
  - Engine rpm: 50
  - Data name: variable

- The Litron Laser software was run in remote mode and the desirable set values were input. In the case that the laser unit was used in the local mode, this step was carried out in the local panel.
  - Laser repetition rate: 2.5 kHz
  - Laser power [%]: 80
  - Q-switch mode: trigger mode

- The DaVis software was run and the desirable set values were checked.
  - Camera mode: double frame mode
  - Carry out the intensity calibration of the high speed camera after turning off the laboratory room light and covering the camera lens lid.
  - Trigger source: external mode,
  - Image rate: 2.5 kHz
  - Total number of recorded images: variable
  - Inter-frame time: 100 μs
  - Laser and camera offset time:

Laser	1st pulse [μs]	2nd pulse [μs]
	0	-5
Camera	1st frame [μs]	2nd frame [μs]
	0	0

  - Laser mode: double pulses mode
  - Size of Interested area and resolution: 40 x 40 mm^2
  - Image resolution: 1024 x 1024

3.6.3 Operating procedure

Once the hardware and software were prepared, the experiment could be carried out. The operating procedure is as follows:

- Adjust the amounts of fuel, air, and air with seeding particles through each needle valve depending on an equivalence ratio.
- Runt the induction motor for the research engine.
- Switch on the ignition unit.
- Run the engine control code: the code waits a trigger signal.
- Run the LabVIEW script for the data acquisition, and switch on the select button, “armed” button, in the software: the script also waits for a trigger signal.
- Click on the laser-on and shutter-on button in the Litron Lasers software subsequently. Since the Q-switch mode is trigger mode, the laser beam is not emitted until the trigger signal from the high speed controller is transmitted to the laser unit. This is controlled by the engine control system.
- Click on the record button in the DaVis software: the software waits for a trigger signal from the engine control system.
- Push the manual button that sends a trigger signal to the engine control system and data acquisition system.
- Check whether the LabVIEW and DaVis software finish saving the data.

Once the data were saved in the computer, the following steps were conducted.

- Cut off the fuel supply.
- Close the valve to supply air with seeding particles.
- Switch off the spark ignition unit.
- Stop the induction motor for the research engine.
- Turn off the temperature control unit for the cylinder and intake pipelines.
- Stop and reset the engine control code.
- Stop and reset the LabVIEW script for the data acquisition.
- Close the shutter and turned off the laser.
- Check whether the data is saved properly.

After completing experiment, the optical head was disassembled to clean the top and side windows having seeding particles and lubrication oil, and to prevent its deformation by the thermal stress, which could cause cracking window.

3.6.4 Electrical interference

Since various kinds of electrical equipment such as the induction motor, the spark ignition unit, and others were used in this research, it was reasonable that perfectly preventing the occurrence of electrical interference between the components was thought of as almost impossible. In the current work, it was often experienced that the flame images had electrical noise and even the malfunction of the laser control unit took place because of electrical interference. Although the phenomena were unavoidable, in order to minimize its effects, several practical techniques were carried out as follows:

- The electrical device and cables were stayed as far away as possible from the wires related to the spark plug.
- Earth cables were connected to the cases of the electrical device, and the lengths were as short as possible.
- The electrical device was not located on the metal plate supported by the scaffolding to avoid directly contacting the metal.
- The unused ports of the terminal in the data acquisition system and other device were properly terminated using 50 Ω BNC terminator.
- The unused cables were disconnected from the electrical device.
- The local mode when the laser control unit is operated was preferred instead of the remote mode. In the remote mode, the RS232 cable was used for the laser control unit to communicate with the software in the computer. It was thought that the cable might be affected by electrical interference causing the malfunction of the laser control unit.

The electrical interference was mostly eliminated by the above mitigation actions, and the experimental data could be collected and used to conduct data processing and post processing.

Chapter 4 Image processing and methodology for analysis

This chapter provides an overview of the PIV image processing and the methodology for analysis. The procedure of processing the PIV flame images consists of two steps. The first step is to enhance a quality of the flame images, which is called image pre-processing in the present study. Since the difference of the pixel intensities between the unburned and burned area in the flame image was distinguishable, the image pre-processing was required to determine the desirable threshold to separate two areas. In the second step, using the pre-processed images, the image binarization is carried out to divide the unburned and burned area. And then the flame contour images can be derived. Flame propagation speed, unburned gas velocity, and so forth are calculated based on the flame contour images. The methodology is described in detail and the preliminary results are shown in this chapter.

4.1 Derivation of the flame contour from the PIV images

4.1.1 Image pre-processing

In this research, olive oil droplets were illuminated by the high repetition double-pulsed laser and acted as the tracking particles to present the information on the flow field of the fuel-air mixture till being burned by flame. Meanwhile, using a proper image processing, the illumination of the seeding particles could be used to extract the flame front images from their raw PIV images. Ultimately, flame front image was used to measure flame propagation speed, which in turn was employed for calculating the burning velocity mentioned in Sec. 2.1. Although the seeding particles were homogeneously distributed within the fuel-air mixture, the reflection of illuminated light was unavoidable due to the offset of laser sheets, the non-uniform geometrical property of combustion chamber, and the inhomogeneous mixture in the unburned area. This reflected light caused a fluctuation of pixel intensities and made it difficult to discriminate the burned and unburned zones in the PIV image. Therefore, the first step, so called image pre-processing, needs to enhance the pixel intensities to separate those two zones.

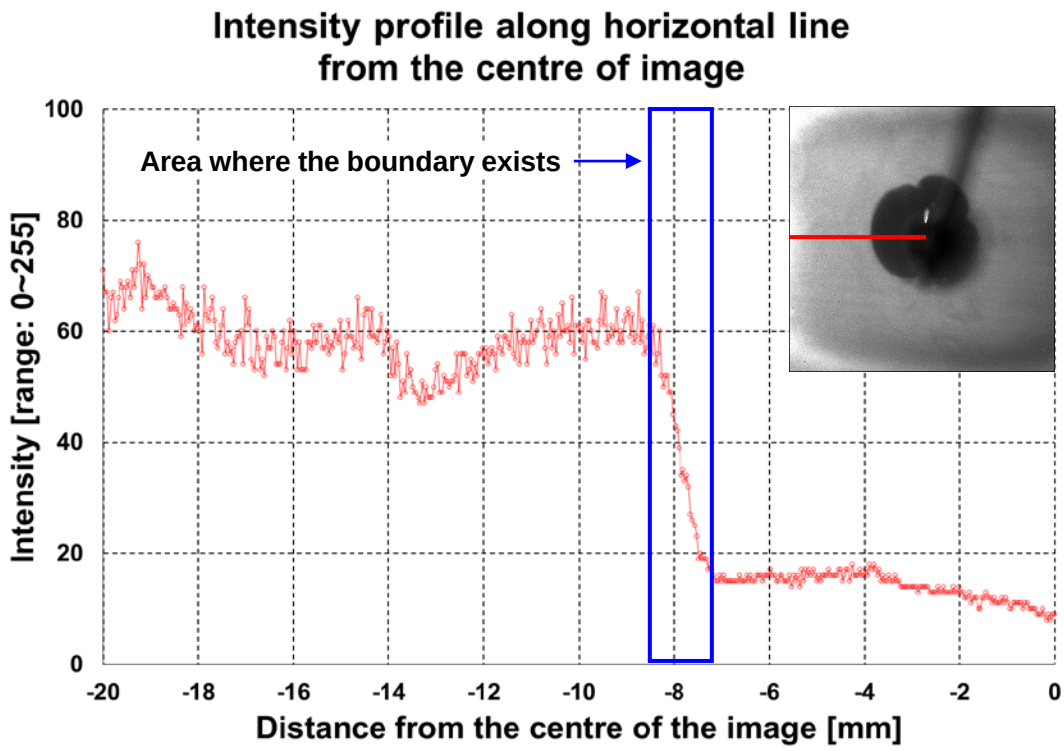

Figure 4.1 Intensity profile of the fuel-air mixture with seeding particles along horizontal line at the centre of the image. Fuel: CH_4-air mixture / equivalence ratio: 1.0 / time when image was taken: 3.2 ms after ignition / ignition timing: 27.6 °CA bTDC / pressure: 5 bar abs / temperature 439 K / engine speed: 50 rpm

Figure 4.1 shows the intensity profile of the fuel-air mixture with seeding particles along the horizontal line in the left direction from the centre of the flame image that is located at the upper right inset. The combustible mixture was a stoichiometric methane-air mixture, and the flame image was taken at 3.2 ms after the start of the ignition. The ignition timing was set as 27.6 ºCA bTDC. The pressure and temperature was 5 bar abs and 439 K respectively when the combustion started, and the engine speed was 50 rpm. Although the fluctuation of the intensity is quite strong, the boundary between the unburned and burned zone is clearly distinguishable, which was represented by the points with a sharp increase in intensity: refer to the blue box in Figure 4.1. In order to determine the flame front within this area, a sequence of filtering algorithms embedded in the DaVis software were employed.

The first filter was a local deviation filter, in which a pixel intensity was replaced with the local standard deviation. The value is calculated with surrounding eight pixels and the centre pixel itself: refer to Eq. (4.1) and Figure 4.2 (LaVision 2010). Through the local standard deviation filter, the signal noise caused by the flame luminescence, reflection, or other potential factors could

be eliminated from the raw image to some extent: the intensity profile after the local deviation filter is conducted is shown in Figure 4.5 (b).

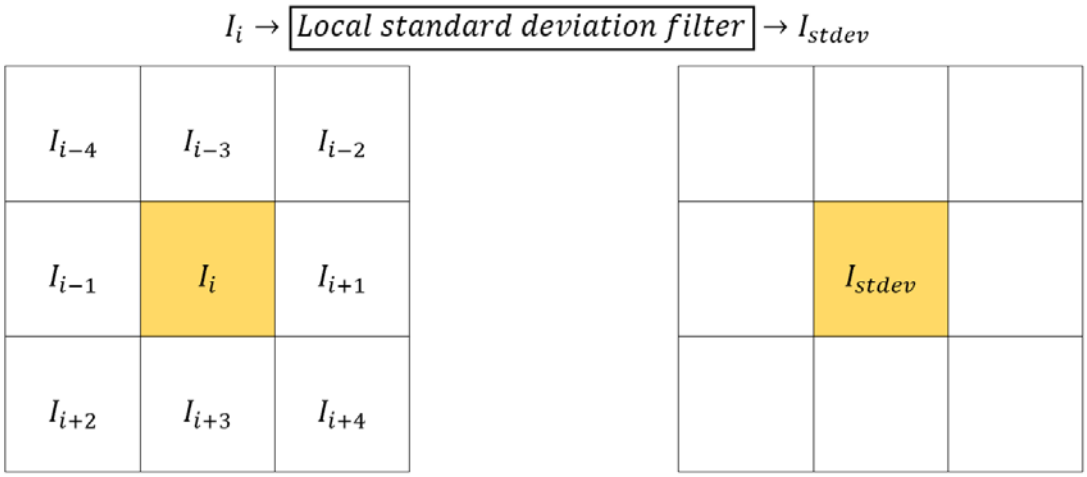

Figure 4.2 An illustration of the local standard deviation filter where the surrounding eight pixels and the centre pixel itself are

$$I_{stdev} = \sqrt{\frac{1}{n-2}\sum_{i=0}^{n-1}\left(I_{i-4} - I_{avg}\right)^2} \qquad \textbf{Eq.}\ (4.1)$$

$$I_{avg} = \frac{I_{i-4} + I_{i-3} + I_{i-2} + I_{i-1} + I_i + I_{i+1} + I_{i+2} + I_{i+3} + I_{i+4}}{n}$$

$$n = number\ of\ pixles, 9$$

The second algorithm was to eliminate inappropriately high intensities that cause the difficulty in determining the threshold value for image binarization. These inappropriately high intensities could stem from the inhomogeneous distribution of the seeding particles, the reflection of the light source, and others. Figure 4.3 shows the histogram of intensities of the image which was processed by the local deviation filter. The appropriate threshold value had to be determined in order to eliminate inappropriately high intensities from the image. The process of gaining the appropriate threshold was carried out by the trial-and-error method after determining the range where it might be located. Through the method, the desirable threshold to cut off high intensities was determined. As seen in Figure 4.3, the maximum frequency of pixel intensities was first found, and the threshold intensity where frequency was

0.5 or 1.0 % of the maximum value was determined. The result of the second algorithm is shown in Figure 4.5 (c).

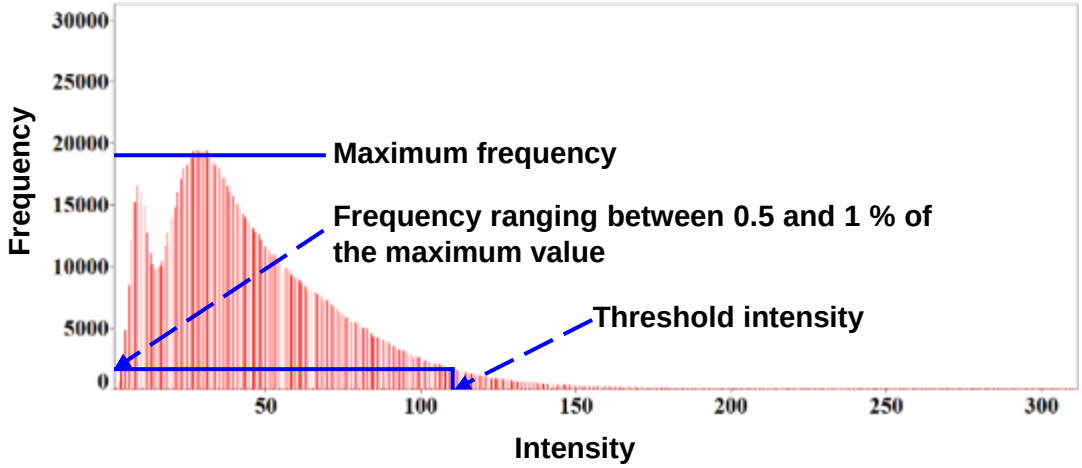

Figure 4.3 Histogram of pixel intensities of the image processed by the local deviation filter

The final algorithm is a sliding average filter, which makes the change of pixel intensities smooth. The artificial wrinkles of the image that was processed by the second algorithm could be eliminated through this step. Figure 4.4 and Eq. (4.2) represent how the intensity of a pixel was calculated by the sliding average filter. When applying this filter, the pixel scale length was three, and the computation was carried out four times, that is, from left to right, from right to left, from top to bottom, and from bottom to top through the image (LaVision 2015). The result of this filter is shown in Figure 4.5 (d).

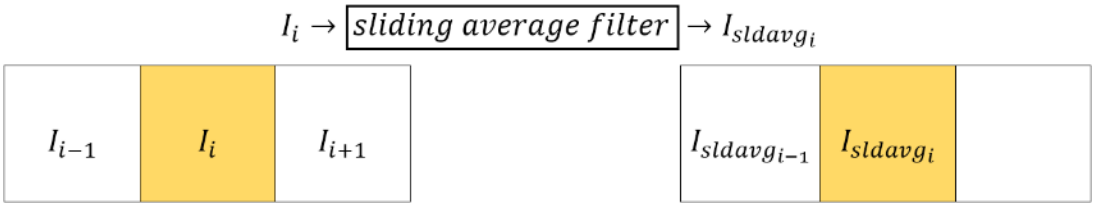

Figure 4.4 An illustration of the sliding average filter where the scale length is three pixels

$$I_{sldavg_i} = \frac{n-1}{n} \times I_{sldavg_{i-1}} + \frac{1}{n} \times I_i \qquad \textbf{Eq. (4.2)}$$

$$I_{sldavg_0} = I_0$$

$$n = scale\ lenth, 3$$

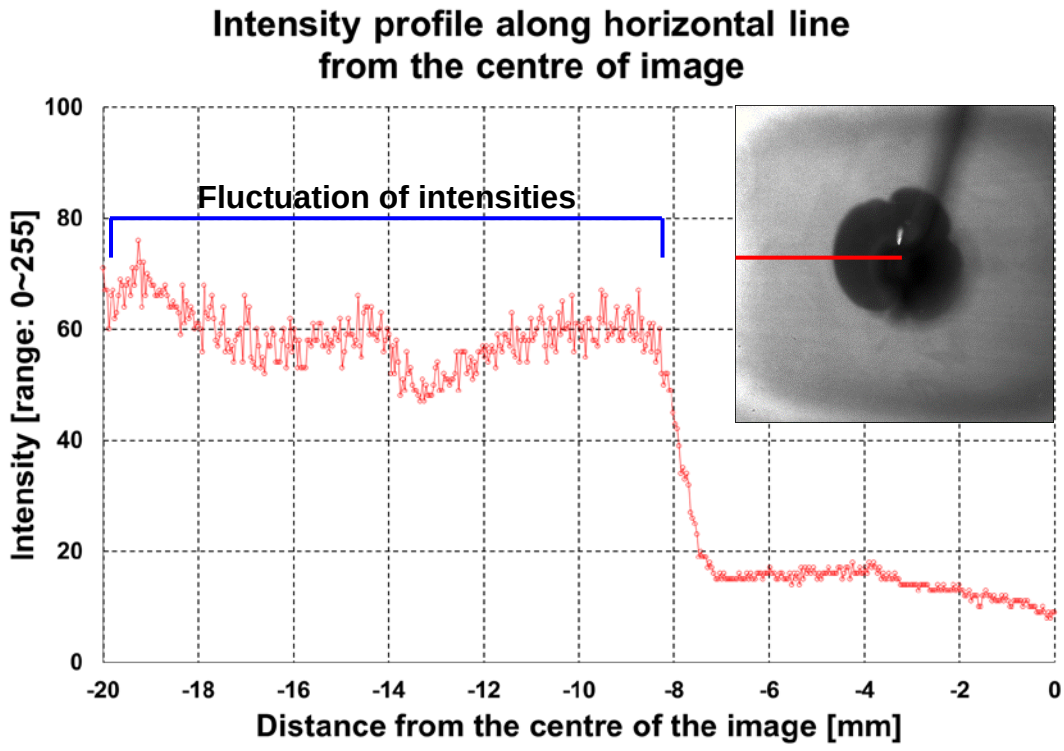
Intensity profile along horizontal line from the centre of image
Fluctuation of intensities
Intensity [range: 0~255]
100
80
60
40
20
0
-20
-18
-16
-14
-12
-10
-8
-6
-4
-2
0
Distance from the centre of the image [mm]

(a)

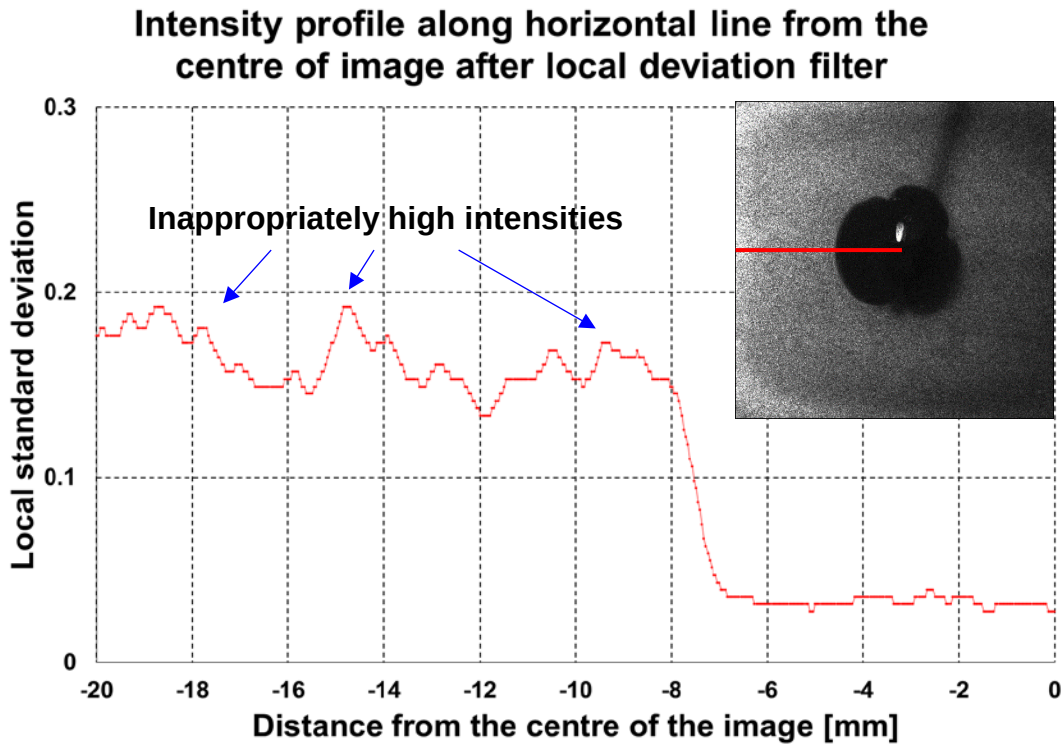
Intensity profile along horizontal line from the centre of image after local deviation filter
Inappropriately high intensities
Local standard deviation
0.3
0.2
0.1
0
-20
-18
-16
-14
-12
-10
-8
-6
-4
-2
0
Distance from the centre of the image [mm]

(b)

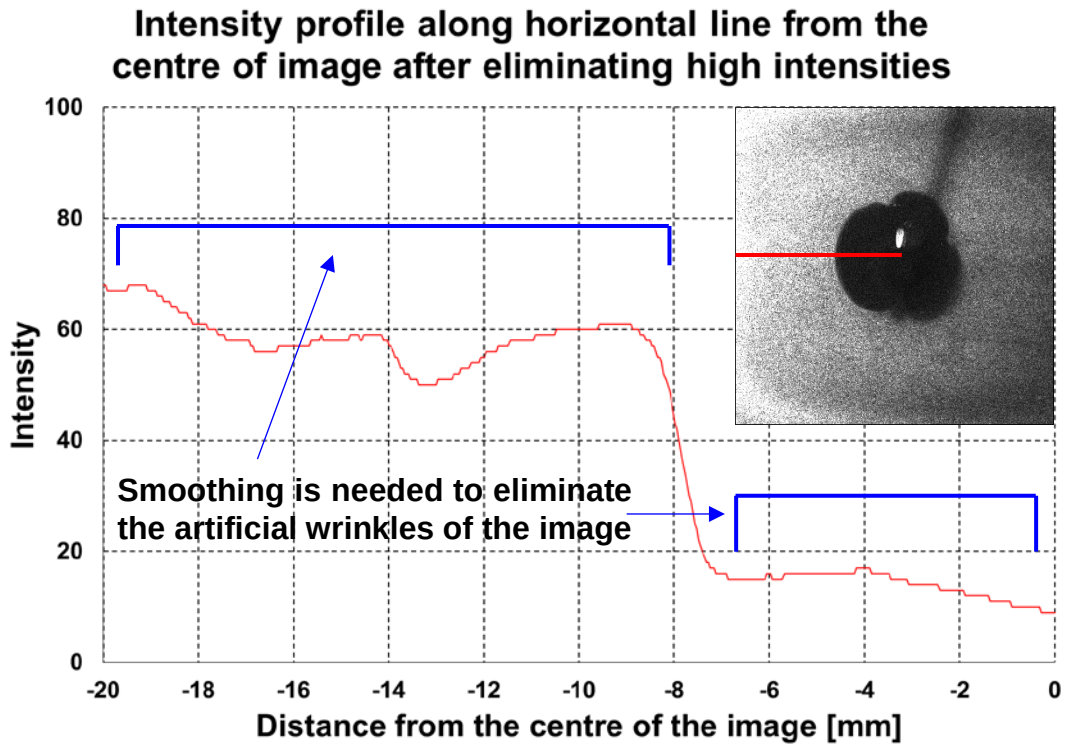

(c)

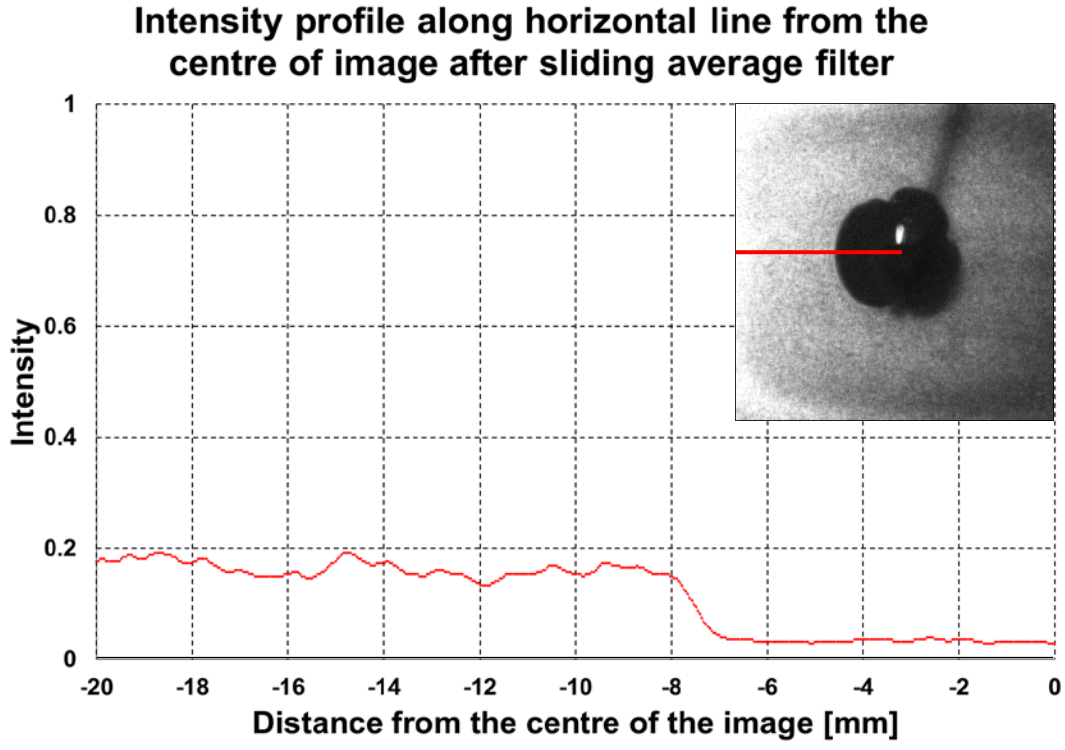

(d)

Figure 4.5 A sequence of steps to obtain the image for image binarization. Fuel: CH_4-air mixture / equivalence ratio: 1.0 / time when image was taken: 3.2 ms after ignition / ignition timing: 27.6 °CA bTDC / pressure: 5 bar abs / temperature 439 K / engine speed: 50 rpm

4.1.2 Image binarization and derivation of flame contour

The purpose of the image pre-processing mentioned in Sec. 4.1.1 was to obtain the flame image that had the desirable change of the gradient in the intensity at the area where a combustible mixture changes into the burned gas. In this section, the process of deriving a flame contour image is described, with the use of the flame image obtained by the image pre-processing. In order to obtain a flame contour image, image binarization was carried out. Otsu's threshold selection method has been adopted frequently to determine a threshold value for image binarization. This method was developed by Otsu and uses the grey-level histogram of a flame image (Otsu 1979). In Otsu' threshold selection method, the prerequisite for desirable image binarization is that the grey-level histogram of an image has to show bimodal distribution. That is, two peaks in the histogram have to show up distinctly. The threshold value for the binarization of two areas can be selected through a point within the deep and sharp valley of the histogram (Otsu 1975).

Figure 4.6 shows an example of the intensity histogram. In Figure 4.6 (a) of, the relatively bright area is the burned side, and the dark area represents the unburned area. The image was taken in natural light photography (Ling 2014). As seen in Figure 4.6 (c), since two distinguishable peaks and the deep and sharp valley between them exist, it seems appropriate to apply Otsu's threshold selection method to the image that is taken in natural light photography. Otsu's threshold selection method shows a good performance in image binarization when it is used for images that are taken in natural light or Schlieren photography (Ling 2014). Nevertheless, the effort to fulfil the prerequisite for the application of Otsu's threshold selection method was made in the image pre-processing, the distribution of intensities of a PIV flame image showed that the method was not appropriate to the current work.

Figure 4.7 shows an example of the intensity histogram of the pre-processed image mentioned in Sec. 4.1.1. The fuel-air mixture was a methane-air mixture, and its equivalence ratio was stoichiometric. The flame image was recorded at 3.2 ms after the ignition, and the spark plug was ignited at 27.6 °CA bTDC. The initial pressure and temperature at the start of the combustion was 5 bar abs and 439 K respectively, and the engine speed was 50 rpm. The relatively dark area in Figure 4.7 (a) represents the burned side, and the unburned side is the bright area. As seen in Figure 4.7 (b), the quality of the image binarization that was carried out through Otsu's threshold selection method is

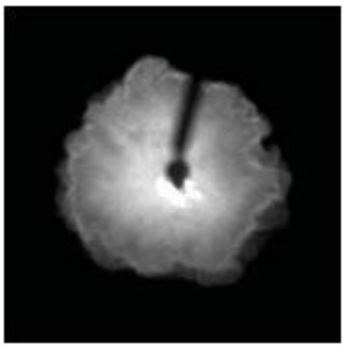

(a) Raw image
in natural photography

(b) Image
after applying Otsu's method

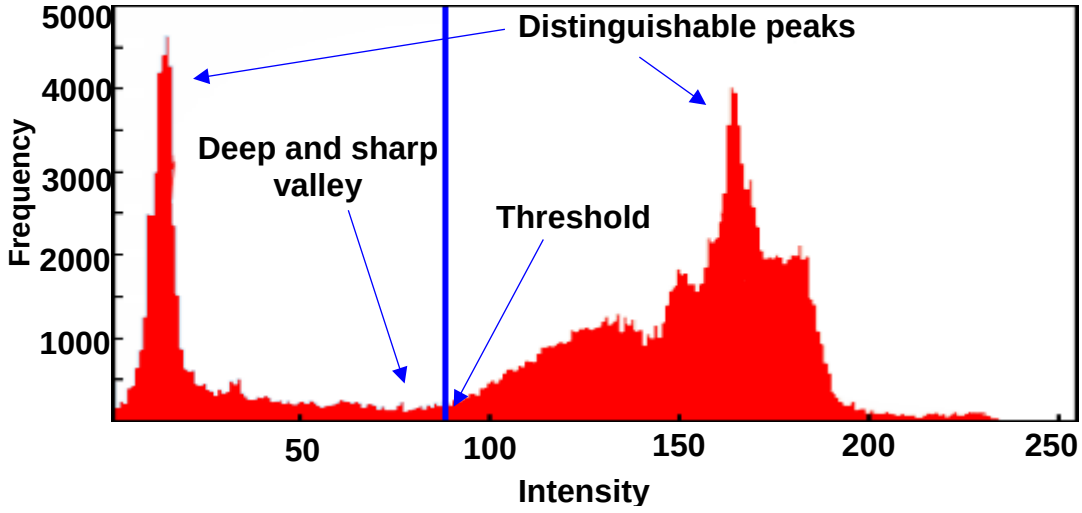

(c) Intensity histogram of raw image

Figure 4.6 An example of intensity histogram; the figure was taken in natural light photography and is reproduced from Ling (2014)

quite low, and it seems impossible to distinguish clearly between the unburned and burned area. This is because the threshold value calculated Otsu's method is biased toward a relatively high value. This bias is caused by the direction where the laser sheet is emitted. Since the laser sheet was provided from the left side, the left side of Figure 4.7 (a) is relatively brighter than the right side, and the intensity difference between two sides appears: refer to Figure 4.8. In addition, the lead to ignite spark and spark plug can also affect the undesirable threshold value for the image binarization. Hence, it was confirmed that Otsu's threshold selection method, which considered the global threshold value of an image, was not appropriate to the image binarization of this research.

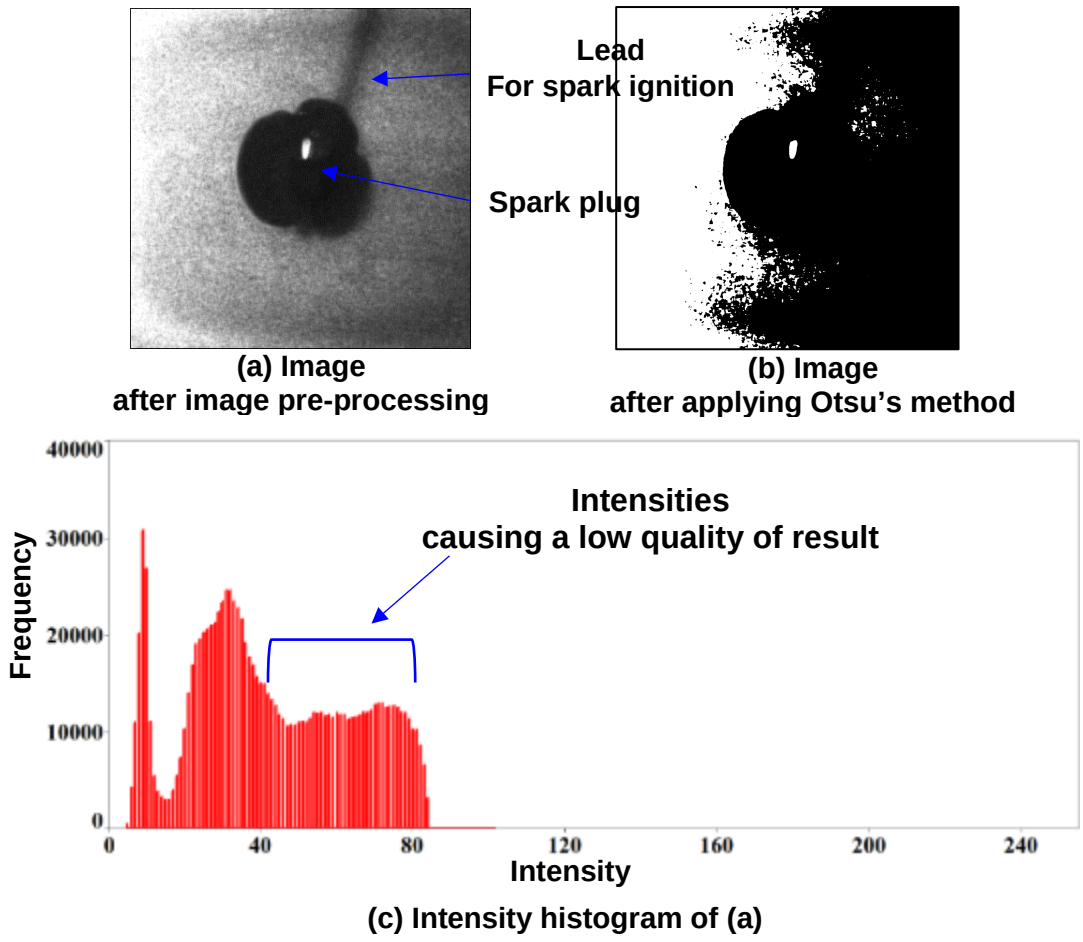

Figure 4.7 An example of the intensity histogram of the pre-processed image mentioned in Sec. 4.1.1. Fuel: CH_4-air mixture / equivalence ratio: 1.0 / time when image was taken: 3.2 ms after ignition / ignition timing: 27.6 °CA bTDC / pressure: 5 bar abs / temperature: 439 K / engine speed: 50 rpm

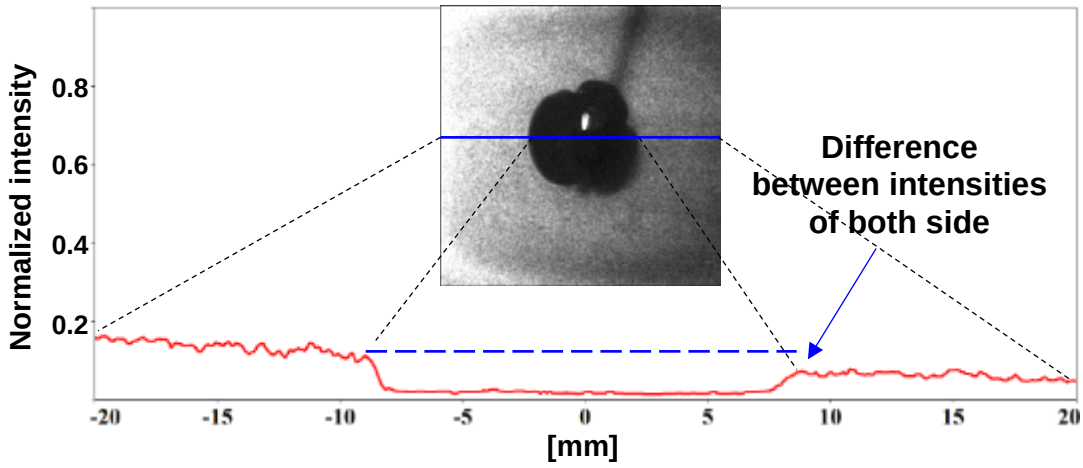

Figure 4.8 Intensity profile of the pre-processed image mentioned in Sec. 4.1.1. Fuel: CH_4-air mixture / equivalence ratio: 1.0 / time when image was taken: 3.2 ms after ignition / ignition timing: 27.6 °CA bTDC / pressure: 5 bar abs, temperature: 439 K / engine speed: 50 rpm

Alternatively, the adaptive threshold selection method was adopted. In the image processing field, the method has been investigated by many researchers (Trier and Jain 1995, Sezgin and Sankur 2004, Bradley and Roth 2007). Compared with using a fixed threshold value for a binary image, referred to as a global threshold value (Otsu 1979), the adaptive threshold selection method has advantages of obtaining a more reliable binary image where there is the spatial change of illumination in an image and the variation of the brightness between images in a live video stream exists. This is because local threshold values are applied to the corresponding to the local areas in an image. In order to calculate a local threshold value, it is essential to allocate a sub-area in the image, and then the intensity of each area is cumulated continuously, which is referred to as a summed-area table or integral image. The following Eq. (4.3) and Eq. (4.4) shows how the intensity of each pixel is calculated (Bradley and Roth 2007).

$$I_{(x,\ y)} = f_{(x,\ y)} + I_{(x-1,\ y)} + I_{(x,\ y-1)} - I_{(x-1,\ y-1)} \qquad \textbf{Eq.}\ (4.3)$$

$$\sum_{x=x_1}^{x_2} \sum_{y=y_1}^{y_2} f_{(x,\ y)} = I_{(x_2,\ y_2)} - I_{(x_2,\ y_2-1)} - I_{(x_1-1,\ y_2)} + I_{(x_1-1,\ y_1-1)} \qquad \textbf{Eq.}\ (4.4)$$

Figure 4.9 shows an example of image binarization of the current work. A temporary binary image was extracted through the adaptive threshold selection method, and then the background and undesirable parts were eliminated. The image binarization was carried out with the separate MATLAB script, which was coded by the author. In relation to the image binarization, it should be said that there was the limitedly manual modification of binary images while carrying out the image binarization. Especially, there was the case that the part nearby the lead to ignite spark could not be eliminated clearly. When this took place, the part was modified manually, using the photographic software, GIMP.

After obtaining binary images through the process mentioned above, the work to gain flame contour images was carried out. In this process, Canny edge detection algorithm was adopted. The edge detection algorithm is widely employed to extract the edges of images (Moeslund 2009). Canny edge detection algorithm consists of several steps. The application of Gaussian filter is the first step to obtain a smooth image, eliminating undesirable noises

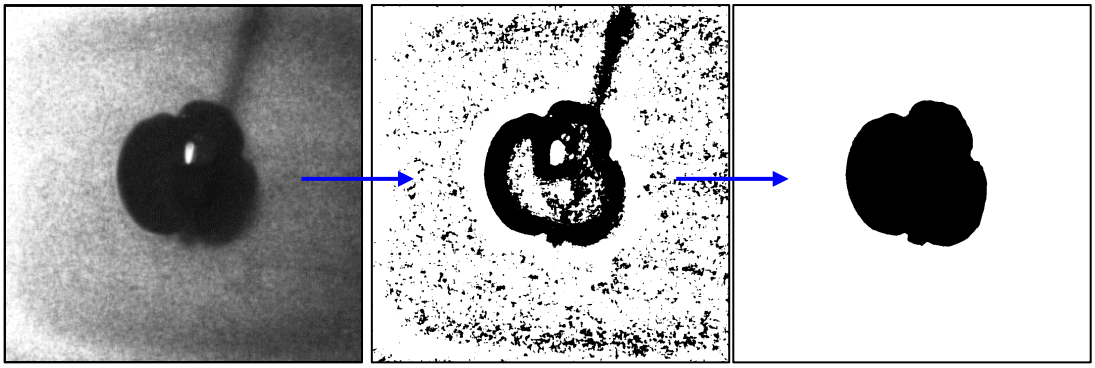

(a)
Image after the pre-processing

(b)
Image after adaptive thresholding technique

(c)
Binary image after Masking & elimination of undesirable parts

Figure 4.9 Derivation of a binary image. Fuel: CH_4-air mixture / equivalence ratio: 1.0 / time when image was taken: 3.2 ms after ignition / ignition timing: 27.6 °CA bTDC / pressure: 5 bar abs / temperature: 439 K / engine speed: 50 rpm

in it. And then the calculation for the gradient of the intensities in the image is made. After the process of eliminating the false parts of the edge detection, the algorithm applies a low and high threshold, which are calculated with the gradient of the intensities and known as double threshold, to achieve temporary edges. After examining the edges, undesirable edges or lines that are not connected to the desirable edge are excluded. The edge detection algorithm eventually determines the edge (Canny 1986, Moeslund 2009). Through this algorithm, the flame contour image could be obtained.

Figure 4.10 shows the entire process of deriving a flame contour image from the PIV flame image. Figure 4.10 (e) represents the flame contour image that is superimposed on the raw image, and Figure 4.10 (f) is the enlarged image of the red-box area. In order to make sure whether the location of the flame front is suitable or not, the variation in the radial velocity of the unburned gas with respect to the distance from the centre of the image was investigated. This validation is crucial. If the location of the flame front is improper, the undesirable value of the unburned gas velocity at each point of the flame contour line will be extrapolated, which is introduced in Sec. 4.2.2. The radial velocity of the unburned gas was measured using the PIV system. The distance between the point of which the pixel composed the flame contour line and the location where the radial unburned gas velocity became the minimum value was about 0.9 mm: see Figure 4.11. Although it is hard to be said that the distance is the exactly same as the flame thickness. However, considering

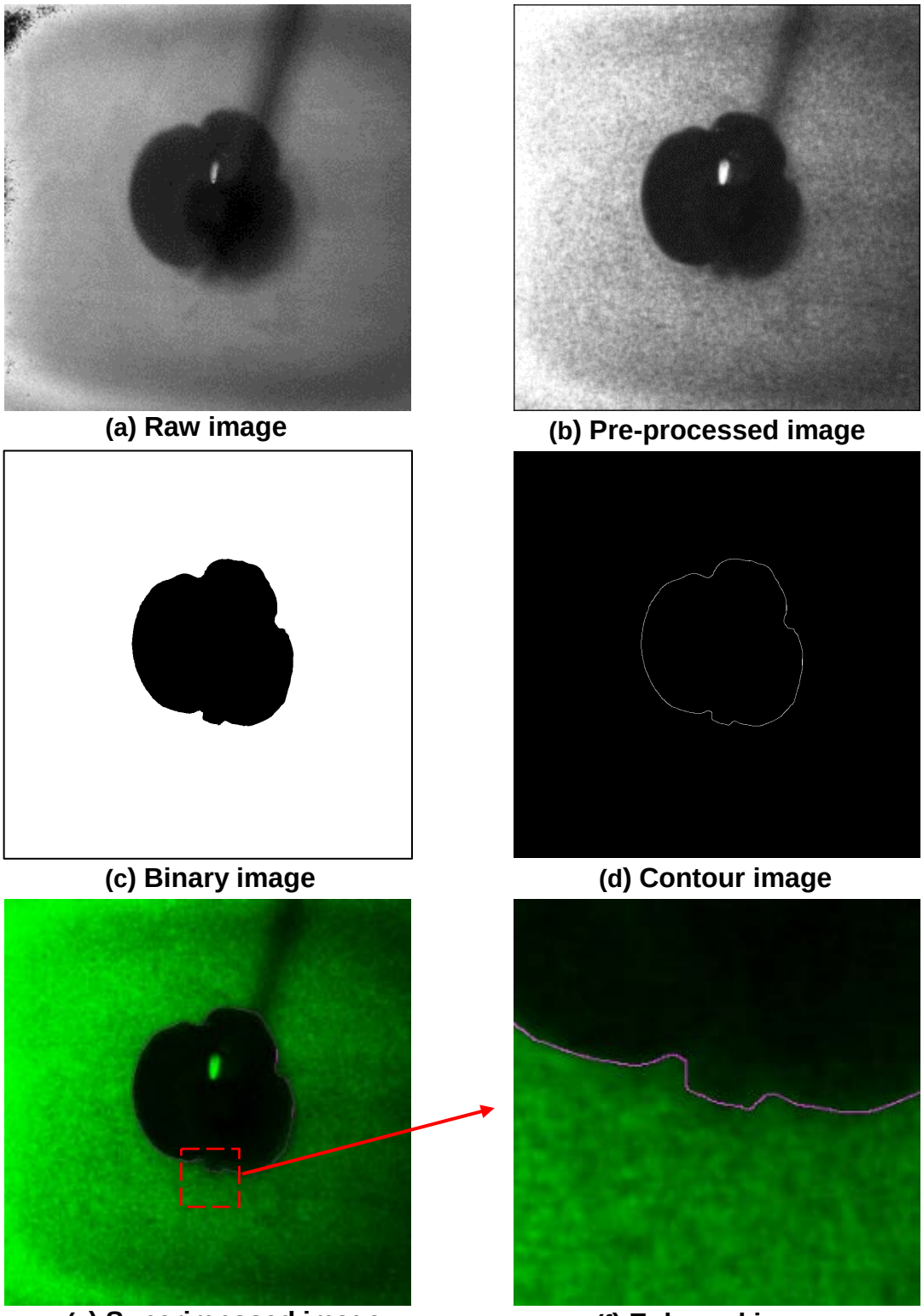

(a) Raw image

(b) Pre-processed image

(c) Binary image

(d) Contour image

(e) Superimposed image
(raw image + contour image)

(f) Enlarged image

Figure 4.10 Illustration of deriving a flame contour image and the superimposed contour image on the raw flame image; CH_4-air mixture / equivalence ratio: 1.0 / time when image was taken: 3.2 ms after ignition / ignition timing: 27.6 °CA bTDC, pressure: 5 bar abs, temperature 439 K / engine speed: 50 rpm

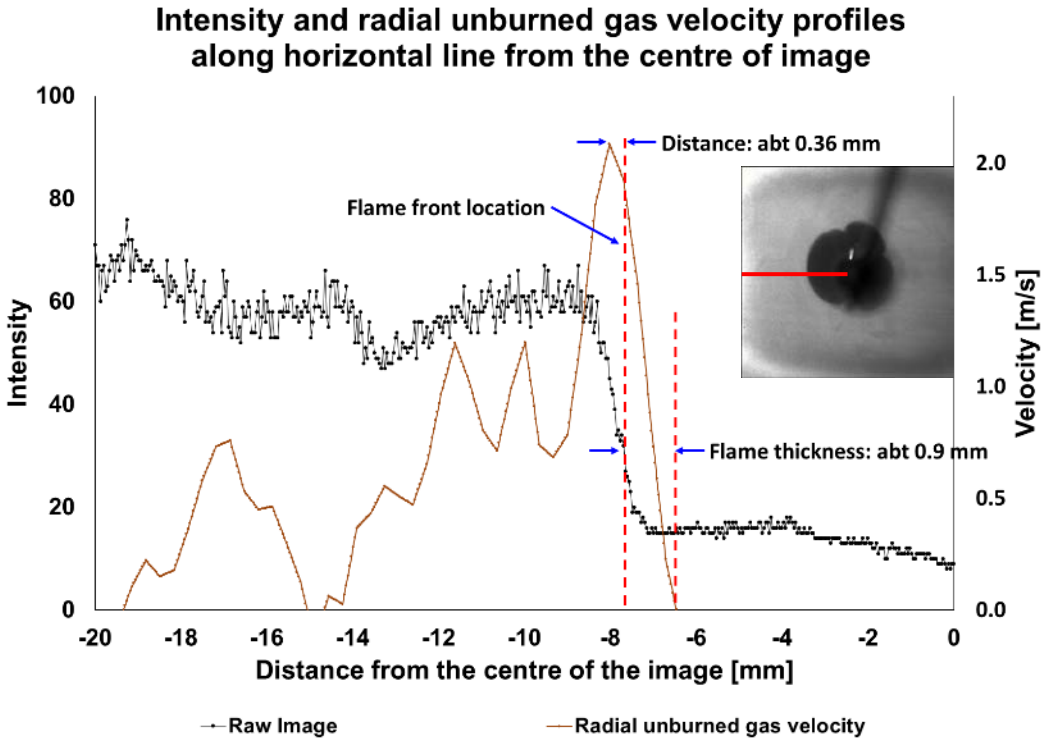

Figure 4.11 Intensity and radial unburned gas velocity profiles along the horizontal line from the centre of the image. Fuel: CH_4-air mixture / equivalence ratio: 1.0 / time when image was taken: 3.2 ms after ignition / ignition timing: 27.6 °CA bTDC / pressure: 5 bar abs / temperature 439 K / engine speed: 50 rpm

the intensity profile of the raw image, it seems reasonable that the flame front exists within the red-dashed lines. According to Law's research (2006), where a laminar premixed spherical flame propagates outwardly with the use of hydrocarbon-air mixtures, the flame thickness is about 1 mm and similar to the one shown in Figure 4.11.

As mentioned in the result of the simulation by Groot and De Goey (2002), the unburned gas velocity progressively increases until it approaches near the preheat zone, and then it starts decreasing after the value becomes maximum at a certain point ahead the preheat zone. As the combustible mixture moves toward the reaction zone, the fresh gas velocity decreases. After that, it eventually becomes zero when it enters the reaction zone. According to the relevant researches (Balusamy et al. 2011, Varea et al. 2012), the maximum unburned gas velocity appears at 0.3 or 0.4 mm before the flame front. As shown in Figure 4.11, the distance between the location of the flame front and the point where the maximum value of the radial unburned gas velocity

appears is about 0.36 mm. Based on the above validation, it was confirmed that the location of the flame front in this research was appropriate for the measurements of flame propagation speed and other properties.

4.2 Methodology for analysis

4.2.1 Derivation of the normal direction to each point of the flame contour line and the relevant derivatives

Through the review of the relevant literature and the measurement of the mean velocities mentioned Sec. 2.1 and 3.4.3 respectively, it was assumed that the combustion condition in the current work was laminar. Under the laminar condition, the direction in which flame propagates has to be normal to the flame front. Hence, it was essential to obtain the normal direction at each point of a flame contour line in order to measure the flame propagation speed. For the derivation of the normal direction, Fourier transform was employed.

Figure 4.12 shows the profiles of x- and y-coordinate along the flame contour line. The fuel in the experiment was a stoichiometric methane-air mixture. The image was recorded at 3.2 ms after the start of ignition, and the ignition timing was 27.6º CA bTDC of which the initial pressure and temperature were 5 bar in absolute pressure and 439 K respectively. The point index is counted in the clockwise direction, and the starting point is represented as a red box shown in Figure 4.12 (A).

Where the x-coordinate is the function of the point index t, its derivative can be represented in the following equations: this is also applied to the case of the y-coordinate.

$$F\left[\frac{d^n x(t)}{dt^n}\right] = (ik)^n X(k) \qquad \textbf{Eq.}\ (4.5)$$

$$\frac{d^n x}{dt^n} = F^{-1}[(ik)^n X(k)] \qquad \textbf{Eq.}\ (4.6)$$

where F and F^{-1} are the forward and inverse Fourier transform respectively, n is a differential coefficient, k is the variable in the frequency domain.

In order to apply the forward and inverse Fourier transform, a fast Fourier transform FFT was adopted. It computes a sequence of data through the discrete Fourier transform, which is named DFT. The computation of the DFT is to convert a series of data into an equally-length sequence of data in a frequency domain (Heideman et al. 1984, Brigham 1988). Eq. (4.7) and Eq. (4.8) represent a forward and inverse fast Fourier transform respectively:

$$X(k) = F[(x(t)] = \sum_{t=1}^{m} x(t) e^{\frac{-2\pi i}{m}(t-1)(k-1)} \qquad \textbf{Eq.} (4.7)$$

$$x(t) = F^{-1}[X(k)] = \sum_{k=1}^{m} X(k) e^{\frac{2\pi i}{m}(t-1)(k-1)} \qquad \textbf{Eq.} (4.8)$$

where m is the total number of data.

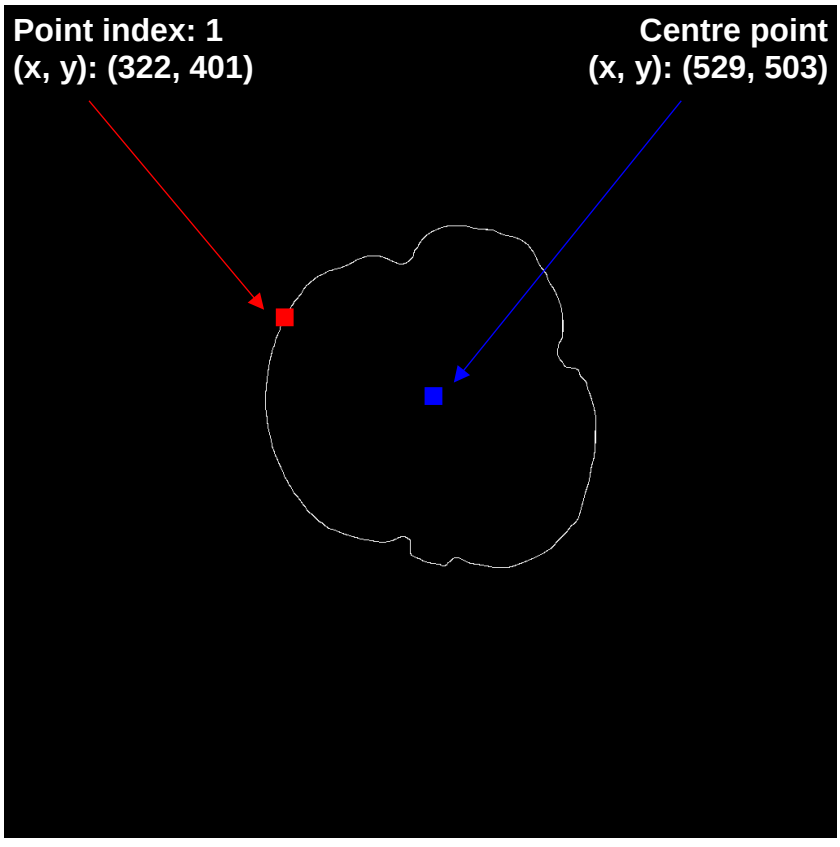

(A)

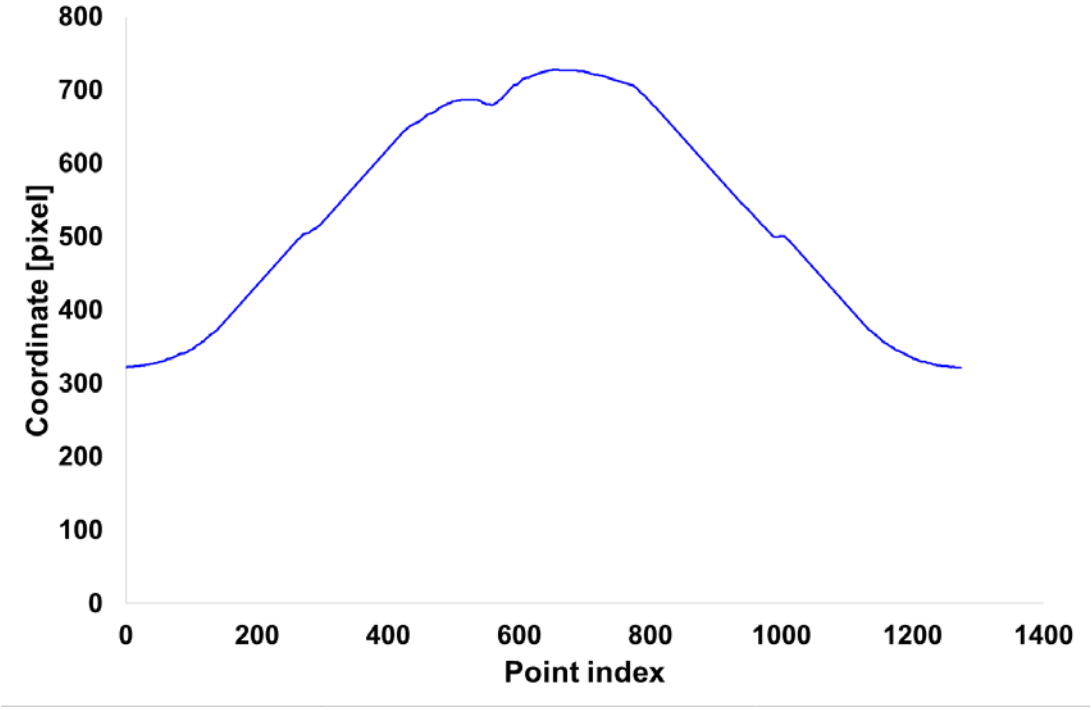

(B)

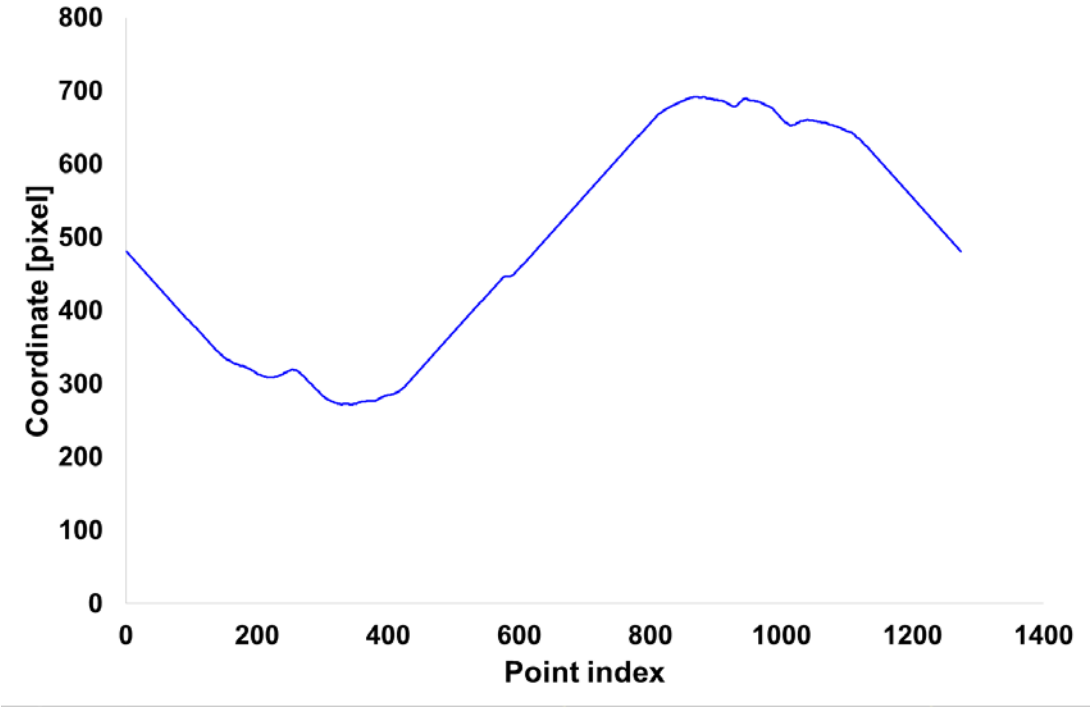

(C)

Figure 4.12 Flame contour line (A), and the changes of x- (B) and y-coordinate (C) with respect to point index: the index is counted in the clockwise

Assuming that a particle moves along the flame contour line of Figure 4.12 at a constant speed, the direction of the acceleration vector at a point is normal to the velocity vector which is tangential to the contour line at that point (Zill and Cullen 2006). The tangential and normal velocity vectors can be calculated as the following equations.

$$\frac{dx}{dt} = F^{-1}[(ik)X(ik)], \qquad \frac{dy}{dt} = F^{-1}[(ik)Y(ik)] \qquad \textbf{Eq.}\ (4.9)$$

$$\frac{d^2x}{dt^2} = F^{-1}[-k^2X(ik)], \qquad \frac{d^2y}{dt^2} = F^{-1}[-k^2Y(ik)] \qquad \textbf{Eq.}\ (4.10)$$

By using Eq. (4.9) and Eq. (4.10), the directions of the tangential and normal velocity can be calculated as follows.

$$\theta_{tangential} = tan^{-1}\frac{\frac{dy}{dt}}{\frac{dx}{dt}} \qquad \textbf{Eq.}\ (4.11)$$

$$\theta_{normal} = tan^{-1}\frac{\frac{d^2y}{dt^2}}{\frac{d^2x}{dt^2}} \qquad \textbf{Eq.}\ (4.12)$$

where $\theta_{tangential}$ and θ_{normal} are the degrees of the tangential and normal velocity vectors at a point on the flame contour line respectively.

Figure 4.13 shows the flame contour image, its enlarged images, and the tangential and normal vectors images which were obtained through the aforementioned Eq. (4.11) and Eq. (4.12). In Figure 4.13 (B), (D), and (F), each blue-solid arrow indicates the tangential vector at each point on the flame contour line, and each red-solid arrow represents the normal vector at the point. In Figure 4.13 (D) and (F), compared with the smooth-curved and abrupt curved parts, the directions of the tangential and normal vectors in the smooth-flat part gradually change. In order to represent the wrinkled or curved amount at each point on the flame contour line, the curvature at each point was calculated using Eq. (4.9) and Eq. (4.10). Curvature C_k at a point is defined as

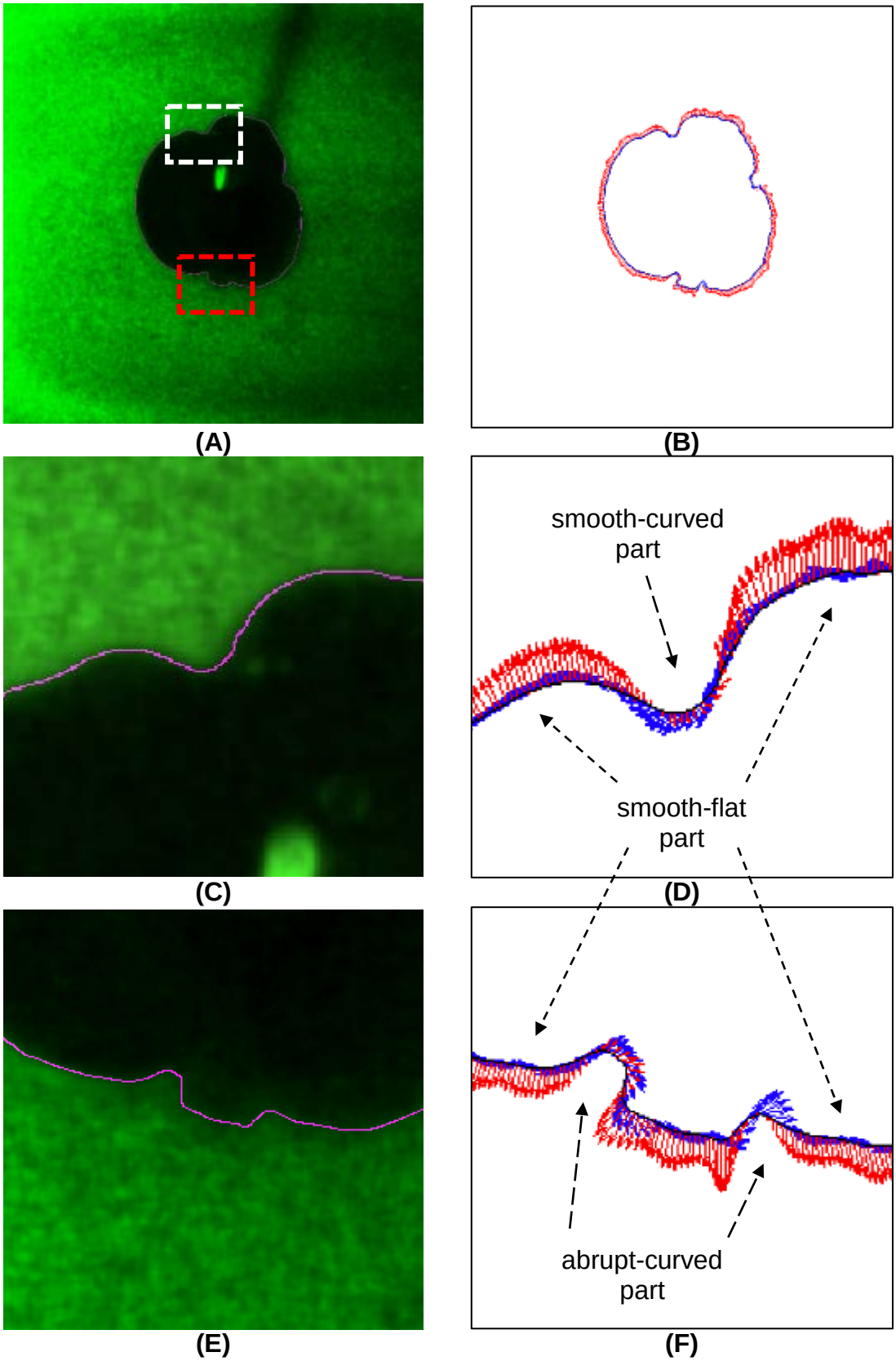

Figure 4.13 Illustration of the images: (A) is the flame contour image superimposed on the raw image, (B) is the tangential and normal vectors image of (A). (C) and (E) are the enlarged images of the white-dotted and red-dotted boxes in (A) respectively, and (D) and (F) are their enlarged vectors images

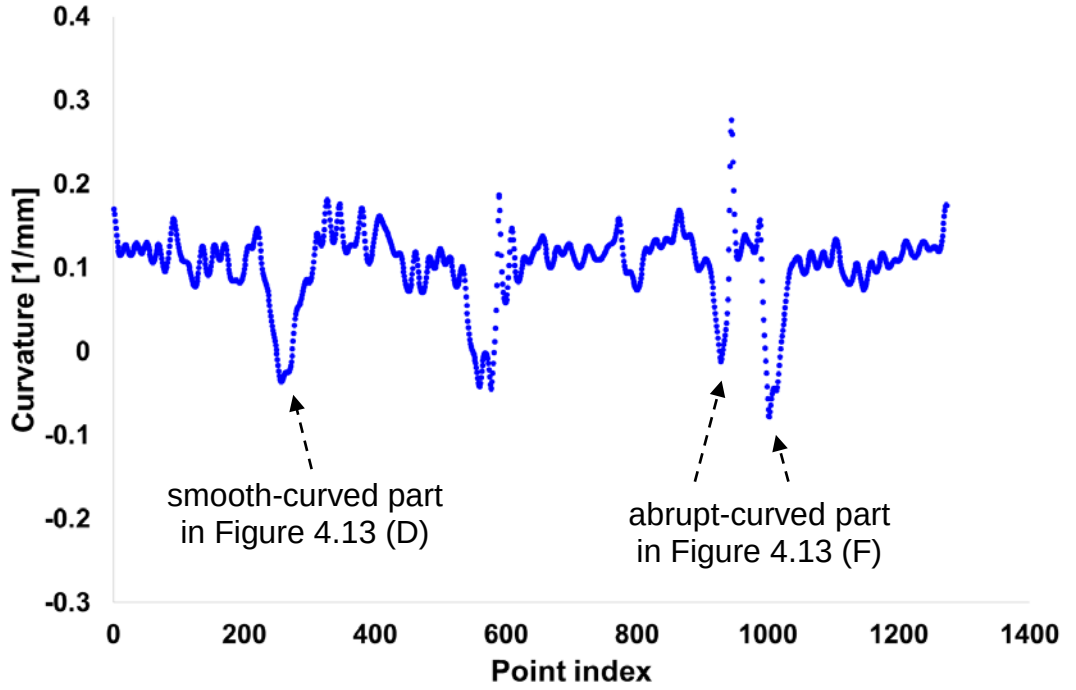

Figure 4.14 Change of curvature of the flame contour line in Figure 4.12 (A) with respect to point index

the following equation (Zill and Cullen 2006): the derivation of curvature is described in Appendix D.

$$C_k = \frac{\frac{d^2y}{dt^2}\frac{dx}{dt} - \frac{d^2x}{dt^2}\frac{dy}{dt}}{\left\{\left(\frac{dx}{dt}\right)^2 + \left(\frac{dy}{dt}\right)^2\right\}^{\frac{3}{2}}} \qquad \textbf{Eq.}\ (4.13)$$

The calculated curvature can have a positive or negative value. The positive value means that the shape of the line is convex, whereas the negative value indicates that the shape is concave. Figure 4.14 shows the change of curvature of the flame contour line in Figure 4.12 (A) with respect to point index. The curvature of the smooth-curved part in Figure 4.13 (D) changes from the positive to the negative value. Similarly, the sign of curvature of the abrupt-curved part also varies.

In the current research, since a flame contour line gradually becomes longer as the flame propagates outwardly, the number of points consisting of the

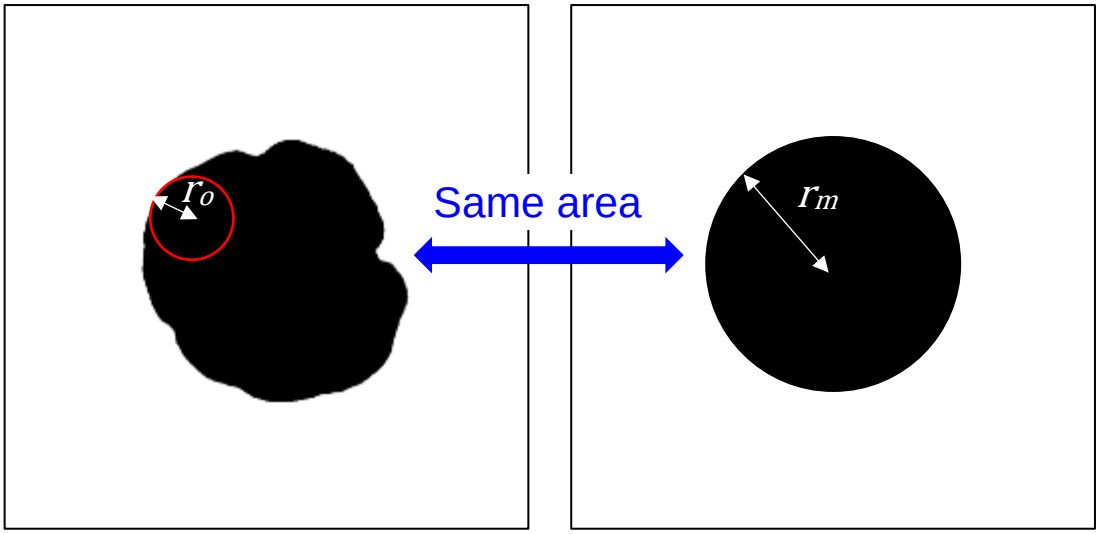

Figure 4.15 An illustration of the mean flame radius and the radius of the osculating circle at each point.

contour line also becomes large. Because of this, the location of the first point of a point index varies. To compare the curvatures of developing flame, a point index was represented in angle. In addition, since a flame size continuously varies as it propagates, it is necessary to derive a dimensionless number to quantify how much curved the flame contour line is. To normalise curvature, the mean flame radius was calculated. As seen in Eq. (4.14), since curvature at a point is a reciprocal number of the radius of the corresponding osculating circle, it can be normalised through the mean flame radius. The normalised curvature is named wavenumber k in this paper and defined as the ratio of the flame mean radius to the radius of an osculating circle. Figure 4.15 shows an example of the mean flame radius and the radius of an osculating circle. Figure 4.15 (A) is a flame binary image: the unburned area is white, and the burned area is black. The black area in Figure 4.15 (B) is identical to the one in (A) in size. The equations related to the normalisation are as follows:

$$r_o = \frac{1}{C_k} \qquad \textbf{Eq.} \ (4.14)$$

$$r_m = \frac{1}{C_{km}} = \sqrt{\frac{Corresponding\ area}{\pi}} \qquad \textbf{Eq.} \ (4.15)$$

$$k = \frac{r_m}{r_o} \qquad \textbf{Eq.}\ (4.16)$$

$$C_k \propto k \qquad \textbf{Eq.}\ (4.17)$$

where r_o is the radius of an osculating circle at a point on the flame contour line, r_m the corresponding mean flame radius, and C_{km} the curvature of a circle having the identical dimension to the burned area in a binary flame image. As seen in Eq. (4.17), curvature C_k is proportional to wavenumber *k*, and the mean wavenumber can be obtained as follows:

$$\bar{k} = \frac{1}{n}\sum_{a=1}^{n} k_a \qquad \textbf{Eq.}\ (4.18)$$

where $\bar{k}$ is the mean wavenumber, n the number of the total points consisting of a flame contour line, a the index of a point, and k_a is an arbitrary wavenumber at the corresponding point.

Figure 4.16 shows the flame contour image and the variation of wavenumber with respect to angle. In Figure 4.16 (A) the direction of counting angle is clockwise, and the left-end point of the magenta horizontal line is the starting point of counting angle. The changes of sign of the wavenumber are seen in the smooth-curved and abrupt-curved parts in Figure 4.16 (B). Through such changes of wavenumber, the occurrence of a curve or wrinkle in the flame contour line can be perceived, and the magnitude can be quantified as flame propagates. Moreover, depending on the gradient of change of wavenumber with respect to angle, it is possible to realise how precipitously the flame surface varies. It is shown in Figure 4.16 (B) that the slope of wavenumber in the abrupt-curved part is steeper than the one of wavenumber in the smooth-curved part.

The physical meaning of wavenumber defined through and Eq. (4.16) should be mentioned. First, when wavenumber is one at a point on the flame contour line, it is meant that the corresponding flame surface is smoothly curved. If flame propagated outwardly in the ideal condition mentioned in Sec. 2.1, the morphology of the flame would be a circle, which means that the radius of an

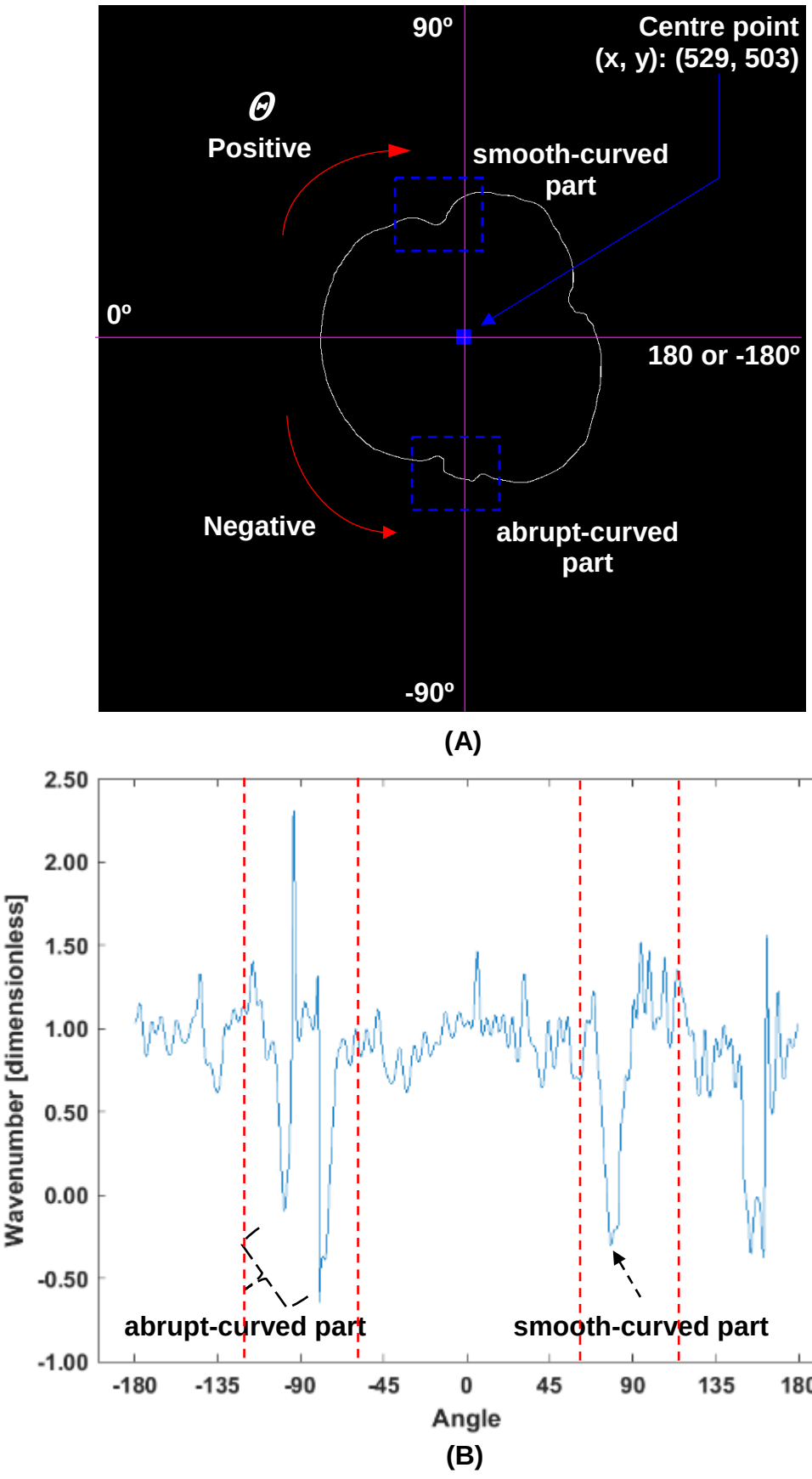

Figure 4.16 Flame contour image (A) and the change of wavenumber with respect to angle (B)

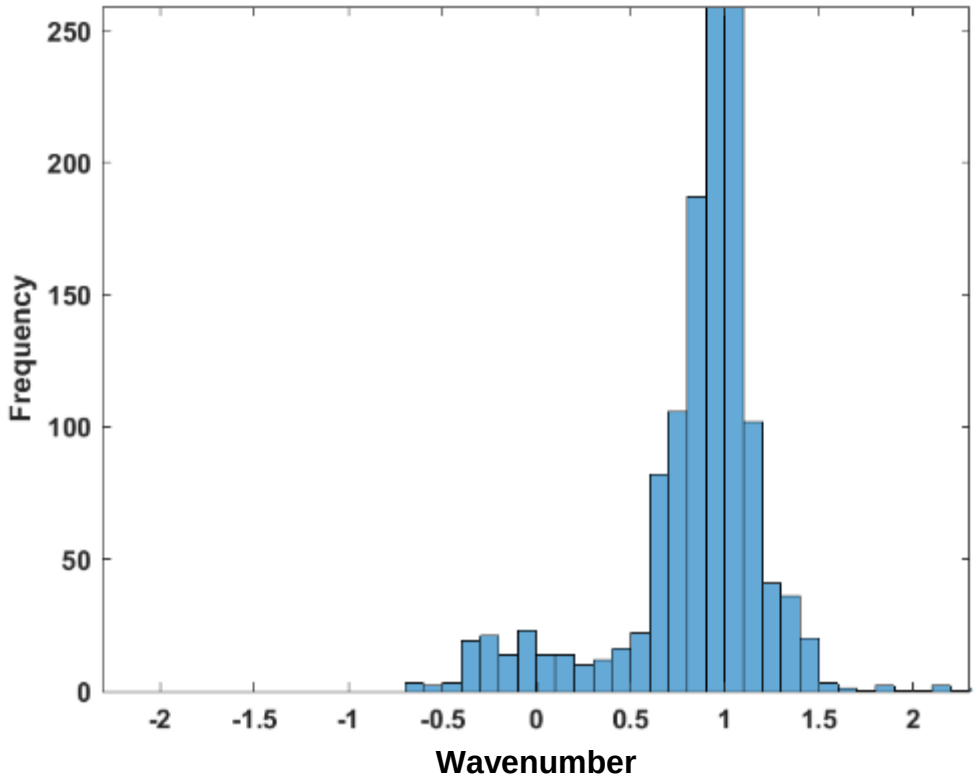

Figure 4.17 Histogram of the wavenumber shown in Figure 4.16 (B)

osculating circle is identical to the mean flame radius. Therefore, the wavenumber would be one. In this regard, it can be said that the flame contour line in Figure 4.16 (A) is smoothly curved at most of the points. Except for several certain parts, the wavenumber ranges between 0.7 and 1.3, which is shown in Figure 4.17.

Where wavenumber is positive, the corresponding flame surface is convex toward the unburned area. And in the case that wavenumber is negative, the flame shape is concave toward the unburned area. As seen in the smooth-curved part of Figure 4.16, the flame changes from a convex to concave shape toward the unburned area with respect to angle, and then becomes convex. While the flame shape changes, the sign of wavenumber varies. And when the flame shape is convex (concave), the corresponding wavenumber is positive (negative). In addition, depending on the gradient of wavenumber, it can be learned how dramatically a flame shape changes. Compared with the concave of the smooth-curved part, the flame shape changes sharply in the concaves of the abrupt-curved part, and its gradients are steeper.

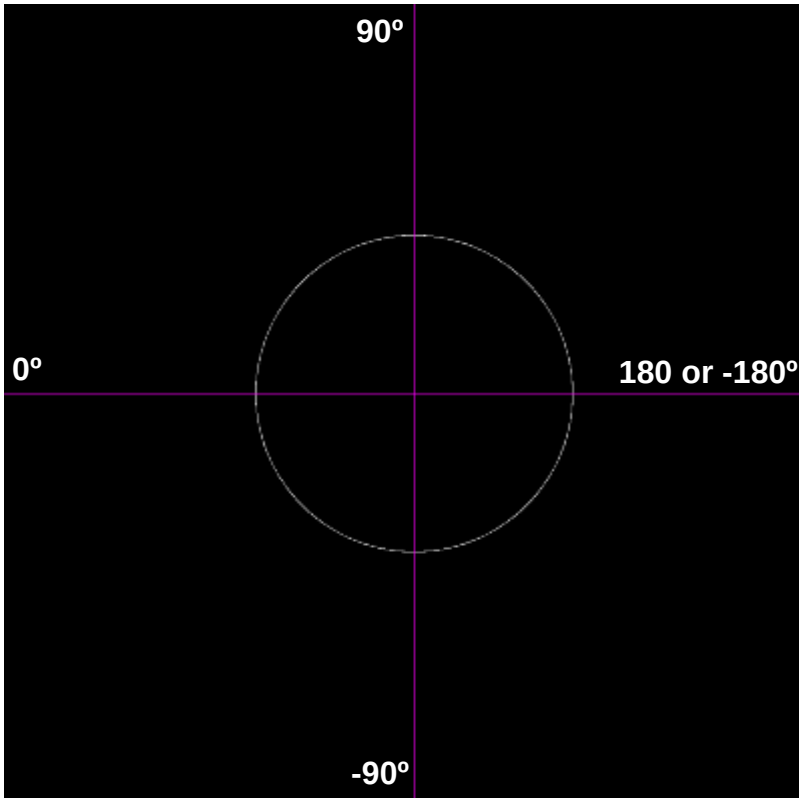

(A) Corresponding circle

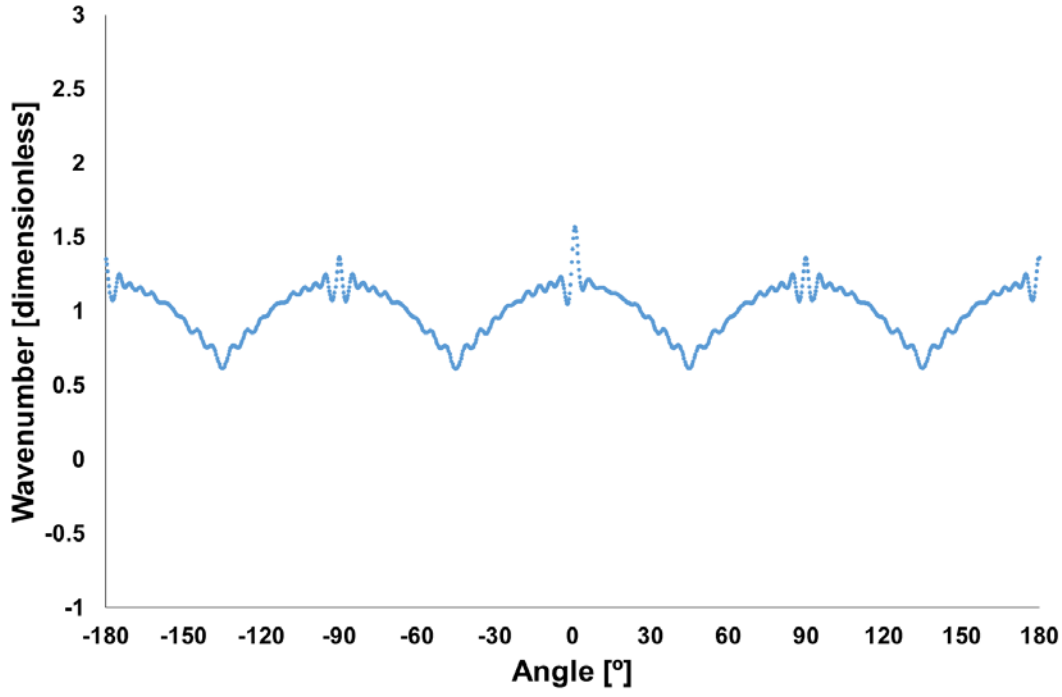

(B) Wavenumber *vs* angle

Figure 4.18 Corresponding circle having the identical area to the burned area shown in Figure 4.16 (A) and change of the wavenumber

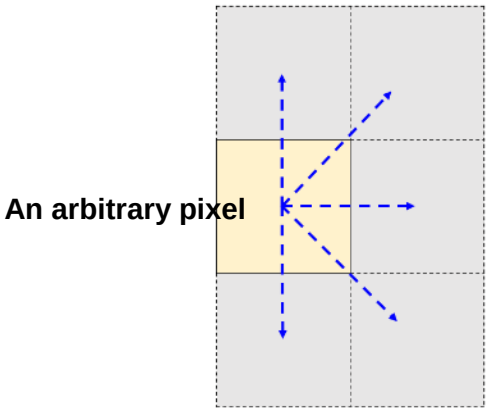

Figure 4.19 An illustration of the moving direction of an arbitrary pixel

It is also important to suggest a certain value or range that is used as the criterion for making the judgment on whether the flame is smoothly curved or not. For this, the wavenumber of the corresponding circle that has the identical area to the burned area shown in Figure 4.16 (A) was calculated, and Figure 4.18 shows the result. As seen in Figure 4.18 (A), the surface of the corresponding circle is smoothly curved along with the circumference. Assuming that flame propagates at the radial direction and the flame propagation speed has the same value at every direction without the effect of thermal expansion of unburned gas, the circle would be the ideal shape that the flame could have. Theoretically, according to the definition of the wavenumber introduced in Eq. (4.16), the values of wavenumber at the entire points consisting of the circle have to be one.

However, as seen in Figure 4.18 (B), the wavenumber changes with respect to angle, and the range is between 1 ± 0.3. The variation of the wavenumber in the circle originates from image resolution: the image resolution in the current work was 1024 x 1024. When the index of pixels consisting of a circle is enumerated in the clockwise direction, the moving direction of an arbitrary pixel is one of the five directions, which are the horizontal, vertical or diagonal direction: refer to Figure 4.19. It is obvious that the resolution of an image is the factor in affecting the calculation of wavenumber. As the resolution of an image rises, the range where the change of wavenumber would be reduced. Under the experimental condition of the current research, it can be said that a flame contour line is smoothly-curved where its wavenumber ranges between 0.7 and 1.3.

In order to secure the reliability of results of the aforementioned measurements such as normal direction, curvature, and wavenumber, the raw

x- and y-coordinates consisting of a flame contour line were compared with the ones that are computed through the forward and inverse Fourier transform. The result of the comparison is shown Figure 4.20, and the x- and y-coordinates are for the flame contour line seen in Figure 4.16 (A).

As can be seen in Figure 4.20 (A) and (B), most of the deviations of the x- and y-coordinates are distributed between +0.5 and -0.5. Figure 4.20 (C) and (D) show the absolute values of deviations of the x- and y-coordinates. Most of the values are less than 0.5. The average values of the x- and y-coordinates are 0.184 and 0.162 respectively, and the standard deviations are 0.197 and 0.186. The difference between the raw coordinates and the computed coordinates was very little, and it was confirmed that the values of normal direction, curvature, and wavenumber were dependable.

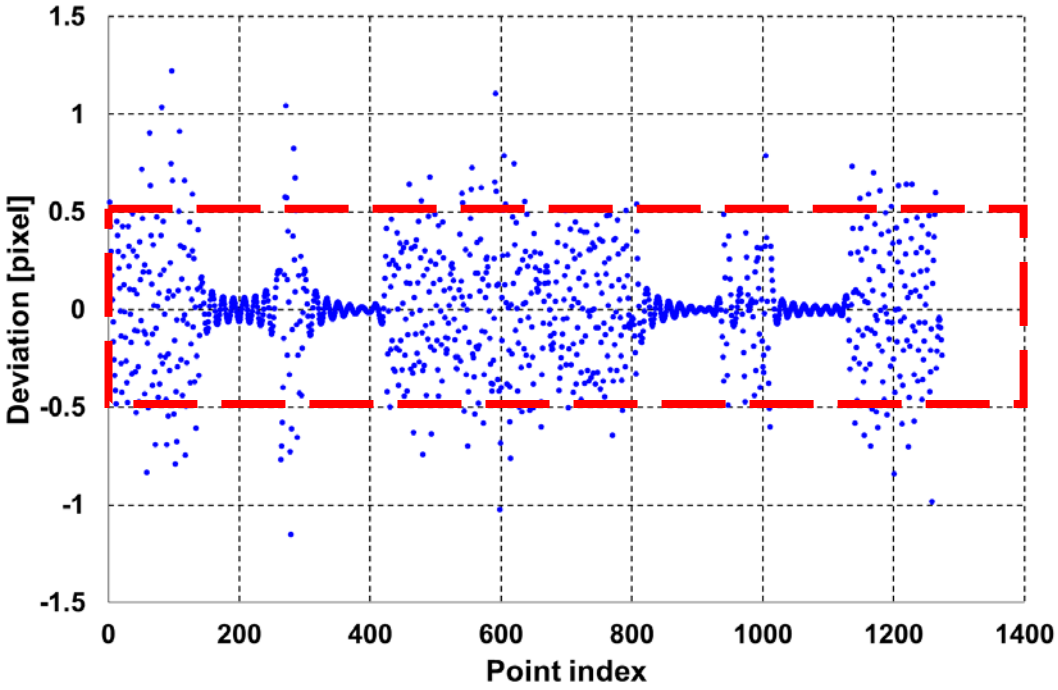

(A)

Deviation of x-coordinate

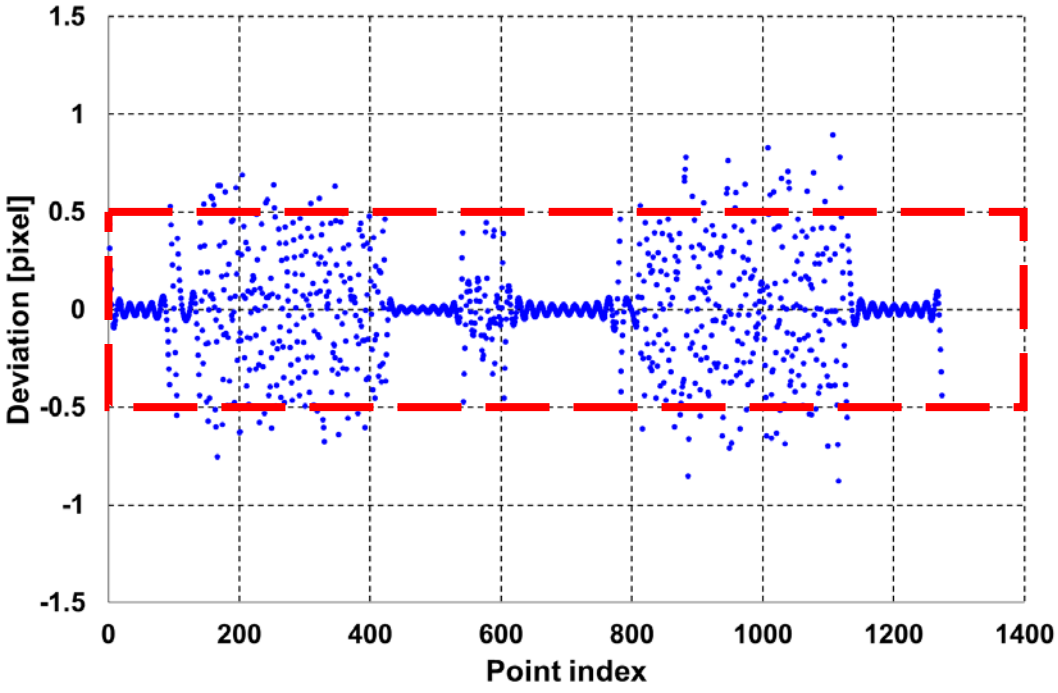

(B)

Deviation of y-coordinate

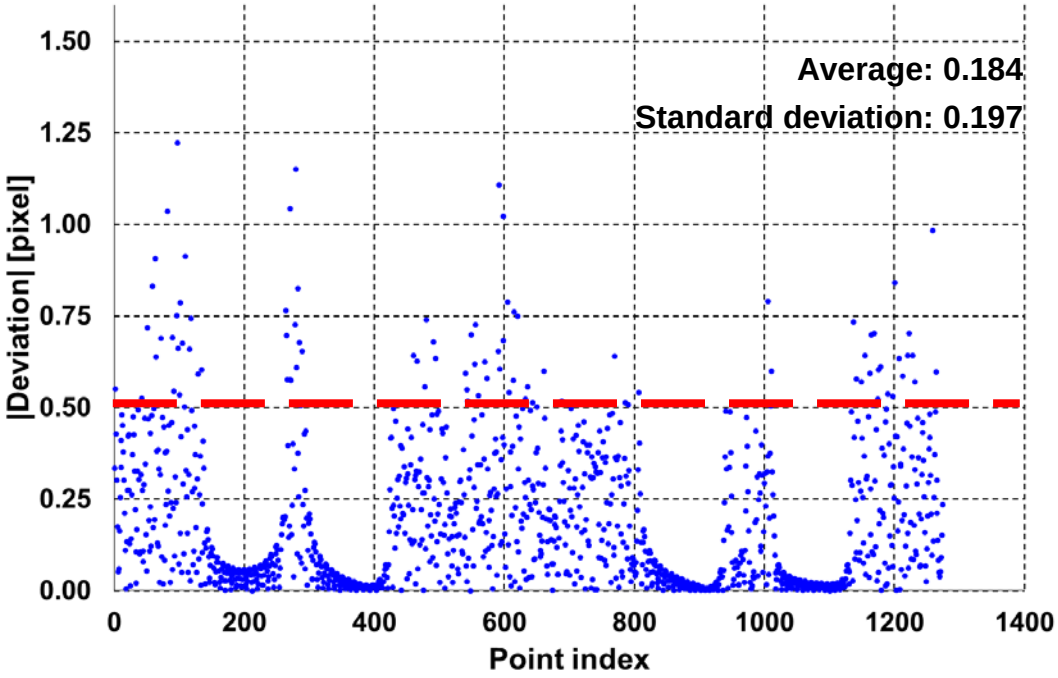

(C)

Absolute value of deviation of x-coordinate

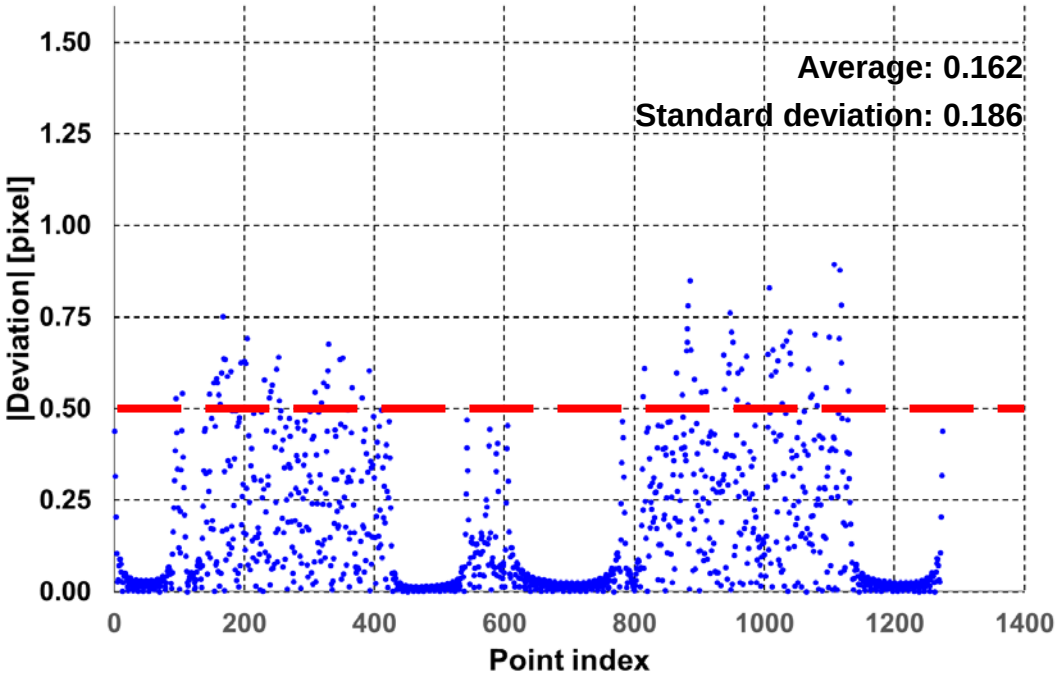

(D)

Absolute value of deviation of y-coordinate

Figure 4.20 Results of deviation and standard deviation of the x- and y-coordinates computed through the forward and inverse Fourier transform

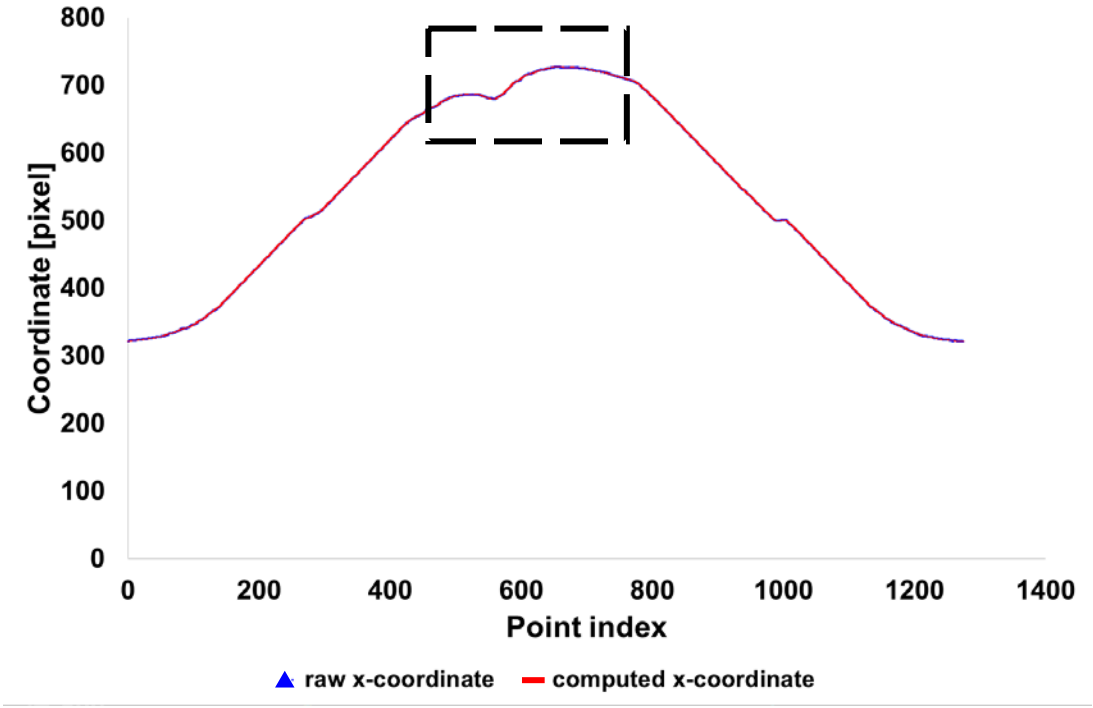

(A)

Comparison of the raw x-coordinate and computed one

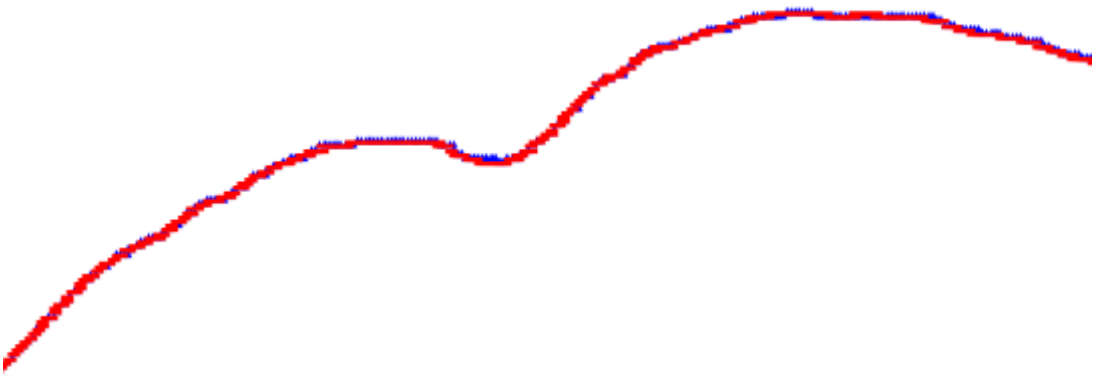

(B)

Enlargement of the black-dashed part of (A)

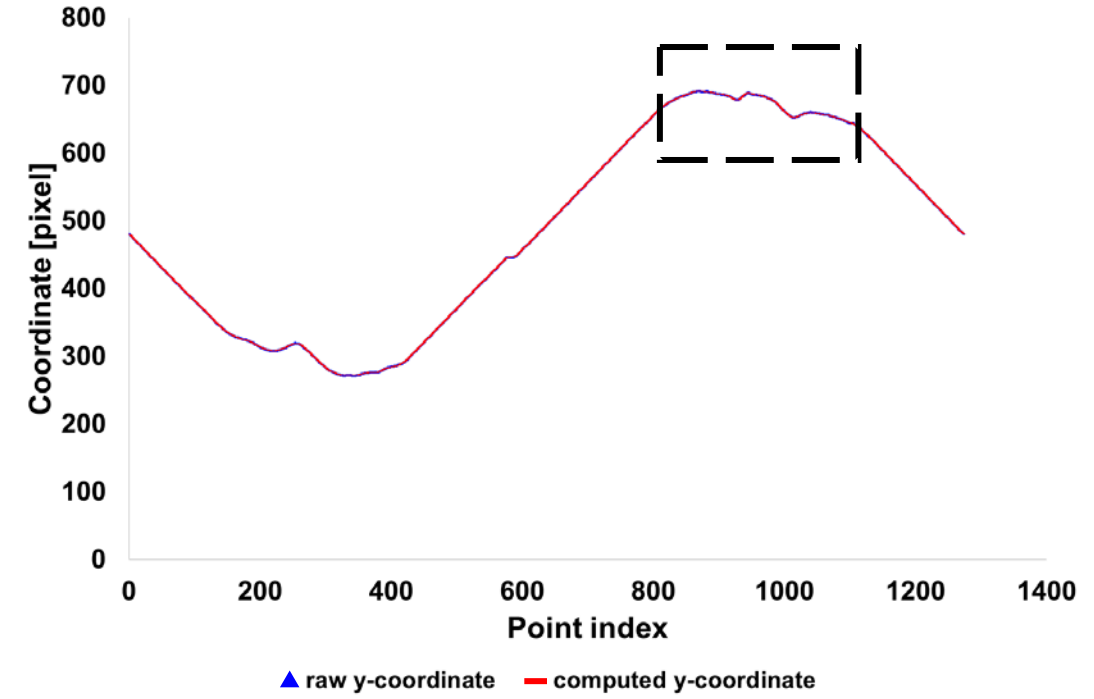

(C)

Comparison of the raw y-coordinate and computed one

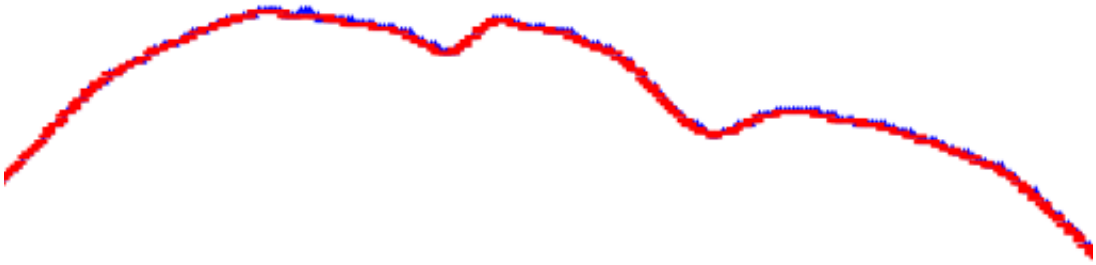

(D)

Enlargement of the black-dashed part of (C)

Figure 4.21 Comparison of the raw x- and y-coordinates with the computed x- and y-coordinates through the forward and inverse Fourier transform

4.2.2 Measurement of displacement, flame propagation speed, unburned gas velocity, and burning velocity in a local area

In order to measure flame propagation speed, it is first to measure the displacement between two points on two flame contour lines. Figure 4.22 shows the measurement of the displacement between two points on the two contour lines. The normal direction line at a sampling point P_1 on the flame contour line L_1, which is the solid-blue line, is obtained first, and then the junction point P_2 on the second flame contour line L_2 is found out. Eq. (4.19) represents the calculation of flame propagation speed.

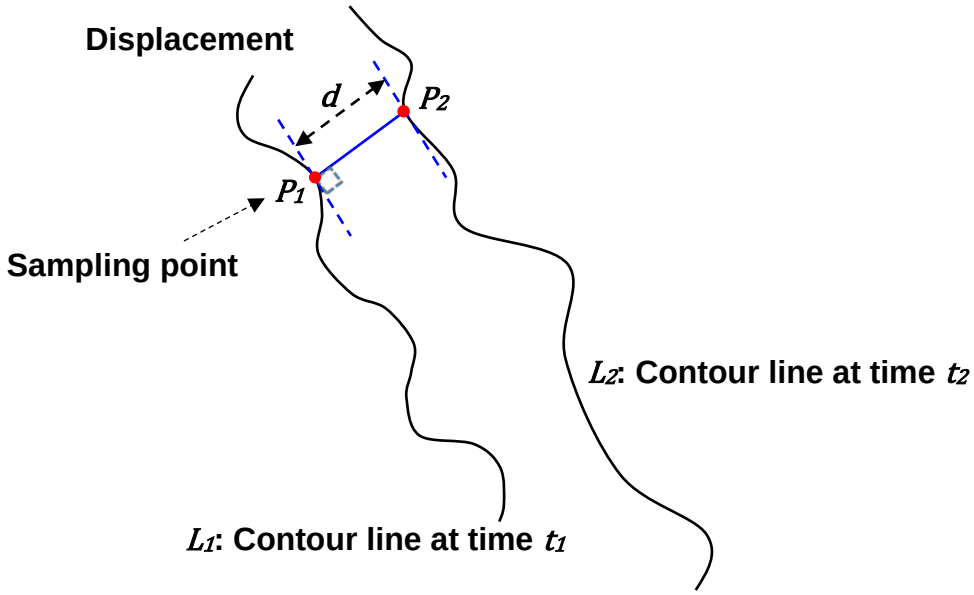

Figure 4.22 A simple sketch of measurements of displacement and flame propagation speed at each point along the flame contour line

$$S = \frac{d}{t_2 - t_1} \qquad \textbf{Eq.}\ (4.19)$$

where S is flame propagation speed, d is displacement of two points on the two flame contour lines, and t_1 and t_2 are the corresponding times.

Figure 4.23 shows a result of the calculation for the flame propagation speed. The fuel and equivalence ratio that were used in the experiment were a methane-air mixture and stoichiometric. The initial pressure and temperature were 5 bar in absolute pressure and 439 K. The ignition timing was 27.6 º CA bTDC. Three white flame contour lines that are seen in Figure 4.23 (A) were obtained at 3.2, 3.6, and 4.0 ms after the start of ignition. (B) in the figure

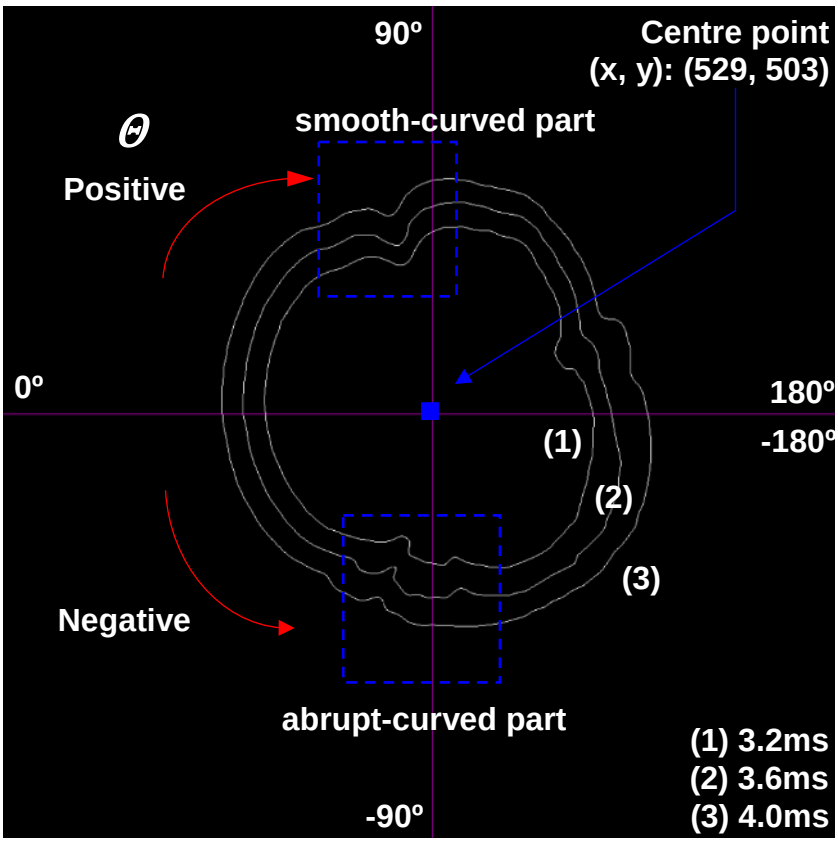
90º
Centre point
(x, y): (529, 503)
θ
smooth-curved part
Positive
0º
180º
-180º
(1)
(2)
(3)
Negative
abrupt-curved part
(1) 3.2ms
(2) 3.6ms
(3) 4.0ms
-90º

(A)

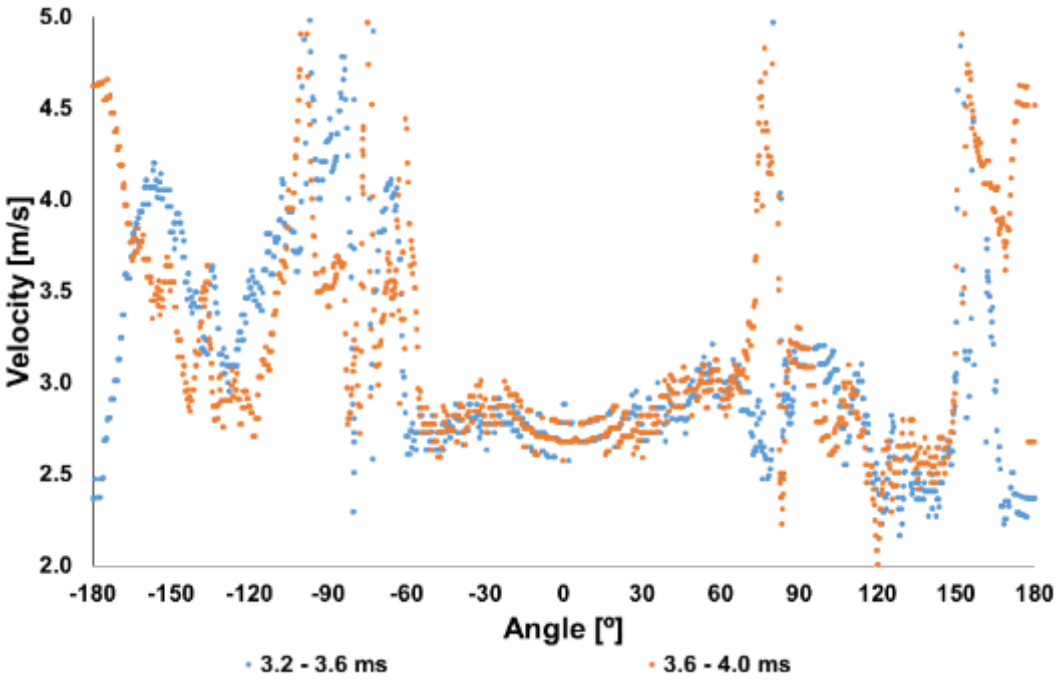
Velocity [m/s]
5.0
4.5
4.0
3.5
3.0
2.5
2.0
-180
-150
-120
-90
-60
-30
0
30
60
90
120
150
180
Angle [º]
3.2 - 3.6 ms
3.6 - 4.0 ms

(B)

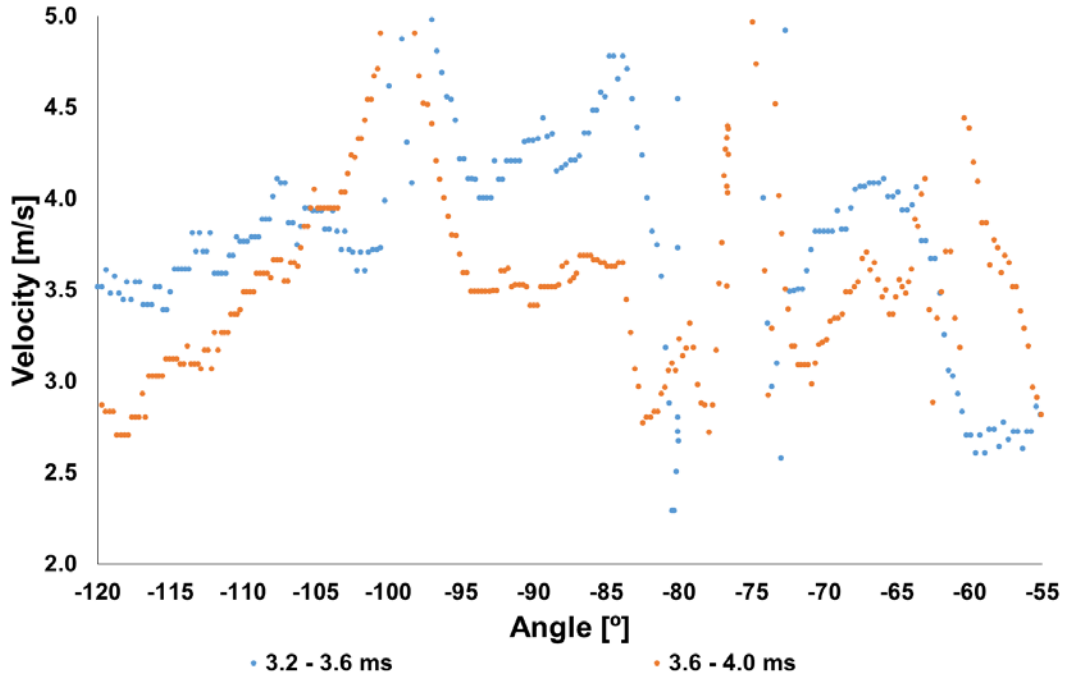

(C)

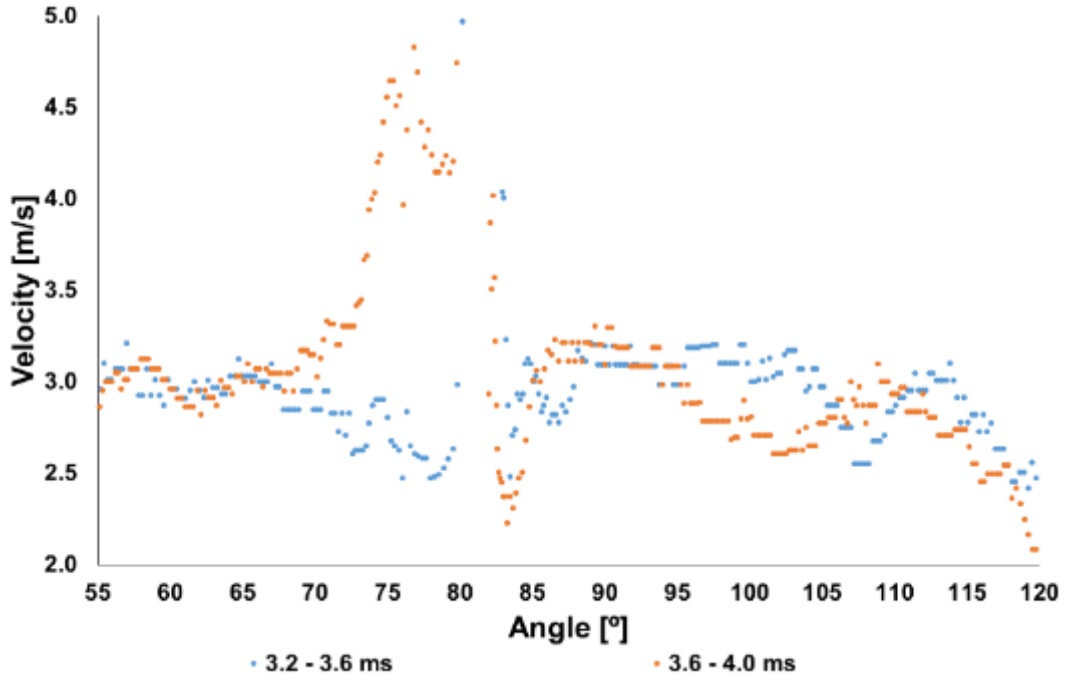

(D)

Figure 4.23 An example of the development of flame (A) and the change of the flame propagation speed with respect to angle (B): (C) is the change of the speed in the abrupt-curved part of (A), and (D) is the change of the speed in the smooth-curved part

represents the change of the flame propagation speed with respect to angle, and (C) and (D) indicate the changes of the speed in the abrupt- and smooth-curved part respectively. In order to compare the changes of flame propagation, unburned gas velocity, and burning velocity in a local area, three sections were selected in the current work. The first section is a convex area on the flame contour line, the second a concave area, and the third a smoothly-curved area. The third section means that the corresponding wavenumber mostly ranges between 0.7 and 1.3. This is shown in Chapter 5.

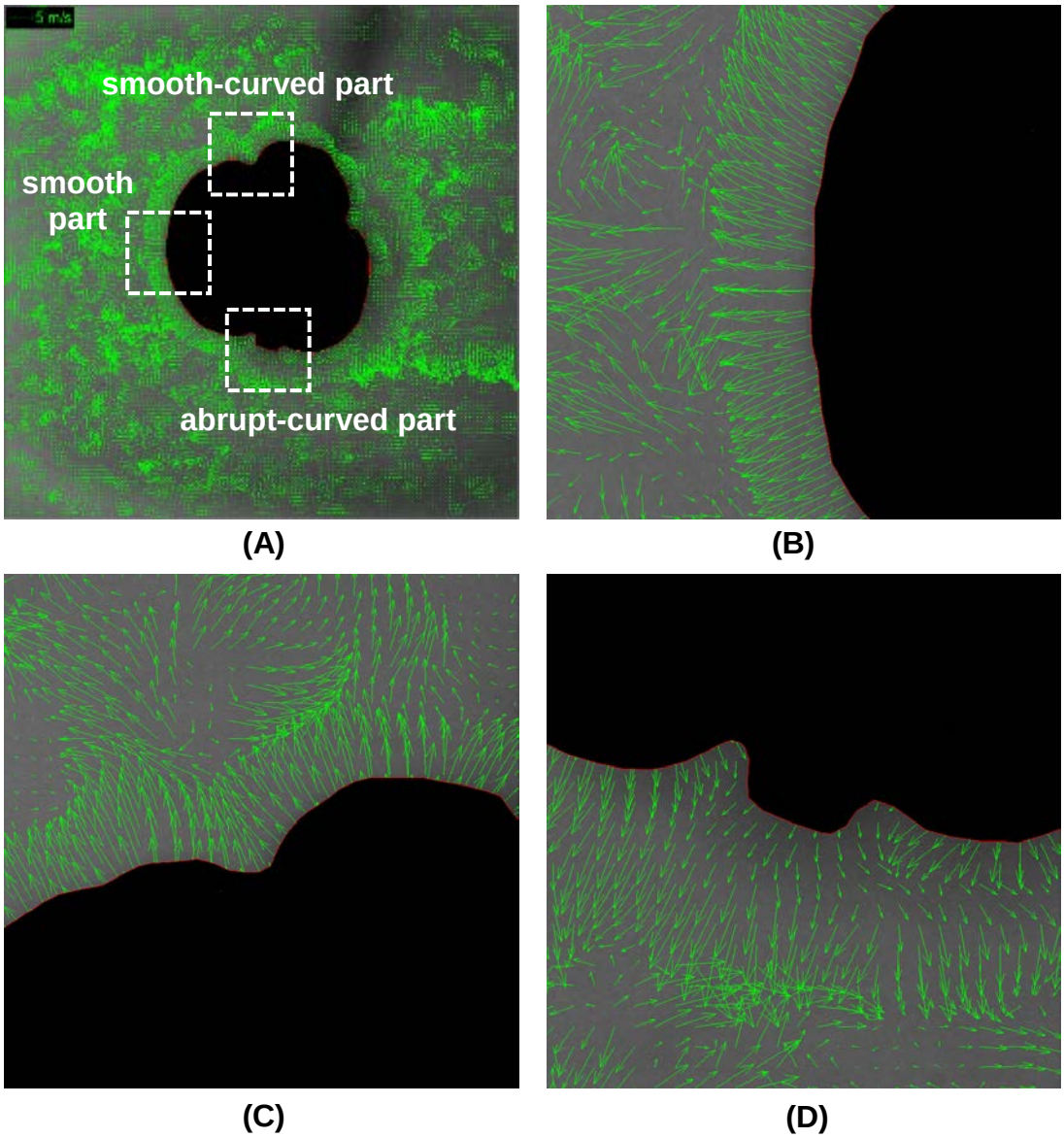

Figure 4.24 The flow field image (A) and its enlargement images: (B) is the enlarged image of the smooth part, (C) is that of the smooth-curved part, and (D) is that of the abrupt-curved part in (A)

The measurement of unburned gas velocity was taken using the PIV system as described in Sec. 3.4.3. Figure 4.24 shows the entire flow field of a flame image and its local flow fields. The fuel-air mixture used in the experiment was a stoichiometric methane-air mixture. The ignition timing was 27.6 º CA bTDC, and the initial pressure and temperature were 5 bar in absolute pressure and 439 K. The flame image for the calculation of the flow field was recorded at 3.2 ms after the start of ignition. As mentioned in 3.4.2, since the interrogation window size and overlap percent between two adjacent windows were 32 x 32 pixels and 75 % respectively, the resolution of a flow field was 256 x 256 pixels. This means that an unburned gas velocity has the same value in 4 x 4 pixels in 1024 x 1024 pixels of a flame image. 256 x 256 pixels of a flow field extended to 1024 x 1024 pixels of a flow field, with the use of bicubic interpolation, which is widely used in numerical analysis and image processing to interpolate data points on two-dimensional regular grid (Keys 1981, LaVision 2010b)

As mentioned in Sec. 3.4.3, since it is assumed that the combustion condition in the current work is laminar, the direction in which the unburned gas propagates has to be considered to be the same as the one where the flame propagates. That is, the direction has to be normal to each point of a flame front. In order to calculate the normal unburned gas velocity at each point of a flame front, the inner product of unburned gas velocity and the normal velocity vector was carried out. Figure 4.25 shows the illustration of inner product of two vectors. The angle of the normal velocity vector θ_{normal} is calculated through Eq. (4.12) in Sec.4.2.1. The angle of the unburned gas velocity θ_{vg} can be calculated as follows:

$$\theta_{V_g} = tan^{-1}\frac{V_{g_y}}{V_{g_x}} \qquad \textbf{Eq.} (4.20)$$

where V_{gx} and V_{gy} are unburned gas velocity vectors in the horizontal and vertical direction respectively. The normal unburned gas velocity V_n can be represented in Eq. (4.21).

$$V_n = \sqrt{{V_{g_x}}^2 + {V_{g_y}}^2} \cdot cos(\theta_{V_g} - \theta_{normal}) \qquad \textbf{Eq.} (4.21)$$

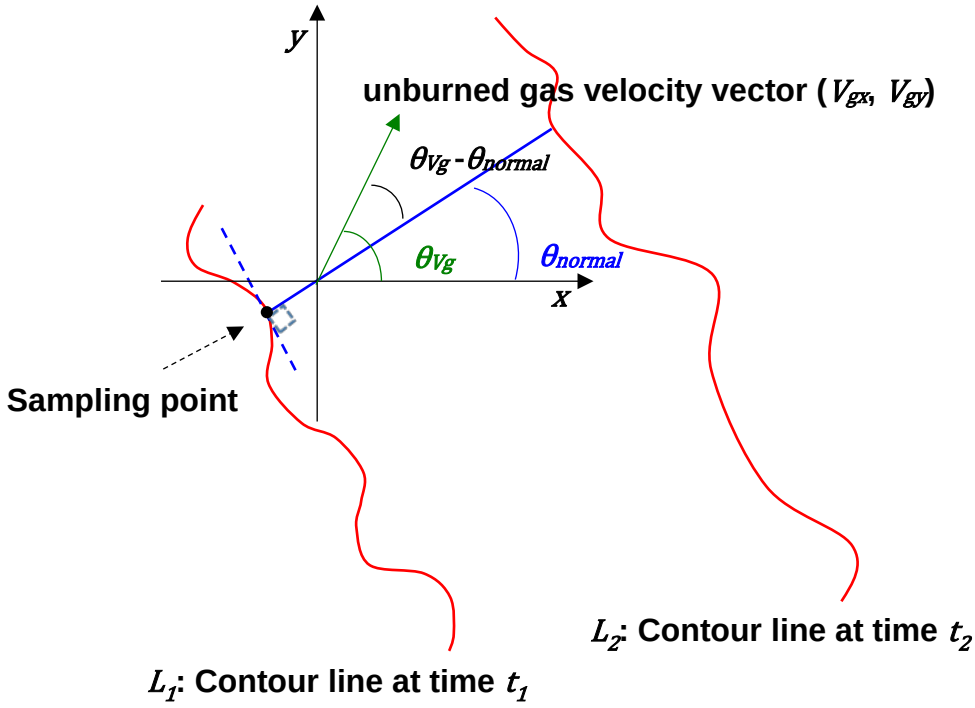

Figure 4.25 A simple sketch of the calculation of the normal unburned gas velocity at each point along a flame contour line

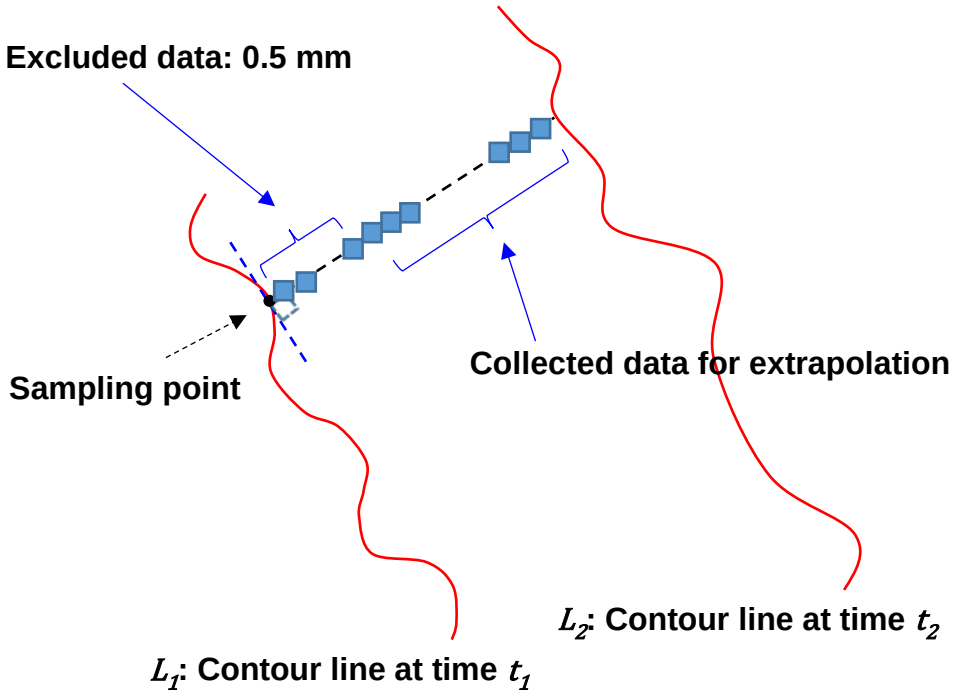

Figure 4.26 An illustration of range of normal unburned gas velocity data that are collected for extrapolation

Figure 4.26 briefly shows how normal unburned gas velocity data are collected for extrapolation. A sequence of normal unburned gas velocities data along the normal direction line were used to carry out the extrapolation for estimating the normal unburned gas velocity at each point of a flame contour line. For this extrapolation, the number of normal unburned gas velocity data has to be determined. As shown in Figure 4.11 in Sec. 4.1.2, the location where the maximum unburned gas velocity shows up is about 0.40 mm before the flame front. And 4 x 4 pixels including a pixel consisting of a flame contour line have to be excluded. This is because the normal unburned gas velocity datum in the 4 x 4 pixels is likely to be calculated using the pixel in the burned area. Considering these, normal unburned gas velocity data located at a flame contour line to 1 mm away from it were excluded for the extrapolation. This corresponds to 25 pixels in a flame image where pixels are arrayed horizontally or vertically.

Normal unburned gas velocity at each point of a flame contour line was calculated by polynomial extrapolation. Among several polynomial curve fittings, the second-degree polynomial curve fitting was adopted by trial and error. Figure 4.27 shows three examples of extrapolating normal unburned gas velocity. In the figure, the x-axis represents the distance from each point of the flame contour line: the positive value means the location ahead of the flame front, that is, the unburned side, whereas the negative one stands for the burned area. The profiles of the normal unburned gas velocity in (B), (C), and (D) are similar to the one shown in Figure 4.11 in Sec. 4.1.2. The maximum unburned velocities appear ahead of the flame front, and then the velocity gradually decreases. The values that are calculated behind the flame front are not zero because the calculation was made through the cross correlation using the difference of intensity in the relevant interrogation windows: refer to Sec. 3.4.1 and 3.4.2. Since it is assumed in the present research that seeding particles are burned up by flame, the values behind the flame front were ignored.

Figure 4.28 shows an example of the calculation for normal unburned gas velocity. The fuel-air mixture was a stoichiometric methane-air mixture. The ignition timing was 27.6 º CA bTDC, and the initial pressure and temperature were 5 bar in absolute pressure and 439 K. The flame contour lines in Figure 4.28 (A) were obtained at 3.2, 3.6, and 4.0 ms after the ignition started. Figure 4.28 (B) shows the variation of the normal unburned gas velocity with respect to angle. (C) and (D) represent the local changes of the normal unburned gas velocity in the smooth curved and abrupt-curved part respectively.

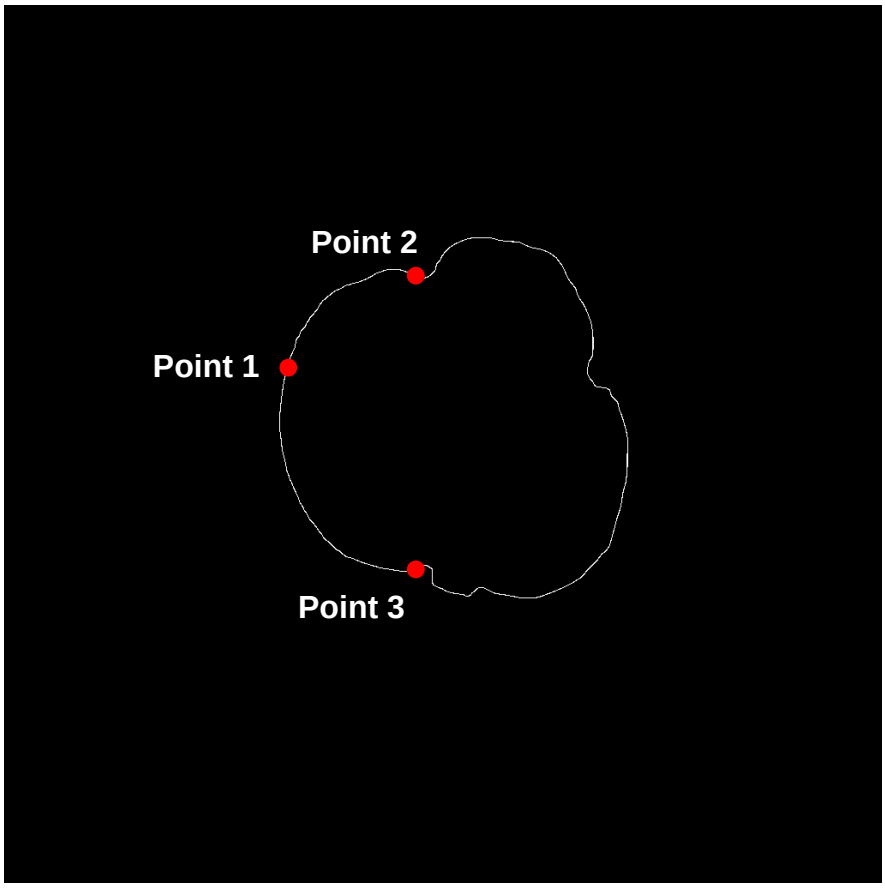
Point 2
Point 1
Point 3

(A)

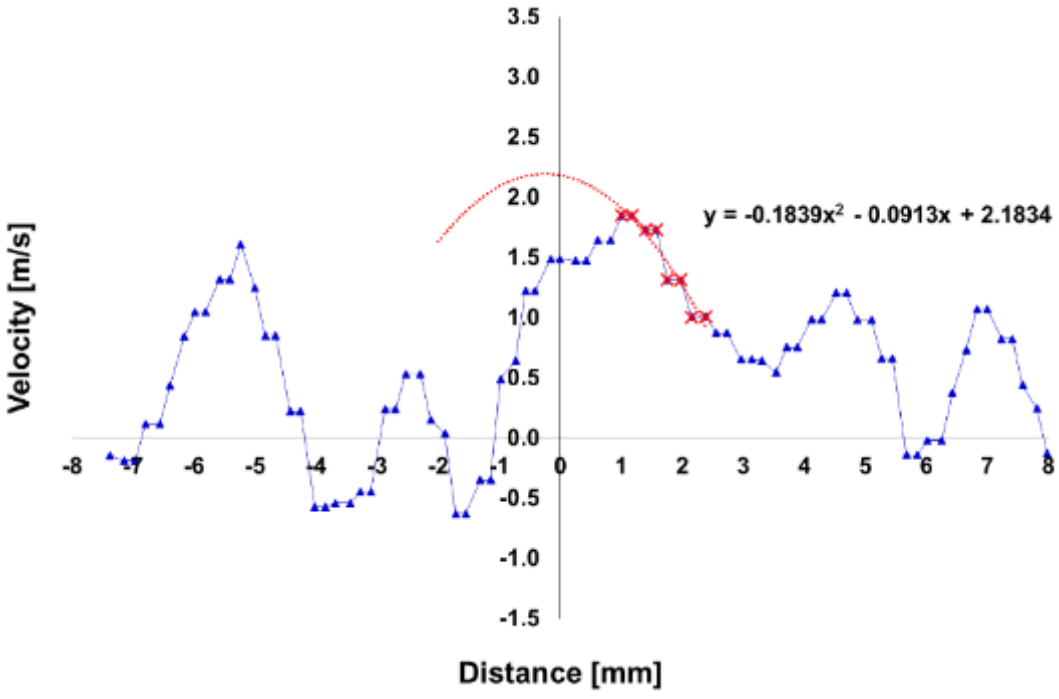
y = -0.1839x² - 0.0913x + 2.1834
Velocity [m/s]
Distance [mm]
3.5
3.0
2.5
2.0
1.5
1.0
0.5
0.0
-0.5
-1.0
-1.5
-8
-7
-6
-5
-4
-3
-2
-1
0
1
2
3
4
5
6
7
8

(B)

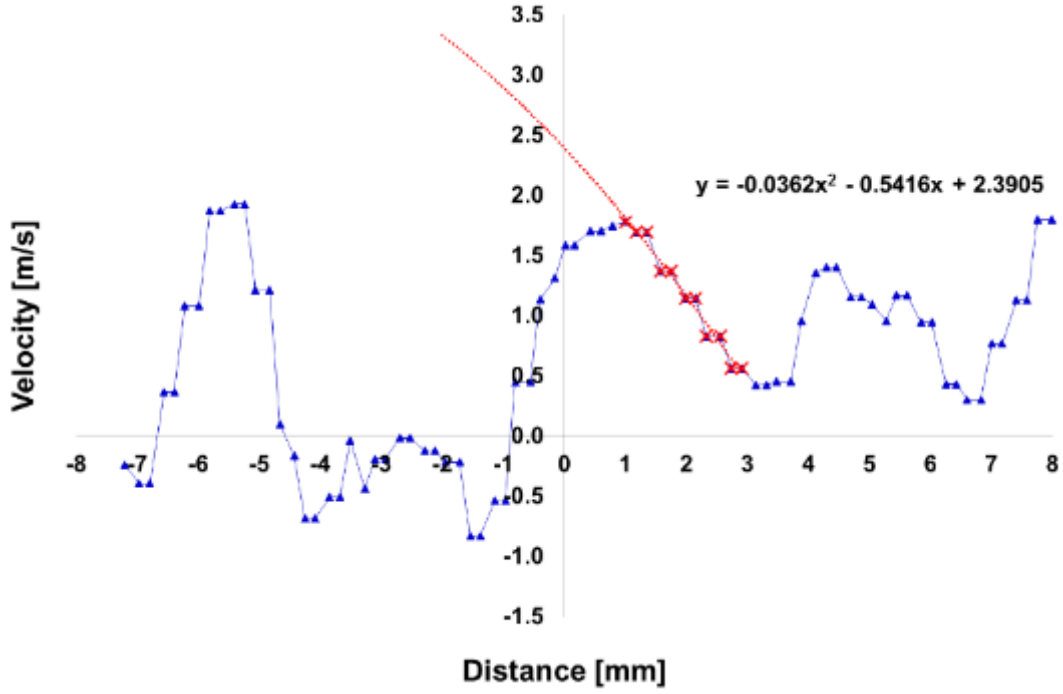

(C)

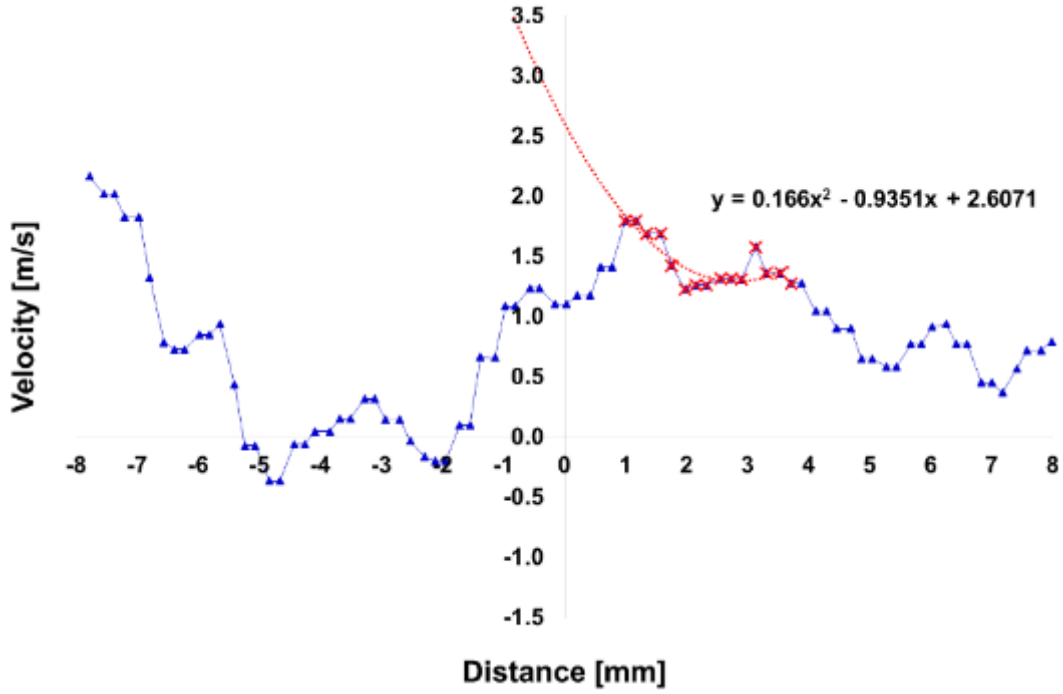

(D)

Figure 4.27 Examples of the extrapolation for the normal unburned gas velocity at each point of the flame contour line

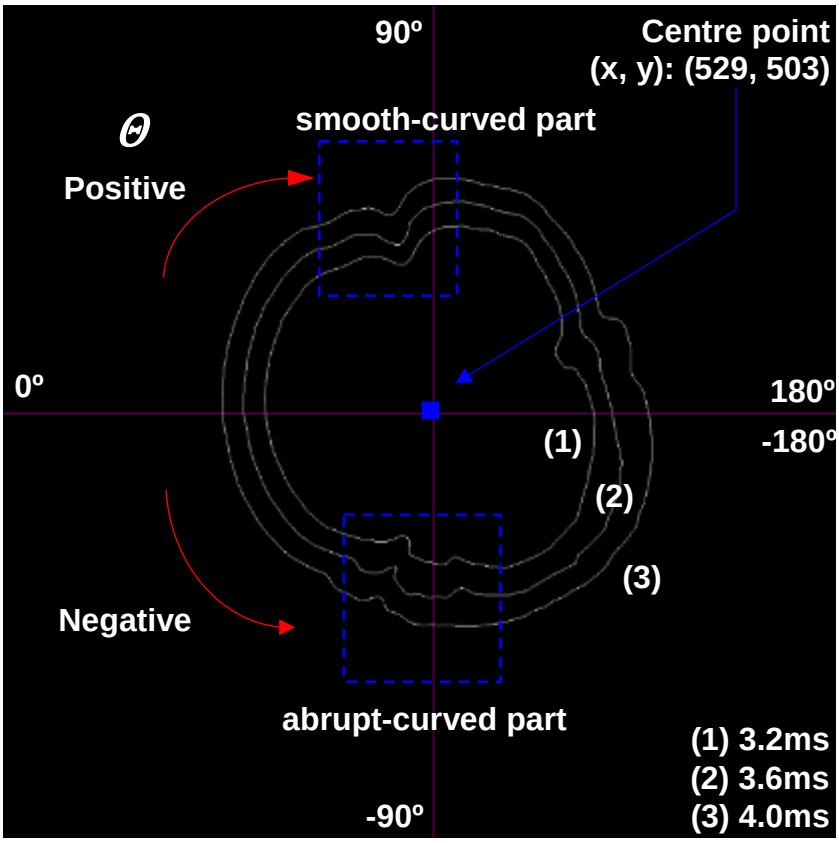
90º
Centre point
(x, y): (529, 503)
Θ
smooth-curved part
Positive
0º
180º
-180º
(1)
(2)
(3)
Negative
abrupt-curved part
(1) 3.2ms
(2) 3.6ms
(3) 4.0ms
-90º

(A)

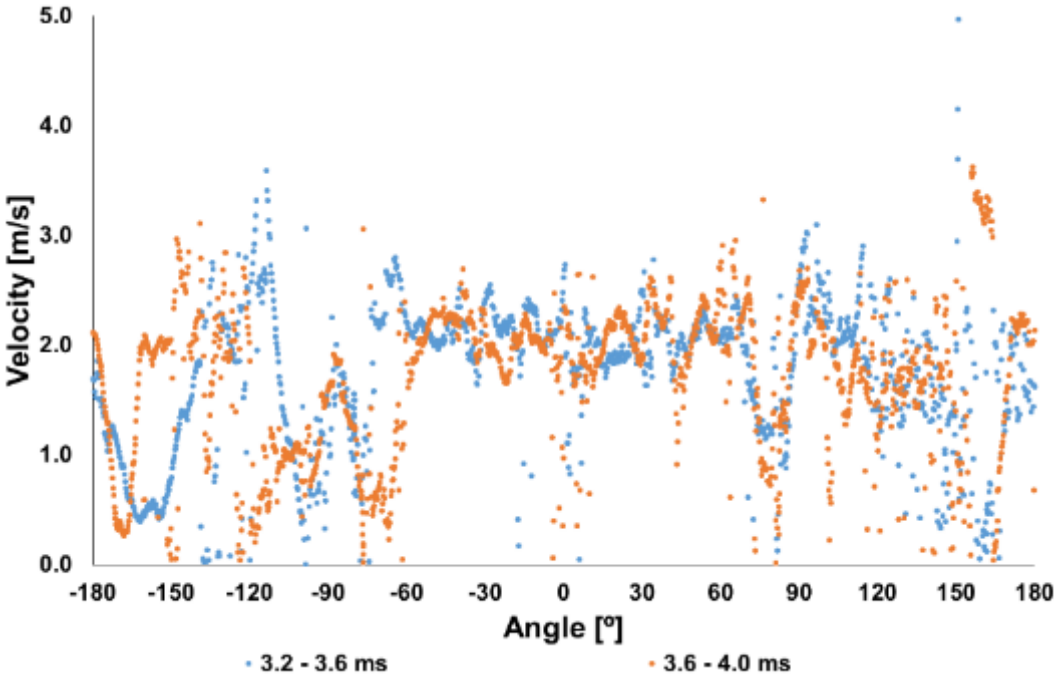
5.0
4.0
3.0
2.0
1.0
0.0
Velocity [m/s]
-180
-150
-120
-90
-60
-30
0
30
60
90
120
150
180
Angle [º]
3.2 - 3.6 ms
3.6 - 4.0 ms

(B)

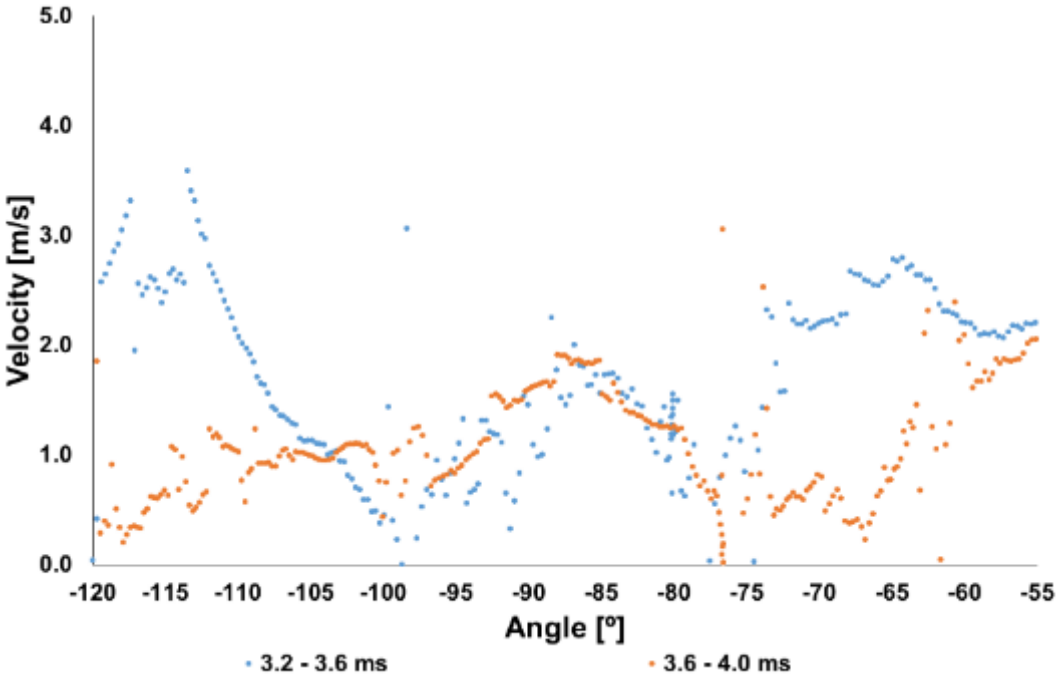

(C)

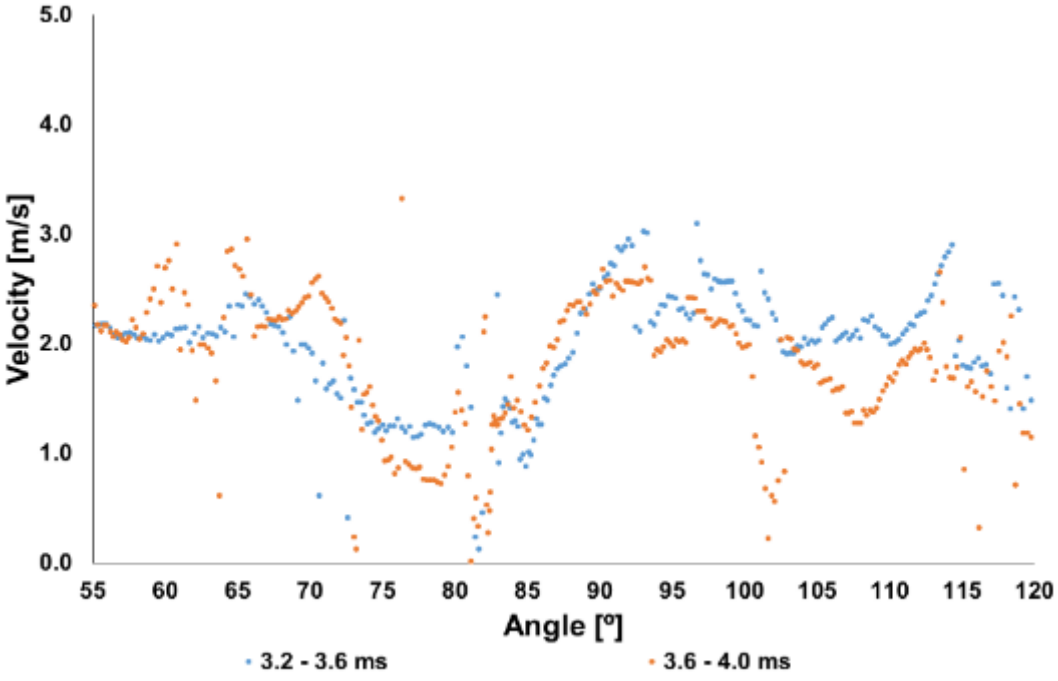

(D)

Figure 4.28 An example of the development of flame (A) and the change of the normal unburned gas velocity with respect to angle (B): (C) is the change of the velocity in the abrupt-curved part of (A), and (D) is the change of the velocity in the smooth-curved part

Using flame propagation speed and normal unburned gas velocity at each point of a flame contour line, burning velocity U can be calculated as follows:

$$U = S - V_n \qquad \textbf{Eq.}\ (4.22)$$

where S is flame propagation speed and V_n is normal unburned gas velocity.

Figure 4.29 shows the result of calculation of the burning velocity, and the experiment condition was the same as that of Figure 4.28

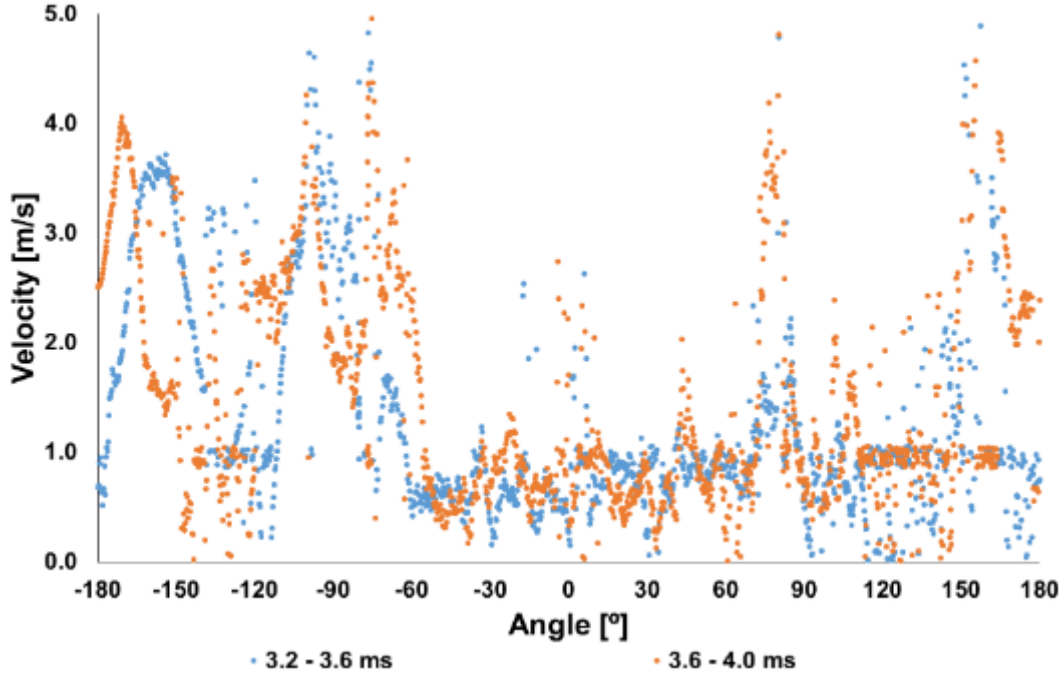

Figure 4.29 An example of the change of burning velocity with respect to angle

4.2.3 Measurement of vorticity in a local area

The calculation of vorticity of each flow field was made by Eq. (3.30) in Sec. 3.4.3 using the information on velocities in the horizontal and vertical directions. Figure 4.30 shows an example of a vorticity map. The flow field and vorticity map were obtained at 3.2 ms after the start of ignition, and ignition timing was 27.6 º CA bTDC. The fuel was a stoichiometric methane-air mixture.

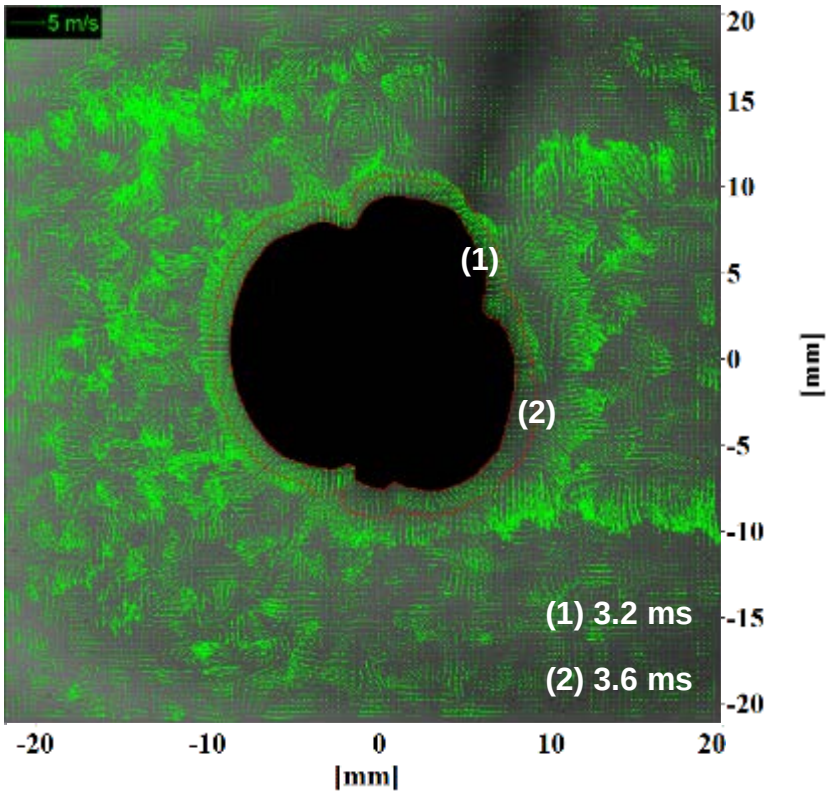

(A) Flow field

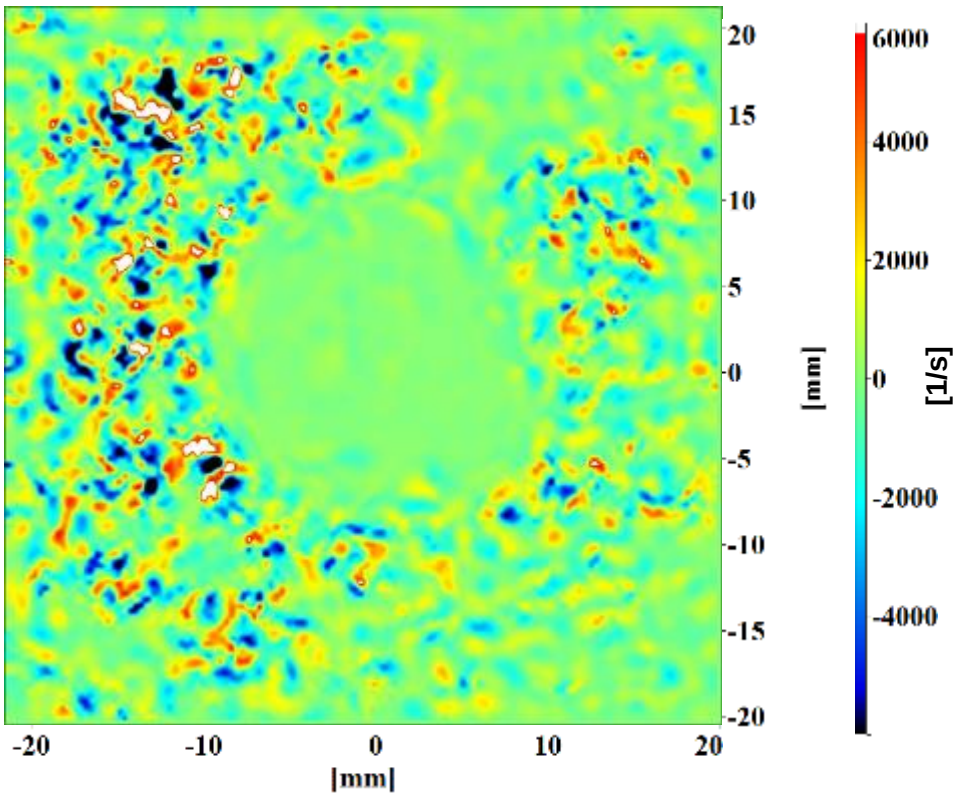

(B) Vorticity map

Figure 4.30 An example of a flow field (A) and its vorticity map (B)

When the combustion started, the initial pressure and temperature were 5 bar in absolute pressure and 439 K respectively. Although Figure 4.30 (B) shows the entire information on the corresponding flow field at the certain time when the combustion proceeds, the area that should be investigated in depth is the vicinity of a flame contour line. This is because the change of unburned gas velocity nearby a flame front is caused by the thermal expansion of the burned gas (Balusamy et al. 2011, Long and Hargrave 2011, Burluka 2015).

The effect of the thermal expansion on unburned gas velocities in the vicinity of a flame contour line is seen in Figure 4.30 (A): the enlarged images are shown in Figure 4.24 (B), (C), and (D). The unburned gas velocities that are away from a flame contour line shows the flows that do not seem relevant to the effect of thermal expansion, and their movements have a tendency to be random. The (1) and (2) red flame contour lines in Figure 4.30 (A) are for the flame images that were recorded at 3.2 and 3.6 ms respectively after the ignition started. When the flame proceeded from (1) to (2), the vorticity data in the area between two consecutive contour lines were collected in order to investigate the correlation between their change and the corresponding wavenumber. Figure 4.31 shows an example of the area between two consecutive flame contour lines and the histogram of the vorticity data collected in it. To examine vorticity data in a local area, a certain section was chosen. Figure 4.32 shows an example of the section where vorticity data are collected and their histogram.

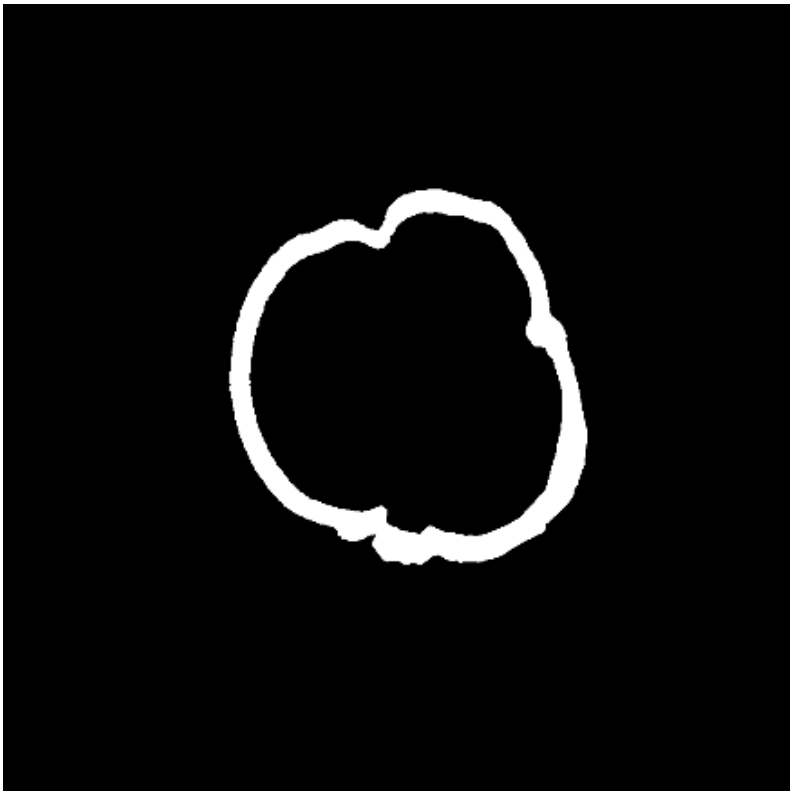

(A)

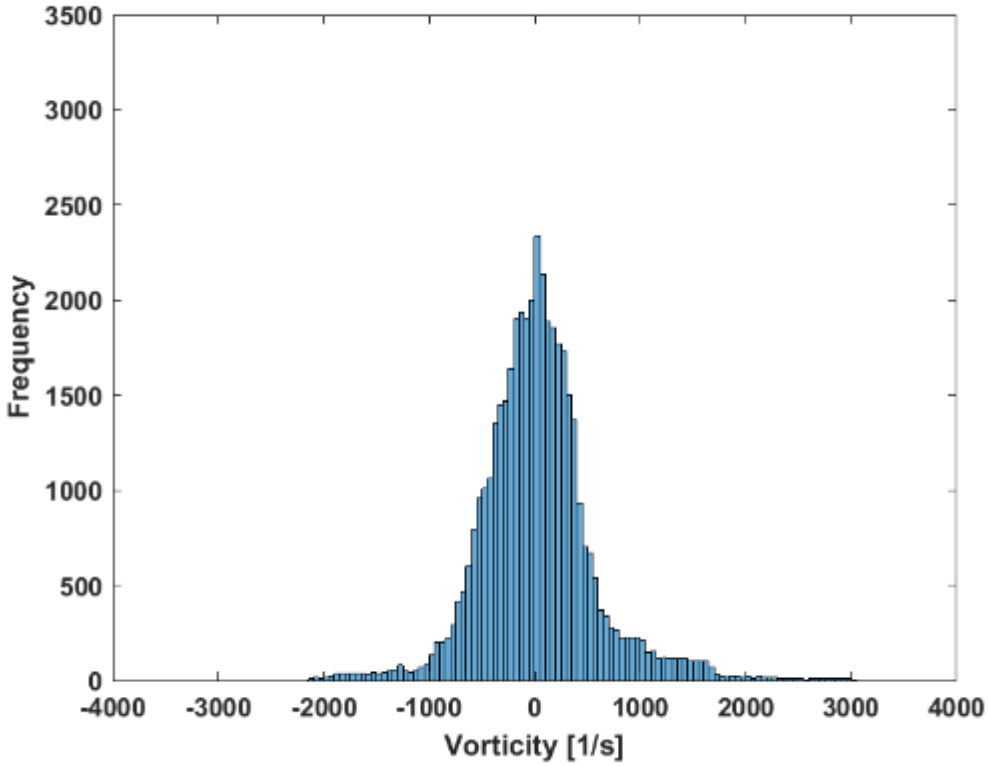

(B)

Figure 4.31 Area between two consecutive flame contour lines (A) and the histogram of the vorticity data collected in it (B)

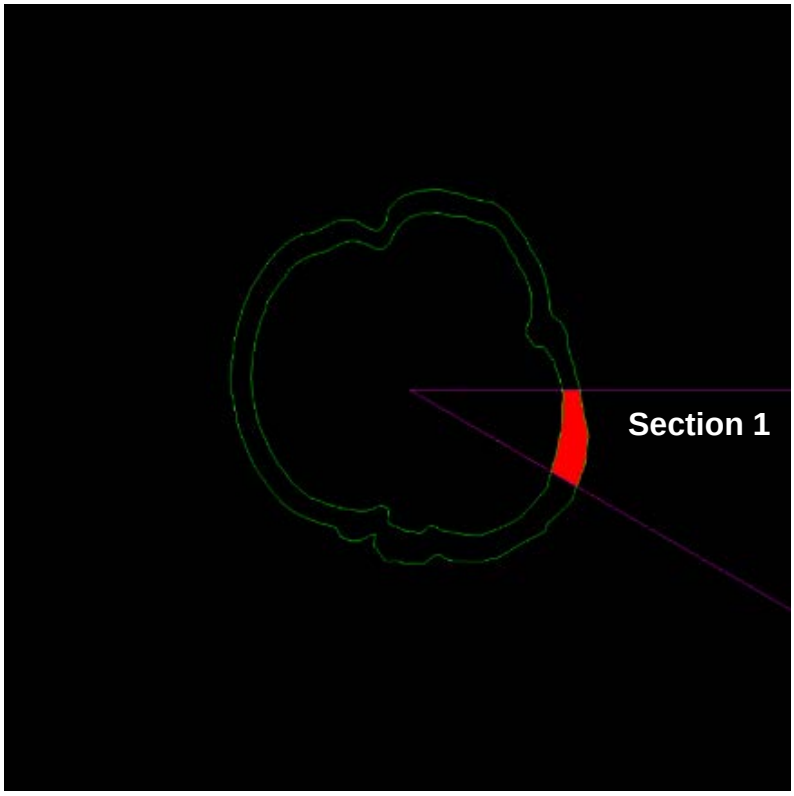

(A)

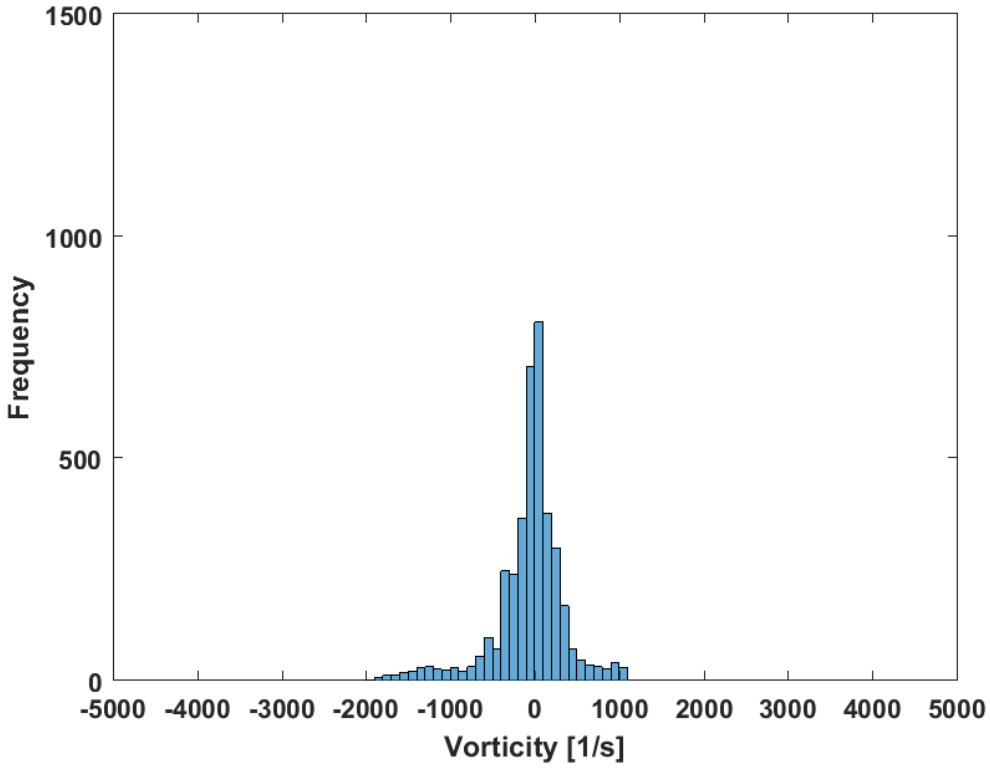

(B)

Figure 4.32 An example of the section where vorticity data are collected (A), and their histogram (B)

4.2.4 Measurement of mean flame propagation speed, flame acceleration, unburned gas velocity, and burning velocity

There are two methods for the calculation of mean flame propagation speed. The first is using the circle that has the identical area to the burned area of a flame image, which is shown in Figure 4.15 in Sec. 4.2.1. Mean radius r_m is measured by Eq. (4.15), and mean flame propagation speed $\bar{S_e}$ can be calculated by the following equation:

$$\bar{S_e} = \frac{dr_m}{dt} \qquad \textbf{Eq.} (4.23)$$

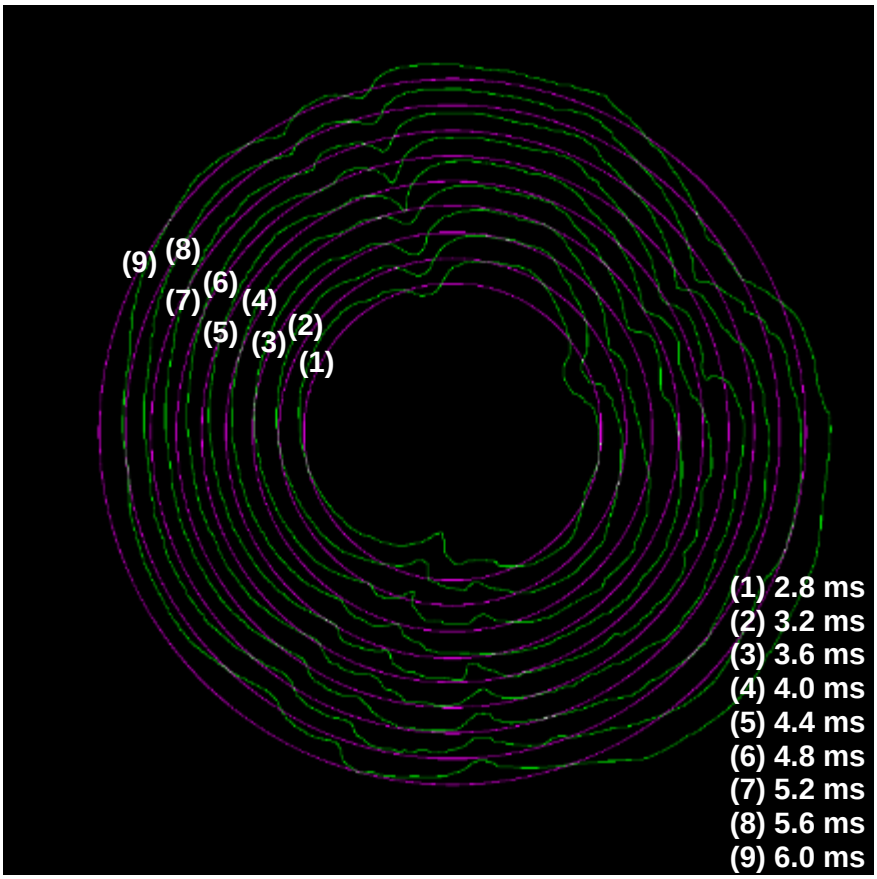

Figure 4.33 An example of flame contour lines (green lines) and the corresponding circles (magenta lines)

Figure 4.33 shows an example of the flame contour lines and the corresponding circles that are used to calculate the mean flame propagation speed $\bar{S_e}$. The green lines indicate flame contour lines, and the magenta lines represent the circles that have the identical areas to the burned areas of the

corresponding flame contour lines. The fuel was a stoichiometric methane-air mixture, and the ignition timing was 27.6 º CA bTDC. The initial pressure and temperature at the start of combustion were 5 bar in absolute pressure and 439 K. The time step between two consecutive flame contour lines was 0.4 ms, and the time when each flame image was obtained is seen in the figure.

The other calculation for mean flame propagation speed is using each flame propagation speed at a point along the flame contour line. That is, after summing the whole values of flame propagation speeds at the entire points consisting of the corresponding flame contour line, the total value is divided by the number of the points. Using the mean flame propagation speed, flame acceleration is calculated. The relevant equations are as follows:

$$\bar{S} = \frac{1}{n}\sum_{k=1}^{n} S_k \qquad \textbf{Eq.}\ (4.24)$$

$$A = \frac{d\bar{S}(t)}{dt} \qquad \textbf{Eq.}\ (4.25)$$

where mean flame propagation speed is $\bar{S}$, n the number of the whole points consisting of a flame contour line, *k* the index of the point, S_k an arbitrary flame propagation speed at the corresponding point, *A* flame acceleration, *t* time.

In relation to mean flame propagation speeds, $\overline{S_e}$ and $\bar{S}$, there is a slight difference. Figure 4.34 shows the result of the comparison. There may be several causes that make the difference. One of the causes can be the direction where flame at each point propagates. As mentioned in Sec. 4.2.1, the direction of flame propagation at each point is perpendicular to it. As seen in Figure 4.35 (A), when the shape of a flame contour line becomes convex or concave, the displacement changes. The variation of displacement along a flame contour line leads to the change of flame propagation speed, and eventually has an influence on the calculation of mean flame propagation speed $\overline{S_n}$. The second cause is the limitation of image resolution. Figure 4.36 shows the change of flame propagation speed of the corresponding circles, which are the part of the entire circles shown in Figure 4.33. Theoretically, although the flame propagation speed in each circle does not change with respect to angle, it varies. This is caused by image resolution, and the range

is about ± 10 cm/s. The resolution of a flame image that was taken in the present research is 1024 x 1024 pixels.

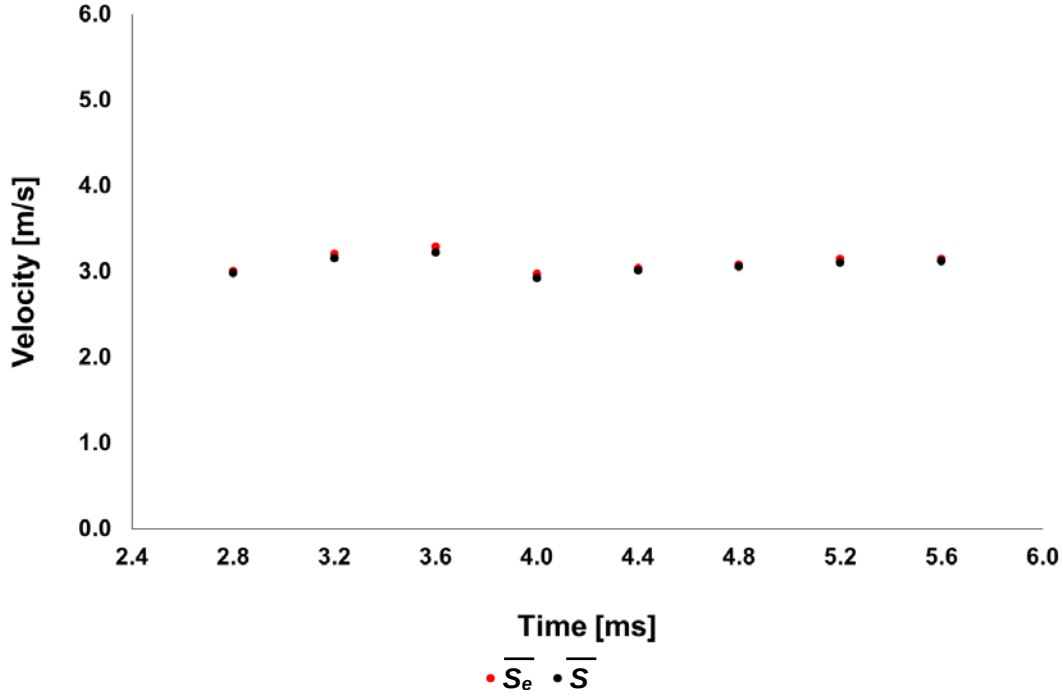

Figure 4.34 Comparison of the two mean flame propagation speeds

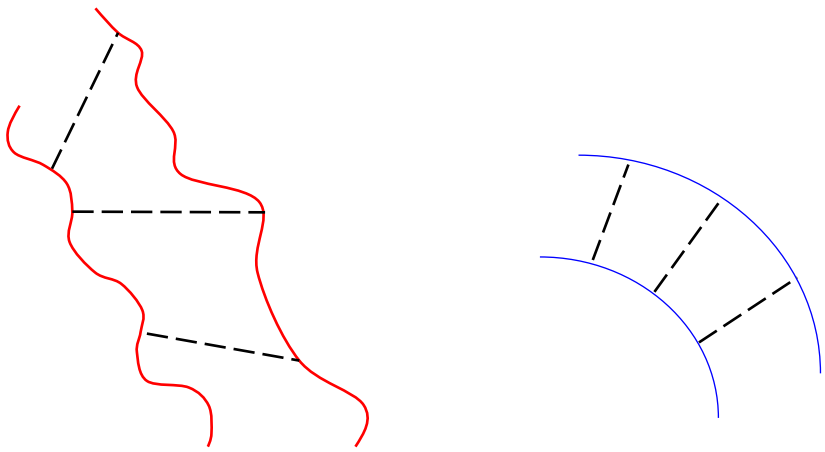

Figure 4.35 A simple sketch for the comparison of the difference between the displacements of the flame contour line (A) and those of circle line (B) having the identical area to the burned area of the flame image

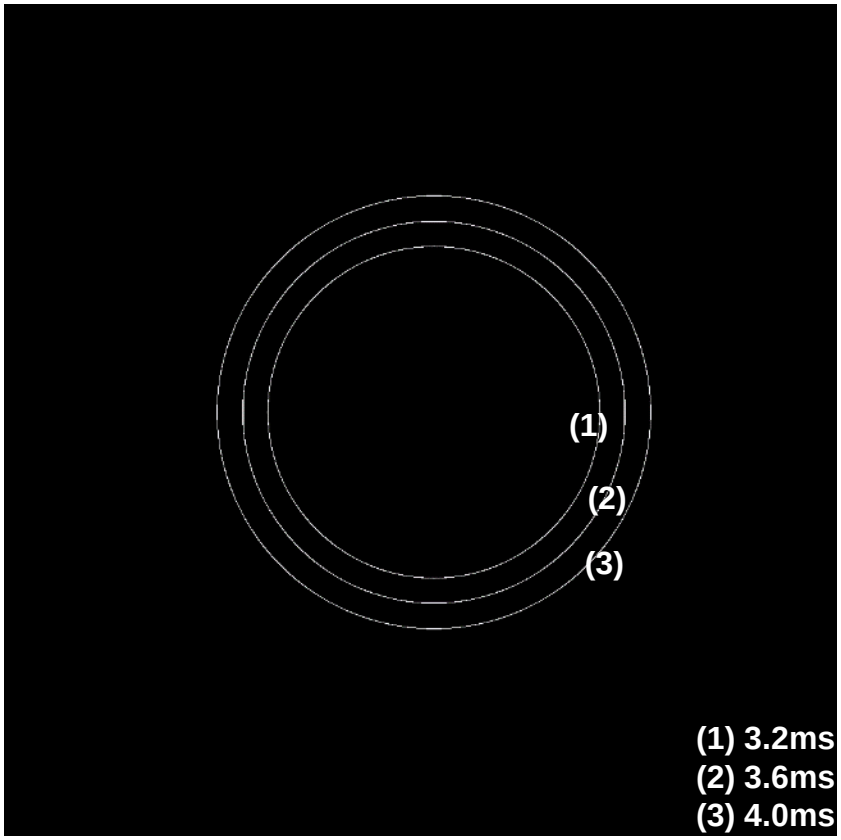

(A)

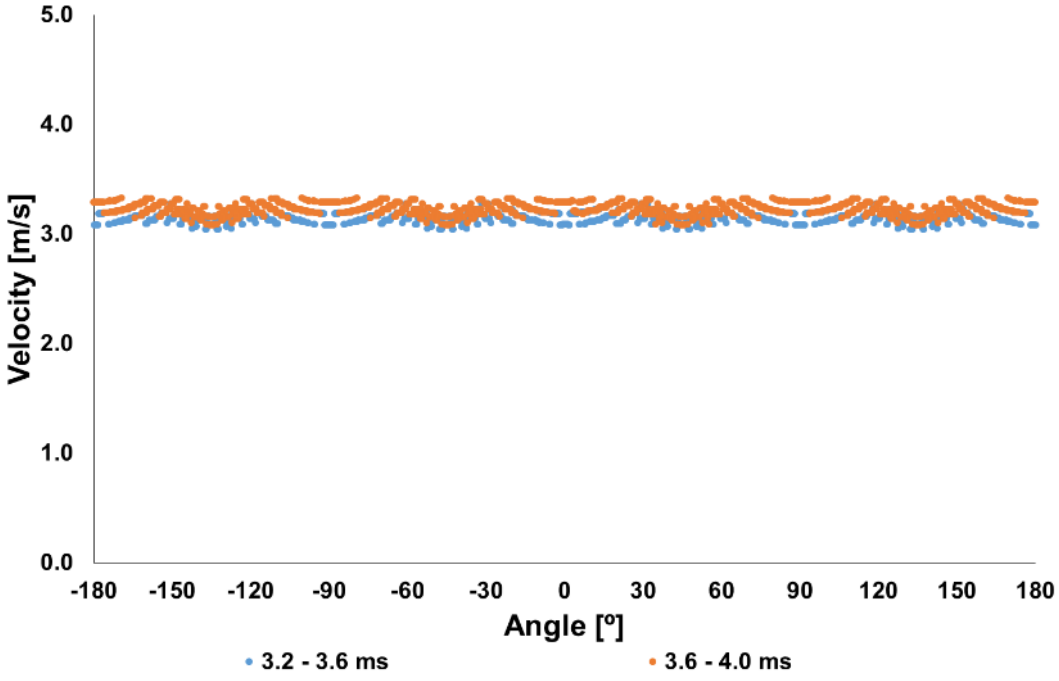

(B)

Figure 4.36 The changes of the flame propagation speed (B) for the corresponding circles (A) with respect to angle

Because of these causes, a difference between two mean flame propagation speeds occurs. However, the difference is 5 cm/s and not large compared with the mean flame propagation speed, which is about 3 m/s. Hence, mean flame propagation speed $\bar{S}$ calculated through Eq. (4.24) was used in this paper.

Mean normal unburned gas velocity $\bar{V}_n$ and burning velocity $\bar{U}$ are also calculated just as $\bar{S}$. The relevant equations are as follows:

$$\bar{V}_n = \frac{1}{n}\sum_{k=1}^{n} V_{n_k} \qquad \textbf{Eq.} (4.26)$$

$$\bar{U} = \frac{1}{n}\sum_{k=1}^{n} U_k \qquad \textbf{Eq.} (4.27)$$

where n is the number of the whole points consisting of a flame contour line, k is the index of a point, V_{n_k} and U_k represent an arbitrary normal unburned gas velocity and burning velocity at a point respectively. Figure 4.37 shows an example of changes of $\bar{S}$, $\bar{V}_n$, and $\bar{U}$ with respect to time that were calculated through Eq. (4.24) to Eq. (4.27).

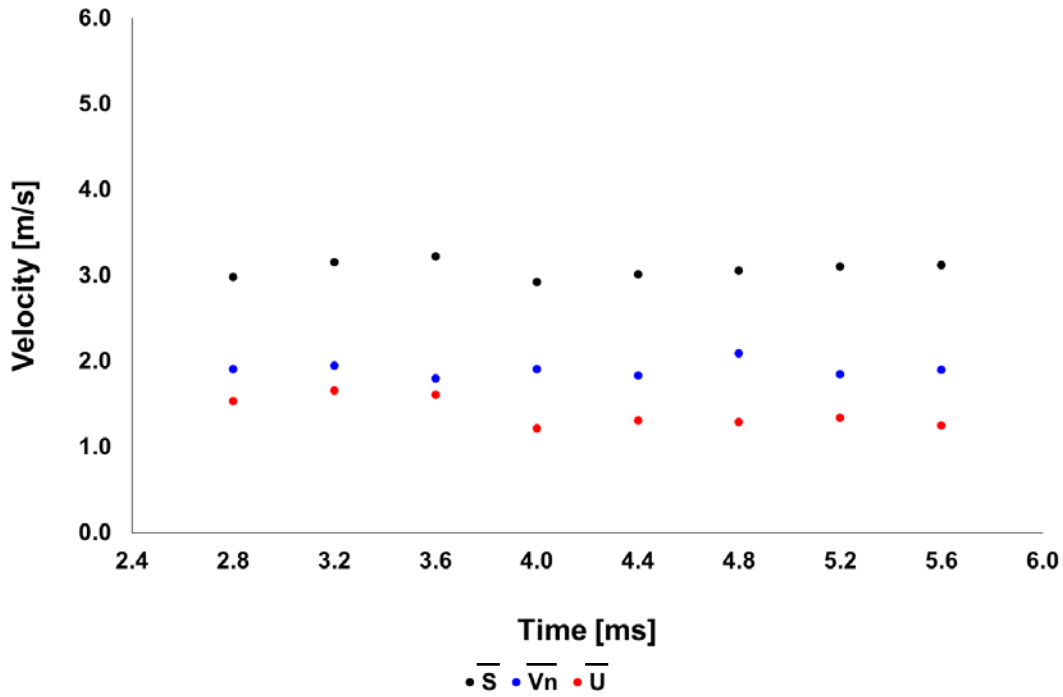

Figure 4.37 An example of changes of the flame propagation speed, normal unburned gas velocity, and burning velocity with respect to time

Chapter 5 Result and discussion

In this chapter, the results of the current research are discussed and analysed. The experimental condition is first described, and then the results of the experiment are presented. When discussing and analysing a flame edges image, three sections are chosen. The first section is a convex part, the second a concave part, and the third a smoothly-cured part. In each section, the results of measurements mentioned in Sec. 4.2 are presented and analysed.

5.1 Engine operating condition

In order to minimize the effect of turbulence inside the cylinder, the research engine was operated at 50 rpm. Through the measurement of mean unburned gas velocity shown in 3.4.3 and the relevant researches (Hussin 2012, Ling 2014, Chen 2016), it was assumed that the experimental condition was laminar. Assuming that the compression stroke of the research engine was an isentropic process, the initial pressure and temperature at the start of ignition were measured, and they were 4 bar in absolute pressure and 414 K respectively. The fuel mixtures that were adopted in the current work were three gaseous fuels: a hydrogen-, methane-, and propane-air mixture. In order to investigate cellular flame under a laminar condition, the hydrogen- and methane-air mixture were lean, and the propane-air mixture was rich: they were close to their flammability. Table 5.1 shows the experimental condition of the current work.

Table 5.1 Experimental condition

Experimental Case	Fuel	Φ	t_{ign} [ºCA bTDC]	P_0 [abs. bar]	T_0 [K]
1	H_2	0.4	36.2	4	414
2	CH_4	0.6	36.2	4	414
3	C_3H_8	2.0	36.2	4	414

ϕ: Equivalence ratio / t_{ign}: ignition timing / P_0: the initial pressure at the start of ignition / T_0: the initial temperature at the start of ignition

5.2 Result of the lean hydrogen-air mixture

The first experimental case is a lean hydrogen-air mixture case. The composition of the mixture was 0.4, and the ignition timing t_{ign} was 36.2 º CA bTDC. The inter-frame time between double frames to obtain the flow field of unburned gas velocity was 0.1 ms, and the time step between two consecutive flame images to measure flame propagation speed was 1.6 ms. When the ignition started, the initial pressure P_0 and temperature T_0 were 4 bar and 414 K respectively.

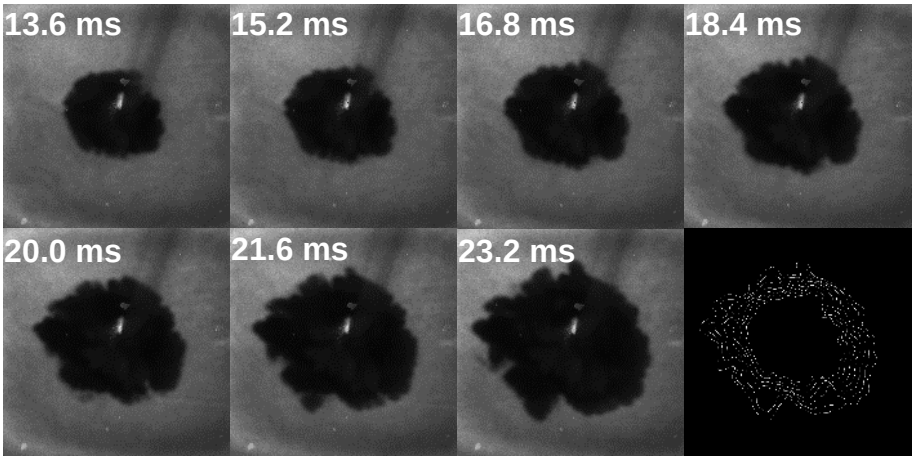

Figure 5.1 Propagating flame images and the corresponding edges image at the experimental case 1. Fuel: H_2-air, ϕ: 0.4, t_{ign}: 36.2° CA bTDC, P_0: 4 bar, T_0: 414 K

Figure 5.1 shows the developing flame images with respect to time and the relevant flame edges image. In the flame images, the white digits represent elapsing time after ignition. The black area in each flame image indicates burned area, the relatively bright grey area represents unburned area, and the white part near the centre is a spark plug.

As the flame develops, it gradually becomes wrinkled and unstable. Especially, until 16.8 ms, the flame is relatively stable and smooth. When the elapsing time is 18.4 ms, the flame starts becoming unstable. While the flame propagates outwardly, some parts become convex or concave toward the unburned side, and the other part has a relatively smooth-curved surface. At a convex, concave, and smoothly-curved part, the characteristics of combustion such as the variation of flame propagation speed were investigated.

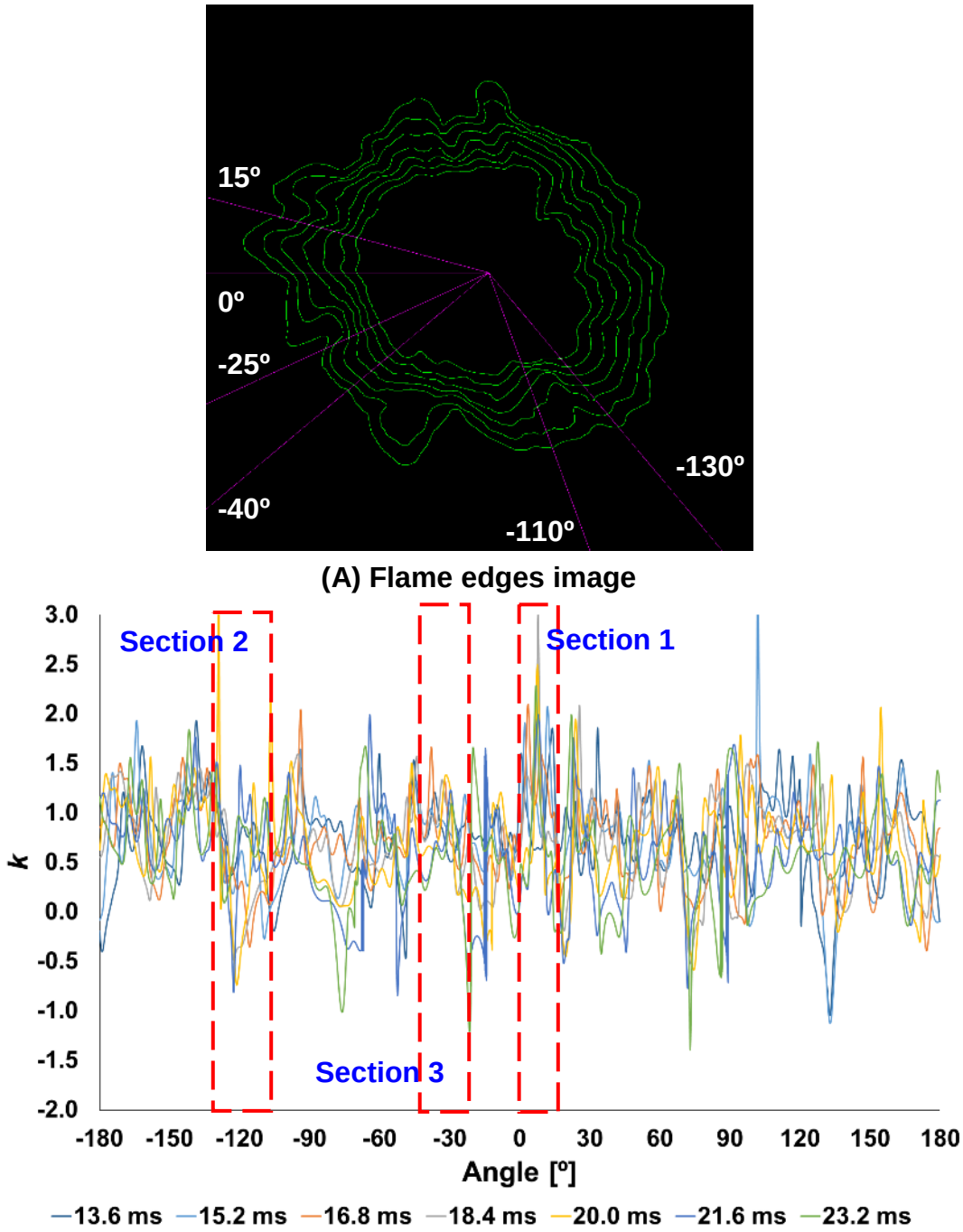

Figure 5.2 Selection of the local areas through the flame edges image (A) and the change of the relevant wavenumber *k* (B)

A distinguishably convex, concave, and smooth-curved part were selected, referring to the flame edges image and the variation of the corresponding wavenumbers. Figure 5.2 shows the selected parts: the section 1, 2, and 3 indicate a convex, concave, and smooth-curved part respectively. Figure 5.2

(A) shows a flame edges image, and the green lines represent flame contour lines as the flame propagates. Figure 5.2 (B) represents the change of wavenumber with respect to angle as the flame develops. In the case of the section 1, wavenumber mostly ranges between 0.7 and 2.0. The range of wavenumber in the section 2 is approximately between -0.5 and 0.5. The wavenumber of the section 3 varies from 0.7 to 1.3 along the selected flame contour line.

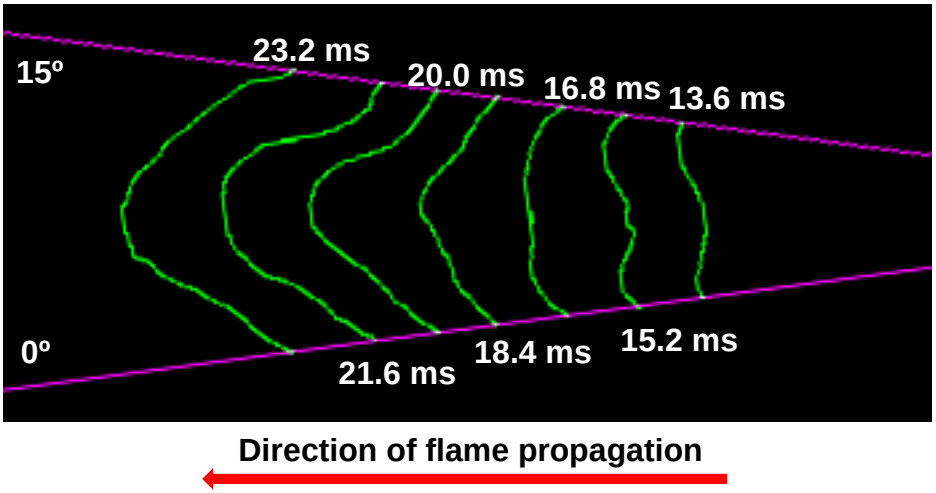

Figure 5.3 The enlarged section 1 image

Figure 5.3 shows the enlarged image of the section 1. The shape of the flame contour line gradually changes as the flame develops. At the region where the angle ranges from 5 to 10º, the flame changes from a concave to convex shape, whereas the diametrically opposed change of the flame shape is seen at the regions in the vicinity of 0 or 15º.

Figure 5.4 represents the change of flame propagation speed and wavenumber with respect to angle in the section 1. In the figure, the black and yellow dots indicate flame propagation speed *S* and wavenumber *k* at each angle respectively. Let's focus on the region ranging from 5 to 10º where the flame changes from a concave to convex shape.

When time is 13.6 ms, wavenumber *k* is about 0.5, and flame propagation speed is about 0.7 m/s. At 15.2 ms, the change of wavenumber with respect to angle is almost similar to the one at 13.6 ms. However, the flame propagation speed starts rising slightly compared with the one at 13.6 ms. The increase of flame propagation speed is kept at 16.8 ms, and the wavenumber also begins increasing at the same time.

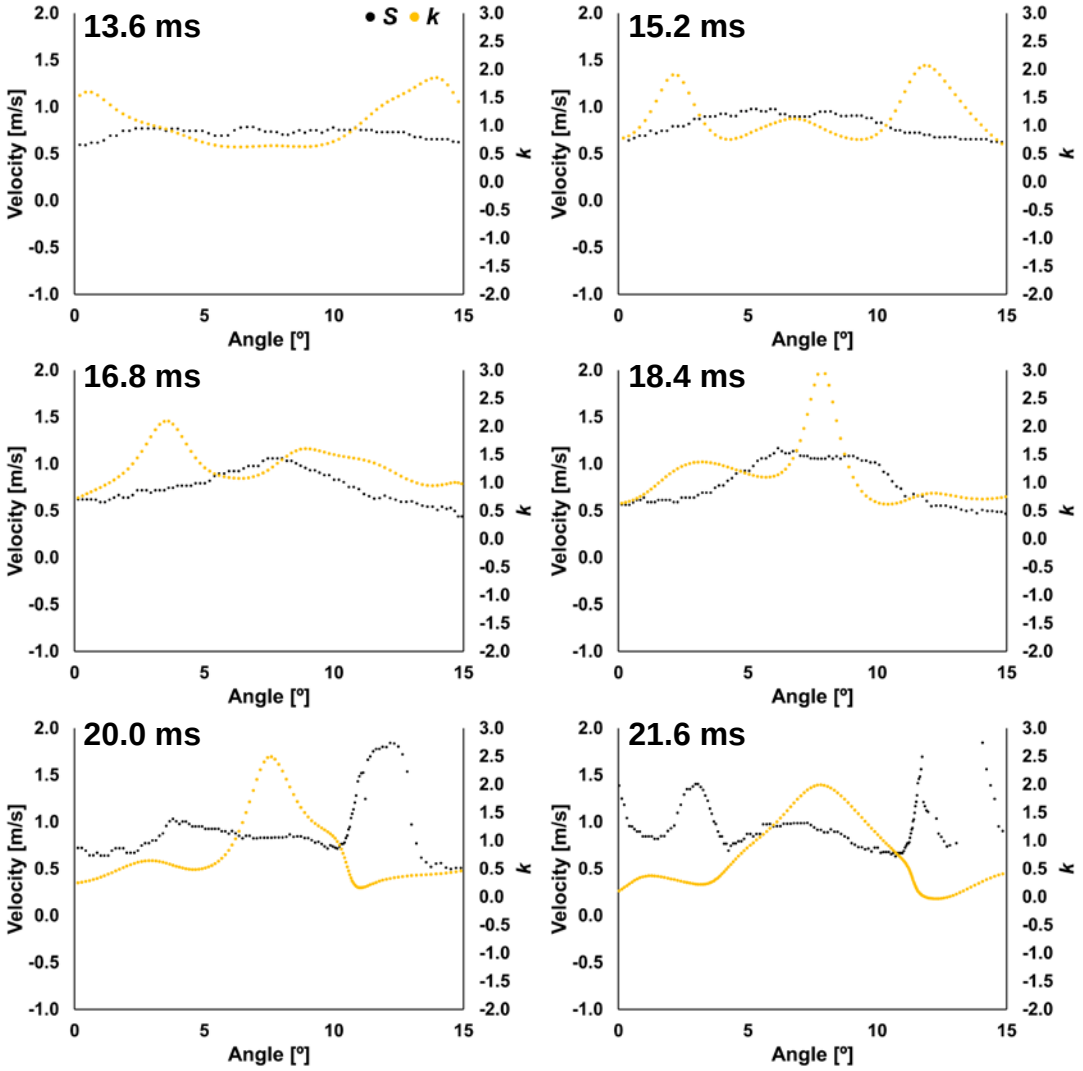

Figure 5.4 Change of flame propagation speed *S* (black dot) and wavenumber *k* (yellow dot) with respect to angle in the section 1 of the experimental case 1. Fuel: H_2-air, ϕ: 0.4, t_{ign}: 36.2° CA bTDC, P_0: 4 bar, T_0: 414 K

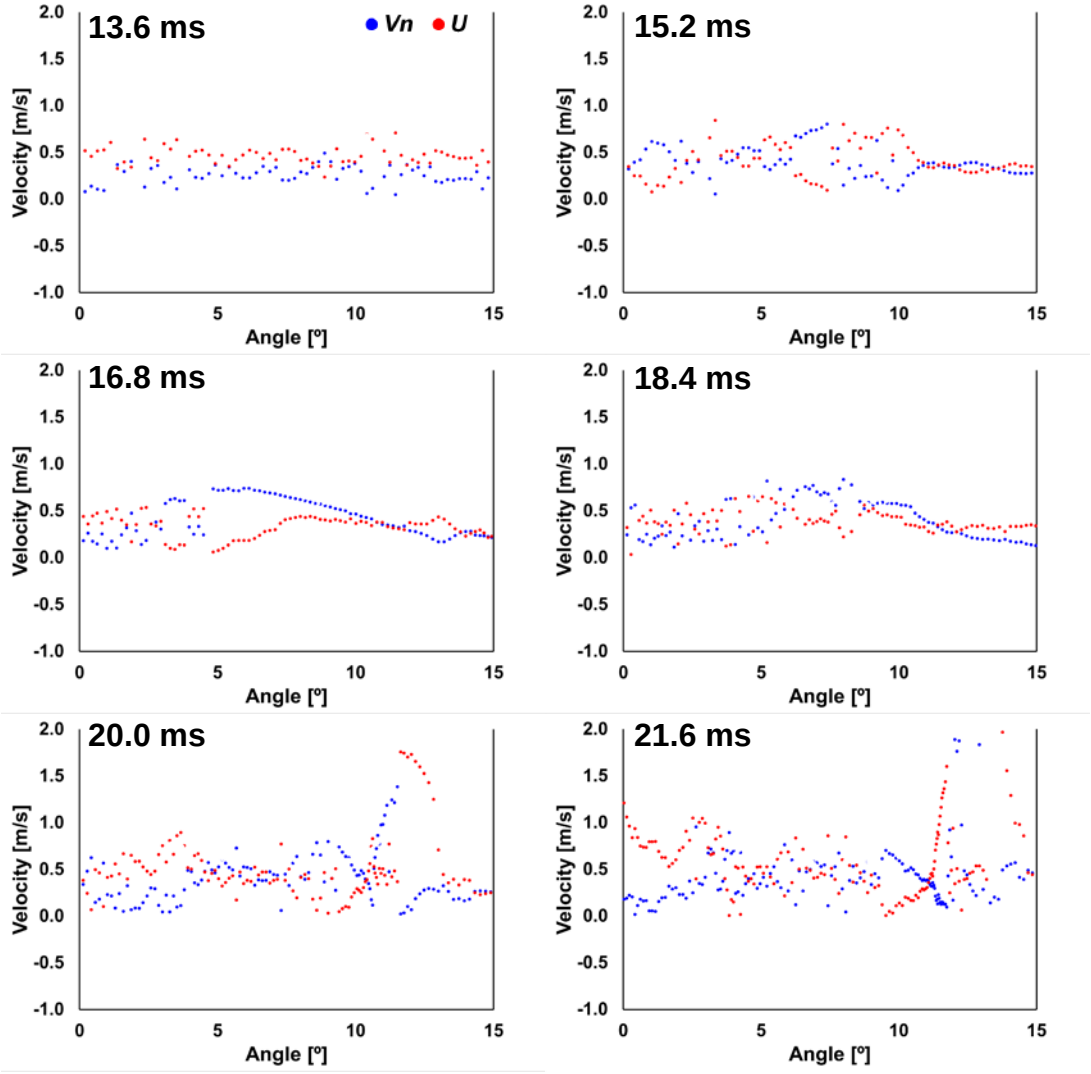

Figure 5.5 Change of normal unburned gas velocity V_n (blue dot) and burning velocity U (red dot) with respect to angle in the section 1 of the experimental case 1. Fuel: H_2-air, ϕ: 0.4, t_{ign}: 36.2° CA bTDC, P_0: 4 bar, T_0: 414 K

At 18.4 ms, wavenumber increases much, and the local maximum value is about 2.5. At this moment, a rise in flame propagation speed stops. When time is 20.0 ms, the increase of wavenumber is kept, and flame propagation speed rather decreases. At 21.6 ms, wavenumber decreases to 2.0, and flame propagation speed slightly increases, which is about 1.1 m/s. It seems that the relationship between wavenumber and flame propagation speed is inversely proportional.

Figure 5.5 shows the change of normal unburned gas velocity and burning velocity with respect to angle in the section 1. The blue and red dots in the figure represent normal unburned gas velocity V_n and burning velocity U at

each angle respectively. Let's concentrating on the region from 5 to 10º where the flame shape changes from a concave to convex shape toward the unburned area.

When time is 13.6 ms, V_n and U are about 0.1 and 0.4 m/s respectively, and the two velocities do not vary much with respect to angle. At 15.2 ms, there is an increase in V_n in the vicinity of 5º, whereas U diminishes. V_n near 10º decreases, and U increases up to 0.5 m/s. When time is 16.8 ms, the changes of V_n and U with respect to angle are similar to the ones at 15.2 ms, but V_n gradually diminishes as the angle changes from 5 to 10º, whereas U rises.

At 18.4 ms, the changes of V_n and U with respect to angle are not much. When time is 20.0 ms, the two velocities generally decreases compared to the ones at 18.4 ms. At the same time, V_n and U change with respect to angle. The values of V_n near 5º are relatively less than the ones in the vicinity of 10º. In contrast, U gradually decreases as the angle changes from 5 to 10º. At 21.6 ms, there are a few increases in the two velocities, and their changes between 5 and 10º are irregular again.

The description of the region between 5 and 10º in Figure 5.4 and Figure 5.5 can be summarized as follows. While time elapses from 13.6 to 16.8 ms, the flame propagation speed gradually increase until the wavenumber approaches one. During the time, the initially stable normal unburned gas velocity and burning velocity become fluctuated, and it is shown that the two velocities at a certain region have relatively larger or smaller than the ones at the other region. When the increase of flame propagation speed stops and the wavenumber has the maximum value at 18.4 ms, the change of normal unburned gas velocity and burning velocity with respect to angle diminishes, and seems stable again. When flame propagation speed decreases and the wavenumber still has the similarly high value which is larger than 1.0, normal unburned gas velocity and burning velocity become fluctuated again, and each velocity has a higher value at a certain region than at the other region.

While the flame propagation speed between 5 and 10º increases from 13.6 to 16.8 ms, the effect of thermal expansion caused by the burned gas should be considered. As mentioned in Sec. 4.2.2, flame propagation speed S consists of the burning velocity U and normal unburned gas velocity V_n which is affected by the thermal expansion of burned gas (Balusamy et al. 2011, Long and Hargrave 2011, Burluka 2015). The flame shape in the region at 13.6 ms is concave, and the unburned gas in front of the flame front may converge more easily than the one at the convex region as the thermal expansion of the

burned gas compresses the unburned gas. Additionally, since flame is a concave shape, additional heat and free radicals can be provided and converged (Hertzberg 1989).

At the same time, since the composition of the hydrogen-air mixture in this experimental case is lean, the preferential diffusion of the hydrogen occurs (Hertzberg 1989, Lipatnikov 2012). Hence, the hydrogen diffusional flow converges at the concave region. The preferential diffusion of the hydrogen makes the local composition become stoichiometric, and the shift of the mixture composition leads to the change of burning velocity: refer to the red-dashed box of Figure 2.11 (A). However, it should be noted that the burning velocity near 10º is larger than the one near 5º when time is 15.2 and 16.8 ms. This means that the composition of the hydrogen-air mixture near 10º becomes relatively rich and the composition near 5º becomes lean. Because of the effect of thermal expansion and the preferential diffusion of the hydrogen, the normal unburned gas velocity and the burning velocity vary as the angle change from 5 to 10º at 15.2 and 16.8 ms in Figure 5.5.

In the regions where the angle is 0-5º and 10-15º, the opposite phenomenon is observed. While time elapses from 13.6 to 16.8 ms, wavenumber changes from 0.7 to 2.0, and flame propagation speed in the regions gradually decreases and is slower than the one between 5 and 10º. During the time, the flame shape is convex toward the unburned gas. At the convex region, the effect of the thermal expansion of the burned gas on the unburned gas is reduced, and heat and free radicals are also dispersed (Hertzberg 1989). Additionally, the preferential diffusion of the hydrogen into the flame front is divergent, and as a result, the composition of the mixture at the convex region becomes leaner.

Figure 5.6 represents the relationship between the flame propagation speed and the wavenumber in the section 1. Flame propagation speed increases precipitously as wavenumber approaches zero. A rapid increase in the flame propagation speed seems to start when the wavenumber is about 0.5. And flame propagation speed gradually decreases as the wavenumber is larger than 0.5. Especially, when the wavenumber ranges from 0.6 to 1.5, the value of the flame propagation speed seems very stable. Although flame propagation speed continues to decreases when the wavenumber is larger than 1.5, the reduction is relatively very small.

Figure 5.7 shows the variation of the local mean flame propagation speed, normal unburned gas velocity, burning velocity, and acceleration with respect

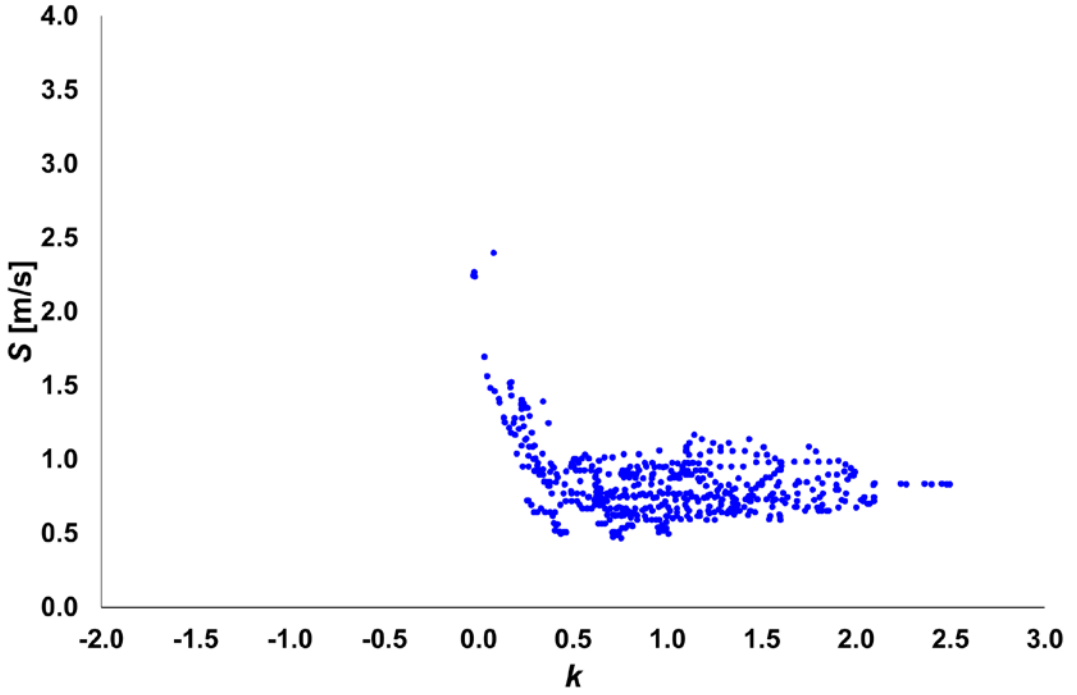

Figure 5.6 Variation of flame propagation speed *S* with respect to wavenumber *k* in the section 1 of the experimental case 1. Fuel: H_2-air / ϕ: 0.4 / t_{ign}: 36.2° CA bTDC / P_0: 4 bar / T_0: 414 K

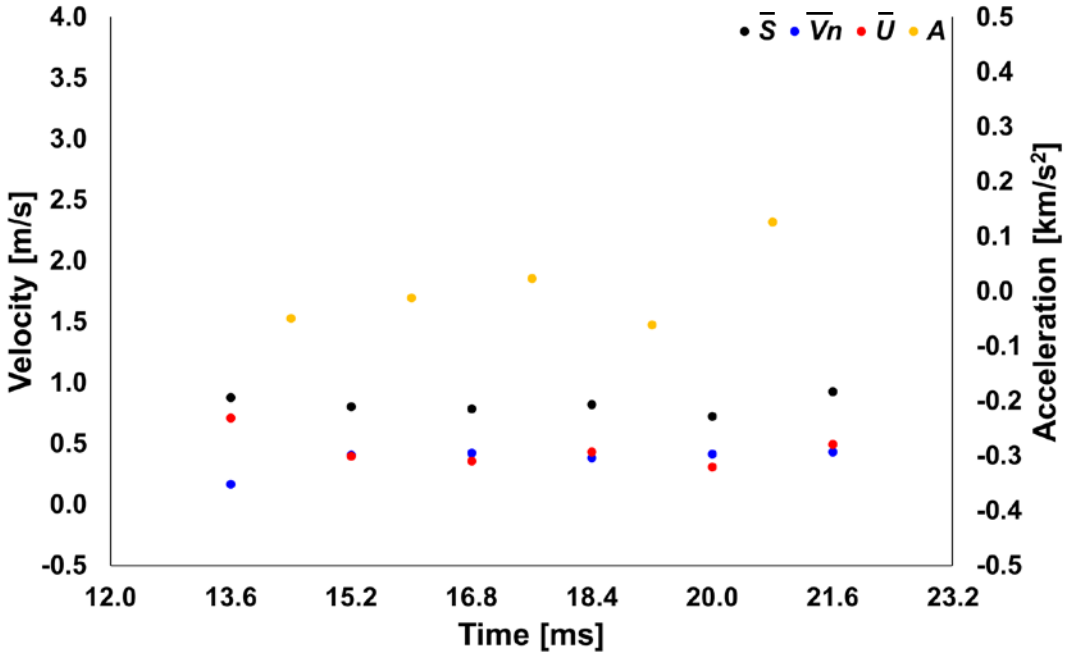

Figure 5.7 Variation of local mean flame propagation speed $\overline{S}$ (black dot), normal unburned gas velocity $\overline{V_n}$ (blue dot), burning velocity $\overline{U}$ (red dot), and acceleration *A* (yellow dot) with respect to time in the section 1 of the experimental case 1. Fuel: H_2-air / ϕ: 0.4 / t_{ign}: 36.2° CA bTDC / P_0: 4 bar / T_0: 414 K

to time in the section 1. While the flame propagates, local mean flame propagation speed $\bar{S}$ has the stable value, which is about 0.9 m/s. During the development of the flame, although local mean normal unburned gas velocity $\bar{V}_n$ and burning velocity $\bar{U}$ change with respect to time, their changes also are not much. Through the explanation about Figure 5.4, it is confirmed that the flame propagation speed near the region where the angle ranges from 5 to 10º generally increase with respect to time. However, as the flame propagates, the change of flame propagation speed near the other region is opposite. While the flame propagation speed between 5 and 10º gradually increase, the speed near the other region decrease simultaneously. The change of flame propagation speed with respect to angle is not reflected in the local mean flame propagation speed, which is also shown in the local mean normal unburned gas velocity and burning velocity. Therefore, it is necessary to compare the local mean values with the ones of the section 3: the section 3 deals with the smooth-curved part. As shown in Figure 5.17, when the flame develops in a smooth-curved shape, the flame propagation speed is between 0.5 and 0.6 m/s. In the section 1, the flame changes into a convex shape toward the unburned gas. It can be learned that the local mean flame propagation speed, normal unburned gas velocity, and burning velocity are generally increased through the effect of thermal expansion caused by the burned gas and the preferential diffusion of the hydrogen.

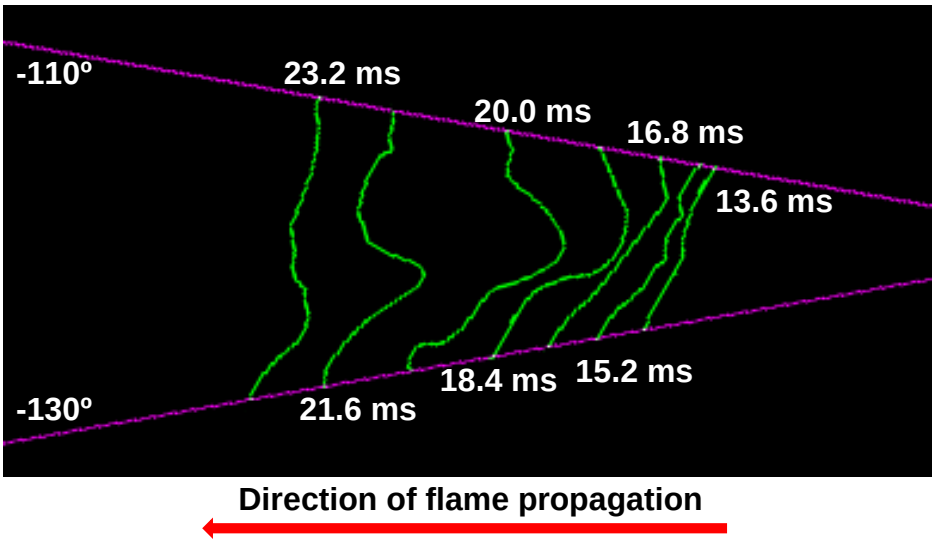

Figure 5.8 The enlarged section 2 image

Figure 5.8 is the enlarged image of the section 2 seen in Figure 5.2 (A). The change of flame shape in this section seems relatively more complex than the

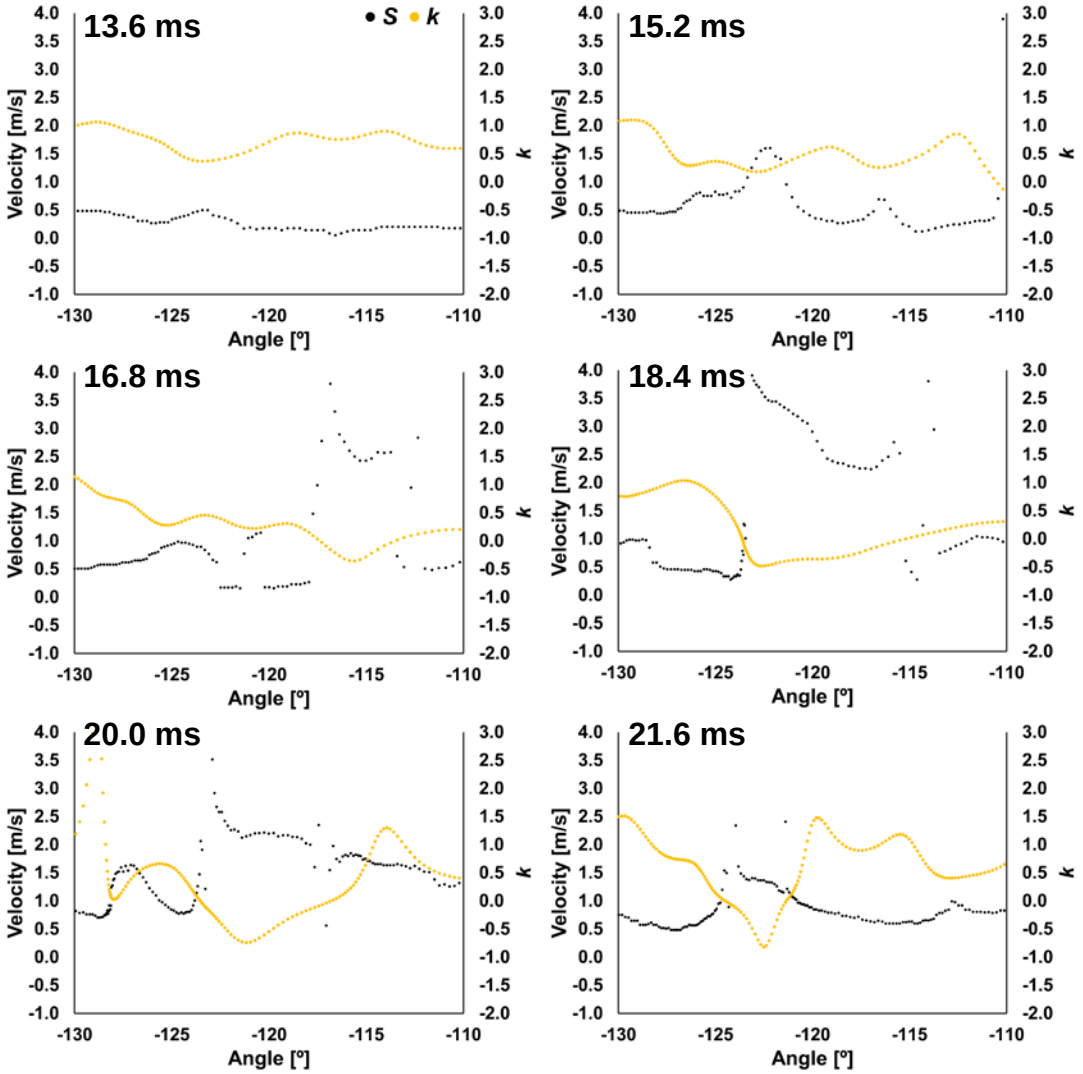

Figure 5.9 Change of flame propagation speed *S* (black dot) and wavenumber *k* (yellow dot) with respect to angle in the section 2 of the experimental case 1. Fuel: H_2-air / ϕ: 0.4 / t_{ign}: 36.2° CA bTDC / P_0: 4 bar / T_0: 414 K

one in the section 1. The flame almost keeps its shape until 16.8 ms, which seems like an inclined straight line. And then, the concave region appears between -120 and -110º at 18.4 ms and the other region seems relatively convex. This shape continues at 20.0 ms. When the time is 21.6 ms, a part of the concave region at 20.0 ms changes into a convex shape, and the other part keeps its concave shape. And then, the flame at 23.2 ms returns to the shape which is similar to the one at 13.6 ms.

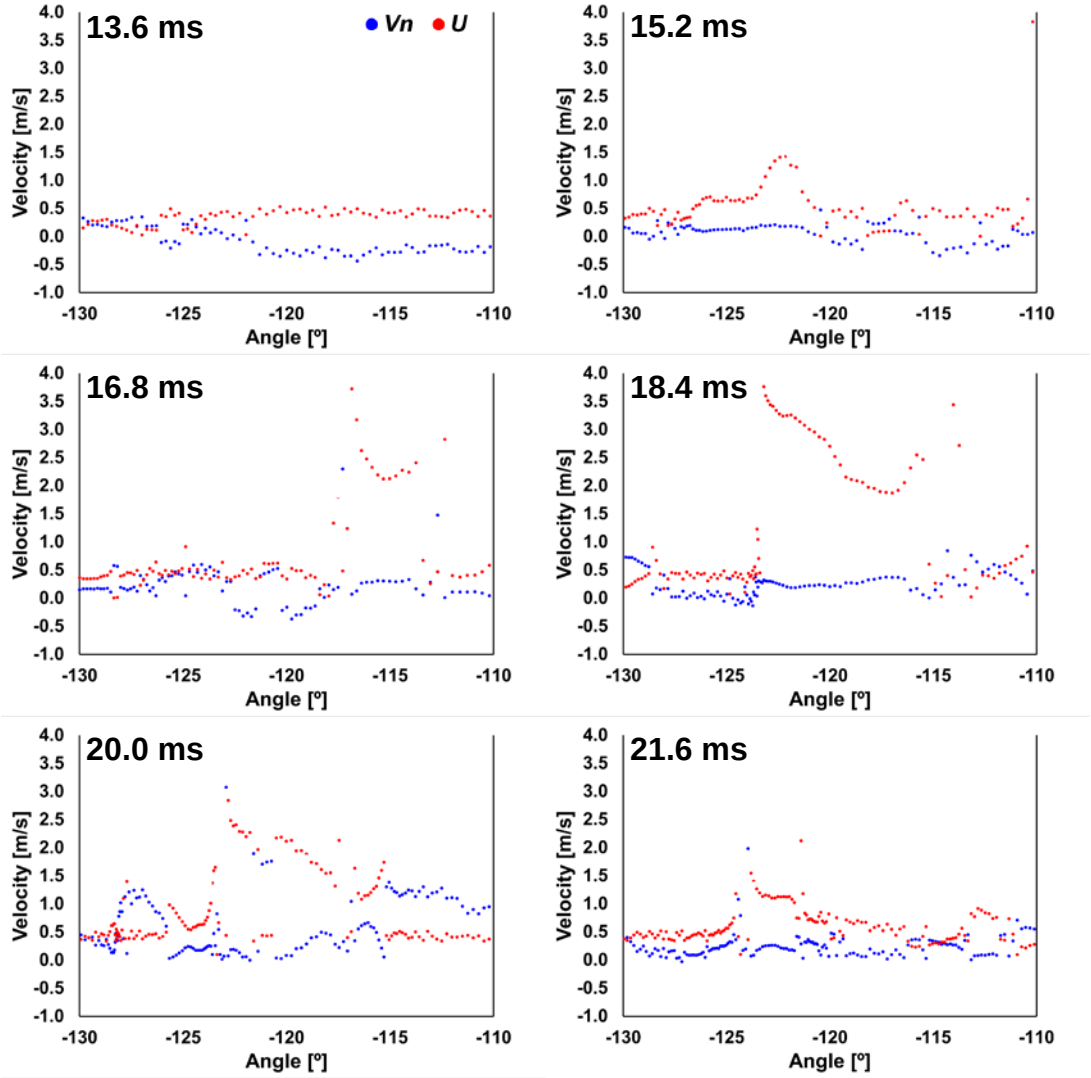

Figure 5.10 Change of normal unburned gas velocity V_n (blue dot) and burning velocity U (red dot) with respect to angle in the section 2 of the experimental case 1. Fuel: H_2-air / ϕ: 0.4 / t_{ign}: 36.2° CA bTDC / P_0: 4 bar / T_0: 414 K

The change of flame propagation speed and wavenumber with respect to angle is shown in Figure 5.9. The black and yellow dots in the figure represent flame propagation speed S and wavenumber k at each angle respectively. Until 15.2 ms, wavenumber ranges between 0.5 and 1.0 at most of the angles, and flame propagation speed also varies from 0.4 to 0.5 m/s except several points. When time is 16.8 and 18.4 ms, a large increase in the flame propagation speed occurs between -125 and -115º. At this moment, the corresponding wavenumber ranges between -0.5 and 0.0. While time elapses from 20.0 to 21.6 ms, flame propagation speed between -125 and -115º gradually decreases, and the wavenumber slowly increases with the local fluctuation.

Figure 5.10 shows the change of normal unburned gas velocity and burning velocity with respect to angle in the section 2. In the figure, the blue and red dots mean normal unburned gas velocity V_n and burning velocity U at each angle respectively. Except for 13.6 ms, as the flame develops, burning velocity generally changes much with respect to angle, whereas the change of normal unburned gas velocity is not much. Especially, in the region where the angle ranges from -125 to -115º, burning velocity increases radically when time is 16.8 and 18.4 ms, and the normal unburned gas velocity at those moments is close to 0.1 m/s: it seems that the sudden increase in the burning velocity mainly leads to the increase in the flame propagation speed.

And it is noticeable that normal unburned gas velocity is reduced when the wavenumber varies from -0.5 to 0.0 in Figure 5.9. While time elapses from 20.0 to 21.6 ms, flame propagation speed generally decreases and wavenumber increase. Simultaneously, burning velocity generally diminishes and normal unburned gas velocity does not change much. As opposed to the region where flame changes from a concave to convex shape in the section 1, it seems that the change of burning velocity caused by the preferential diffusion of the hydrogen affects is very much. And the burning velocity is the main factor in the change of flame propagation speed when the wavenumber is negative.

Figure 5.11 shows the variation of flame propagation speed with respect to wavenumber in the section 2. When wavenumber is positive and becomes close to zero, flame propagation speed increases. Especially, the wavenumber is less than 0.5, the increase in the flame propagation speed is very large. Since the section 2 shows that the flame shape is mainly concave, it is necessary to concentrate on when the wavenumber is negative. As wavenumber changes from -0.5 to 0.0, the corresponding flame propagation speed increases much, which is similar to when the wavenumber varies from 0.5 to 0.0. As seen in Figure 5.9 to Figure 5.11, compared with the changes of normal unburned gas velocity and burning velocity in the section 1, burning velocity seems to be a more important factor in changing the flame propagation speed than normal unburned gas velocity when the wavenumber changes from -0.5 to 0.0.

As seen in the region ranging between 5 and 10º in Figure 5.4 and Figure 5.5, when wavenumber changes from 0.5 to 0.0, normal unburned gas velocity and burning velocity have a tendency to increase together. On the contrary, when wavenumber varies from -0.5 to 0.0, the change of normal unburned gas velocity is minute and the burning velocity increase sharply: refer to the

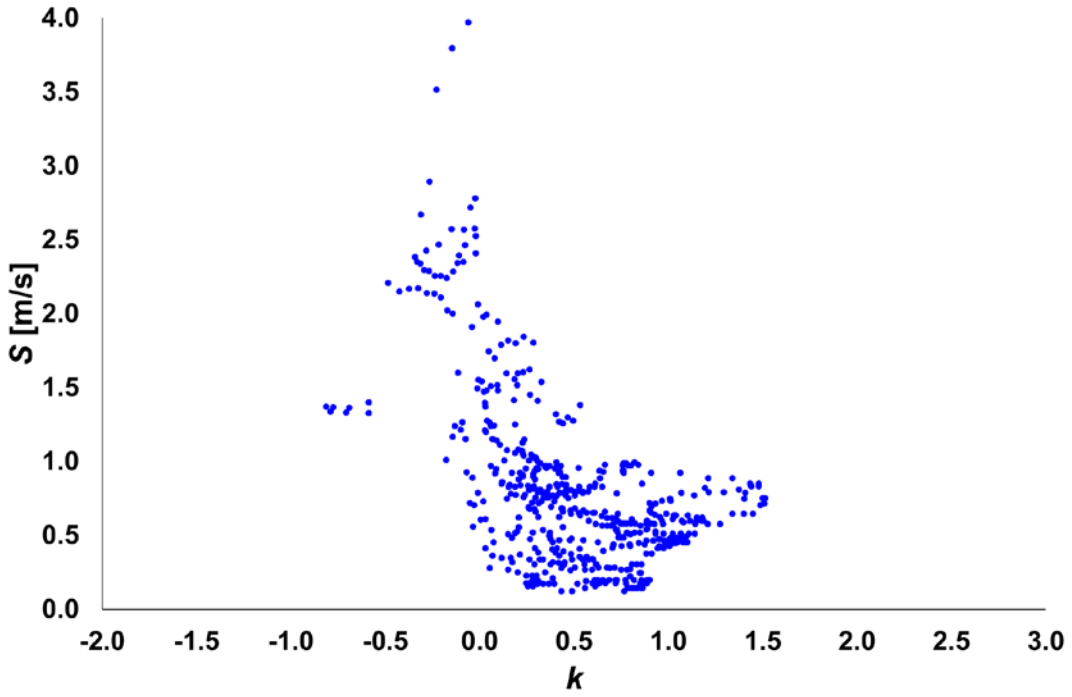

Figure 5.11 Variation of flame propagation speed *S* with respect to wavenumber *k* in the section 2 of the experimental case 1. Fuel: H_2-air / ϕ: 0.4 / t_{ign}: 36.2° CA bTDC / P_0: 4 bar / T_0: 414 K

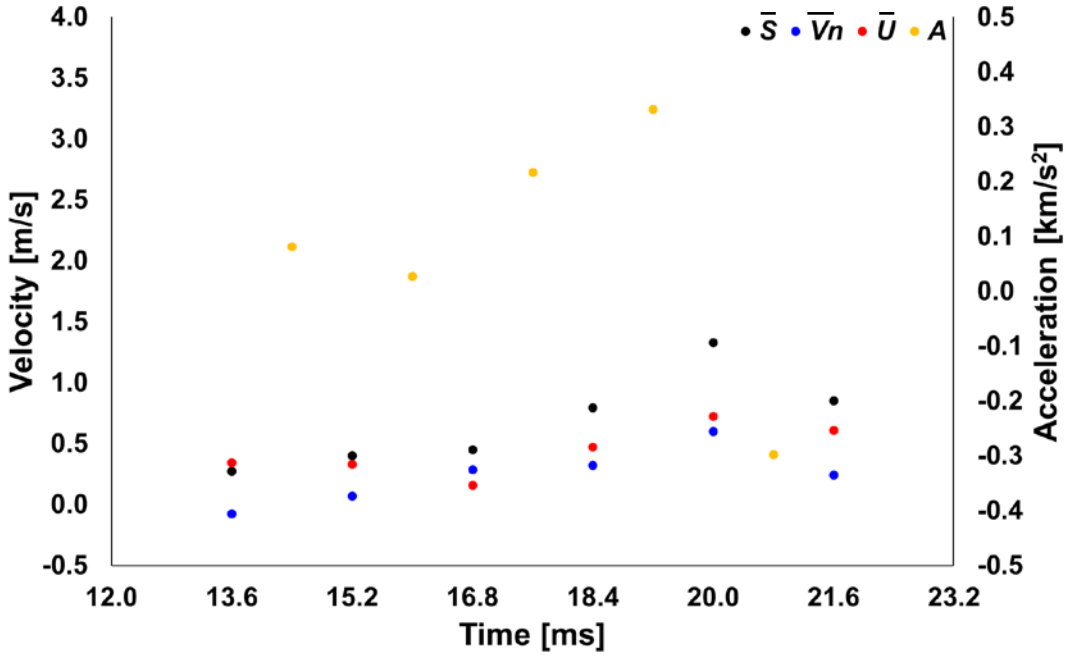

Figure 5.12 Variation of local mean flame propagation speed $\overline{S}$ (black dot), normal unburned gas velocity $\overline{V_n}$ (blue dot), burning velocity $\overline{U}$ (red dot), and acceleration *A* (yellow dot) with respect to time in the section 2 of the experimental case 1. Fuel: H_2-air / ϕ: 0.4 / t_{ign}: 36.2° CA bTDC / P_0: 4 bar / T_0: 414 K

region where angle is from -125 to -115º in Figure 5.9 and Figure 5.10. It can be realized that the effect of preferential diffusion of the hydrogen is prominent when the wavenumber is negative.

Figure 5.12 shows the variation of local mean flame propagation speed (black dot), normal unburned gas velocity (blue dot), burning velocity (red dot), and acceleration (yellow dot) with respect to time in the section 2. As seen in Figure 5.8, until 16.8 ms when the flame shape does not change much, local mean flame propagation speed $\bar{S}$ and burning velocity $\bar{U}$ have a stable value, and local mean normal unburned gas velocity $\bar{V}_n$ starts rising slightly. From 18.4 to 20.0 ms when the flame changes into a concave shape, $\bar{S}$, $\bar{V}_n$, and $\bar{U}$ increase together, and an increase in $\bar{U}$ is relatively larger than the one in $\bar{V}_n$. During the increase, the flame is also accelerated. When the flame perturbation is gradually erased at 21.6 and 23.2 ms, $\bar{S}$, $\bar{V}_n$, and $\bar{U}$ decreases together. It can be learned that the preferential diffusion of the hydrogen has an influence on the change of burning velocity by changing the mixture composition. However, the variation of the normal unburned gas velocity seems smaller than the one in the section 1.

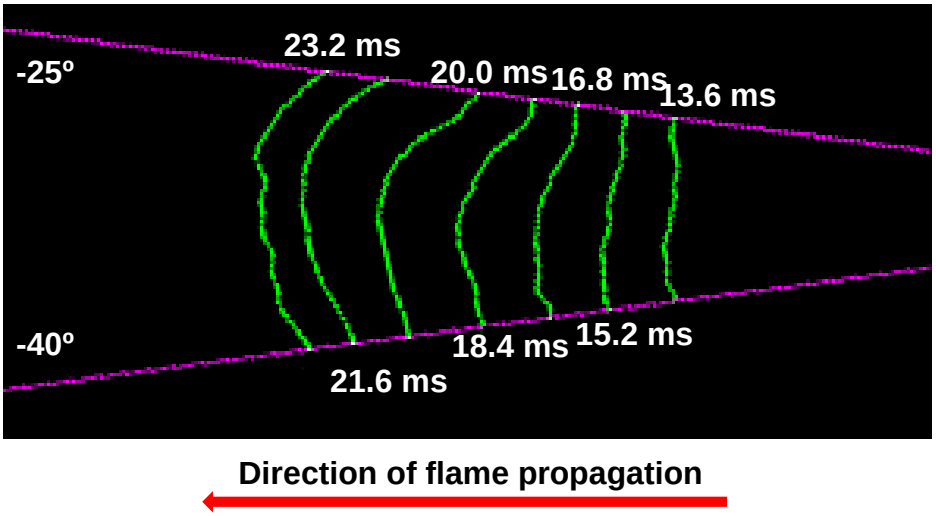

Figure 5.13 The enlarged section 3 image

Figure 5.13 shows the enlarged image of the section 3. Compared to the section 1 and 2 in Figure 5.3 and Figure 5.8, it seems that the variation of flame shape with respect to angle at each time is smooth. And the change of flame shape with respect to time is not much.

Figure 5.14 shows the change of flame propagation speed and wavenumber with respect to angle in section 3. The black and yellow dots represent flame

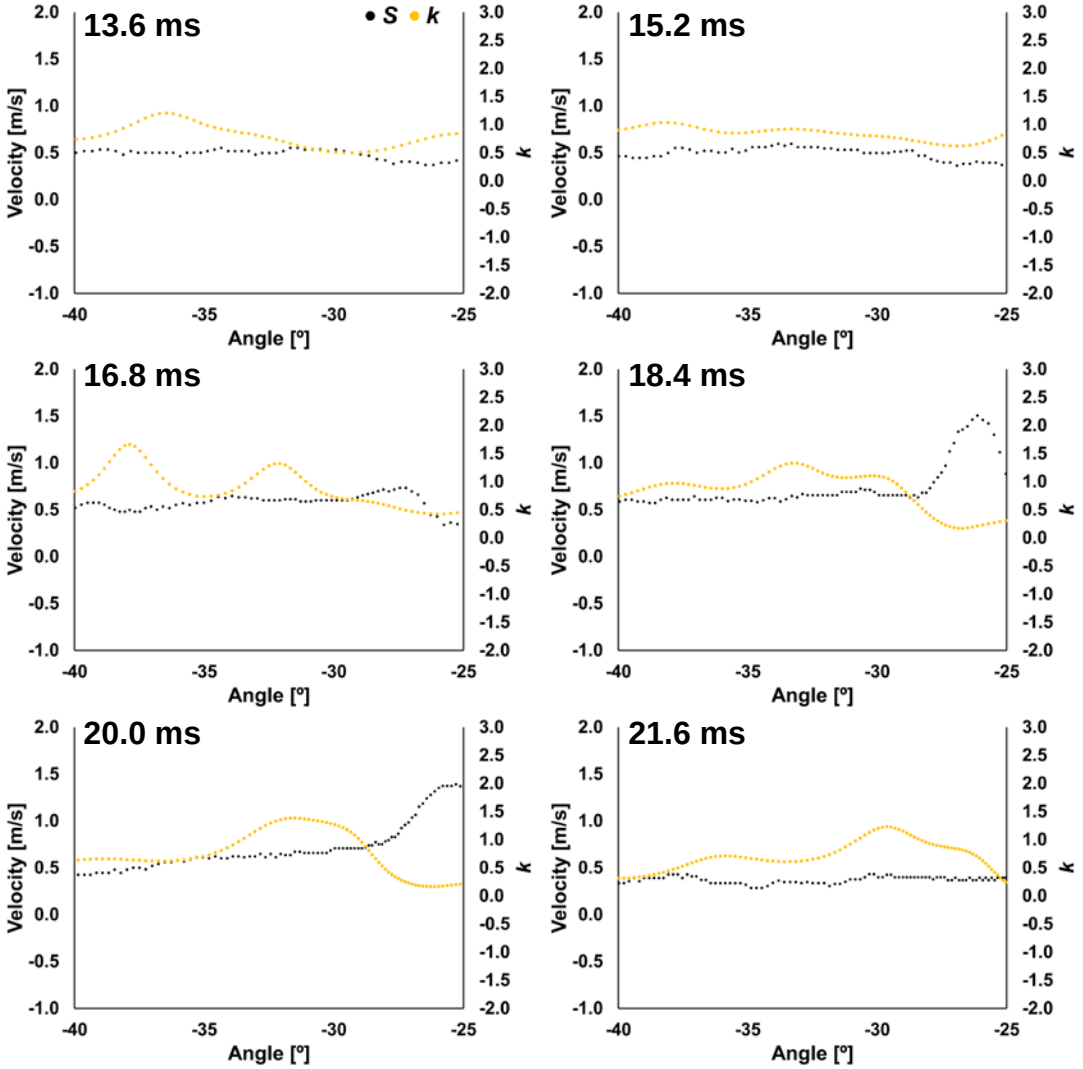

Figure 5.14 Change of flame propagation speed *S* (black dot) and wavenumber *k* (yellow dot) with respect to angle in the section 3 of the experimental case 1. Fuel: H_2-air / ϕ: 0.4 / t_{ign}: 36.2° CA bTDC / P_0: 4 bar / T_0: 414 K

propagation speed *S* and wavenumber *k* at each angle respectively. Except for the certain region where the angle ranges from -30 to -25º at 18.4 and 20.0 ms, the change of flame propagation speed is between 0.4 and 0.5 m/s. And the corresponding wavenumber ranges from 0.5 to 1.0.

The variation of flame propagation speed with respect to angle at each time seems considerably stable compared with the ones in the section 1 and 2. Especially, while wavenumber varies from 0.7 to 1.0, flame propagation speed is about 0.5 m/s and barely changes. When the wavenumber between -30 and -25º at 18.4 and 20.0 ms becomes lower than 0.5, the flame propagation

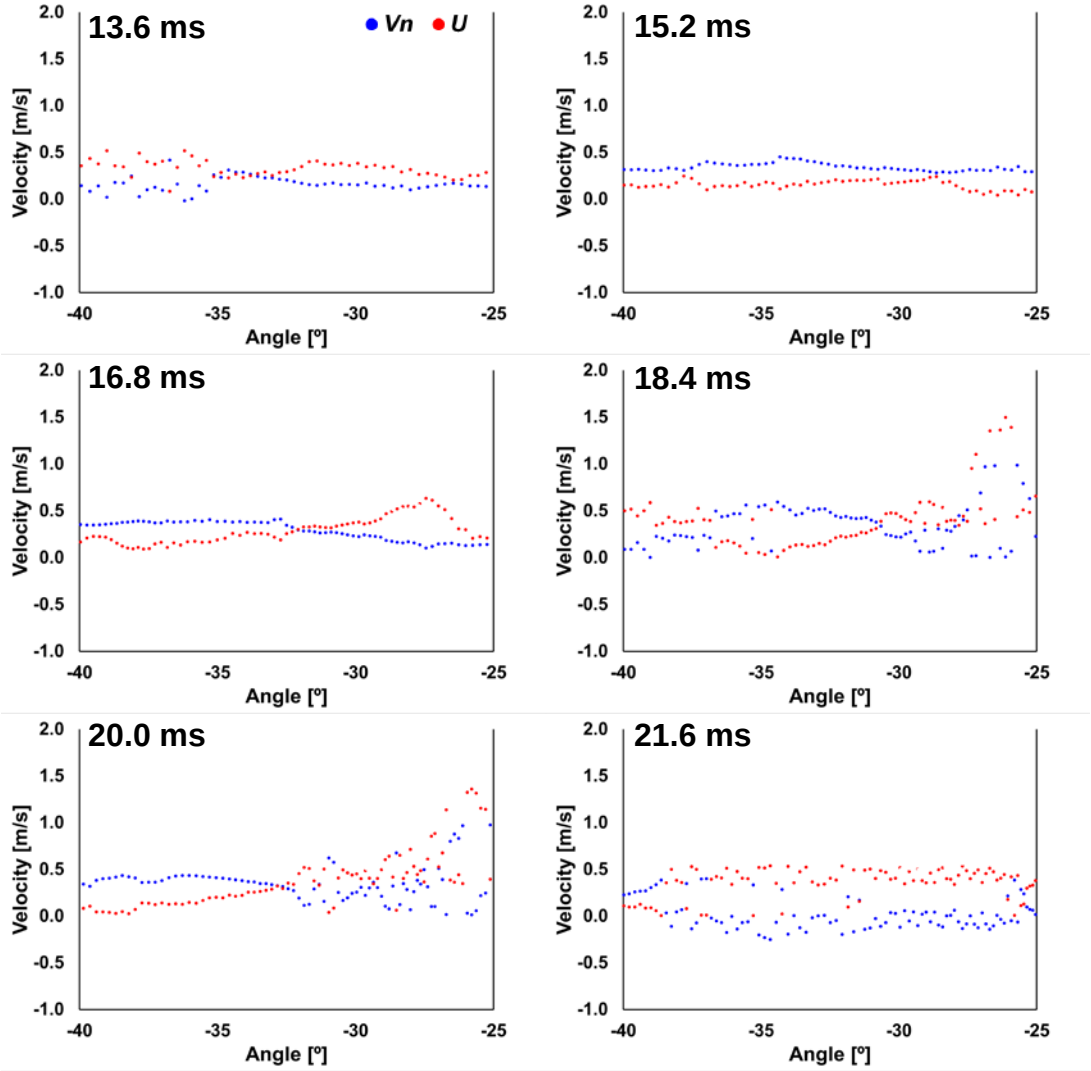

Figure 5.15 Change of normal unburned gas velocity V_n (blue dot) and burning velocity U (red dot) with respect to angle in the section 3 of the experimental case 1. Fuel: H_2-air / ϕ: 0.4 / t_{ign}: 36.2° CA bTDC / P_0: 4 bar / T_0: 414 K

speed rises rapidly, which is about 2.0 m/s. And then the flame propagation speed at 21.6 ms decreases up to 0.3 m/s.

Figure 5.15 shows the change of normal unburned gas velocity V_n (blue dot) and burning velocity U (red dot) with respect to angle in the section 2. Generally, the normal unburned gas velocity and burning velocity do not change much just as the flame propagation speed: both velocities range from 0.1 to 0.4 m/s. When the wavenumber between -30 and -25º at 18.4 and 20.0 ms becomes lower than 0.5 in Figure 5.14, the normal unburned gas velocity and burning velocity increase together, and then return to the stable values.

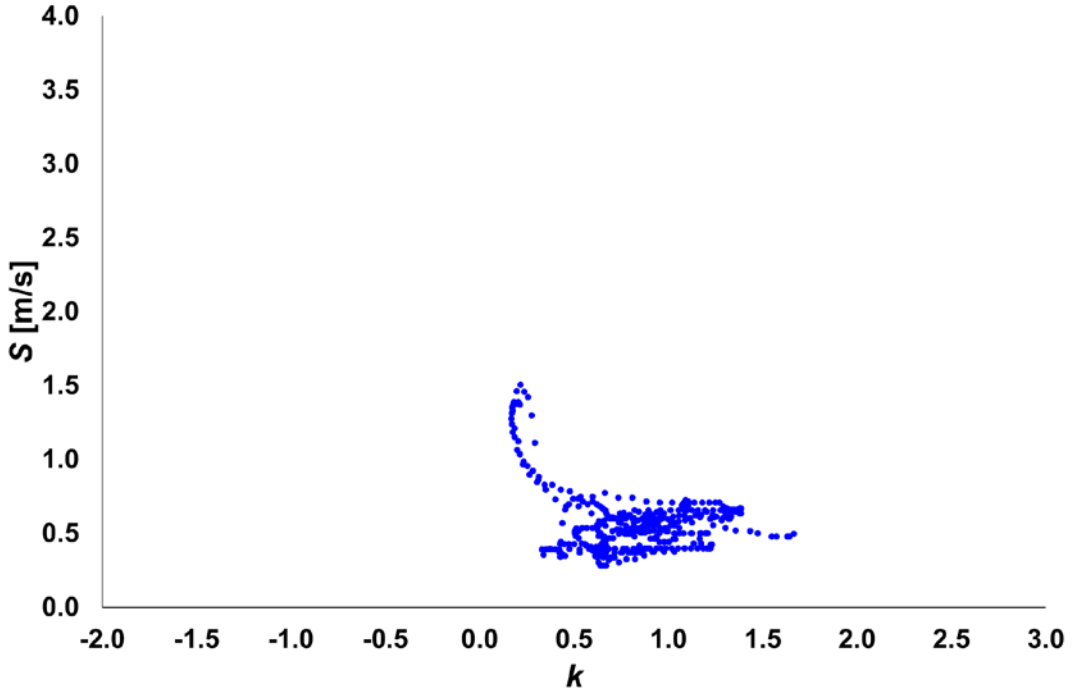

Figure 5.16 Variation of flame propagation speed *S* with respect to wavenumber *k* in the section 3 of the experimental case 1. Fuel: H_2-air / ϕ: 0.4 / t_{ign}: 36.2° CA bTDC / P_0: 4 bar / T_0: 414 K

Figure 5.16 shows the variation of flame propagation speed with respect to wavenumber in the section 3. In this section, the flame contour line at each time is curved smoothly with respect to angle and the flame shape does not change much as the flame develops. Because of this, the change of wavenumber ranges from 0.5 to 1.5 except for the certain region, which is between -30 and -25º at 18.4 and 20.0 ms. As seen in the figure, as the wavenumber changes from 0.5 to 1.3, the flame propagation speed varies from 0.4 to 0.7, and its variation also seems stable.

Figure 5.17 shows the variation of local mean flame propagation speed (black dot), normal unburned gas velocity (blue dot), burning velocity (red dot), and acceleration (yellow dot) with respect to time in the section 3. The local mean flame propagation speed $\bar{S}$ barely changes as the flame propagates, which is about 0.5 m/s. It is seen that although local mean unburned gas velocity $\overline{V_n}$ and burning velocity $\overline{U}$ change their amounts are small.

Through the changes of flame propagation speed, normal unburned gas velocity, burning velocity, and wavenumber in the section 1, 2, and 3, as the flame develops, their relationship can be explained below in terms of wavenumber:

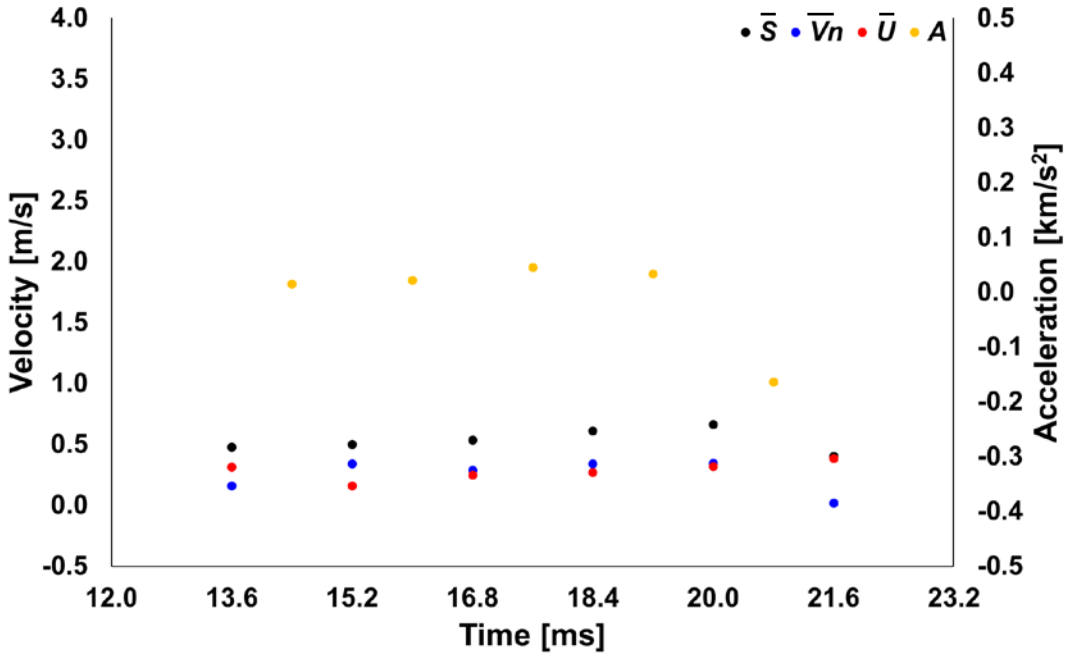

Figure 5.17 Variation of local mean flame propagation speed $\overline{S}$ (black dot), normal unburned gas velocity $\overline{V_n}$ (blue dot), burning velocity $\overline{U}$ (red dot), and acceleration *A* (yellow dot) with respect to time in the section 3 of the experimental case 1. Fuel: H_2-air / ϕ: 0.4 / t_{ign}: 36.2° CA bTDC / P_0: 4 bar / T_0: 414 K

Where wavenumber is positive, which means that flame changes from a flat to convex shape or from a convex to flat shape toward the unburned gas, flame propagation speed decreases as wavenumber increases. While wavenumber changes from 0.0 to 0.5, the flame propagation speed decreases sharply, and normal unburned gas velocity and burning velocity also change radically. As wavenumber becomes larger than 0.5, the gradient of the reduction in the flame propagation speed gradually decreases. During the decrease in flame propagation, normal unburned gas velocity and burning velocity also diminish together, but their changes are not much. After there is perturbation in a flame front and the corresponding wavenumber is larger than zero, the flame tends to change between a flat and convex shape with respect to time. Therefore, the wavenumber has a tendency to keep a positive value.

Where wavenumber is negative, which means that flame changes from a concave to flat shape or from a flat to concave shape toward the unburned gas, flame propagation speed increases as wavenumber approaches zero. Especially, an increase in flame propagation is very large when the wavenumber varies from -0.5 to 0.0. While flame propagation speed increases radically, the burning velocity also rises and seems to have more effects on

the increase than the normal unburned gas velocity. After flame is perturbed and its wavenumber becomes lower than zero, the flame tends to change between a concave and smoothly-curved shape with respect to time. That is, the wavenumber has a tendency to vary between -0.5 and 1.0.

In the view of a spatial change in wavenumber at each time, where wavenumber is relatively large at a certain region, the wavenumber at the adjacent regions is small. And where the wavenumber at a certain region is relatively small, the wavenumber at the neighbouring regions is large. As the absolute value of wavenumber becomes close to zero, the flame propagation speed, unburned gas velocity, and burning velocity increase. Since the preferential diffusion of the hydrogen occurs in this mixture, the local mixture composition becomes richer at the region where the wavenumber is negative and the flame shape is concave toward the unburned gas, whereas the mixture becomes leaner at the adjacent regions where the wavenumber is positive and the flame shape is convex. A spatial change in equivalence ratio of a mixture leads to a spatial change in flame propagation speed. However, the flame propagation speed changes in a certain range, which means that the local equivalence ratio influenced by the preferential diffusion of the hydrogen varies in a certain range.

In the view of a temporal change in wavenumber at a convex or concave region, wavenumber repeats an increase and decrease, and flame propagation speed also repeats a decrease and increase. Since the thermal expansion caused by the burned gas and the preferential diffusion of the hydrogen in this lean mixture take place, the normal unburned gas velocity and burning velocity increase at a concave region and decrease at a convex region. The gradient of the increase and decrease seems related to the gradient of burning velocity that is shown in Figure 2.11 (A) (Hertzberg 1989, Lipatnikov 2012). Where a mixture is locally leaner, flame propagation speed increases more rapidly owing to the preferential diffusion of the hydrogen. Where the local composition of a mixture is richer, flame propagation speed decreases more rapidly. Although there are repeated increases and decreases, the sign of the wavenumber does not change. Where wavenumber is positive, the flame changes from a flat to convex shape or from a convex to flat shape. Where wavenumber is negative, the flame changes from a concave to flat shape or from a flat to concave shape. This means that the local equivalence ratio affected by the preferential diffusion of the hydrogen repeats an increases and decrease in a certain range.

Figure 5.18 shows the change of the local mean wavenumber $\bar{k}$ with respect to time (A) and the relevant vorticity histogram (B) for the section 1. In Figure 5.18 (B), the positive value means the clockwise vorticity of unburned gas, and where the value is negative, the direction of vorticity is anticlockwise. The light blue, brown, grey, yellow, dark blue, and green lines are the histograms of the vorticity data that were obtained at 13.6, 15.2, 16.8, 18.4, 20.0, 21.6 ms respectively. Each vorticity data are for the area between two consecutive flame contour lines: these colour lines are applied in the same way to the section 2 and 3. Since an area between two consecutive flame contour lines becomes large as flame develops, the number of vorticity data also becomes large. Therefore, the unit of frequency is represented as percent in order to compare the change of histograms.

While time elapses from 13.6 to 16.8 ms, the local mean wavenumber gradually increases, and then starts decreasing. Before the local mean wavenumber decreases, the shape of the histogram changes and the frequency of clockwise vorticity increases. As time elapses from 16.8 to 21.6 ms, the local mean wavenumber gradually decrease, and the frequency of the clockwise vorticity gradually decreases. During the time, the shape of the histogram becomes close to symmetry. The shape of the histogram between 21.6 and 23.2 ms is similar to the one between 13.6 and 15.2 ms, and the corresponding local mean wavenumbers are also similar. Although the shape of the flame contour lines at 13.6 and 23.2 ms in Figure 5.3 seem very different, it seems that a large value of the wavenumber near 0 and 15º at 13.6 ms moves between 5 and 10º at 23.2 ms.

Figure 5.19 shows the change of the local mean wavenumber $\bar{k}$ with respect to time (A) and the relevant vorticity histogram (B) for the section 2. From 13.6 to 16.8 ms when the local mean wavenumber gradually decreases, the histogram seems to keep a similar shape and is close to symmetry: it is shown in Figure 5.8 that the flame also keeps the similar shape much as an inclined straight line. When the local mean wavenumber at 18.4 ms has a minimum value, the frequency of clockwise vorticity increases, and as shown in Figure 5.8 the concave part on the flame contour line appears. From 20.0 to 23.2 ms when the local mean wavenumber gradually increases, although the histogram is inclined to a positive value, the increase in the frequency of clockwise vorticity gradually decreases, which seems that the shape of the histogram returns to a symmetrical shape. During the time, the concave part on the flame contour line in Figure 5.8 also gradually disappears.

Figure 5.20 shows the change of the local mean wavenumber $\bar{k}$ with respect to time (A) and the relevant vorticity histogram (B) for the section 3. Until 18.4 ms, the local mean wavenumber keeps a stable value, which is about 0.8, the shape of the histogram barely changes. At 20.0 ms when the decrease in the local mean wavenumber starts, it is shown that the frequency of clockwise vorticity increases. While the local mean wavenumber decreases continuously from 20.0 to 23.2 ms, the frequency of clockwise vorticity gradually decrease, and the shape of the histogram seems to return to a symmetrical shape: during the time, a small size of a convex part on the flame contour line in Figure 5.13 shows up and the shape tends to keep.

Through Figure 5.18, Figure 5.19, and Figure 5.20, the relationship between the change of local mean wavenumber and vorticity histogram can be summarized as follows. First, when an increase or decrease in local mean wavenumber continues, the shape of the corresponding vorticity histograms is close to symmetry. Second, when the trend of local mean wavenumber changes from increase to decrease or from decrease to increase, the shape of histogram becomes asymmetric and the frequency of clockwise vorticity increases.

Since the thermal expansion caused by burned gas affects unburned gas in front of a flame surface (Balusamy et al. 2011, Long and Hargrave 2011, Burluka 2014), it seems reasonable that the shape of vorticity histogram becomes asymmetric when the trend of local mean wavenumber changes. Considering the ideal case where the shape of flame keeps a circle and the direction of the flame propagation at each point on the flame contour line is perpendicular to that point, the stationary unburned gas in front of the flame surface travels in the perpendicular direction. Hence, the clockwise and anticlockwise vorticities occur at the same time and their magnitudes are also identical, which is represented as a symmetrical shape of vorticity histogram. For this reason, when local mean wavenumber continue to increase or decrease, which means that the flame keeps a similar shape, the shape of the vorticity histogram becomes symmetrical. On the contrary, when the trend of local mean wavenumber changes and the shape of the corresponding flame varies, the shape of the vorticity histogram becomes asymmetric.

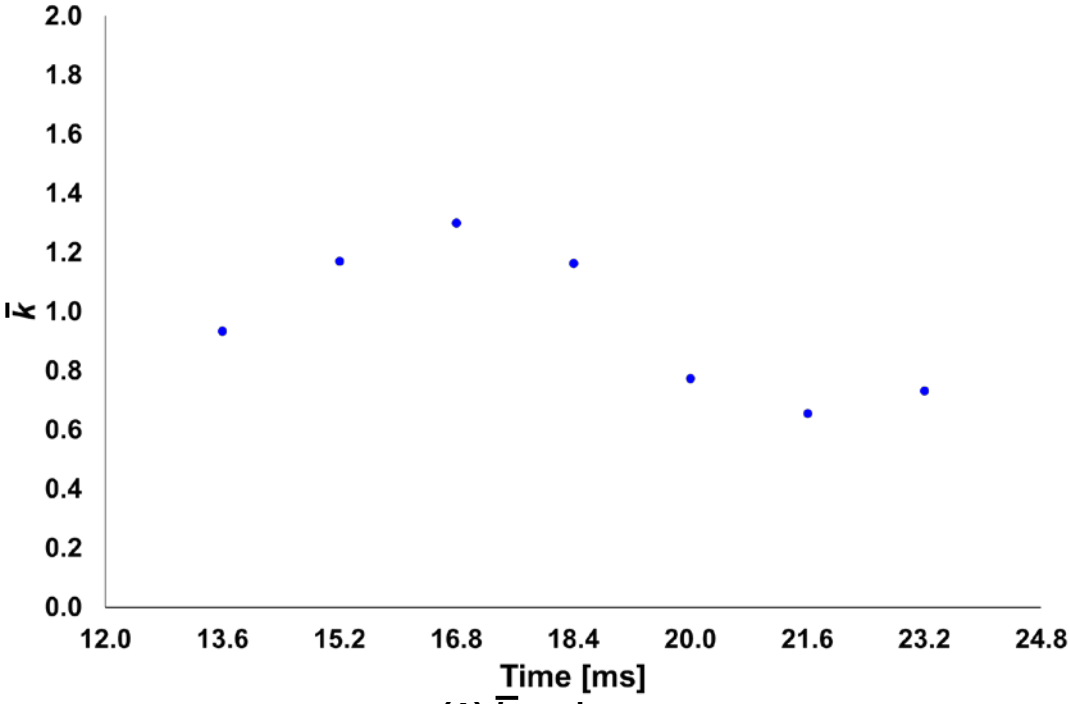

(A) $\overline{k}$ vs time

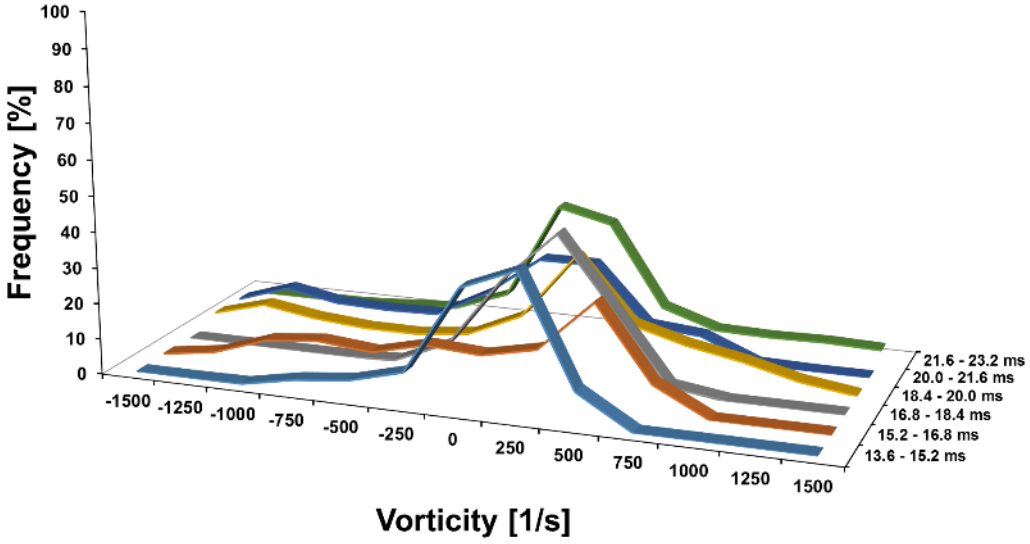

(B) Histogram

Figure 5.18 Change of the local mean wavenumber $\overline{k}$ with respect to time (A) and the relevant vorticity histogram (B) for the section 1 of the experimental case 1. Fuel: H_2-air / ϕ: 0.4 / t_{ign}: 36.2° CA bTDC / P_0: 4 bar / T_0: 414 K

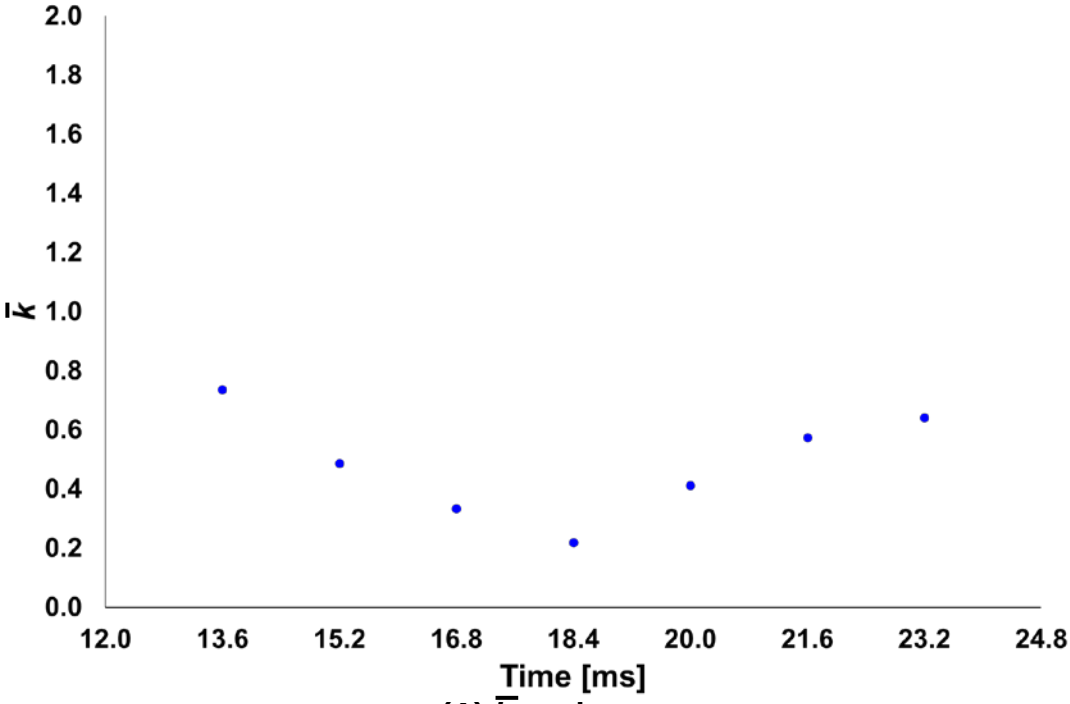

(A) $\overline{k}$ vs time

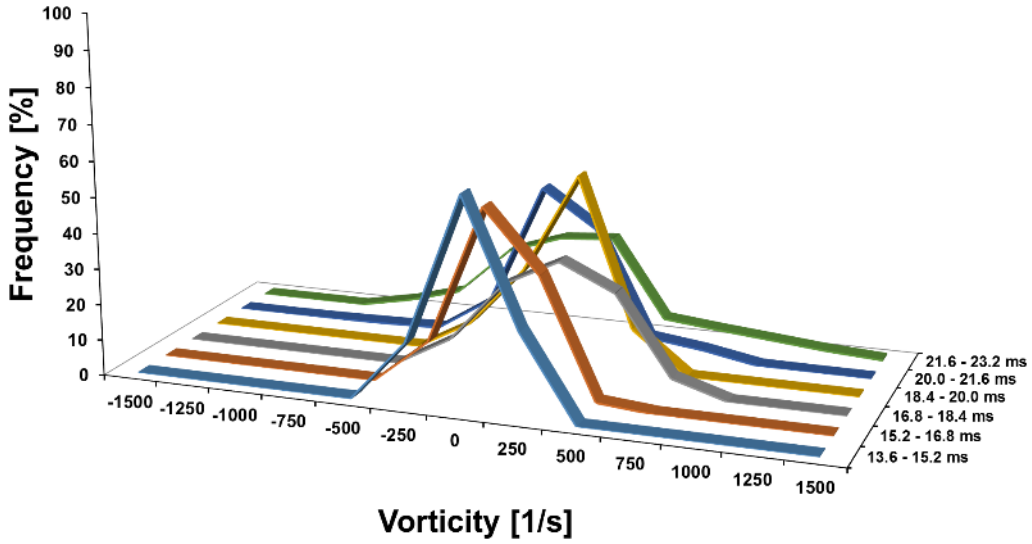

(B) Histogram

Figure 5.19 Change of the local mean wavenumber $\overline{k}$ with respect to time (A) and the relevant vorticity histogram (B) for the section 2 of the experimental case 1. Fuel: H_2-air / ϕ: 0.4 / t_{ign}: 36.2° CA bTDC / P_0: 4 bar / T_0: 414 K

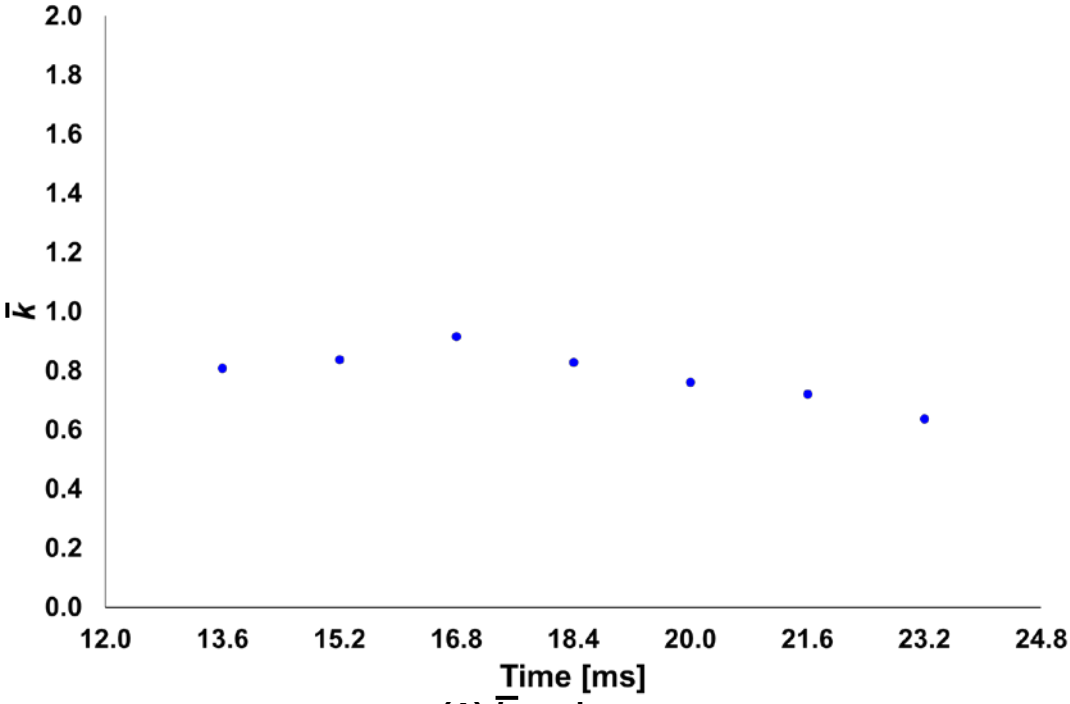

(A) $\overline{k}$ vs time

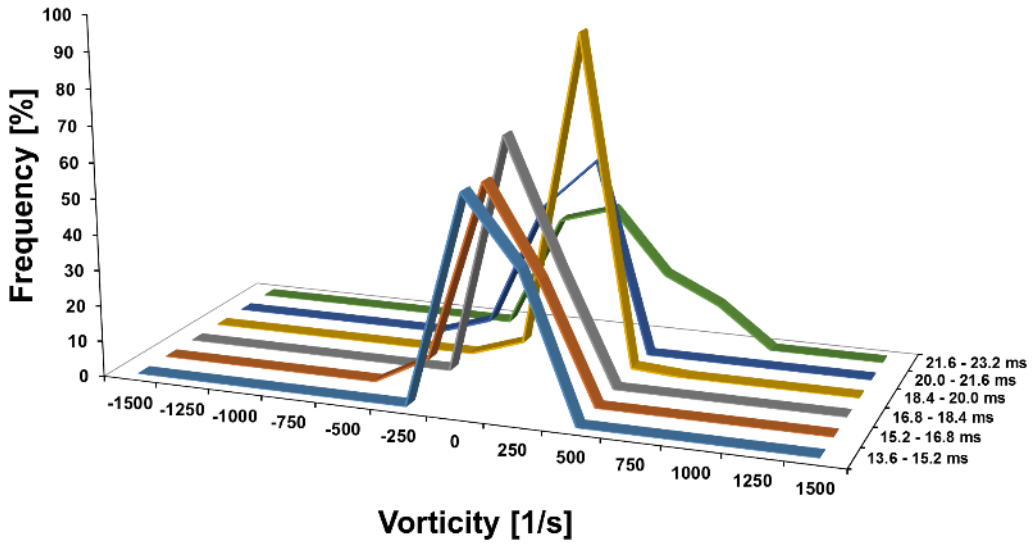

(B) Histogram

Figure 5.20 Change of the local mean wavenumber $\overline{k}$ with respect to time (A) and the relevant vorticity histogram (B) for the section 3 of the experimental case 1. Fuel: H_2-air / ϕ: 0.4 / t_{ign}: 36.2° CA bTDC / P_0: 4 bar / T_0: 414 K

In summary, in a convex region, as wavenumber increases, flame propagation speed gradually decreases. The relationship between the two is inversely proportional. Where wavenumber increases (decreases), normal unburned gas velocity and burning velocity generally decrease (increase). While the flame propagates, flame propagation speed is slightly changed. At the same

time, normal unburned gas velocity and burning velocity vary within a certain range. In a concave region, as wavenumber approaches zero, flame propagation speed increase sharply. Where wavenumber is close to zero, burning velocity mainly changes and is the main factor in the increase of flame propagation speed. In a smoothly-curved region, while wavenumber changes, flame propagation speed has a stable value. Normal unburned gas velocity and burning velocity are also barely changed.

In a spatial change in wavenumber at each time, where wavenumber is relatively large (small) at a certain region, the wavenumber at the adjacent regions is small (large). In a temporal change in wavenumber at a convex or concave region, wavenumber increases and decreases repeatedly, and flame propagation speed repeats decrease and increase.

Where local mean wavenumber keeps increasing or decreasing, the shape of the corresponding vorticity histogram is close to symmetry for a value of vorticity. Where local mean wavenumber changes from increase (decrease) to decrease (increase), the shape of the histogram becomes asymmetric, and clockwise vorticity is dominant.

These phenomena are also observed in the lean methane-air mixture and rich propane-air mixture experiment.

5.3 Result of the lean methane-air mixture

The experimental case 2 is a lean methane-air mixture case. The equivalence ratio of the mixture was 0.6, and the ignition timing t_{ign} was 36.2º CA bTDC. The inter-frame time between double frames to gain the flow field of unburned gas velocity was 0.1 ms, and the time step between two consecutive flame images to measure flame propagation speed was 0.8 ms. When the ignition started, the initial pressure P_0 and temperature T_0 were 4 bar and 414 K respectively.

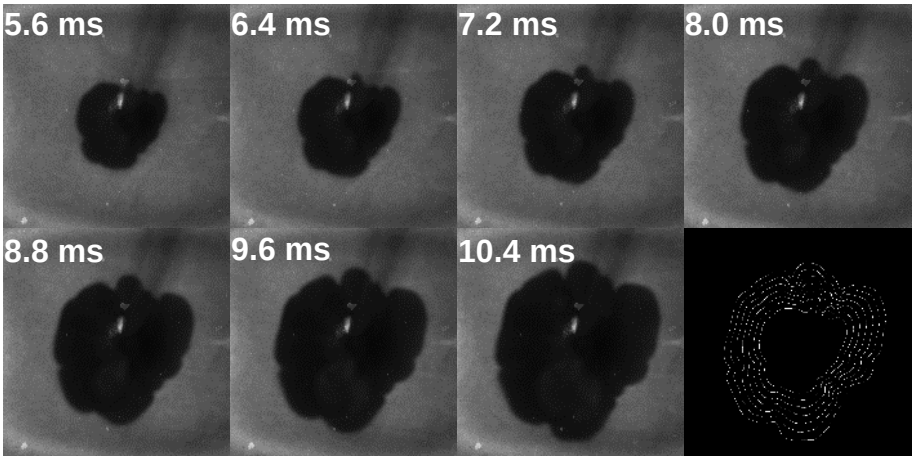

Figure 5.21 Propagating flame images and the corresponding edges image at the experimental case 2. Fuel: CH_4-air / ϕ: 0.6 / t_{ign}: 36.2° CA bTDC / P_0: 4 bar / T_0: 414 K

Figure 5.21 shows the outwardly propagating flame images with respect to time and the corresponding flame edges image. The white digits in the flame images indicate elapsing time after ignition. The black area in each flame image represents burned area, the relatively bright grey area is unburned area, and the white part near the centre is a spark plug.

Compared with the experimental case 1, the flame propagation speed of the lean methane mixture seems faster than that of the lean hydrogen mixture. When the flame starts being wrinkled in earnest, time is 7.2 ms and earlier than the lean hydrogen mixture flame. Relatively, the flame surface is smoother than that of the lean hydrogen mixture. In the case of the lean hydrogen mixture flame, after the flame is distorted, many convex and concave parts on each flame surface appear and then change irregularly. In contrast, the number of convex and concave parts of the lean methane

mixture flame is less, and it is seen that the wrinkled parts of the flame surface keeps their shapes.

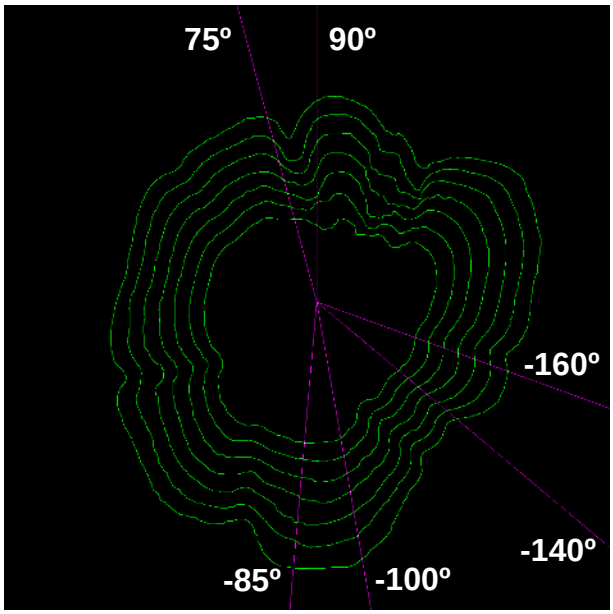

(A) Flame edges image

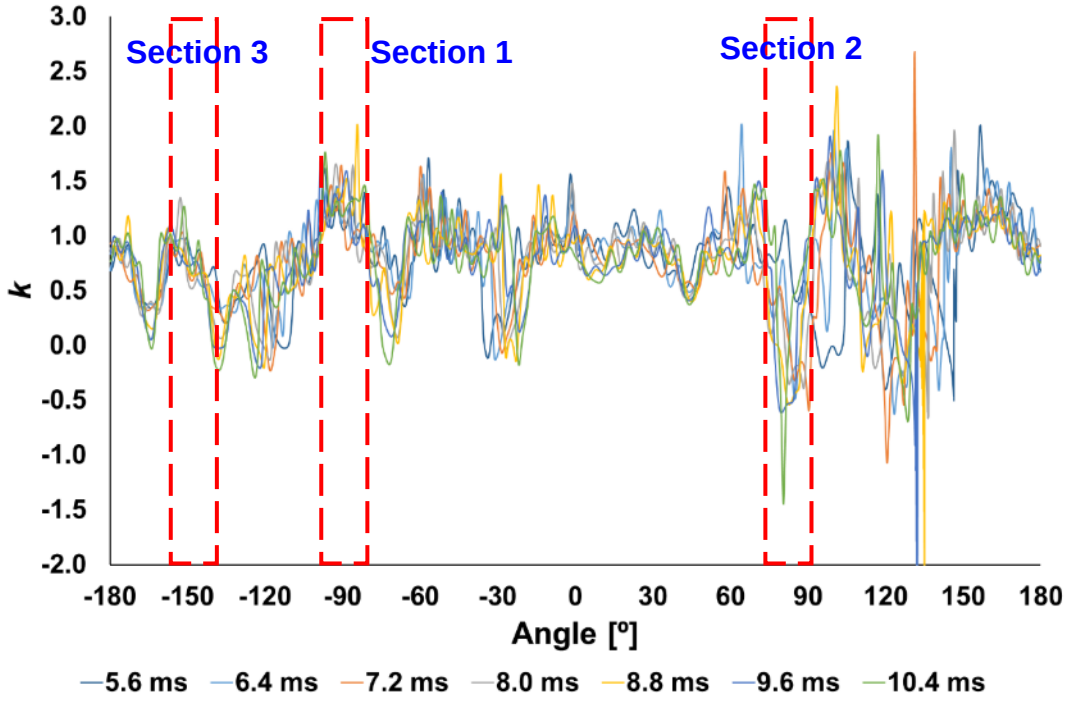

(B) *k* vs angle

Figure 5.22 Selection of the local areas through the flame edges image (A) and the change of the relevant wavenumber *k* (B)

Figure 5.22 shows the flame edges image (A) and the change of wavenumber with respect to angle at each time (B). The green lines in Figure 5.22 (A)

represent the flame contour lines of the lean methane-air mixture and show how the flame develops. It is seen in Figure 5.22 (B) that the variation of wavenumber with respect to angle ranges from -1.5 to 1.6. Compared with the lean hydrogen-air mixture in the experimental case 1, the range of the variation of the wavenumber with respect to angle is relatively narrow, and the range with respect to time is also narrow. Referring to Figure 5.22 (A) and (B), the section 1, 2, and 3 were selected. The wavenumber of the section 1 ranges from 0.8 to 1.6, and that of the section 2 varies from -0.6 to 1.1. And the range of the wavenumber of the section 3 is approximately between 0.5 and 1.0.

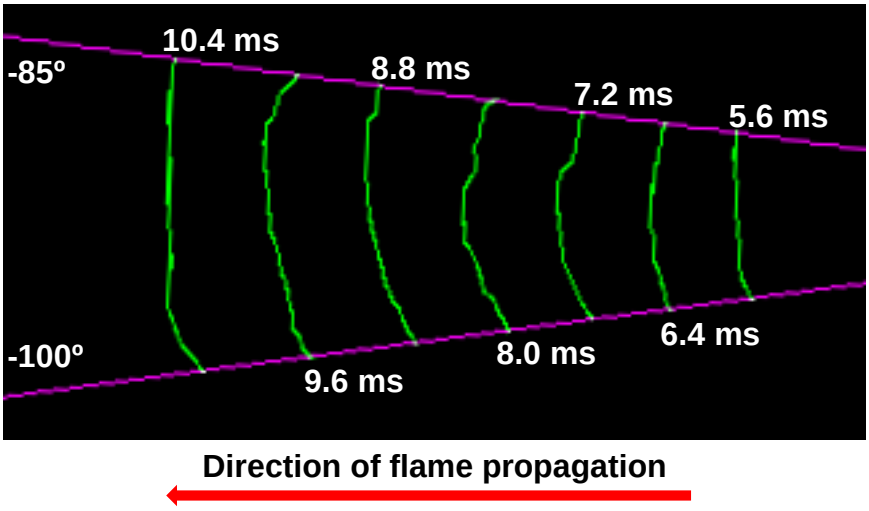

Figure 5.23 The enlarged section 1 image

Figure 5.23 shows the enlarged image of the section 1. As the flame develops, the flame contour line between -95 and 90º changes into a convex shape, and then keeps its shape. On the contrary, the flame contour line near -100 and -85º gradually changes into a concave shape, and then it returns to a convex shape. The change of the flame shape seems similar to that of the flame shape of the lean hydrogen-air mixture, which is seen in Figure 5.3. However, the flame shape of the lean methane-air mixture changes more gently with respect to angle and time, and the flame propagates faster.

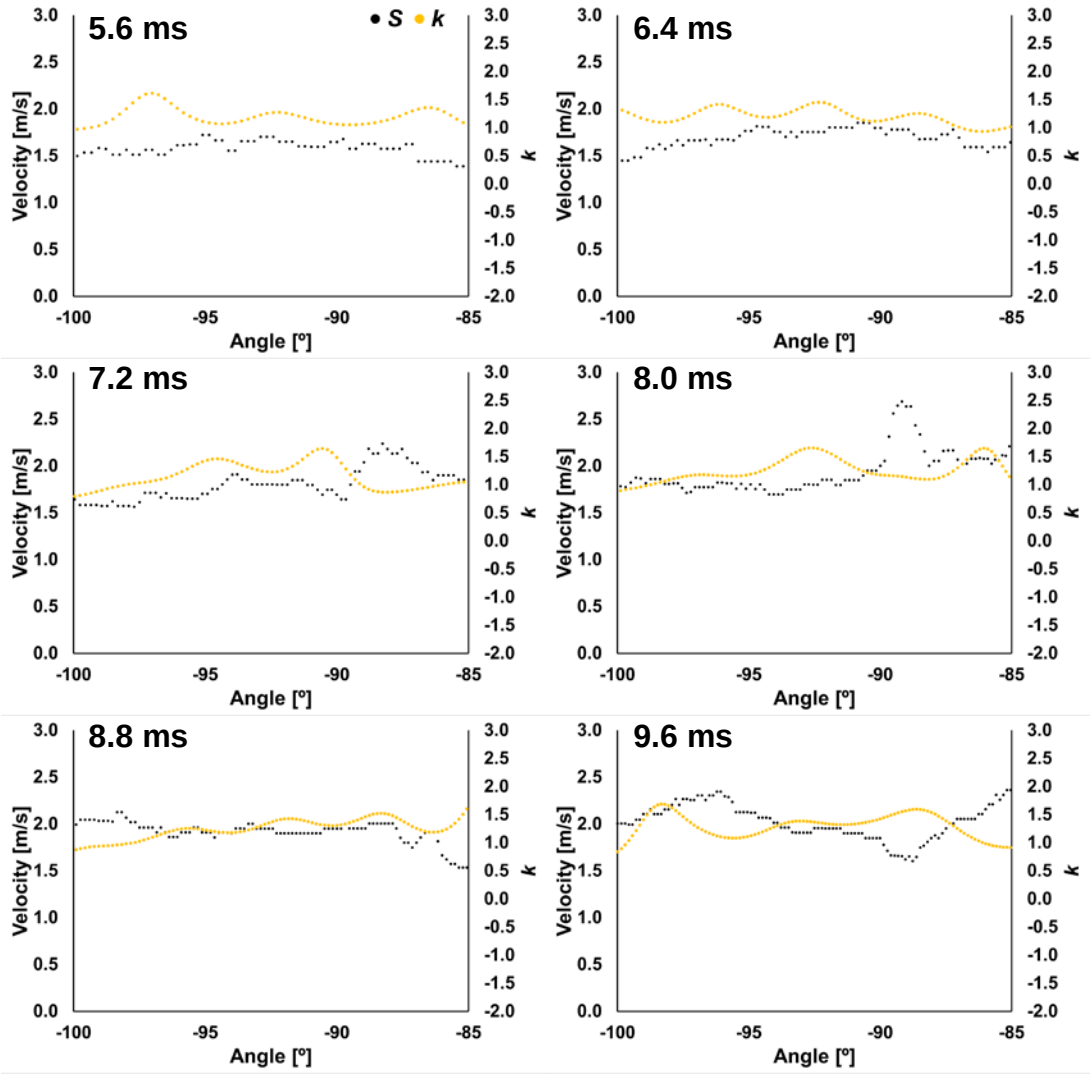

Figure 5.24 Change of flame propagation speed *S* (black dot) and wavenumber *k* (yellow dot) with respect to angle in the section 1 of the experimental case 2. Fuel: CH_4-air / ϕ: 0.6 / t_{ign}: 36.2° CA bTDC / P_0: 4 bar / T_0: 414 K

Figure 5.24 shows the change of flame propagation speed and wavenumber with respect to angle in the section 1. The black and yellow dots in the figure represent flame propagation speed *S* and wavenumber *k* at each angle respectively. Since it is distinctly seen in the region between -95 and -90° that the flame develops in a convex shape, the changes of flame propagation speed and wavenumber at that region are described in the detail.

Until 8.0 ms, wavenumber *k* generally increases, and the range is between 1.1 and 1.6. During the time, although flame propagation speed *S* slightly decreases to 1.5 m/s, the decrease is not much. At 8.8 ms, *k* decreases and

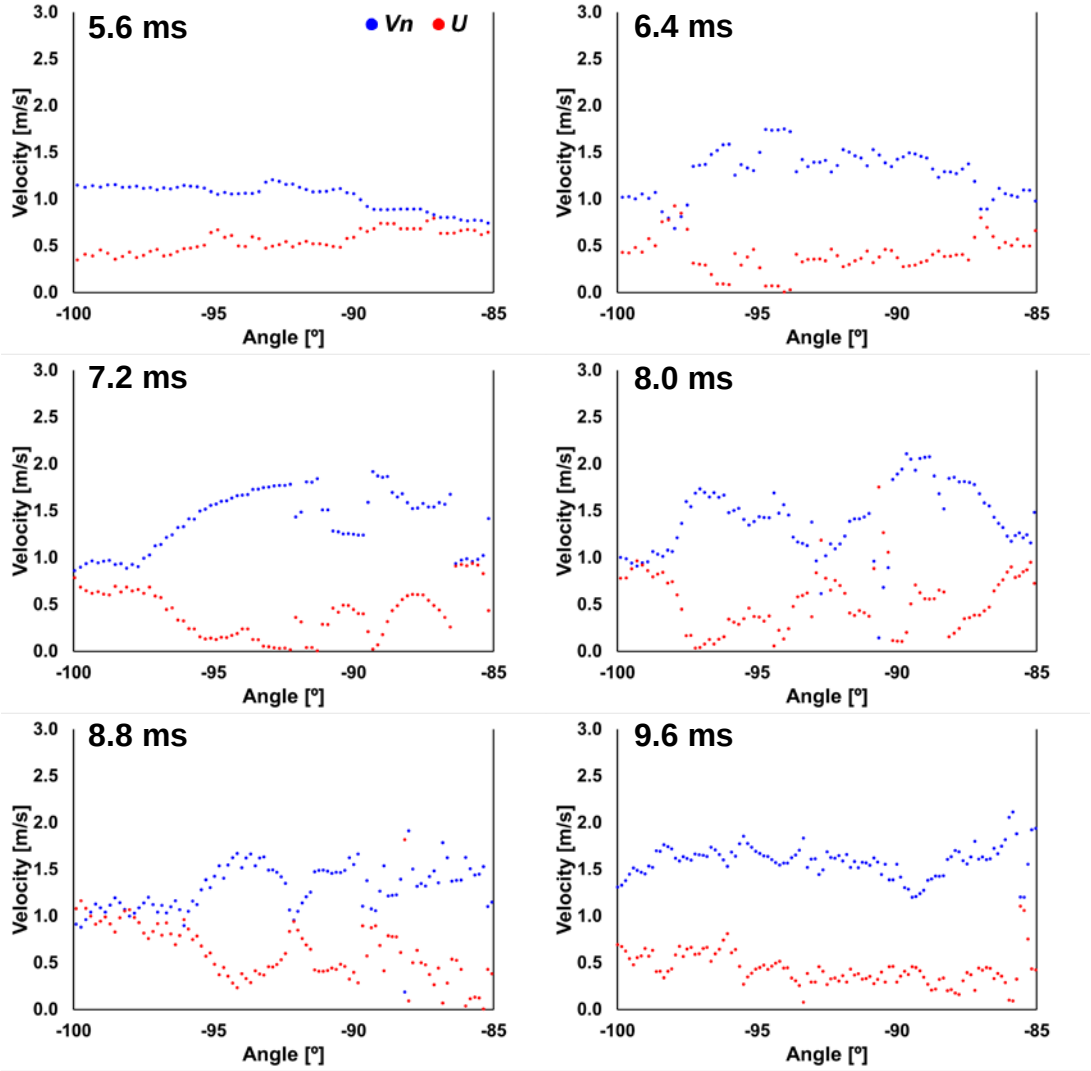

Figure 5.25 Change of normal unburned gas velocity V_n (blue dot) and burning velocity U (red dot) with respect to angle in the section 1 of the experimental case 2. Fuel: CH_4-air / ϕ: 0.6 / t_{ign}: 36.2° CA bTDC / P_0: 4 bar / T_0: 414 K

approaches one. Simultaneously, S rises up to 2.0 m/s, but the increase is not much. When time is 9.6 ms, k is kept, and S barely changes. Similar to the lean hydrogen-air mixture, the relationship between wavenumber and flame propagation speed is inversely proportional. However, the change of wavenumber is not as much as that of wavenumber in the lean hydrogen-air mixture, and the variation of flame propagation speed is also relatively large.

Figure 5.25 shows the change of normal unburned gas velocity and burning velocity with respect to angle in the section 1. In the figure, the blue and red dots indicate normal unburned gas velocity V_n and burning velocity U at each angle respectively. Since the flame changes into a convex shape in the region

between -95 and -90º, the change of V_n and U at that region is mainly investigated in the section1.

At 5.6 ms, V_n and U have stable values and are about 1.1 and 0.5 m/s respectively. When time is 6.4 ms, V_n generally increases, and the V_n near -95º is larger than the one near -90º. U also starts fluctuating, and the U near -95º is smaller than the one near -90º. The changes of V_n and U are kept until 7.2 ms. From 8.0 ms to 8.8 ms, V_n barely changes and U slightly increases. Locally, the V_n in the vicinity of -95 and -90º is larger than the one near -92.5º, and the U near -95 and -90º is smaller than the one near -92.5º. At 9.6 ms, V_n and U are about 1.5 and 0.5 m/s, the two velocities barely change with respect to angle.

The following can be summarized through Figure 5.24 and Figure 5.25. While wavenumber increases, flame propagation speed gradually decreases. When flame propagation speed diminishes, the initially stable normal unburned gas velocity and burning velocity become fluctuated, and each velocity locally changes. When wavenumber and flame propagation speed are kept, the normal unburned gas velocity and burning velocity become stable again: this phenomenon is observed in the lean hydrogen mixture.

When flame changes into a convex shape, the thermal expansion of the burned gas has less effect on the unburned gas because heat and free radicals are dispersed (Borghi et al 1998, Lipatnikov 2012, Burluka 2014). This leads to the decreases of normal unburned gas velocity. In addition, the preferential diffusion of the methane into the flame front is divergent at a convex region, and the composition of the methane-air mixture at that region becomes leaner (Hertzberg 1989, Nakahara and Kido 1998). Hence, the burning velocity diminishes.

Figure 5.26 shows the relationship between the flame propagation speed S and wavenumber k in the section 1. The range of wavenumber of the section 1 is between 0.8 and 1.6. As wavenumber decreases, the flame propagation speed increases, but the gradient is gentle. The relationship between S and k is inversely proportional, and is also seen in the lean hydrogen-air mixture.

However, although the wavenumber of the lean methane-air mixture varies as flame propagates, it does not approach zero: k=0 means that the flame shape is flat. Compared to the lean hydrogen-air mixture, the range of change of the wavenumber is relatively narrow. This means that although flame changes into a convex shape the range of the change is not much. As seen in Figure 5.3 and Figure 5.23, the change of a flame shape of the lean hydrogen-air

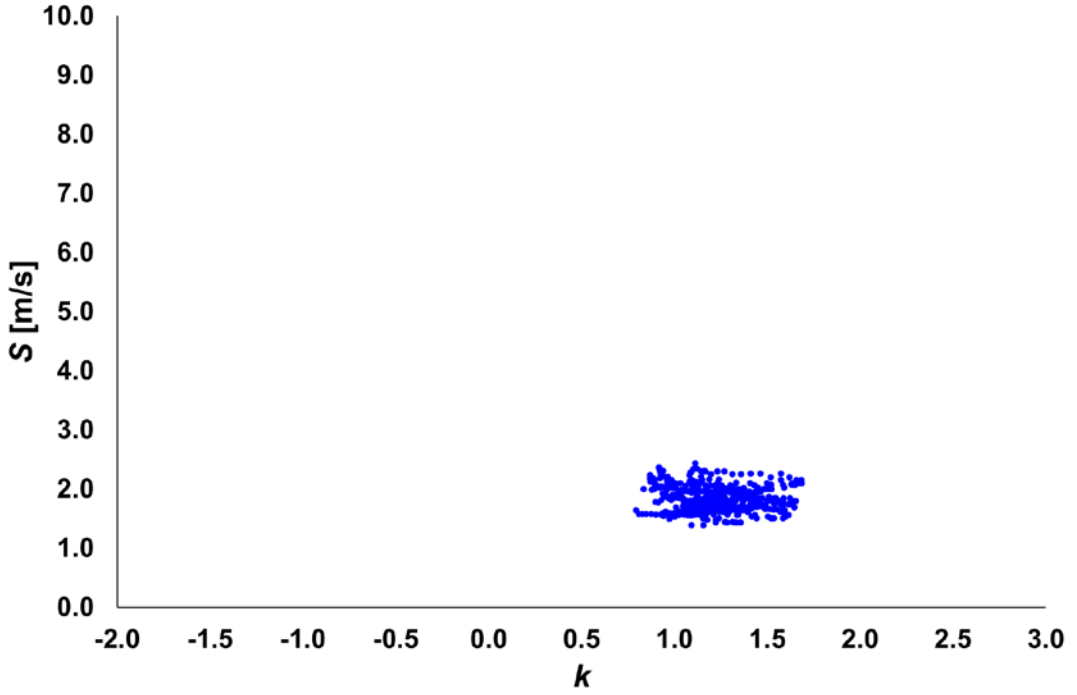

Figure 5.26 Variation of flame propagation speed *S* with respect to wavenumber *k* in the section 1 of the experimental case 2. Fuel: CH_4-air / ϕ: 0.6 / t_{ign}: 36.2° CA bTDC / P_0: 4 bar / T_0: 414 K

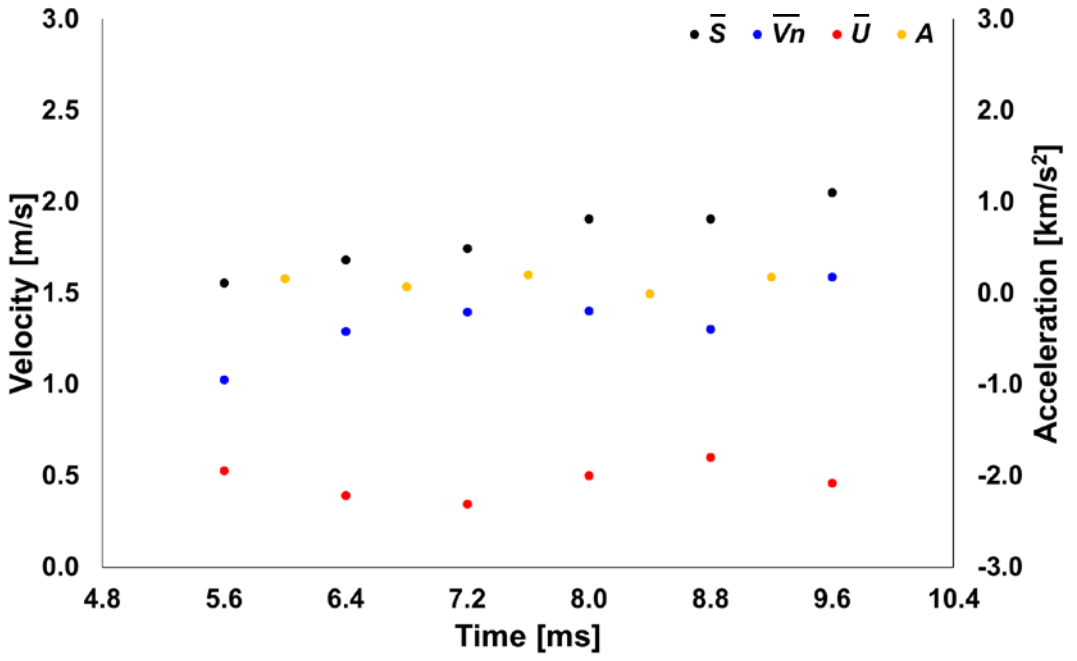

Figure 5.27 Variation of local mean flame propagation speed $\overline{S}$ (black dot), normal unburned gas velocity $\overline{V_n}$ (blue dot), burning velocity $\overline{U}$ (red dot), and acceleration *A* (yellow dot) with respect to time in the section 1 of the experimental case 2. Fuel: CH_4-air / ϕ: 0.6 / t_{ign}: 36.2° CA bTDC / P_0: 4 bar / T_0: 414 K

mixture is relatively large. This seems related to the diffusivities of reactants. The diffusivities of hydrogen, methane, and oxygen are 1.86, 0.47, and 0.43 cm^2/sec respectively (Hertzberg 1989). Since methane is less diffusive than hydrogen, it can be said that the effect of preferential diffusion of methane is less under a lean condition.

Figure 5.27 shows the variation of local mean flame propagation speed $\bar{S}$ (black dot), normal unburned gas velocity $\overline{V_n}$ (blue dot), burning velocity $\overline{U}$ (red dot), and acceleration *A* (yellow dot) with respect to time in the section 1. While the flame propagates, $\bar{S}$ gradually increases. Since there is not a large change in $\bar{S}$, *A* barely changes, and the value is close to zero. During the increase of the $\bar{S}$, although $\overline{V_n}$ also rises from 1.0 to 1.5 m/s, $\overline{U}$ barely changes and the range is between 0.3 and 0.5 m/s. Where flame changes into a convex shape, $\bar{S}$ is generally faster than that of the lean hydrogen-air mixture case, and increases from 1.5 to 2.0 m/s. And $\overline{V_n}$ has more effect on increase of the $\bar{S}$ than $\overline{U}$.

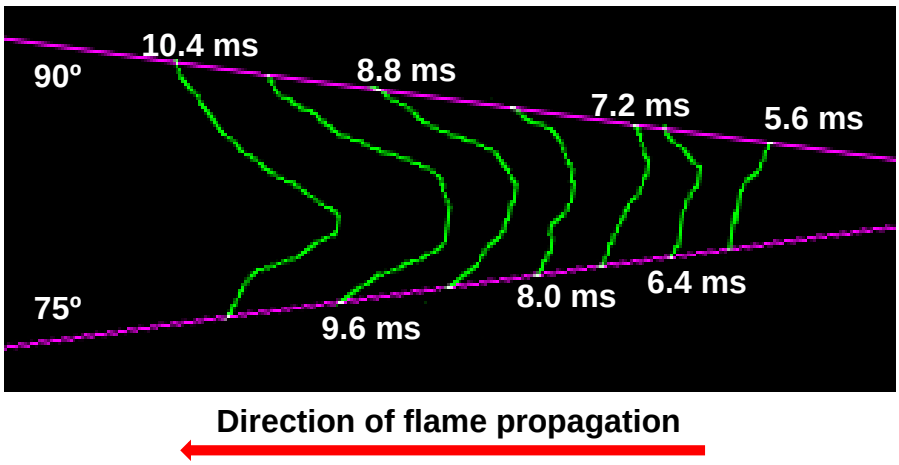

Figure 5.28 The enlarged section 2 image

Figure 5.28 shows the enlarged image of the section 2. Until 7.2 ms, the flame contour lines are not disturbed much with respect to angle. At 8.0 ms, a concave part appears near 90º, and the timing is earlier than the lean hydrogen-air mixture. After that, the flame shape becomes more concave until 10.4 ms, and it seems that the concave part moves toward 75º as time goes by. In the case of the lean hydrogen-air mixture, the flame changes into a concave shape, and then, it returns to a relatively flat: refer to Figure 5.8. However, the flame of the lean methane-air mixture changes into a concave

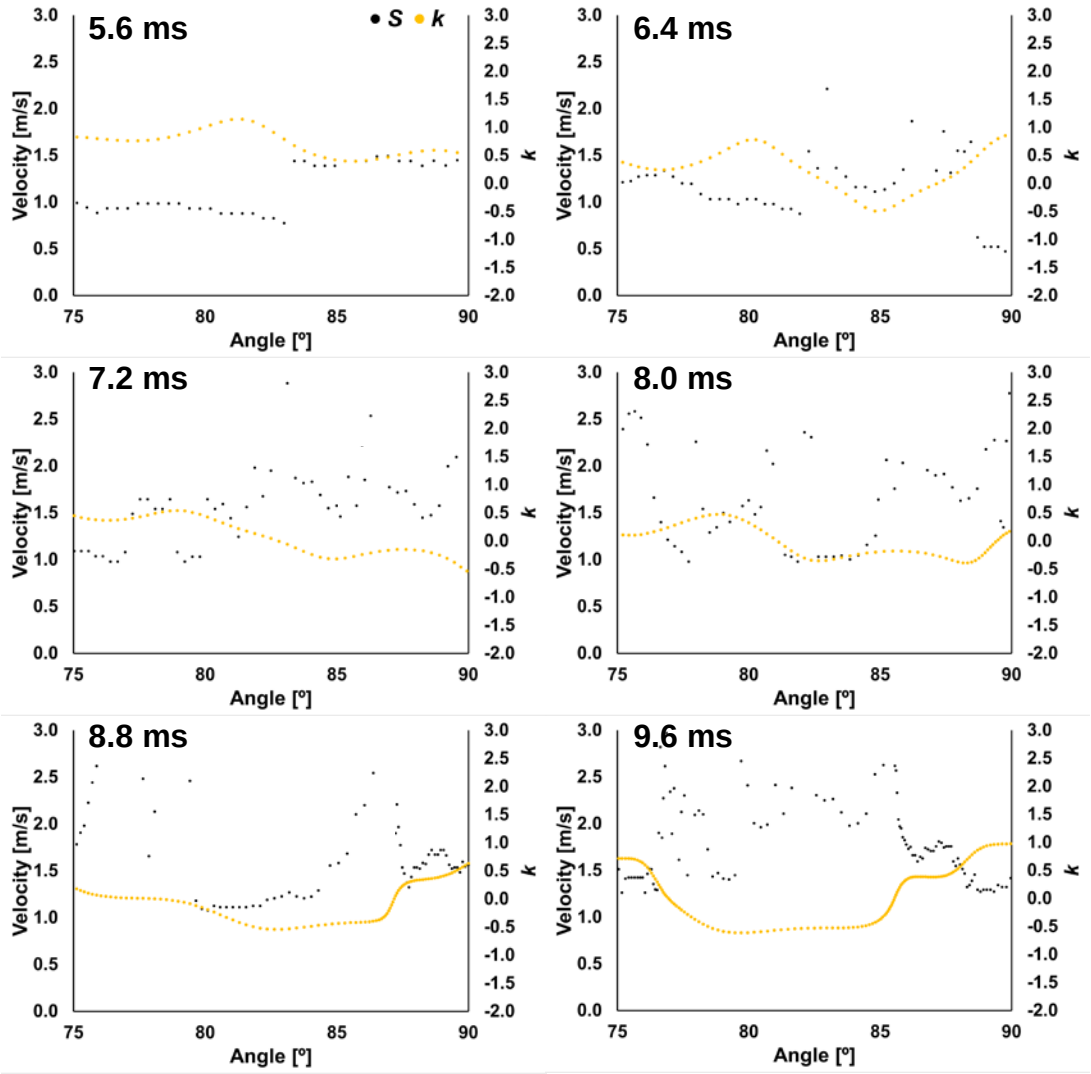

Figure 5.29 Change of flame propagation speed *S* (black dot) and wavenumber *k* (yellow dot) with respect to angle in the section 2 of the experimental case 2. Fuel: CH_4-air / ϕ: 0.6 / t_{ign}: 36.2° CA bTDC / P_0: 4 bar / T_0: 414 K

shape, and then tends to keep its shape.

Figure 5.29 shows the change of flame propagation speed and wavenumber with respect to angle in the section 2. The black and yellow dots in the figure indicate flame propagation speed *S* and wavenumber *k* at each angle. At 5.6 ms, the *k* between 85 and 90º is smaller than the one at the other region, and the *S* between 85 and 90º is larger than the one at the other region. When time is 6.4 ms, the change of *k* with respect to angle is similar to that at 5.6 ms. However, the *k* between 85 and 90º locally decreases up to -0.5, the corresponding *S* increases. The change of *k* and *S* at 6.4 ms is kept similarly until 8.0 ms. From 8.8 to 9.6 ms, the *k* between 80 and 85º is smaller than the

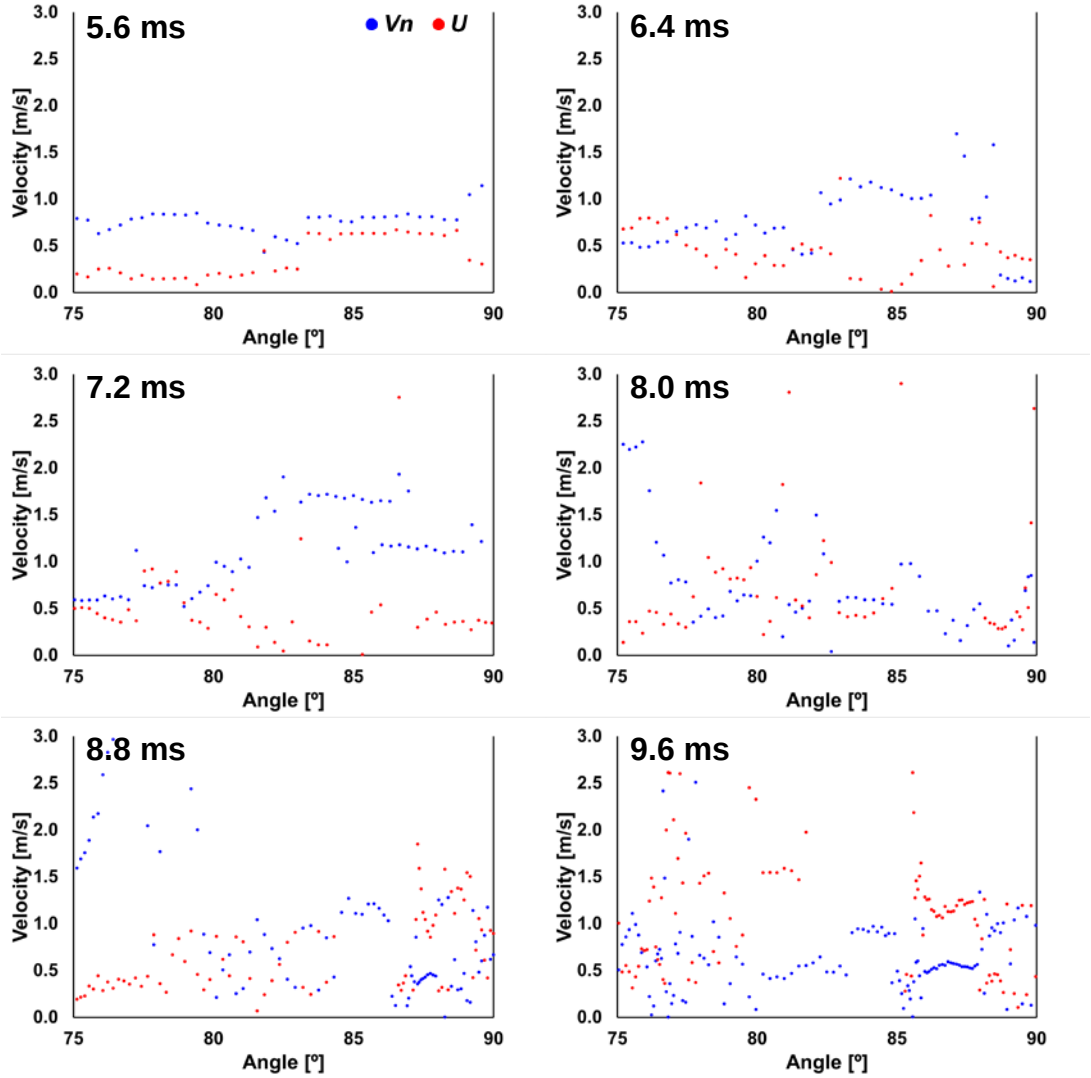

Figure 5.30 Change of normal unburned gas velocity V_n (blue dot) and burning velocity U (red dot) with respect to angle in the section 2 of the experimental case 2. Fuel: CH_4-air / ϕ: 0.6 / t_{ign}: 36.2° CA bTDC / P_0: 4 bar / T_0: 414 K

one at the other region, and the S between 80 and 85º is larger than the one at the other region. The local change of wavenumber ranges between -0.6 and 1.0, and the one of flame propagation speed ranges between 0.8 and 2.9 m/s.

Figure 5.30 shows the change of normal unburned gas velocity and burning velocity with respect to angle in the section 2. The blue and red dots in the figure represent normal unburned gas velocity V_n and burning velocity U at each angle respectively. When time is 5.6 ms, the V_n seems stable and the value is about 0.8 m/s. And although the U between 85 and 90º is larger than the one at the other angle, U locally does not fluctuate much, and ranges

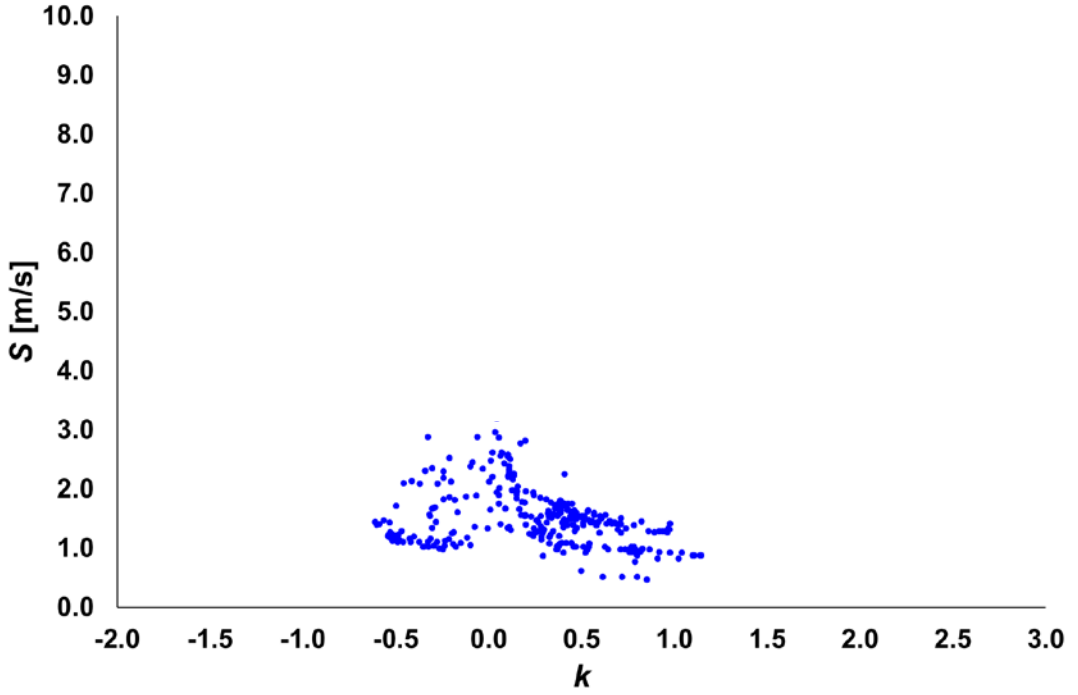

Figure 5.31 Variation of flame propagation speed *S* with respect to wavenumber *k* in the section 2 of the experimental case 2. Fuel: CH_4-air / ϕ: 0.6 / t_{ign}: 36.2° CA bTDC / P_0: 4 bar / T_0: 414 K

between 0.2 and 0.6 m/s. At 6.4 ms when wavenumber changes with respect to angle, V_n and U start fluctuating locally. V_n generally increases, and the V_n between 85 and 90º is larger than the one at the other angle. The U at that region is smaller than the one at the other angle. The local change of V_n and U at 6.4 ms is mostly kept at 7.2 ms. When time 8.0 ms, V_n generally decreases, and the U between 80 and 85º starts increasing. From 8.8 to 9.6 ms, although V_n still fluctuates locally, it generally keeps its value. During the time, U fluctuates more severely, and generally increases. The local change of normal unburned gas velocity ranges between -0.1 and 2.3 m/s, and the one of burning velocity ranges between 0.2 and 2.5 m/s.

Figure 5.31 shows the variation of flame propagation speed S with respect to wavenumber k in the section 2. Where k is positive, S decreases as k increase. Especially, where $0 < k < 0.3$, S decreases dramatically as k increases. As k becomes larger than 0.3, S progressively diminishes. Where k is negative, the diametrically opposite phenomenon is shown. As k decreases, S also decreases. Where $-0.3 < k < 0$, S decreases dramatically as k decreases. It is shown that S rises as k approaches zero. Especially, where $-0.3 < k < 0.3$, the change of S is very much: this is also seen in the section 2 of the lean hydrogen-air mixture.

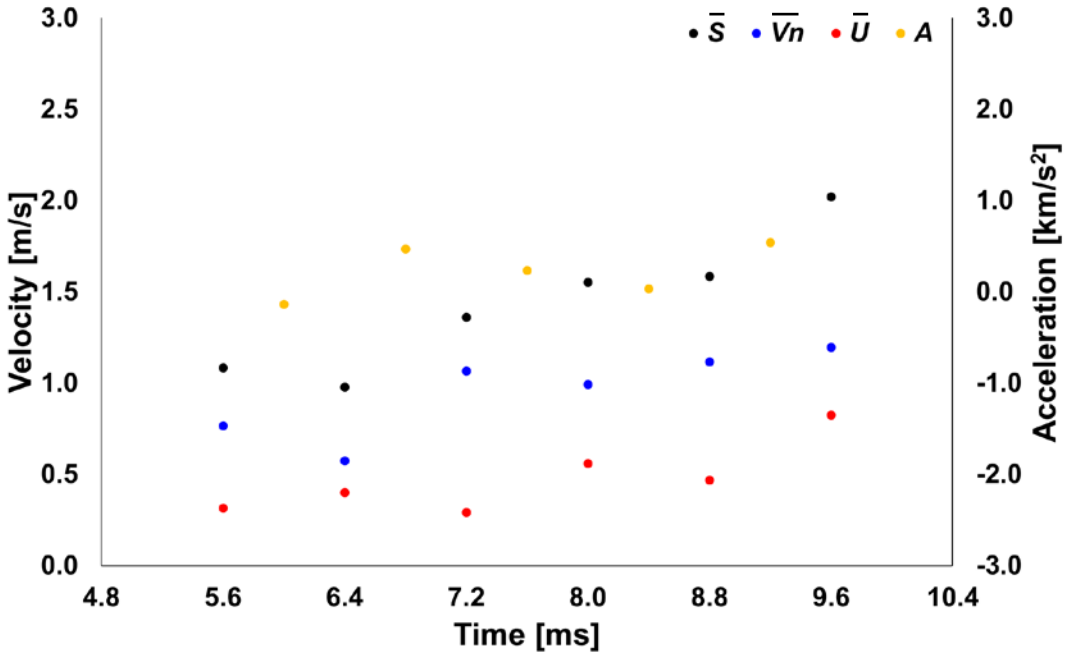

Figure 5.32 Variation of local mean flame propagation speed $\bar{S}$ (black dot), normal unburned gas velocity $\overline{V_n}$ (blue dot), burning velocity $\bar{U}$ (red dot), and acceleration *A* (yellow dot) with respect to time in the section 2 of the experimental case 2. Fuel: CH_4-air / ϕ: 0.6 / t_{ign}: 36.2° CA bTDC / P_0: 4 bar / T_0: 414 K

Figure 5.32 shows the variation of local mean flame propagation speed $\bar{S}$ (black dot), normal unburned gas velocity $\overline{V_n}$ (blue dot), burning velocity $\bar{U}$ (red dot), and acceleration *A* (yellow dot) with respect to time in the section 2. While the flame propagates, $\bar{S}$ gradually increases from 1.1 to 2.1 m/s. Since there is not a large increase in $\bar{S}$, the value of *A* is close to zero. After 7.2 ms, while $\bar{S}$ increases, although $\bar{U}$ also increases, $\overline{V_n}$ barely changes. It seems that $\bar{U}$ is the main factor in the increase of $\bar{S}$. As seen in Figure 5.28, a concave shape of flame appears in earnest at 8.0 ms. At this moment, the preferential diffusion of the methane takes place and leads to the rise of the $\bar{U}$.

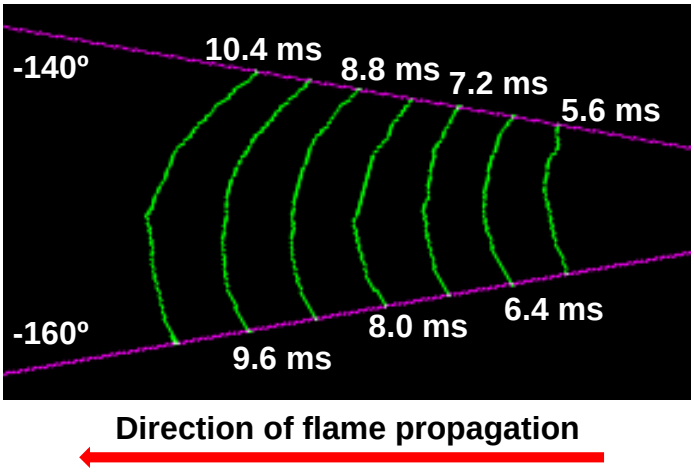

Figure 5.33 The enlarged section 3 image

Figure 5.33 shows the enlarged image of the section 3. Although the region near -140º seems relatively concave, it is seen that the variation of the flame shape with respect to angle at each time is significantly smooth compared to the section 1 and 2. While the flame propagates, its shape is kept without a large disturbance. Compared with the lean hydrogen-air mixture, the local variation of a flame shape seems less, and the flame propagation speed is faster.

Figure 5.24 shows the change of flame propagation speed *S* (black dot) and wavenumber *k* (yellow dot) with respect to angle in the section 3. Generally, the *k* between -160 and -150º is larger than the one between -150 and -140º, and the difference between the two regions is kept until 9.6 ms. Concentrating on the region between -160 and -150º where the corresponding *k* is about 1.0, the *k* barely change with respect to time, and the *S* ranges from 1.3 to 1.5 m/s. At 8.0 ms, although the *k* locally increases up to 1.3, the increase is not much, and the variation of the corresponding *S* is also little. In the section 3, it seems that the variation of *S* with respect to *k* is not much.

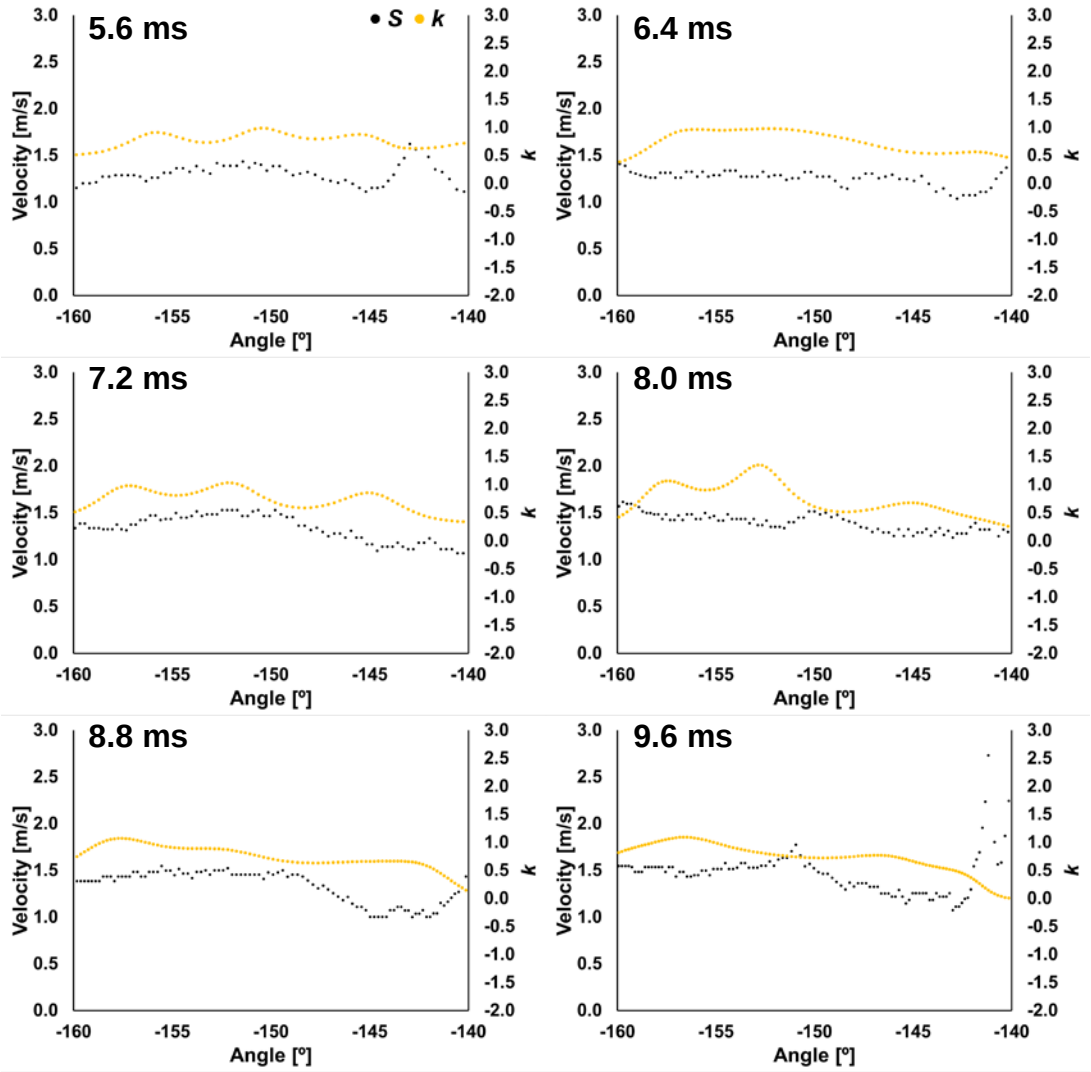

Figure 5.34 Change of flame propagation speed *S* (black dot) and wavenumber *k* (yellow dot) with respect to angle in the section 3 of the experimental case 2. Fuel: CH_4-air / ϕ: 0.6 / t_{ign}: 36.2° CA bTDC / P_0: 4 bar / T_0: 414 K

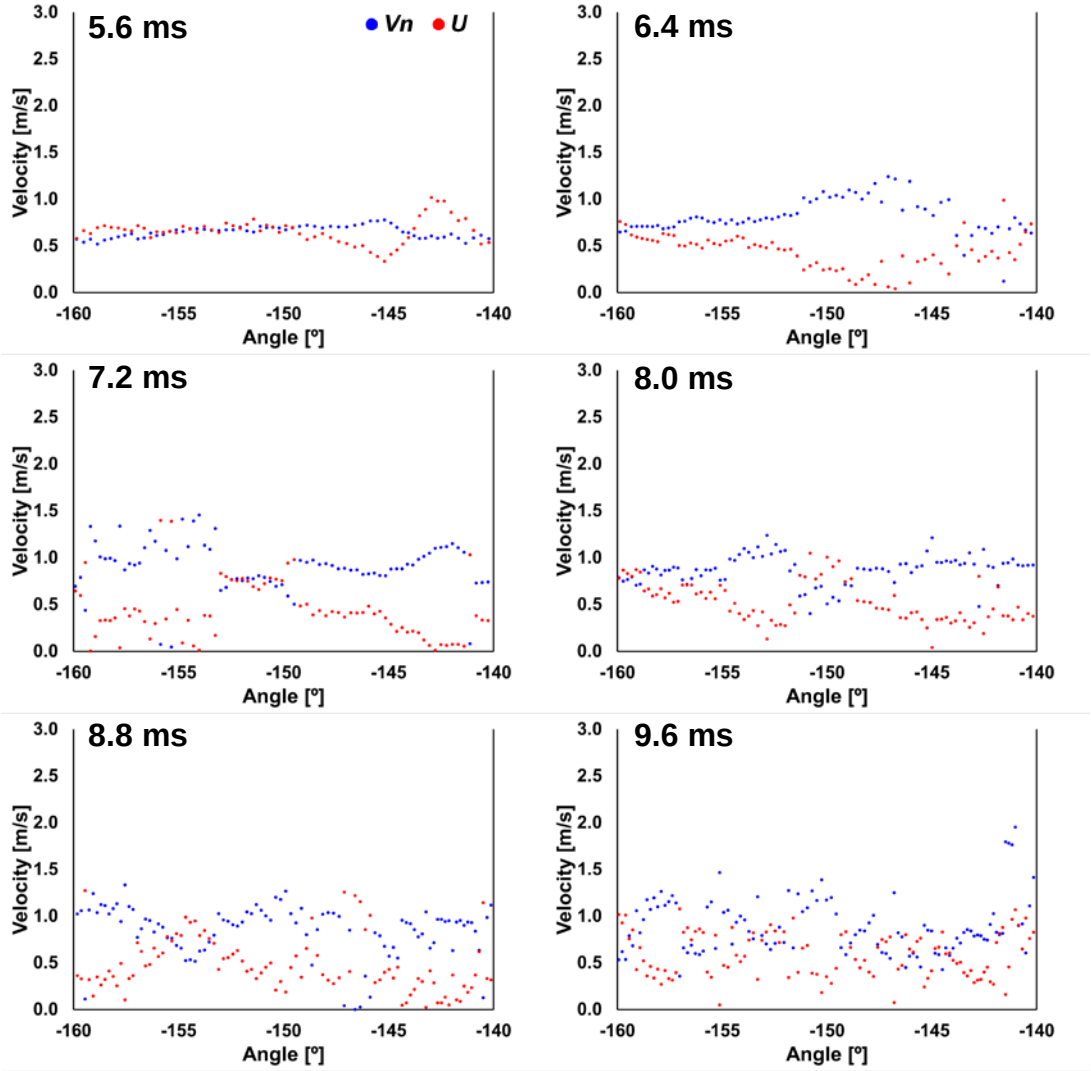

Figure 5.35 Change of normal unburned gas velocity V_n (blue dot) and burning velocity U (red dot) with respect to angle in the section 3 of the experimental case 2. Fuel: CH_4-air / ϕ: 0.6 / t_{ign}: 36.2° CA bTDC / P_0: 4 bar / T_0: 414 K

Figure 5.35 shows the change of normal unburned gas velocity V_n (blue dot) and burning velocity U (red dot) with respect to angle in the section 3. Focusing on the region between -160 and -150º, V_n and U repeat increase and decrease with respect to time. When time is 5.6 ms, V_n and U are stable and about 0.5 m/s. From 6.4 and to 7.2 ms, the two velocities fluctuate with respect to angle, V_n generally increase, and U decreases. At 8.0 ms, V_n decreases, and U increases. It seems that the two velocities become stable again. When time is 8.8 and 9.6 ms, the two velocities fluctuate with respect to angle again. In the section 3, although V_n and U changes with respect to angle and time, their changes are not much compared to the ones in the

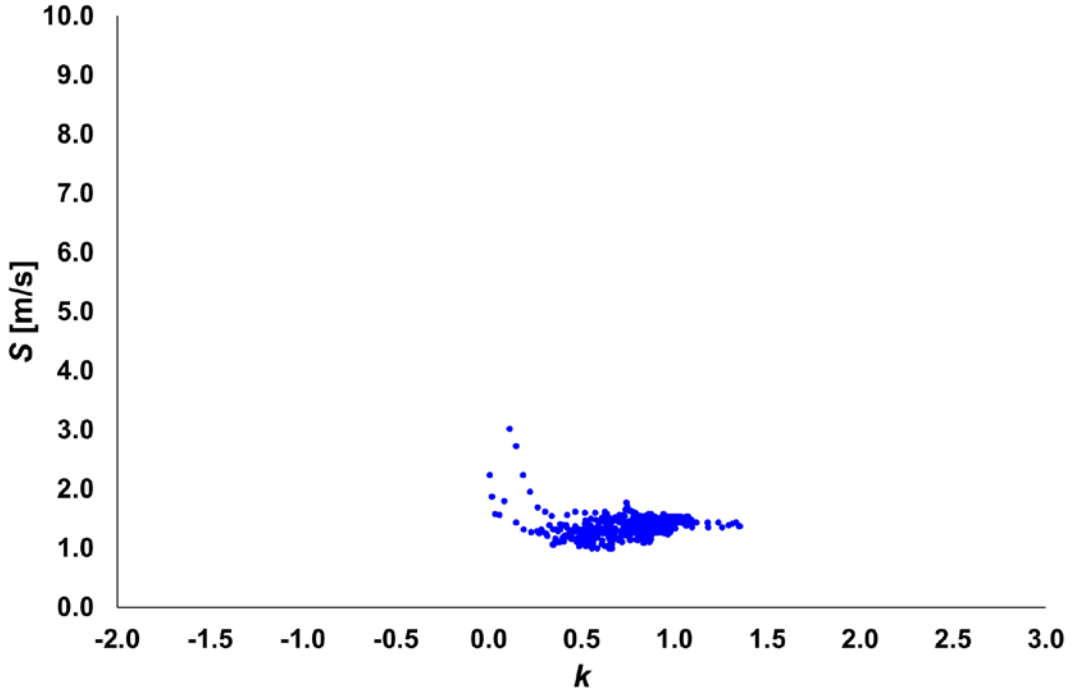

Figure 5.36 Variation of flame propagation speed *S* with respect to wavenumber *k* in the section 3 of the experimental case 2. Fuel: CH_4-air / ϕ: 0.6 / t_{ign}: 36.2° CA bTDC / P_0: 4 bar / T_0: 414 K

section 1 and 2. V_n ranges between 0.5 and 1.4 m/s, and *U* changes between 0.1 and 1.2 m/s. Where the change of a flame shape with respect to angle at each time is smooth and the flame shape is kept, it seems that the changes of V_n and *U* are not much.

Figure 5.36 shows the variation of flame propagation speed *S* with respect to wavenumber *k* in the section 3. As seen in Figure 5.33, the flame contour line at each time is curved smoothly with respect to angle. And as the flame propagates, the flame shape is kept without any large disturbance. Owing to these, most of the wavenumbers range from 0.5 to 1.0, and the flame propagation speed has barely changes in the range.

Figure 5.37 shows the variation of local mean flame propagation speed $\bar{S}$ (black dot), normal unburned gas velocity $\overline{V_n}$ (blue dot), burning velocity $\bar{U}$ (red dot), and acceleration *A* (yellow dot) with respect to time in the section 3. Different from the section 1 and 2, as the flame propagates, $\bar{S}$ barely changes in the section 3, and the value is about 1.3 m/s. Since $\bar{S}$ keeps its speed, *A* barely changes. Except for 5.6 ms, $\overline{V_n}$and $\bar{U}$ barely change and seem stable. Their values are about 0.8 and 0.5 m/s respectively.

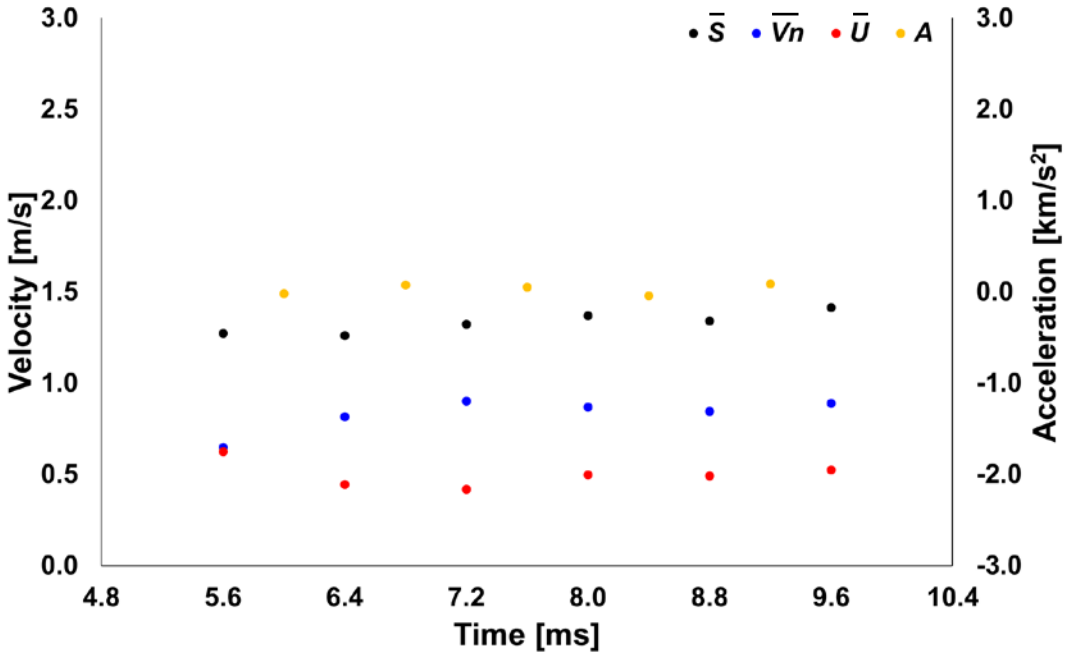

Figure 5.37 Variation of local mean flame propagation speed $\bar{S}$ (black dot), normal unburned gas velocity $\overline{V_n}$ (blue dot), burning velocity $\bar{U}$ (red dot), and acceleration *A* (yellow dot) with respect to time in the section 3 of the experimental case 2. Fuel: CH_4-air / ϕ: 0.6 / t_{ign}: 36.2° CA bTDC / P_0: 4 bar / T_0: 414 K

As seen in Figure 5.35, the normal unburned gas velocity and burning velocity change with respect to angle and time. However, in the case that burning velocity at a certain region increase (decrease), the one at the adjacent region decrease (increase). And burning velocity at a certain region repeats increase and decrease with respect to time: this spatial and temporal change is seen in the normal unburned gas velocity. Because of the thermal expansion of the burned gas and the preferential diffusion of the deficient methane, the normal burned gas velocity and burning velocity change with respect to angle and time (Hertzberg 1989, Nakahara and Kido 1998, Balusamy et al. 2011, Long and Hargrave 2011). However, it seems that such the spatial and temporal change of the two velocities is not as large as in the section 1 and 2.

Figure 5.38 shows the change of local mean wavenumber $\bar{k}$ with respect to time (A) and the relevant vorticity histogram (B) for the section 1. In Figure 5.38 (B), a positive value means the clockwise vorticity of unburned gas, and a negative value indicates the anticlockwise vorticity. The light blue, brown, grey, yellow, dark blue, and green lines are the histograms of the vorticity data that were obtained at 5.6, 6.4, 7.2, 8.0, 8.8, and 9.6 ms respectively. And each vorticity data are for the area between two consecutive flame contour lines:

these colour lines are applied in the same way to the section 2 and 3. Since an area between two consecutive flame contour lines becomes large as the flame propagates, the number of vorticity data becomes large. Hence, the unit of frequency is represented as percent in order to compare the change of histograms.

In Figure 5.38 (A), $\bar{k}$ slightly decreases until 7.2 ms, and then slightly increases. The flame is a convex shape and keeps its shape without a large disturbance as shown in Figure 5.23. Until 7.2 ms, the frequency of clockwise vorticity is larger than that of anticlockwise vorticity, and the shape of the histogram is similarly kept. From 7.2 to 8.8 ms, the shape of the histogram is inclined to the right direction, and it is seen that the frequency of clockwise vorticity increases. At 8.8 ms, the shape of the histogram is slightly inclined to the left direction, and the shape of the histogram is kept until 10.4 ms. During the time, $\bar{k}$ is barely changed.

Figure 5.39 shows the change of local mean wavenumber $\bar{k}$ with respect to time (A) and the relevant vorticity histogram (B) for the section 2. Until 8.0 ms, $\bar{k}$ gradually decreases: as seen in Figure 5.28, the flame changes into a concave shape. During the time, the frequency of clockwise vorticity is larger than that of anticlockwise vorticity, and the shape of the histogram is inclined to the right direction. From 8.8 to 10.4 ms, $\bar{k}$ increases, and after the shape of the histogram is inclined more to the right direction, it is inclined again to the left direction. However, the frequency of clockwise vorticity is still larger than that of anticlockwise vorticity.

Figure 5.40 shows the change of local mean wavenumber $\bar{k}$ with respect to time (A) and the relevant vorticity histogram (B) for the section 3. $\bar{k}$ barely changes with respect to time. As shown in Figure 5.33, the flame is curved smoothly with respect to time, and the flame shape is kept without any large perturbation. The frequency of clockwise vorticity is larger than that of anticlockwise vorticity. Although the shape of the histogram is inclined to the right direction. It is not changed much with respect to time.

It seems difficult to suggest a particular dominant vorticity about a certain value of $\bar{k}$. However, the change of $\bar{k}$ with respect to the change of a histogram shape may be said. Where $\bar{k}$ keeps increasing or decreasing, it seems that the shape of a histogram is kept. And where the sign of gradient of $\bar{k}$ changes, an increase in the frequency of clockwise vorticity occurs.

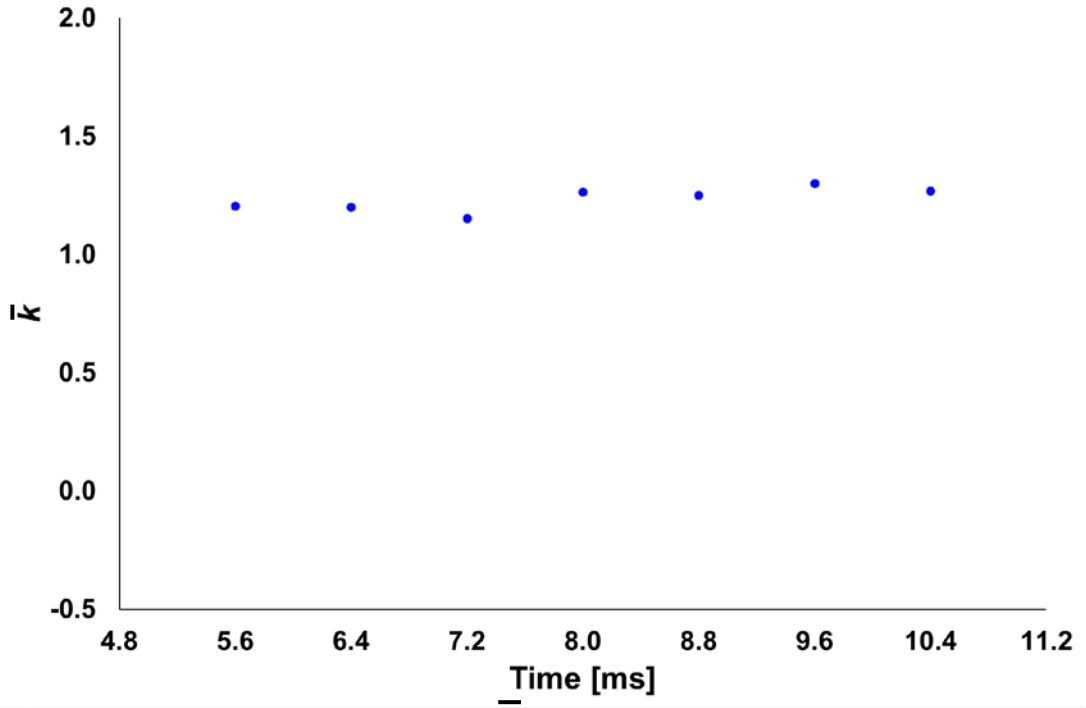

(A) $\bar{k}$ vs time

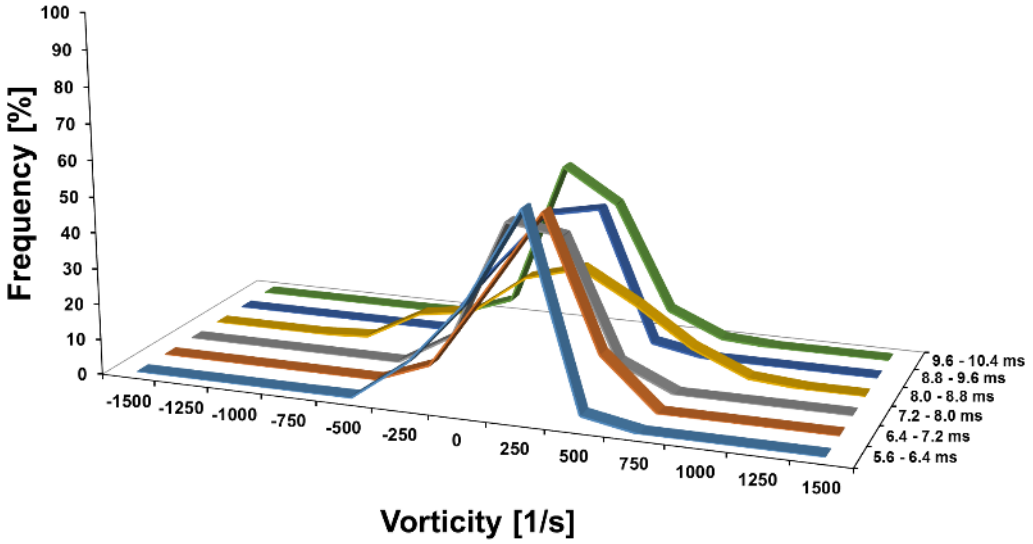

(B) Histogram

Figure 5.38 Change of the local mean wavenumber $\bar{k}$ with respect to time (A) and the relevant vorticity histogram (B) for the section 1 of the experimental case 2. Fuel: CH_4-air / ϕ: 0.6 / t_{ign}: 36.2° CA bTDC / P_0: 4 bar / T_0: 414 K

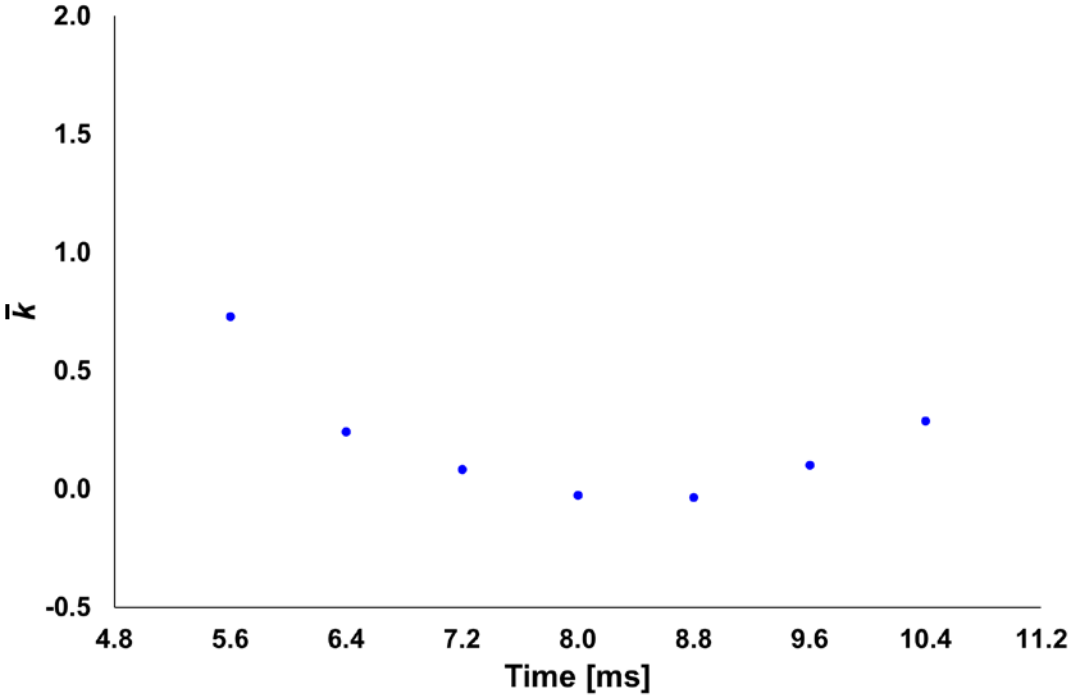

(A) $\bar{k}$ vs time

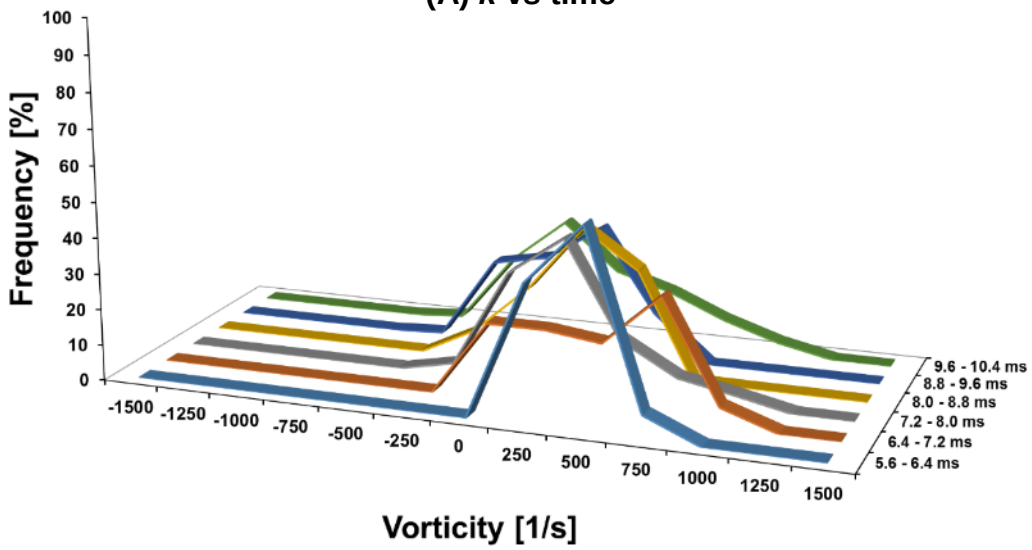

(B) Histogram

Figure 5.39 Change of the local mean wavenumber $\bar{k}$ with respect to time (A) and the relevant vorticity histogram (B) for the section 2 of the experimental case 2. Fuel: CH_4-air / ϕ: 0.6 / t_{ign}: 36.2° CA bTDC / P_0: 4 bar / T_0: 414 K

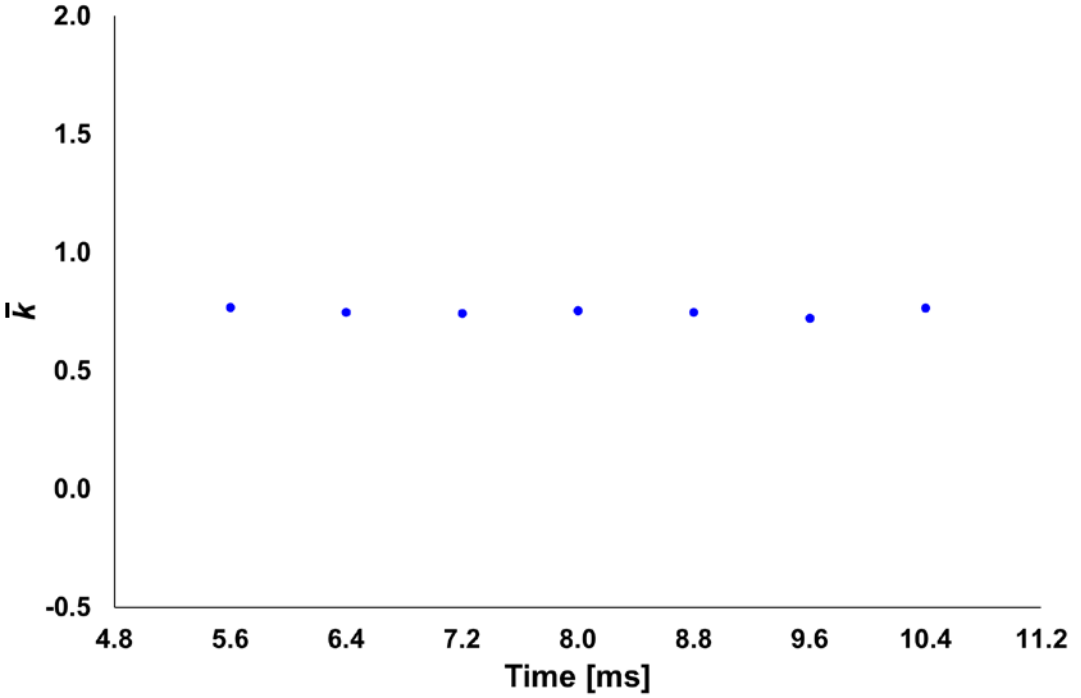

(A) $\bar{k}$ vs time

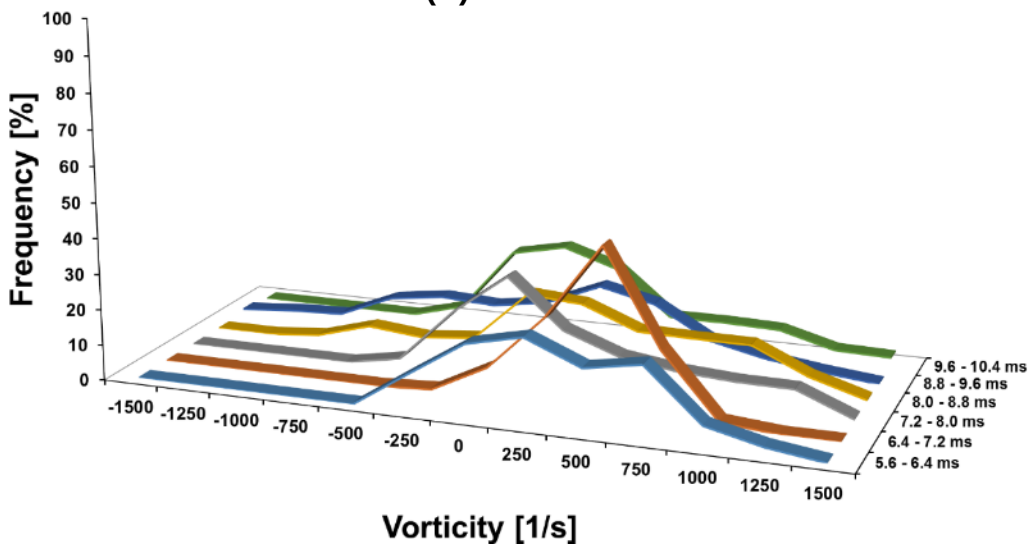

(B) Histogram

Figure 5.40 Change of the local mean wavenumber $\bar{k}$ with respect to time (A) and the relevant vorticity histogram (B) for the section 3 of the experimental case 2. Fuel: CH_4-air / ϕ: 0.6 / t_{ign}: 36.2° CA bTDC / P_0: 4 bar / T_0: 414 K

5.4 Result of the rich propane-air mixture

A rich propane-air mixture was adopted in the experimental case 3. The equivalence ratio of the mixture was 2.0, and the ignition timing t_{ign} was 36.2º CA bTDC. In order to obtain the flow field of unburned gas, the double frame mode was used in the PIV system, and the inter-frame time between double frames was 0.1 ms. The time step between two consecutive flame images to measure flame propagation speed was 0.8 ms. When ignition started, the initial pressure P_0 and temperature T_0 were 4 bar and 414 K respectively.

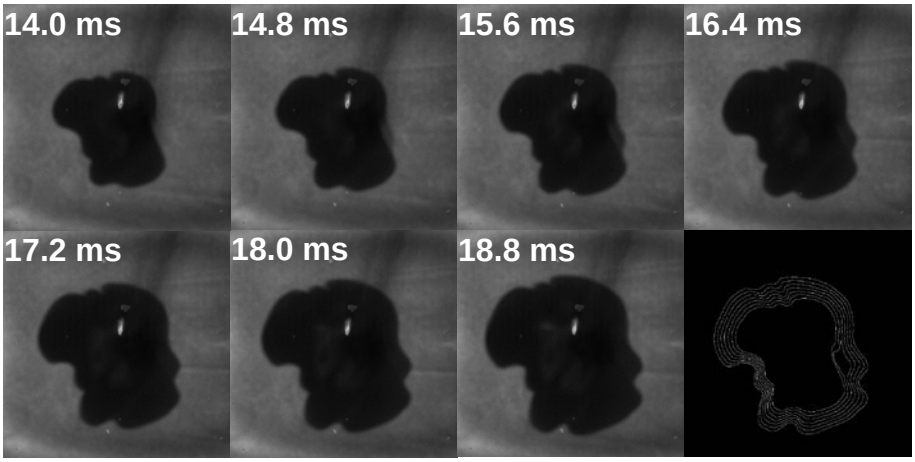

Figure 5.41 Propagating flame images and the corresponding edges image at the experimental case 3. Fuel: C_3H_8-air / ϕ: 2.0 / t_{ign}: 36.2° CA bTDC / P_0: 4 bar / T_0: 414 K

Figure 5.41 shows the propagating flame images with respect to time and the corresponding flame edges image. In each flame image, the white digit represents elapsing time after the start of ignition. The black area in the flame images indicate burned area, the relatively bright grey area is unburned area, and the white part near the centre is a spark plug. When time is 14.0 ms, the flame already becomes wrinkled, and several convex and concave parts appear. As shown in the studies of Markstein (1951) and Izumikawa et al. (1988), the cell size of the rich C_3H_8 mixture is smaller than that of the lean methane-mixture. After the flame is distorted at 14.0 ms, it tend to keep its shape to the end, which is also shown in the lean hydrogen- and methane-mixture.

Figure 5.42 shows the flame edges image (A) and the change of the wavenumber with respect to angle at each time (B). The green lines in Figure

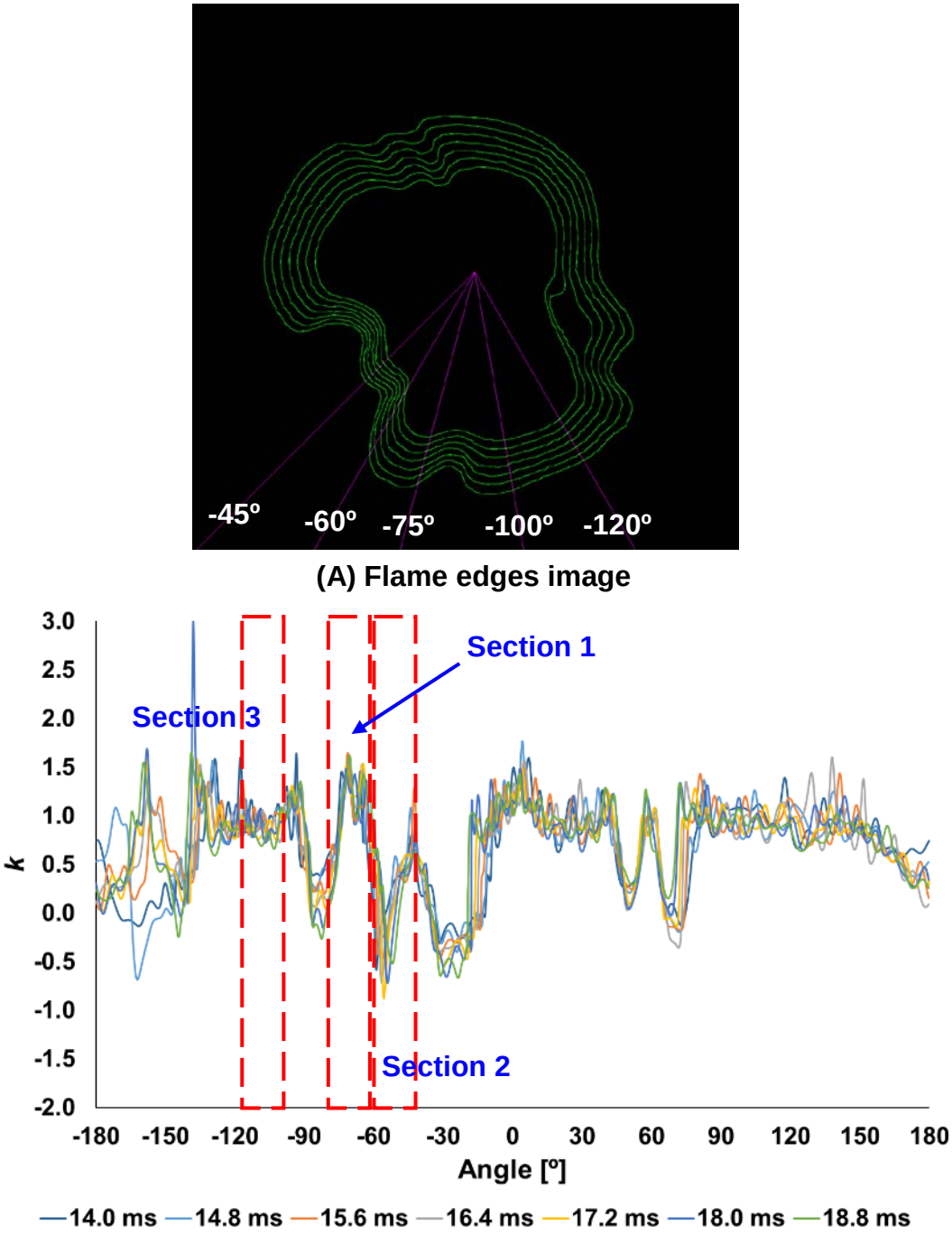

Figure 5.42 Selection of the local areas through the flame edges image (A) and the change of the relevant wavenumber *k* (B)

5.42 (A) indicate a flame contour line at each time. Referring to Figure 5.42 (A) and (B), the section 1, 2, and 3 were selected. In the section 1, flame has a convex shape, and wavenumber mostly ranges between 0.5 and 1.5. The flame of the section 2 changes into a concave shape, and wavenumber varies

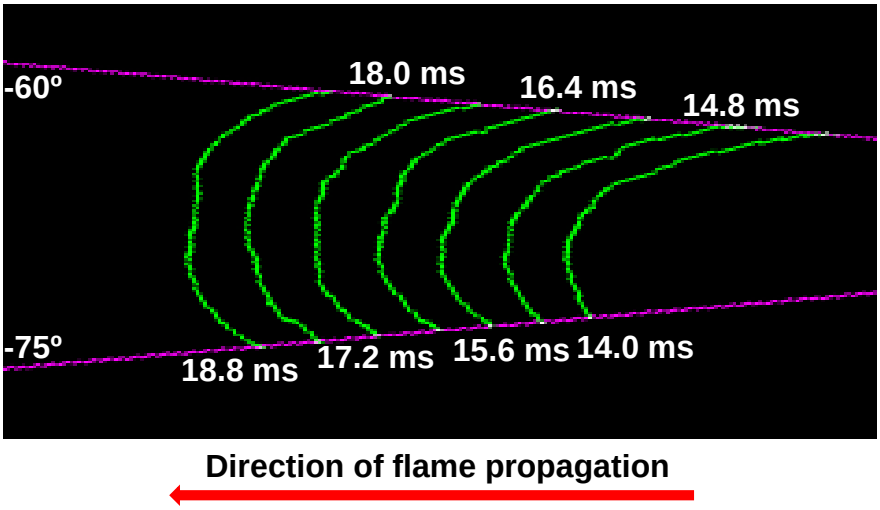

Figure 5.43 The enlarged section 1 image

from -0.9 to 0.6. In the section 3, the flame shape is similar to the arc of a circle, and the range of wavenumber is mostly between 0.7 and 1.3.

Figure 5.43 shows the enlarged image of the section 1. At 14.8 ms, the flame contour line near -75º is convex, and the one near -60º is concave. As the flame propagates, the convex part seems to move toward -70º, and concave parts emerge near -75 and -60. This shape is kept continuously, and a locally large distortion is barely seen in each flame contour line.

Figure 5.44 shows the change of flame propagation speed *S* (black dot) and wavenumber *k* (yellow dot) with respect to angle in the section 1. Except for the region near -60º at 14.0 ms, *k* mostly ranges between 0.5 and 1.5, and *S* varies from 0.6 to 1.0 m/s. Focusing on the region between -70 and -65º where a convex shape is kept, *k* is almost kept until 14.8 ms and the corresponding *S* barely changes. At 15.6 and 16.4 ms, the *k* near-65º generally decreases up to 1.0, *S* slightly increases and its value is about 1.0 m/s. At 17.2 and 18.0 ms, *k* continues to increase, and its value is about 1.5. During the time, *S* decreases up to 0.7 m/s, and the change is not large. The relationship between *k* and *S* is inversely proportional, and is similar to the section 1 of the lean hydrogen- and methane-air mixture.

Figure 5.45 shows the change of normal unburned gas velocity V_n (blue dot) and burning velocity *U* (red dot) with respect to angle in the section 1. Since a convex part is dealt with in the section 1, the change of V_n and *U* at the region between -70 and -65º is mainly discussed. At 14.0 ms, V_n and *U* are about 0.5 and 0.2 m/s respectively. When time is 14.8 ms, V_n barely change, and *U* slightly increases up to 0.4 m/s. At 15.6 ms, V_n and *U* barely change,

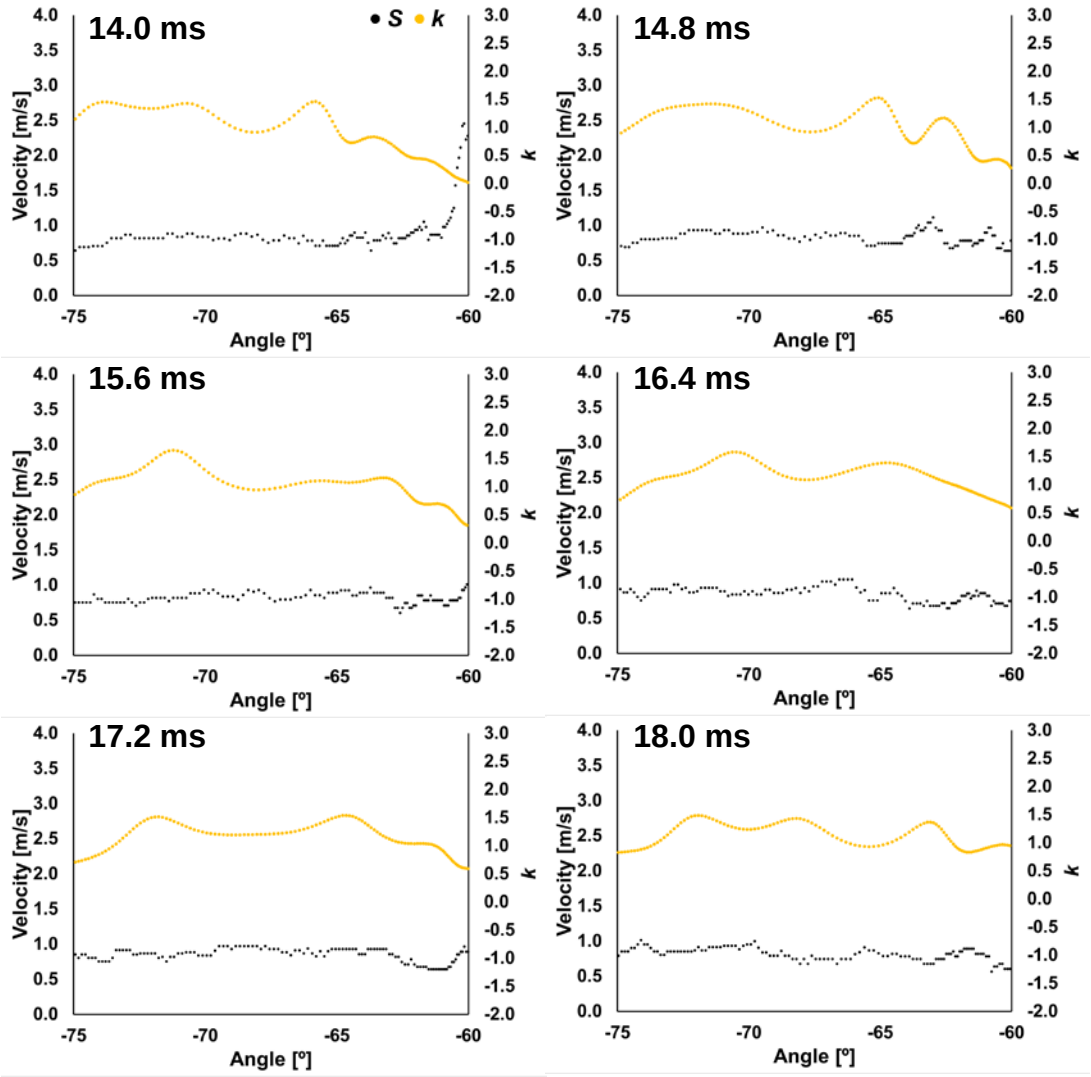

Figure 5.44 Change of flame propagation speed *S* (black dot) and wavenumber *k* (yellow dot) with respect to angle in the section 1 of the experimental case 3. Fuel: C_3H_8-air / ϕ: 2.0 / t_{ign}: 36.2° CA bTDC / P_0: 4 bar / T_0: 414 K

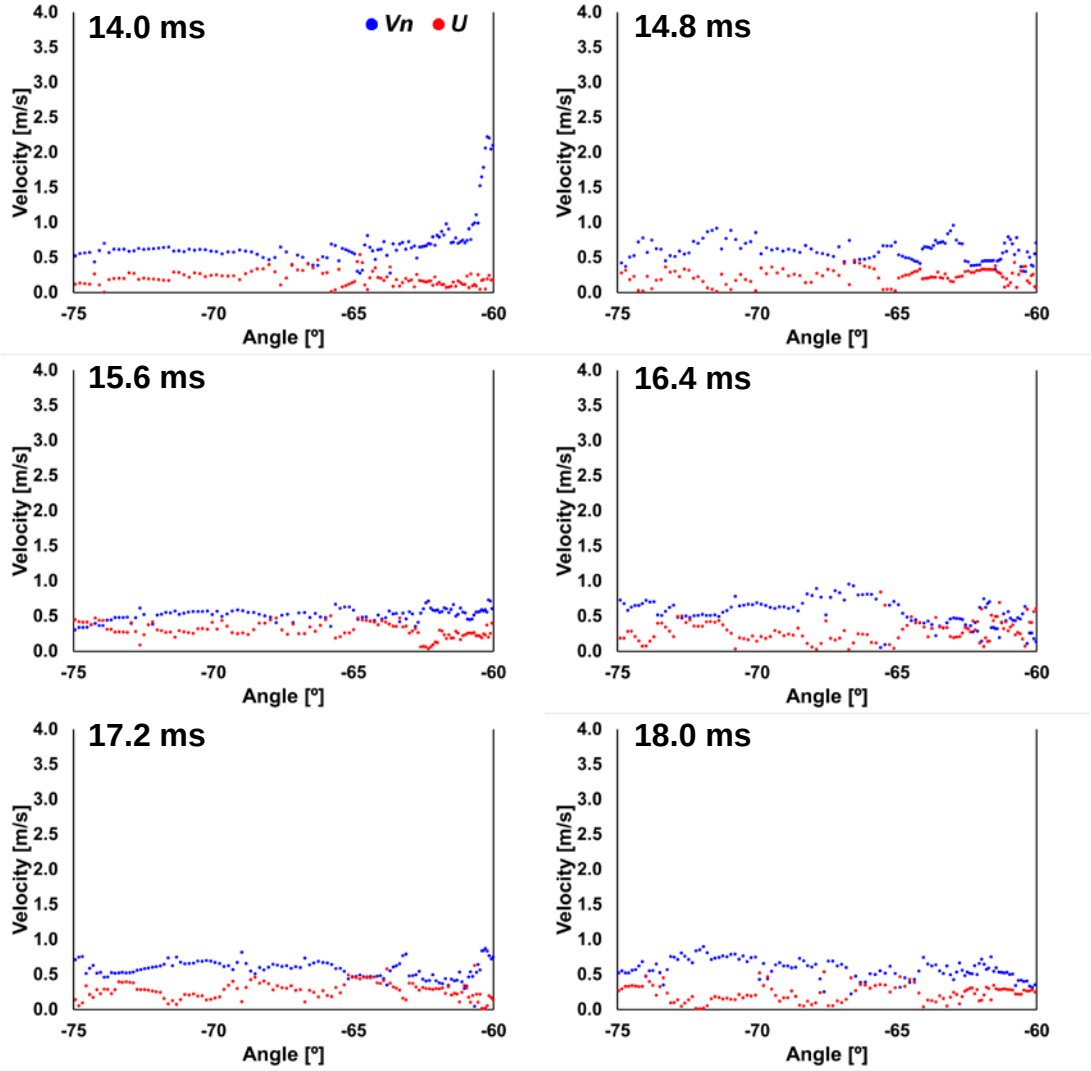

Figure 5.45 Change of normal unburned gas velocity V_n (blue dot) and burning velocity U (red dot) with respect to angle in the section 1 of the experimental case 3. Fuel: C_3H_8-air / ϕ: 2.0 / t_{ign}: 36.2° CA bTDC / P_0: 4 bar / T_0: 414 K

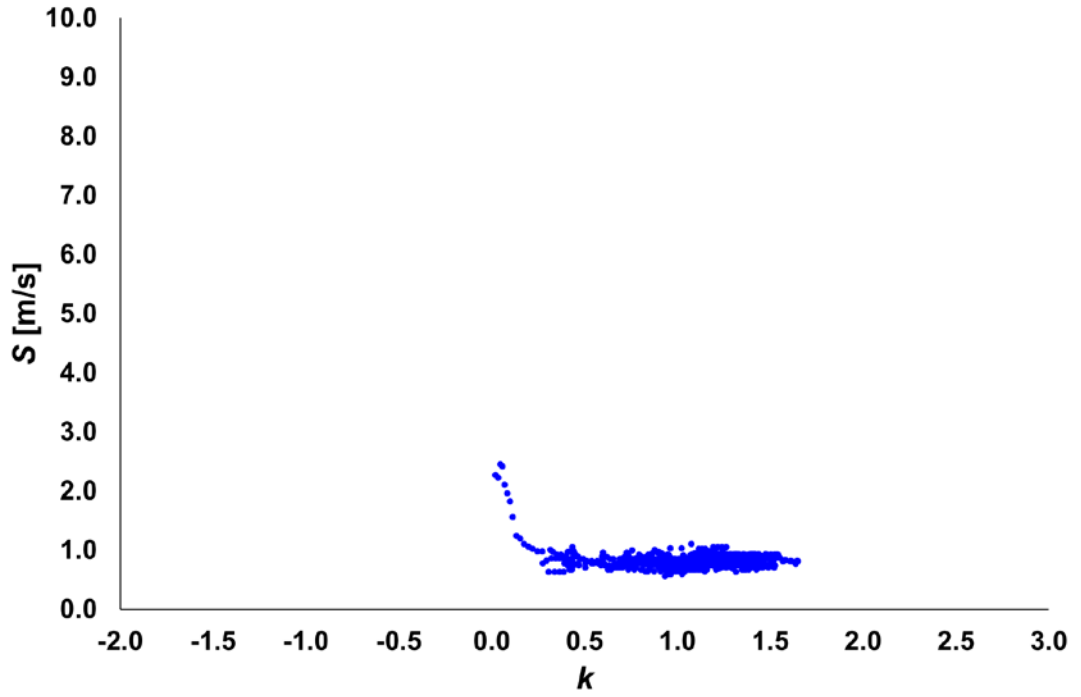

Figure 5.46 Variation of flame propagation speed *S* with respect to wavenumber *k* in the section 1 of the experimental case 6. Fuel: C_3H_8-air / ϕ: 2.0 / t_{ign}: 36.2° CA bTDC / P_0: 4 bar / T_0: 414 K

and their values are about 0.5 and 0.4 m/s respectively. When time is 16.4 ms, V_n slightly increases up to 0.8 ms, and *U* decreases to 0.2 m/s. From 17.2 to 18.0 ms, V_n decreases again to 0.6 m/s, and *U* is about 0.4 m/s. It seems that V_n increases (decrease) after *U* increases (decreases). And when *U* at the region between -70 and -65º increases (decreases), the one at the neighbouring regions decreases (increases), which is also seen in V_n.

Figure 5.46 shows the variation of flame propagation speed *S* with respect to wavenumber *k* in the section 1. *k* mostly ranges between 0.5, and *S* varies from 0.6 to 1.0 m/s. As *k* becomes larger than 0.5, *S* gradually decreases. However, the change of *S* is not large, and the gradient is also very gentle. When *k* approaches zero, *S* increases relatively sharply. When flame is a convex shape, *k* is positive. And the relationship between and *S* and *k* is inversely proportional, and is also seen in the one in the section 1 of the lean hydrogen- and methane-air mixture.

Figure 5.47 shows the variation of local mean flame propagation speed $\bar{S}$ (black dot), normal unburned gas velocity $\overline{V_n}$ (blue dot), burning velocity $\bar{U}$ (red dot), and acceleration *A* (yellow dot) with respect to time in the section 1. While the flame develops, the change of $\bar{S}$ is little, and the value is about 1.0 m/s.

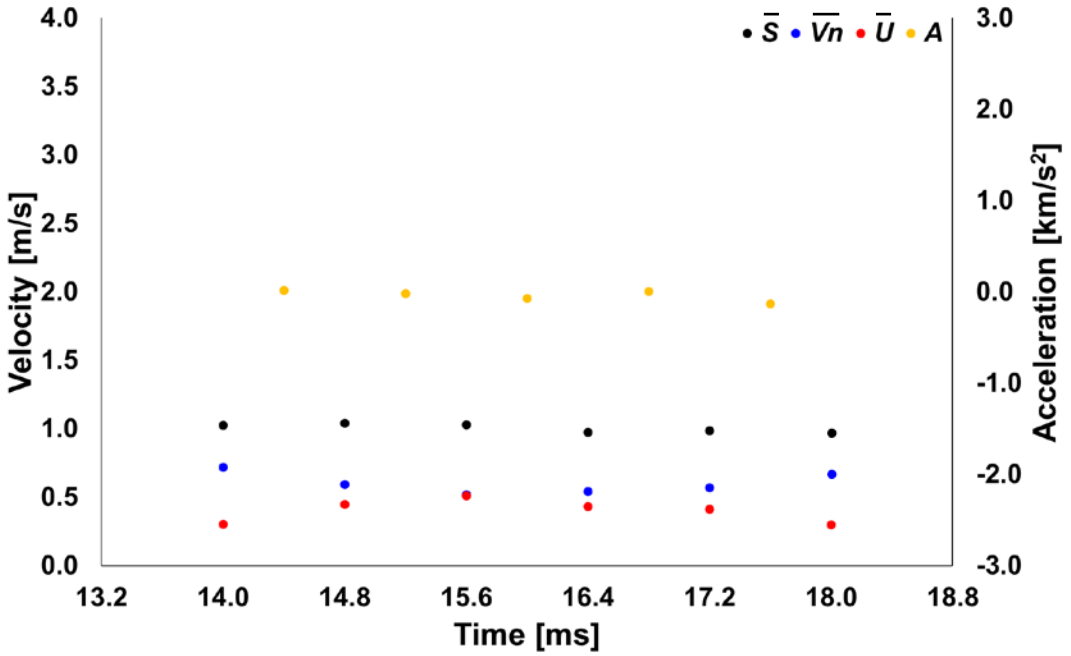

Figure 5.47 Variation of local mean flame propagation speed $\bar{S}$ (black dot), normal unburned gas velocity $\overline{V_n}$ (blue dot), burning velocity $\bar{U}$ (red dot), and acceleration *A* (yellow dot) with respect to time in the section 1 of the experimental case 3. Fuel: C_3H_8-air / ϕ: 2.0 / t_{ign}: 36.2° CA bTDC / P_0: 4 bar / T_0: 414 K

Because of this, *A* is about zero, and the flame in the section 1 does not accelerate or deaccelerate with time.

Until 15.6ms, $\overline{V_n}$ gradually decreases from 0.7 to 0.5 m/s. Simultaneously, $\bar{U}$ gradually increases from 0.2 to 0.5 m/s. From 14.0 to 15.6 ms, the preferential diffusion of the oxygen occurs at each flame. The preferential diffusion appearing at concave regions improves the equivalence ratio of the local mixture, which leads to the increase of local burning velocity (Hertzberg 1989, Nakahara and Kido 1998). Hence, it can be thought that the increase of the local burning velocity at the concave regions mainly affects the increase of the $\bar{U}$.

From 16.4 to 18.0 ms, $\overline{V_n}$ gradually increases again up to 0.7 m/s. While $\overline{V_n}$ rises, $\bar{U}$ gradually decreases up to 0.2 m/s. While $\bar{U}$ diminishes, a convex region gradually becomes larger than the neighbouring concave regions. The preferential diffusion of the oxygen at the convex region makes the composition of the local region become richer, and hence, $\bar{U}$ gradually decreases (Hertzberg 1989, Nakahara and Kido 1998).

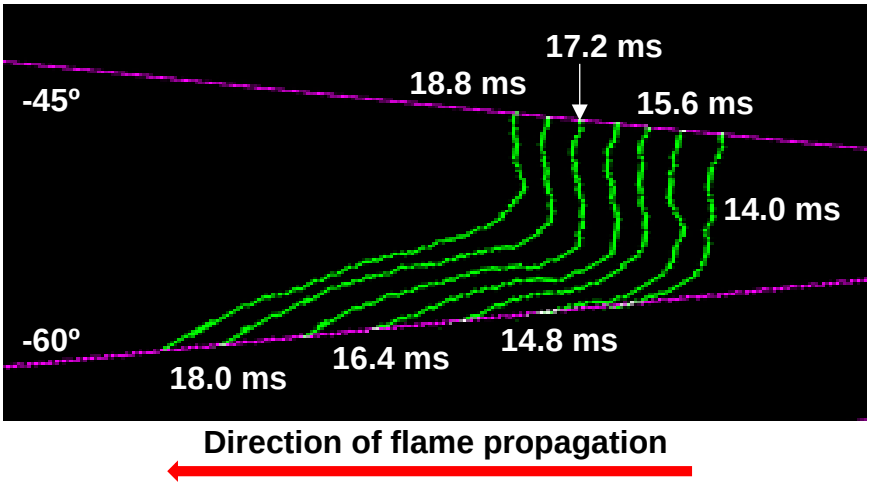

Figure 5.48 The enlarged section 2 image

Figure 5.48 shows the enlarge image of the section 2. At 14.0 ms, the flame contour line seems relatively less curved than other lines. The region in the vicinity of -60º is concave, and the other is convex. As the flame propagates, the region near -60º gradually changes into a convex shape, and the concave region at 14.0 ms seems to move gradually toward -45º. At each time, there are the points where the flame contour line is sharply curved. Compared to the section 2 of the lean hydrogen- and methane-air mixture, although the flame is distorted, the flame shape seems to be kept continuously.

Figure 5.49 shows the change of flame propagation speed *S* (black dot) and wavenumber *k* (yellow dot) with respect to angle in the section 2. At 14.0 ms, the *S* near -60º dramatically increases while the *k* changes from 0.3 to -0.5. The abnormal increase of *S* is also seen in the other graphs. The unnatural increase is artefact. Where *k* changes dramatically, there is an apex in the vicinity of the relevant region or the flame surface is changed with a sharp point. This can cause the undesirable derivation of the normal direction at that region, which can lead to the large increase of *S*. Such *S* data are artefacts and not reliable. Therefore, the abnormal S values are excluded in Figure 5.51 and Figure 5.52. Except for the abnormal *S* data, *k* mostly ranges between -0.9 and 0.6, and S varies from 0.4 to 1.5 m/s. Where *k* is positive, *S* gradually decrease as it increases. On the contrary, where *k* is negative, *S* gradually increases as it increases.

Figure 5.50 show the change of normal unburned gas velocity V_n (blue dot) and burning velocity *U* (red dot) with respect to angle in the section 2. At 14.0 and 14.8 ms, V_n and *U* near -60º dramatically change, which is similar to the *S* in Figure 5.49. The abnormal increase of V_n appears where wavenumber

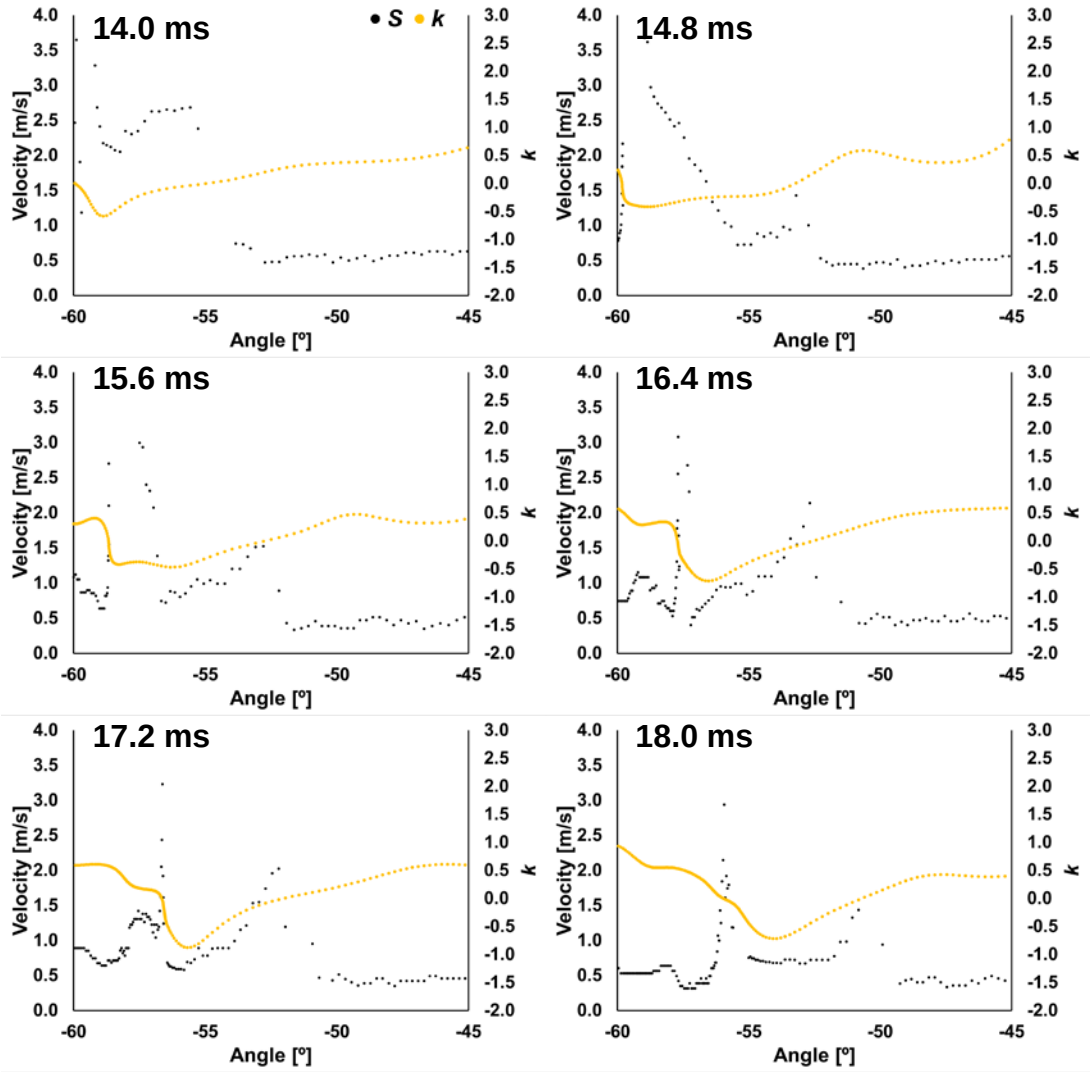

Figure 5.49 Change of flame propagation speed *S* (black dot) and wavenumber *k* (yellow dot) with respect to angle in the section 2 of the experimental case 3. Fuel: C_3H_8-air / ϕ: 2.0 / t_{ign}: 36.2° CA bTDC / P_0: 4 bar / T_0: 414 K

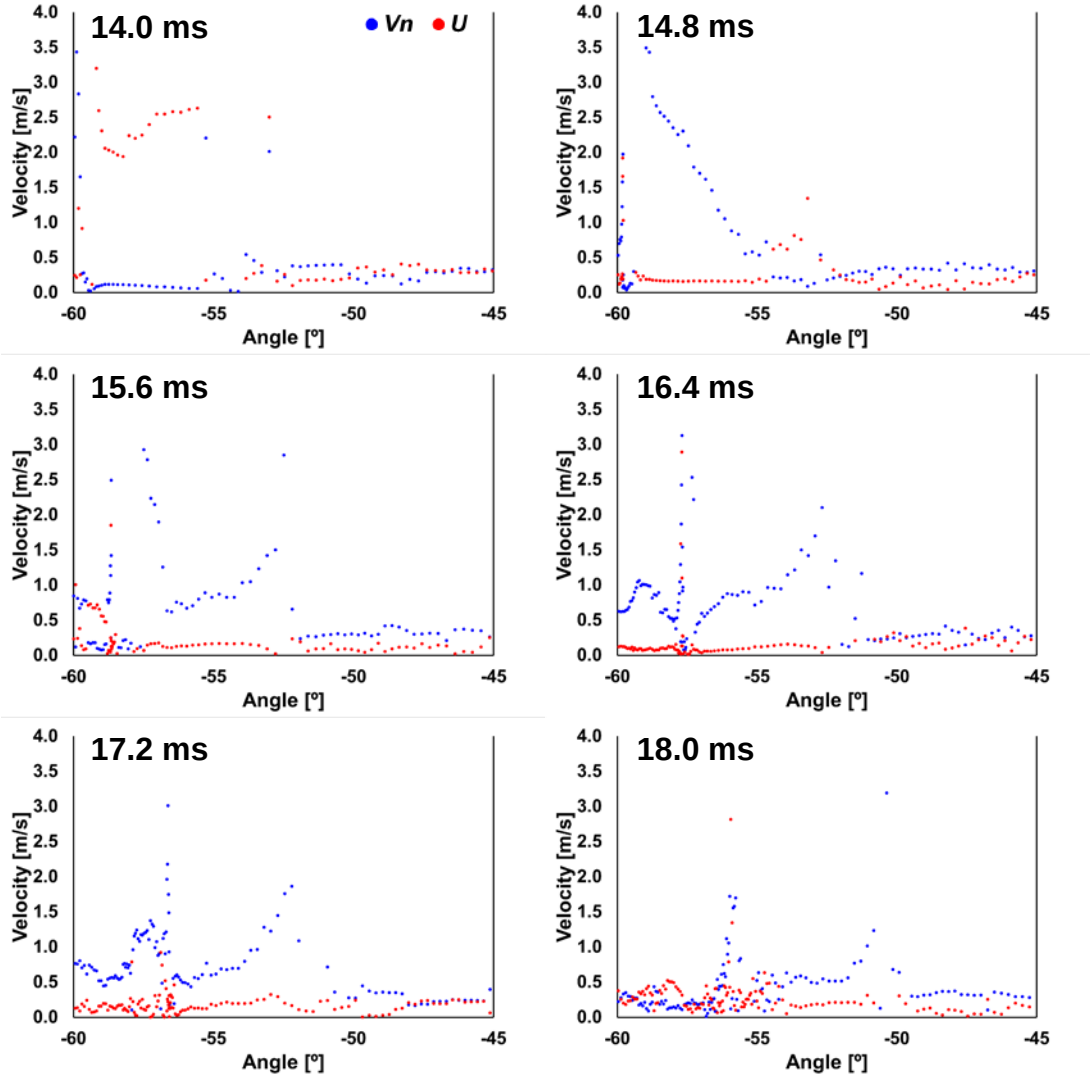

Figure 5.50 Change of normal unburned gas velocity V_n (blue dot) and burning velocity U (red dot) with respect to angle in the section 2 of the experimental case 6. Fuel: C_3H_8-air / ϕ: 2.0 / t_{ign}: 36.2° CA bTDC / P_0: 4 bar / T_0: 414 K

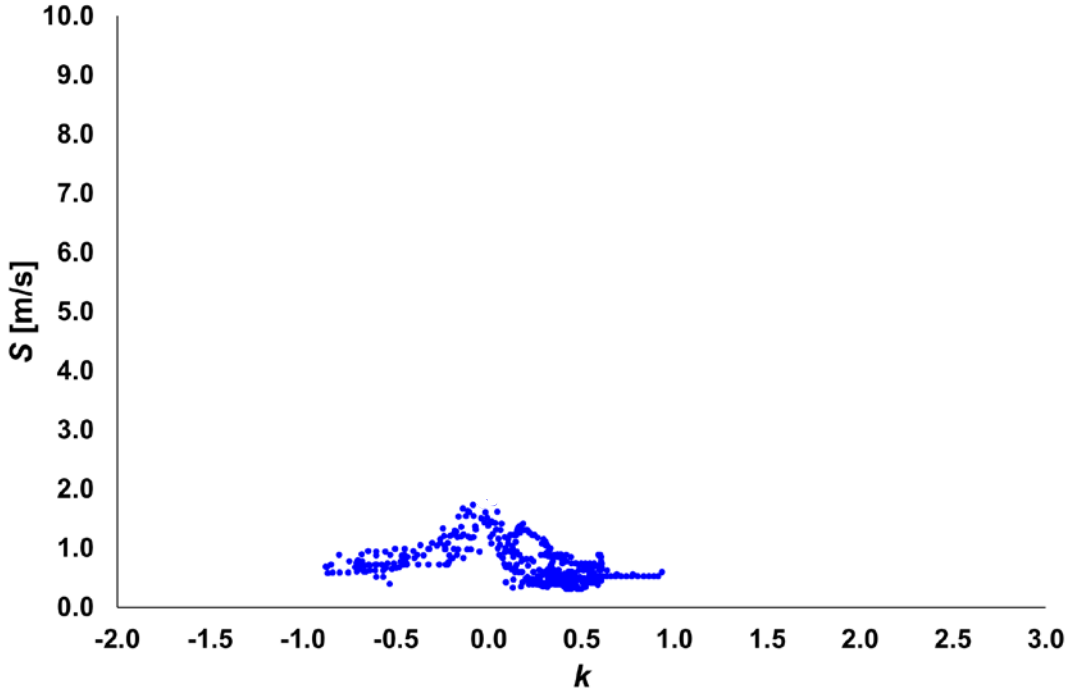

Figure 5.51 Variation of flame propagation speed *S* with respect to wavenumber *k* in the section 2 of the experimental case 3. Fuel: C_3H_8-air / ϕ: 2.0 / t_{ign}: 36.2° CA bTDC / P_0: 4 bar / T_0: 414 K

dramatically changes, and is also shown in the other graphs. Where the large change of wavenumber occurs, the corresponding flame surface is changed with a sharp point. This results in the undesirable derivation of the normal direction at that region. Therefore, the abnormal V_n can be extrapolated at that region and cause the undesirable value of U. For this reason, the abnormal values of V_n and U are excluded in Figure 5.52. Except for the undesirable values, V_n ranges between 0.6 and 0.7 m/s until 16.4 ms, and U varies from 0.1 and 0.2 m/s. From 17.2 to 18.0 ms, V_n gradually decreases up to 0.2 m/s, whereas U increases up to 0.6 m/s.

Figure 5.51 shows the variation of flame propagation speed S with respect to wavenumber k in the section 2. The values of k mostly range between -0.9 and 0.6, and S varies from 0.4 to 1.8 m/s. Where k is positive, as it increases, S decreaes. Especially, where $0 < k < 0.3$, as it increases, S dramatically decreases. And where $k > 0.3$, the decrease of S is gradual. Where k is negative, as it increases, S increases. Where $-0.3 < k < 0$, S dramatically increases with the rise of k. The change of S is large as k apporaches zero, which is also seen in the section 2 of the lean hydrogen- and methane-air mixture.

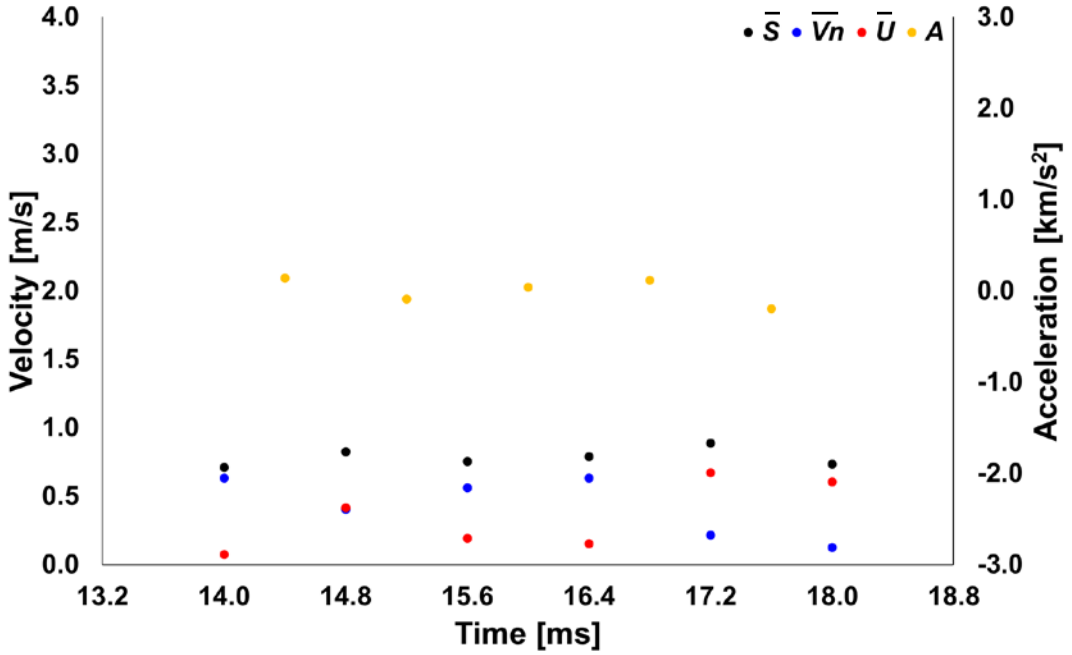

Figure 5.52 Variation of local mean flame propagation speed $\bar{S}$ (black dot), normal unburned gas velocity $\overline{V_n}$ (blue dot), burning velocity $\bar{U}$ (red dot), and acceleration *A* (yellow dot) with respect to time in the section 2 of the experimental case 3. Fuel: C_3H_8-air / ϕ: 2.0 / t_{ign}: 36.2° CA bTDC / P_0: 4 bar / T_0: 414 K

Figure 5.52 shows the variation of local mean flame propagation speed $\bar{S}$ (black dot), normal unburned gas velocity $\overline{V_n}$ (blue dot), burning velocity $\bar{U}$ (red dot), and acceleration *A* (yellow dot) with respect to time in the section 2. While the flame develops, $\bar{S}$ varies from 0.7 to 0.9 m/s. Since the change of $\bar{S}$ is not large, *A* is close to zero. Until 16.4 ms, $\overline{V_n}$ and $\bar{U}$ barely change, and their values are about 0.6 and 0.2 m/s respectively. From 17.2 to 18.0 ms, $\overline{V_n}$ gradually diminishes, and becomes 0.2 m/s. On the contrary, $\bar{U}$ slowly increases up to 0.5 m/s.

It seems that the increase of $\bar{U}$ at 17.2 and 18.0 ms results from the preferential diffusion of the oxygen, which is also seen in the section 2 of the hydrogen- and methane-air mixture. However, since $\overline{V_n}$ decreases when $\bar{U}$ increases, the increase of $\bar{S}$ is not much. Hence, the concave part of the flame contour line at 17.2 ms is not changed much as time goes by.

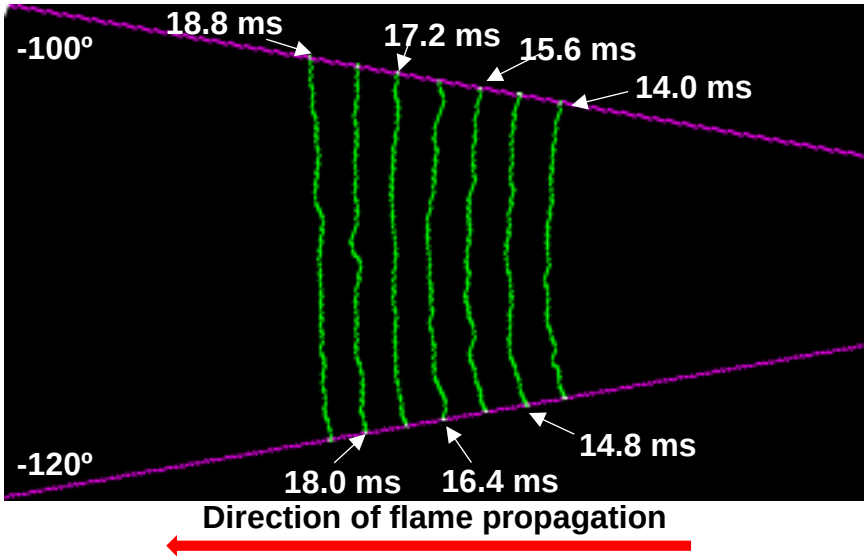

Figure 5.53 The enlarged section 3 image

Figure 5.53 shows the enlarged image of the section 3. Since the figure is a part of the entire flame edges image and enlarged, the flame contour line at each time looks like a straight line. In reality, each flame contour line is smoothly curved and is almost similar to the arc of a circle. While the flame propagates, the flame shape is kept continuously without a large distortion.

Figure 5.54 shows the change of flame propagation speed and wavenumber with respect to angle in the section 3. The black and yellow dots indicate flame propagation speed *S* and wavenumber *k* at each angle respectively. At each time, the change of wavenumber is not large, and the *k* ranges between 0.7 and 1.3. And the variation of *S* is also not large, and the value changes from 0.6 to 0.9 m/s. The change of k with respect to time is not large, and the corresponding S has a stable value. When *k* increases (decreases), *S* decreases (increases). Although the relationship between *k* and *S* is inversely proportional, the change of *S* is little compared with that of the section 1 and 2.

Figure 5.55 shows the change of normal unburned gas velocity V_n (blue dot) and burning velocity *U* (red dot) with respect to angle in the section 3. At each time, although V_n and *U* change with respect to angle, their changes are not large. In the case of V_n, the value ranges between 0.4 and 0.8 m/s, and *U* varies from 0.1 to 0.5 m/s. At each angle, although V_n and *U* change with respect to time, their variation is not large. Compared to the change of V_n and *U* in the section 1 and 2, the V_n and *U* of the section 3 barely change with respect to time.

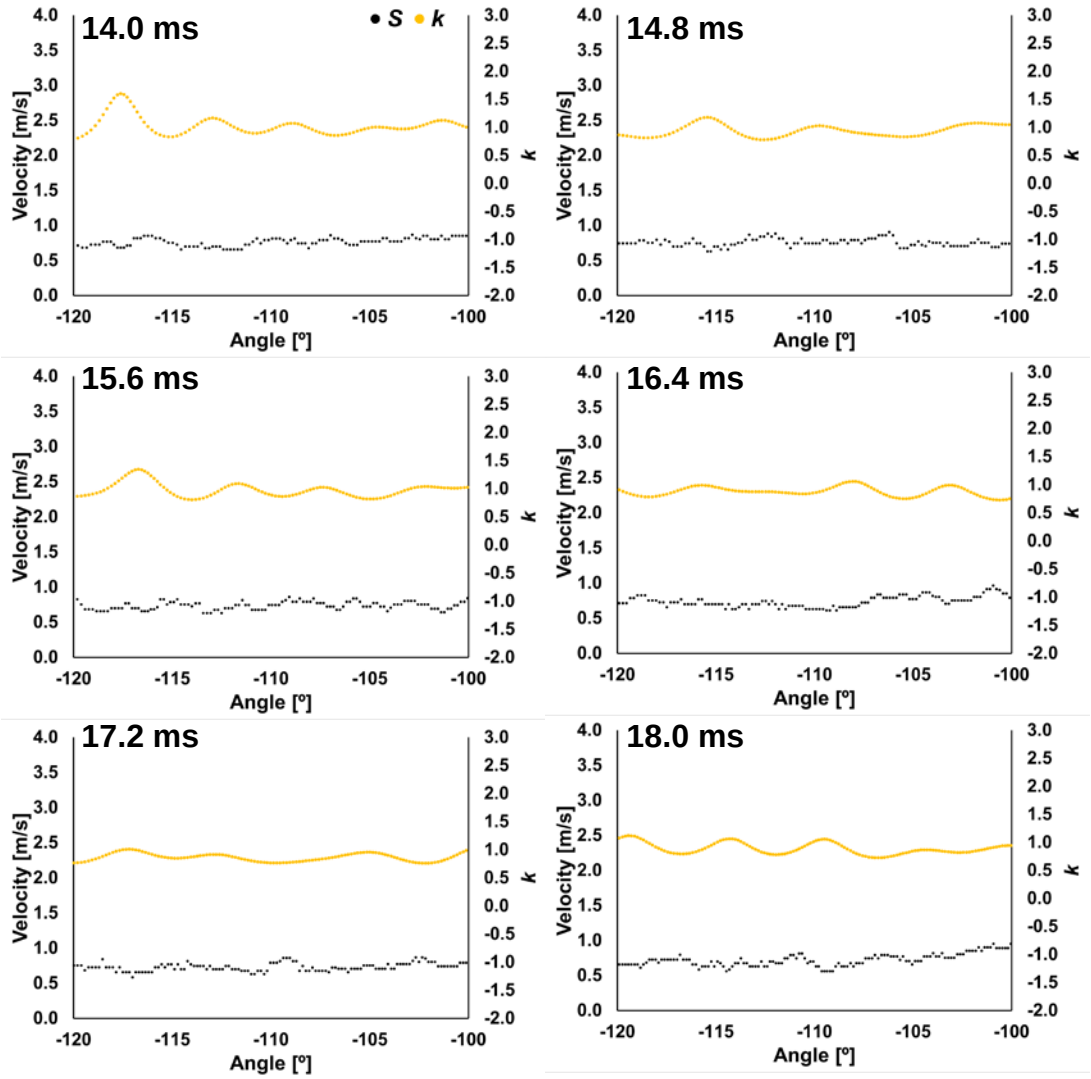

Figure 5.54 Change of flame propagation speed *S* (black dot) and wavenumber *k* (yellow dot) with respect to angle in the section 3 of the experimental case 3. Fuel: C_3H_8-air / ϕ: 2.0 / t_{ign}: 36.2° CA bTDC / P_0: 4 bar / T_0: 414 K

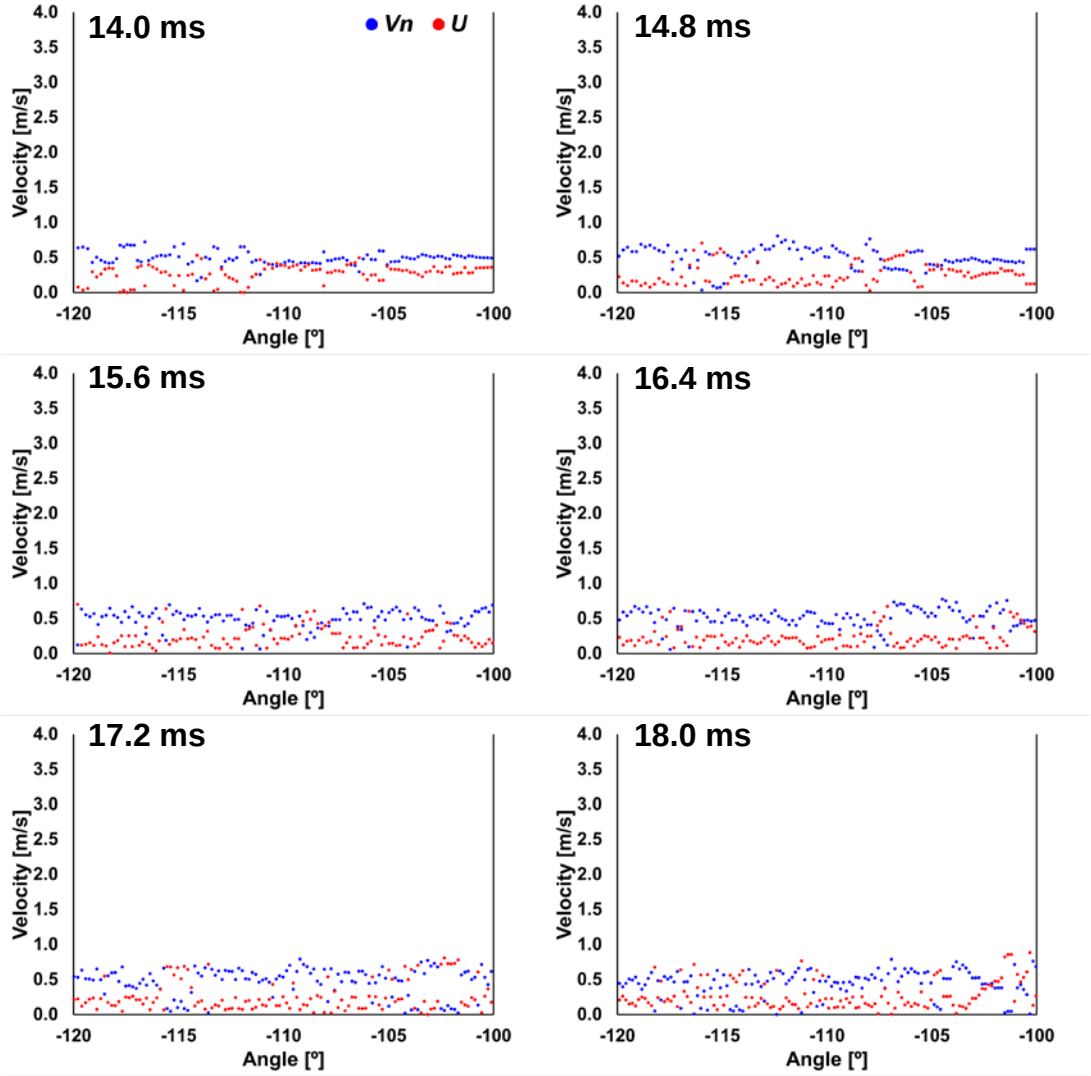

Figure 5.55 Change of normal unburned gas velocity V_n (blue dot) and burning velocity U (red dot) with respect to angle in the section 3 of the experimental case 3. Fuel: C_3H_8-air / ϕ: 2.0 / t_{ign}: 36.2° CA bTDC / P_0: 4 bar / T_0: 414 K

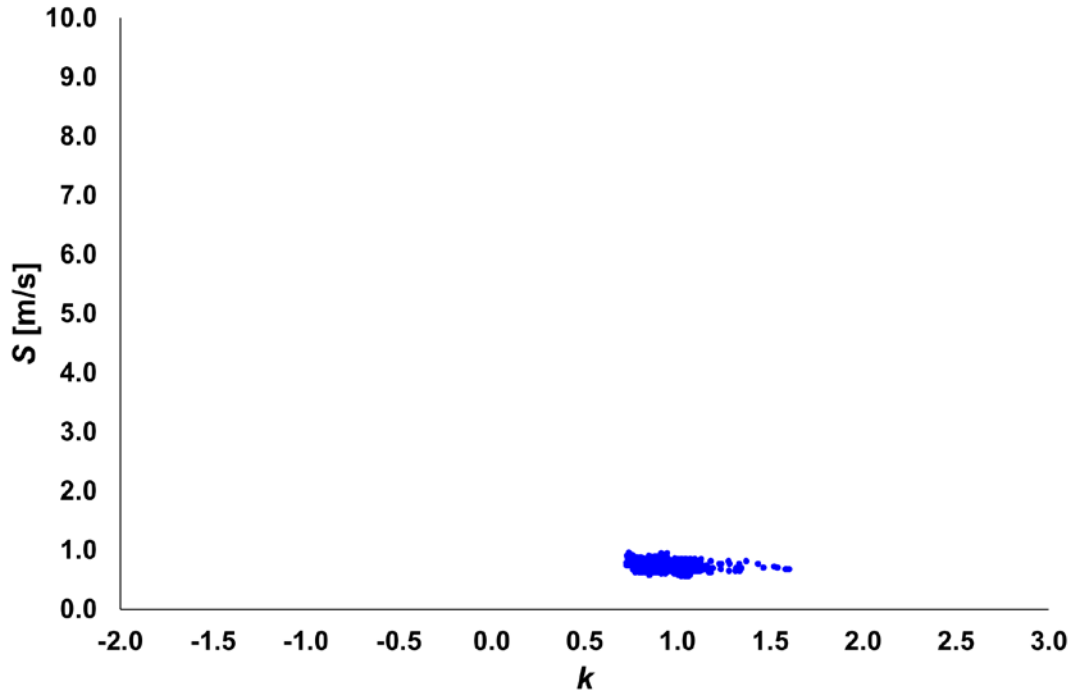

Figure 5.56 Variation of flame propagation speed *S* with respect to wavenumber *k* in the section 3 of the experimental case 3. Fuel: C_3H_8-air / ϕ: 2.0 / t_{ign}: 36.2° CA bTDC / P_0: 4 bar / T_0: 414 K

Figure 5.56 shows the variation of flame propagation speed *S* with respect to wavenumber *k* in the section 3. As shown in Figure 5.53, the flame contour line at each time is smoothly curved, and the change of the flame shape is not large. Without a large distortion, the flame shape is kept continuously. Because of the stable flame propagation, most of the *k* values range between 0.7 and 1.3. While *k* changes within the range, *S* barely changes. The range of *S* is between 0.5 and 0.9 m/s. As *k* is larger than 1.3, *S* gradually decreases, but its variation is not large.

Figure 5.57 shows the variation of local mean flame propagation speed $\bar{S}$ (black dot), normal unburned gas velocity $\overline{V_n}$ (blue dot), burning velocity $\bar{U}$ (red dot), and acceleration *A* (yellow dot) with respect to time in the section 3. As the flame develops, $\bar{S}$ barely changes, and its value is about 0.8 m/s. Since $\bar{S}$ keeps the stable value, *A* is close to zero and barely change with respect to time. In the case of $\overline{V_n}$ and $\bar{U}$, their values are also stable. $\overline{V_n}$ ranges between 0.5 and 0.6 m/s, and $\bar{U}$ varies from 0.2 to 0.3 m/s. Different from the $\overline{V_n}$ and $\bar{U}$ of the the section 1 and 2, the $\overline{V_n}$ and $\bar{U}$ in the section 3 barely change with respect to time.

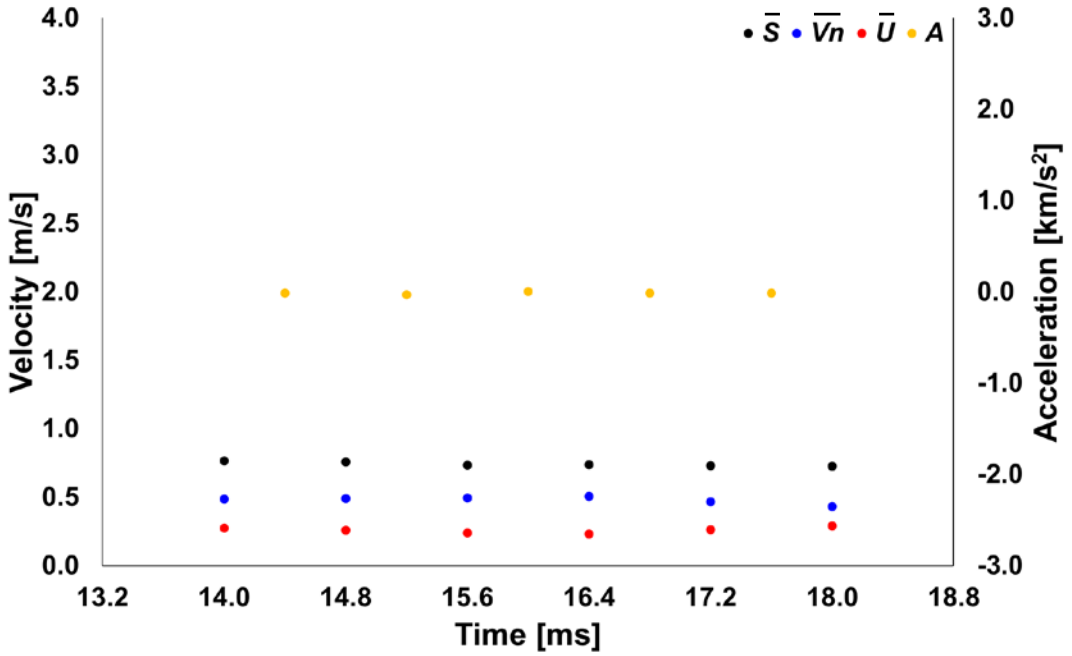

Figure 5.57 Variation of local mean flame propagation speed $\bar{S}$ (black dot), normal unburned gas velocity $\overline{V_n}$ (blue dot), burning velocity $\bar{U}$ (red dot), and acceleration *A* (yellow dot) with respect to time in the section 3 of the experimental case 3. Fuel: C_3H_8-air / ϕ: 2.0 / t_{ign}: 36.2° CA bTDC / P_0: 4 bar / T_0: 414 K

Through the results of the section 1, 2, and 3, the relationship between flame propagation speed, normal unburned gas velocity, burning velocity, and wavenumber can be described below.

Where wavenumber is negative, which means that a flame shape is concave toward unburned gas, flame propagation speed increases as the wavenumber increases. Especially, where wavenumber changes from -0.3 to 0.0, the flame propagation increases sharply. While there is the large increase in flame propagation speed, burning velocity also rises. The wavenumber at the region where flame is perturbed and its shape is concave tends to keep a negative value. Although wavenumber repeats increase and decrease with respect to time, it does not become larger than one.

Where wavenumber is positive, which means that a flame shape is convex toward unburned gas, flame propagation speed decreases as wavenumber increases. When wavenumber changes from 0.0 to 0.5, flame propagation speed decreases dramatically. Flame propagation speed seems significantly stable when wavenumber ranges between 0.7 and 1.3. Where wavenumber becomes larger than 1.3, the flame propagation speed gradually decreases, but its change is not large. As flame propagates, the wavenumber at the

region where the flame changes into a convex shape tends to keep a positive value, and barely change a negative value.

Wavenumber at a region repeats increase and decrease with respect to time, and the corresponding flame propagation speed also repeats decrease and increase: it is observed distinctly in the section 1 and 2. Since the preferential diffusion of the oxygen in this rich propane-air mixture and the thermal expansion caused by the burned gas occur, burning velocity and normal unburned gas velocity increase (decrease) at a concave (convex) region (Hertzberg 1989, Nakahara and Kido 1998, Lipatnikov 2012). The change of flame propagation speed seems related to the gradient of burning velocity, which is shown Figure 2.11 (A) (Hertzberg 1989). The rich propane-air mixture becomes locally leaner at a concave region because of the preferential diffusion of the oxygen, and then the burning velocity at that region becomes improved, which leads to the increase of flame propagation speed. If the gradient of burning velocity is steep, the change of flame propagation speed will be large. At a convex region, the preferential diffusion of the oxygen makes the local mixture composition richer. This results in the decreases of burning velocity and flame propagation speed. As seen in Figure 5.46 and Figure 5.51, wavenumber and flame propagation speed change in a certain range. This means that the local mixture composition influenced by the preferential diffusion of the oxygen changes within a certain range.

At each time, wavenumber changes with respect to angle. Where wavenumber at a certain region has a large (small) value, the wavenumber at the neighbouring regions is relatively small (large). As wavenumber becomes close to zero, flame propagation speed increases, and normal unburned gas velocity and burning velocity also rise. As the absolute value of wavenumber becomes larger than zero, flame propagation speed gradually decreases, and normal unburned gas velocity and burning velocity also diminish. In a concave region where wavenumber is relatively small the preferential diffusion of the oxygen makes the local mixture composition leaner. Hence, burning velocity at that region is improved and the thermal expansion of the burned gas also enhances the normal unburned gas velocity. In a convex region where wavenumber is relatively large, the local composition becomes richer because of the preferential diffusion of the oxygen. Therefore, burning velocity at the convex region diminishes. And the effect of thermal expansion of the burned gas is dispersed, which leads to the decrease of normal unburned gas velocity (Hertzberg 1989, Nakahara and Kido 1998, Lipatnikov 2012).

Figure 5.58 shows the change of local mean wavenumber $\bar{k}$ with respect to time (A) and the relevant vorticity histograms (B) for the section 3. In Figure 5.58 (B), a positive value indicates the clockwise vorticity of unburned gas, and the direction of vorticity is anticlockwise where a value is negative. The light blue, brown, grey, yellow, dark blue, and green line are the histograms of the vorticity data that were collected at 14.0, 14.8, 15.6, 16.4, 17.2, and 18.0 ms respectively. And each vorticity data are for an area between two consecutive flame contour lines: these colour lines are applied in the same way to Figure 5.59 (B) and Figure 5.60 (B). Since an area between two consecutive flame contour lines becomes large as flame propagates, the number of vorticity data also becomes large. Hence, the unit of frequency is represented as percent in order to compare the change of histograms.

Since the flame in the section 1 develops in a convex shape and the flame shape is kept continuously without a large disturbance, $\bar{k}$ generally increases. When time elapses from 14.0 to 15.6 ms, $\bar{k}$ gradually increases. During the time, the frequency of clockwise vorticity is larger than that of anticlockwise vorticity. From 16.4 ms, the change of $\bar{k}$ is small, which is about 1.2. While the $\bar{k}$ barely changes, the shape of histogram is not changed large, and the frequency of clockwise vorticity is still larger than that of anticlockwise vorticity. Compared with the lean hydrogen-air mixture, $\bar{k}$ continues to increase, and does not repeat increase and decrease. As $\bar{k}$ keeps the increasing trend, the vorticity histogram is not changed large, which is seen in the section 1 of the lean methane-air mixture: refer to Figure 5.18.

Figure 5.59 shows the change of local mean wavenumber $\bar{k}$ with respect to time (A) and the relevant vorticity histogram (B) for the section 2. A concave part appears in the section 2 and is kept to the end. While time elapses, $\bar{k}$ ranges between 0.0 and 0.2, and the change is not large. Since the flame shape is kept continuously and the $\bar{k}$ barely change, the change of the histogram is not changed large. Generally, the frequency of clockwise vorticity is larger than that of anticlockwise vorticity. The shape of the histogram is almost kept and seems symmetrical for a certain value.

Figure 5.60 shows the change of local mean wavenumber $\bar{k}$ with respect to time (A) and the relevant vorticity histogram (B) for the section 3. As seen in Figure 5.53, since the flame contour line at each time is smoothly curved and the flame shape barely changes with respect to time, the variation of $\bar{k}$ is not large. $\bar{k}$ ranges between 0.9 and 1.0. Until, 15.6 ms, $\bar{k}$ is about 1.0, and the corresponding histograms seem close to a symmetrical shape. From 15.6 to 16.4 ms, $\bar{k}$ slightly decreases, and it is shown in the relevant grey histogram

that the frequency of clockwise vorticity becomes larger than that of anticlockwise vorticity. While time elapses from 16.4 to 18.0 ms, $\bar{k}$ is about 0.9 and barely varies. During that time, the corresponding histograms return to a symmetrical shape and keep it. From 18.0 to 18.8 ms, $\bar{k}$ slight diminishes again. While the $\bar{k}$ decreases, the frequency of clockwise vorticity increases again.

As seen in Figure 5.58, Figure 5.59, and Figure 5.60, local mean wavenumber at each section varies within a certain range, and its change is not large. When local mean wavenumber keeps increasing, decreasing, or its value, the shape of the corresponding histogram has a tendency to be symmetrical. When the trend of local mean wavenumber changes from increase to decrease or from decrease to increase, the shape of the relevant histogram tends to become asymmetric. When the asymmetric shape occurs, the frequency of clockwise vorticity mainly increases.

While combustion proceeds, thermal expansion is caused by burned gas and influences the unburned gas in front of the flame front (Balusamy et al 2011, Long and Hargrave 2011). Assuming that flame propagates outwardly and the flame shape ideally keeps a circle, the direction of the flame at each point of the flame front is perpendicular to that point. Hence, stationary unburned gas in front of the flame front would travel in the perpendicular direction. Since the unburned gas moves radially, the proportion of clockwise and anticlockwise vorticity is identical, and thus the shape of the histogram would be symmetrical. In Figure 5.58, Figure 5.59, and Figure 5.60, it is seen that the shape of histogram becomes asymmetric when the trend of local mean wavenumber changes. However, it is difficult to suggest a dominant vorticity value.

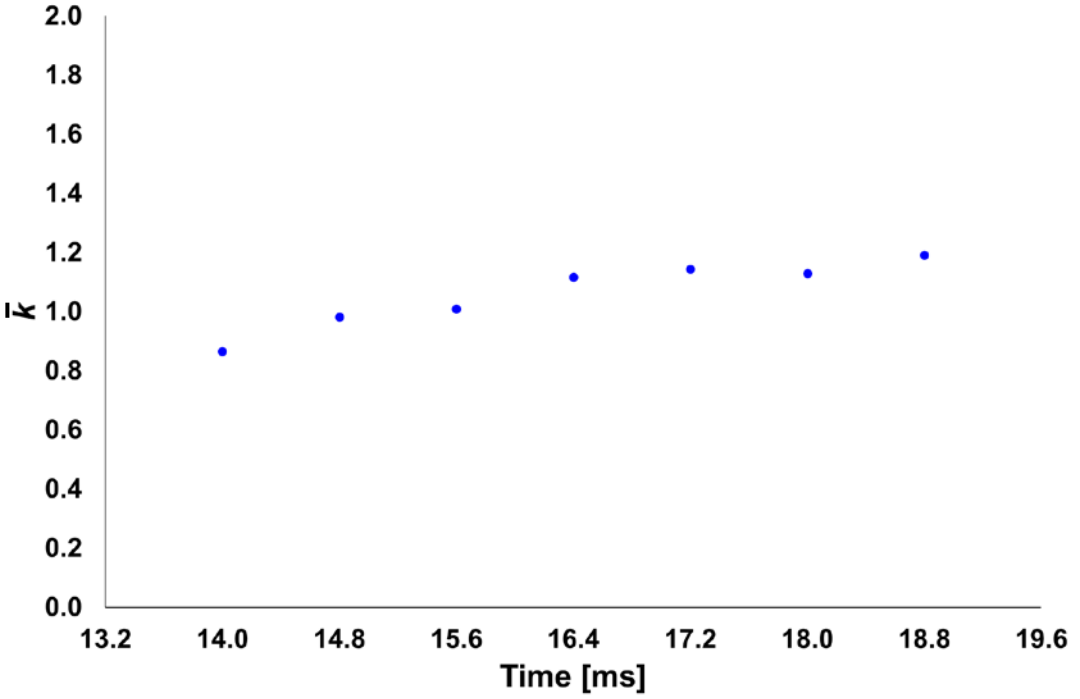

(A) $\overline{k}$ vs time

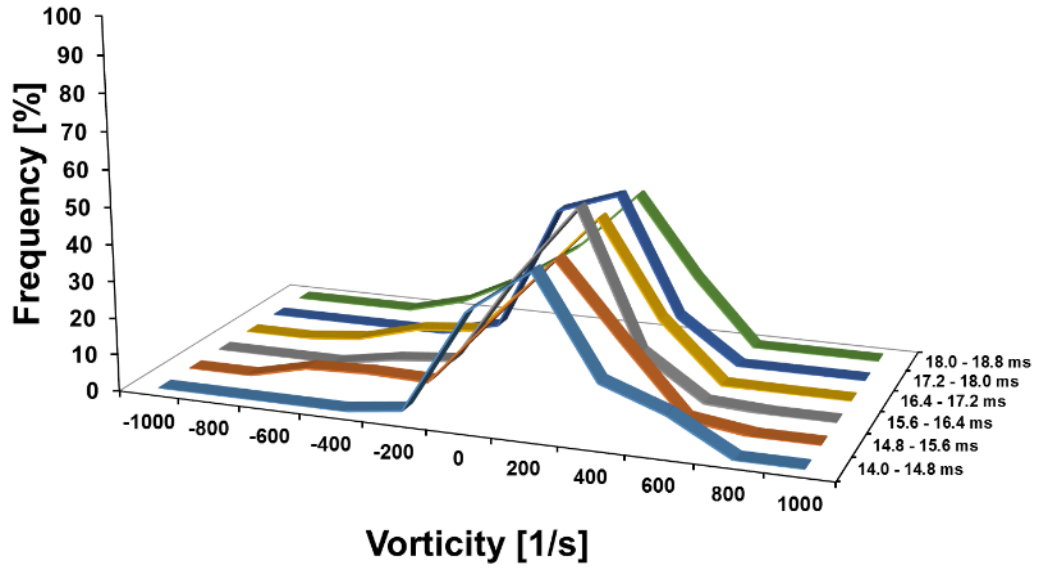

(B) Histogram

Figure 5.58 Change of the local mean wavenumber $\overline{k}$ with respect to time (A) and the relevant vorticity histogram (B) for the section 1 of the experimental case 3. Fuel: C_3H_8-air / ϕ: 2.0 / t_{ign}: 36.2° CA bTDC / P_0: 4 bar / T_0: 414 K

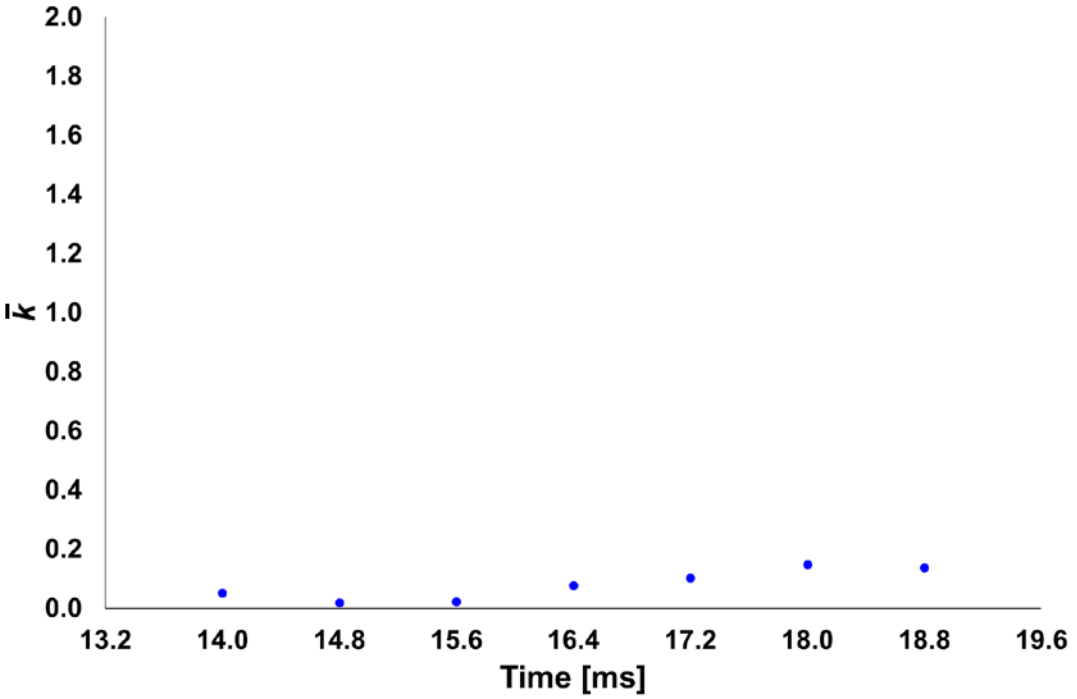

(A) $\bar{k}$ vs time

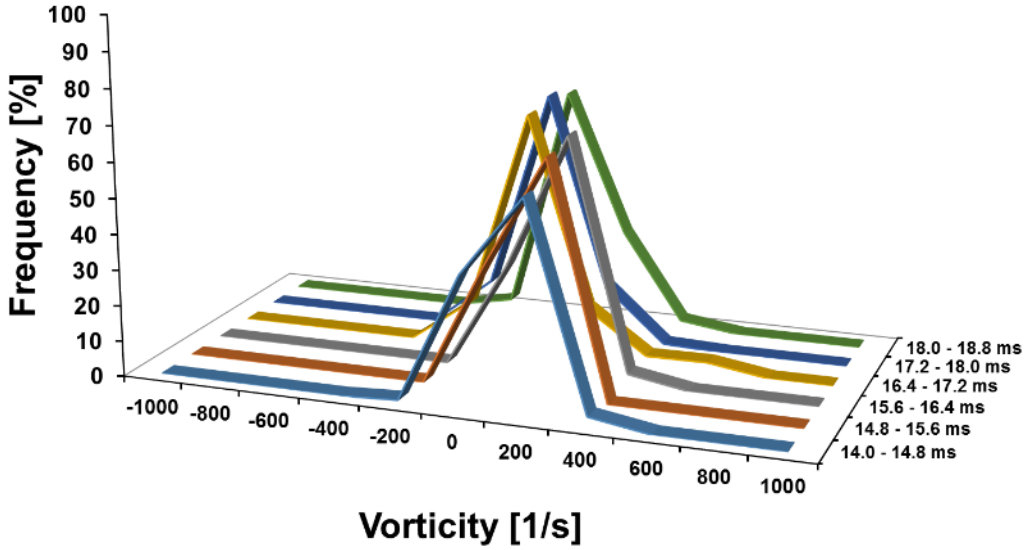

(B) Histogram

Figure 5.59 Change of the local mean wavenumber $\bar{k}$ with respect to time (A) and the relevant vorticity histogram (B) for the section 2 of the experimental case 3. Fuel: C_3H_8-air / ϕ: 2.0 / t_{ign}: 36.2° CA bTDC / P_0: 4 bar / T_0: 414 K

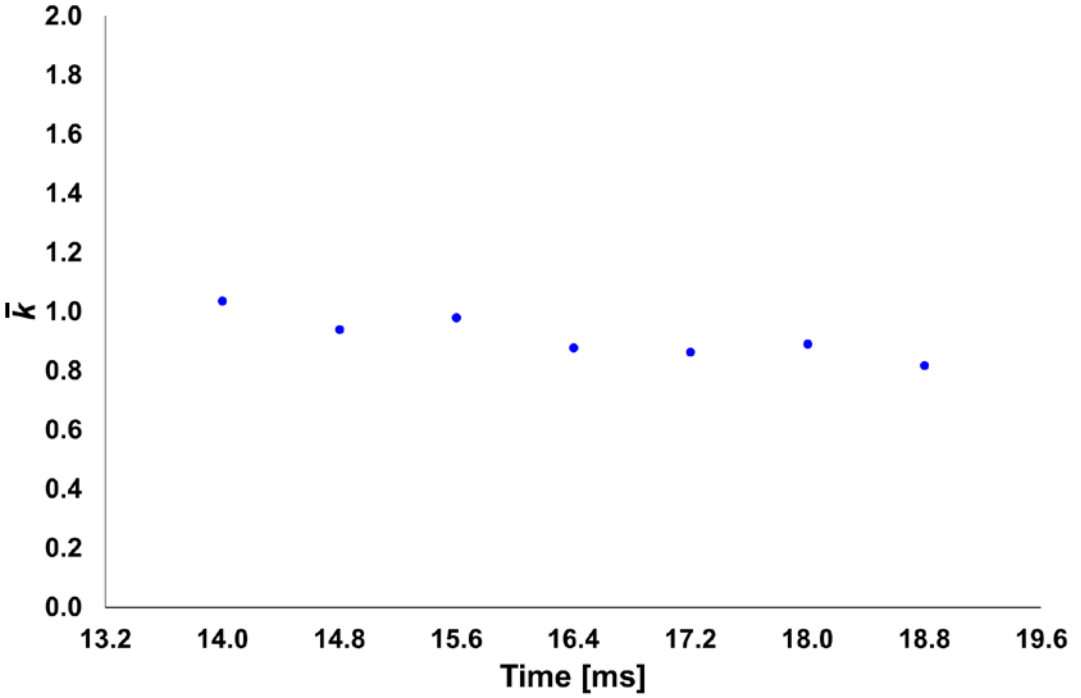

(A) $\overline{k}$ vs time

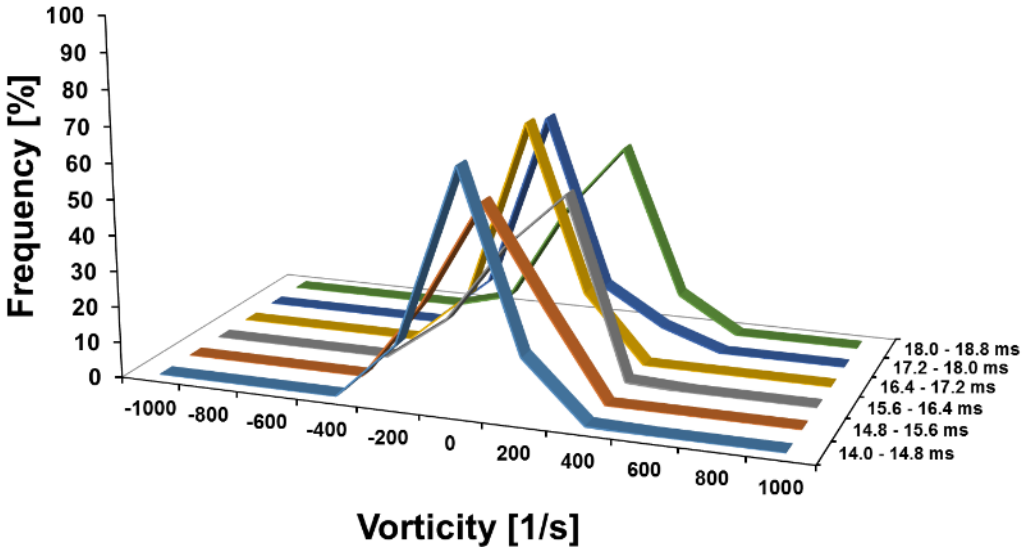

(B) Histogram

Figure 5.60 Change of the local mean wavenumber $\overline{k}$ with respect to time (A) and the relevant vorticity histogram (B) for the section 3 of the experimental case 3. Fuel: C_3H_8-air / ϕ: 2.0 / t_{ign}: 36.2° CA bTDC / P_0: 4 bar / T_0: 414 K

Chapter 6 Summary and recommendation

This chapter summarises the main findings from the results of the lean hydrogen-air, lean methane-air, and rich propane-air mixture experiments. This research concentrated on the measurements of flame propagation speed, normal unburned gas velocity, and burning velocity at a point on a flame front. The study presents how flame propagation speed, normal unburned gas velocity, and burning velocity changed with respect to time and space. And the relationship between the change of local mean wavenumber and the vorticity histogram of unburned gas is provided. It is expected that the results of the experiments can be used as fundamental data to enhance the understanding of combustion process. Especially, the experiment data can contribute to improving the chemical mechanism that is used in simulation software. Although current combustion simulation programs provide various kinds of properties regarding combustion, most of them are average values. It is expected that modelling and simulation for the local change of properties such as flame propagation speed, unburned gas velocity, burning velocity, and so on can be studied more actively using the experiment data of the current research.

6.1 Summary of the lean hydrogen-air mixture experiment

- In a convex region of the flame front: wavenumber changes between 0.7 and 2.0. As wavenumber increases, flame propagation speed gradually decreases. The range is between 0.5 and 1.1 m/s. The relationship between wavenumber and flame propagation speed is inversely proportional. Where wavenumber increases (decreases), normal unburned gas velocity and burning velocity generally decrease (increase), normal unburned gas velocity ranges between 0.1 and 0.8 m/s, the range of burning velocity is between 0.1 and 0.7 m/s.

  While the flame propagates, the local mean flame propagation speed in the convex region is about 0.8 m/s, and is barely changed. The local mean normal unburned gas velocity changes between 0.1 to 0.5 m/s, and the change of the local mean burning velocity ranges between 0.2 and 0.6 m/s. The flame shape changes between a flat and convex shape, and does not become concave.

- In a concave region of the flame front: wavenumber changes between -0.5 and 0.5. As wavenumber approaches 0.0, flame propagation speed dramatically increases, and changes from 0.2 to 3.9 m/s. And normal unburned gas velocity increases from 0.1 to 0.5 m/s, and burning velocity also rises from 0.3 to 3.5 m/s. The change of burning velocity is relatively large and the main factor in the increase of flame propagation speed.

  While the flame propagates, the local mean flame propagation speed in the concave region increases from 0.2 to 1.1 m/s. Simultaneously, the local mean normal unburned gas velocity increases from -0.1 to 0.5 m/s, and the local mean burning velocity also rises from 0.2 to 0.6 m/s. The flame shape changes between a concave and smoothly-curved shape of which the wavenumber is similar to that of a circle.

- In a smoothly-curved region of the flame front: wavenumber changes between 0.7 and 1.3. While wavenumber varies, flame propagation speed has a stable value of which the range is between 0.4 and 0.7 m/s. At the same time, normal unburned gas velocity changes between 0.1 and 0.4 m/s, and burning velocity also changes between 0.1 and 0.4 m/s. Their changes are not large.

  While the flame propagates, the local mean flame propagation speed in the smoothly-curved region is not changed, and its value is 0.5 m/s. The local mean normal unburned gas velocity changes between 0.0 and 0.3 m/s, and the local mean burning velocity ranges between 0.1 and 0.3 m/s. The flame shape is kept, and its wavenumber is similar to that of a circle.

- In a spatial change in wavenumber at each time, where wavenumber is relatively large (small) at a certain region, the wavenumber at the adjacent regions is small (large). In a temporal change in wavenumber at a convex or concave region, wavenumber repeats increase and decrease, and flame propagation speed repeats decrease and increase. The changes of wavenumber and flame propagation speed are within a certain range. As a flame shape locally changes, the local mixture composition is changed by the preferential diffusion of the hydrogen, and the local effect of thermal expansion caused by the burned gas also varies. The change of a local mixture composition and the thermal expansion affect burning velocity and normal unburned gas velocity, which leads to the change of flame propagation speed.

- In the relationship between the change of local mean wavenumber and the vorticity histogram of unburned gas, where an increase or decrease in local mean wavenumber is kept, the shape of the corresponding vorticity histogram is close to symmetry for a value of vorticity. Where the trend of local mean wavenumber changes from increase (decrease) to decrease (increase), the shape of the histogram becomes asymmetric, and clockwise vorticity is dominant.

6.2 Summary of the lean methane-air mixture experiment

- In a convex region of the flame front: wavenumber ranges between 0.8 and 1.6. As wavenumber increases, flame propagation speed gradually decreases from 2.5 to 1.5 m/s. The relationship between wavenumber and flame propagation speed is inversely proportional. Where wavenumber increases (decreases), normal unburned gas velocity and burning velocity generally decrease (increase) and fluctuate. Normal unburned gas velocity changes between 1.0 and 1.5 m/s, and burning velocity ranges between 0.1 and 0.8 m/s.

  While the flame propagates, the local mean flame propagation speed in the convex region increases from 1.5 to 2.0 m/s. The local mean normal unburned gas velocity changes between 1.0 to 1.5 m/s, and the change of the local mean burning velocity ranges between 0.3 and 0.5 m/s. And the convex flame shape is kept without large perturbation.

- In a concave region of the flame front: wavenumber changes between -0.6 and 1.0. As wavenumber becomes close to 0.0, flame propagation speed sharply increases from 0.8 to 2.9 m/s. And normal unburned gas velocity and burning velocity fluctuate severely. The range of normal unburned gas velocity is between -0.1 and 2.3, and burning velocity ranges between 0.2 and 2.5 m/s.

  While the flame propagates, the local mean flame propagation speed in the concave region increases from 0.9 to 1.9 m/s. Simultaneously, the local mean normal unburned gas velocity changes between 0.5 and 1.1 m/s, and the local mean burning velocity increases from 0.2 to 0.8 m/s. After the flame changes into a concave shape, it keeps its shape.

- In a smoothly-curved region of the flame front: wavenumber changes between 0.5 and 1.3. While wavenumber varies, flame propagation speed is barely changed, and the range is between 1.3 and 1.5 m/s. And normal unburned gas velocity locally changes between 0.5 and 1.4 m/s, and burning velocity locally changes between 0.1 and 1.2 m/s.

  While the flame propagates, the local mean flame propagation speed in the smoothly-curved region is barely changed, and its value is 1.3 m/s. The local mean normal unburned gas velocity is about 0.8 m/s,

and the local mean burning velocity is about 0.5 m/s. The flame shape is kept, and its wavenumber is similar to that of a circle.

- Where wavenumber is relatively large (small) at a certain region, the wavenumber at the adjacent regions is small (large). In a convex or concave region, wavenumber repeats increase and decrease with respect to time, and flame propagation speed repeats decrease and increase. The changes of wavenumber and flame propagation speed are within a certain range. As a flame shape locally changes, the local mixture composition is changed by the preferential diffusion of the hydrogen, and the local effect of thermal expansion caused by the burned gas also varies. A change in a local mixture composition is within a certain range, which affects the range of change of flame propagation speed.

- Where local mean wavenumber keeps increasing, decreasing, or its value, the shape of vorticity histogram keeps its shape and is close to symmetry for a value of vorticity. Where the trend of local mean wavenumber changes from increase (decrease) or decrease (increase), the shape of the histograms becomes asymmetric, and clockwise vorticity is dominant.

6.3 Summary of the rich propane-air mixture experiment

- In a convex region of the flame front: wavenumber repeats increase and decrease between 0.5 and 1.5. When wavenumber changes, flame propagation speed varies from 0.6 to 1.0 m/s. The relationship between wavenumber and flame propagation speed is inversely proportional. Where wavenumber increases (decrease), normal unburned gas velocity and burning velocity generally decrease (increase). Normal unburned gas velocity changes between 0.5 and 0.8 m/s, and burning velocity ranges between 0.2 and 0.4 m/s.

  While the flame propagates, the local mean flame propagation speed in the convex region is 1.0 m/s, and barely changes with respect to time. The local mean normal unburned gas velocity changes between 0.5 and 0.7 m/s, and the change of the local mean burning velocity ranges between 0.2 and 0.5 m/s.

- In a concave region of the flame front, wavenumber changes between -0.9 and 0.6. As wavenumber approaches 0.0, flame propagation speed dramatically increases from 0.4 to 1.5 m/s. And normal unburned gas velocity and burning velocity fluctuate severely and generally increase. The range of normal unburned gas velocity is between 0.2 and 0.7, and burning velocity ranges between 0.1 and 0.6 m/s.

  While the flame propagates, the local mean flame propagation speed in the concave region repeats increase and decrease between 0.7 and 0.9 m/s. And the local mean normal unburned gas velocity changes between 0.1 and 0.6 m/s, and the local mean burning velocity ranges between 0.1 to 0.6 m/s.

- In a smoothly-curved region of the flame front, wavenumber ranges between 0.7 and 1.3. While wavenumber varies, flame propagation speed is barely changed, and the range is between 0.6 and 0.9 m/s. Normal unburned gas velocity changes between 0.4 and 0.8 m/s, and burning velocity between 0.1 and 0.5 m/s.

  While the flame propagates, the local mean flame propagation speed in the smoothly-curved region is barely changed, and its value is 0.8 m/s. The local mean normal unburned gas velocity changes between

0.5 and 0.6 m/s, and the local mean burning velocity between 0.2 and 0.3 m/s.

- Wavenumber locally changes at each time. Where wavenumber is relatively large (small) at a certain region, the wavenumber at the neighbouring regions is small (large). In a convex or concave region, wavenumber at a point changes with respect to time. As wavenumber approaches zero, flame propagation speed increases. When a flame shape locally changes, the change of the local mixture composition is caused by the preferential diffusion of the oxygen, which leads to the change of the burning velocity. The thermal expansion caused the burned gas also affects the change of the unburned gas velocity. The changes of unburned gas velocity and burning velocity results in that of flame propagation speed.

- Where local mean wavenumber keeps increasing, decreasing, or its value, the shape of vorticity histogram keeps its shape and is close to symmetry for a value of vorticity. Where the trend of local mean wavenumber changes from increase (decrease) or decrease (increase), the shape of the histograms becomes asymmetric, and clockwise vorticity is dominant.

6.4 Recommendations for future work

Since there were time constraints and the limit of the experimental apparatus, further research could not be carried out. The listed below are the recommendations for the future work and for improving the experimental equipment.

- It is necessary to measure the burning velocity of a hydrogen-, methane-, and propane-air mixture with respect to equivalence ratio. Through the measurement, it would be possible to realise how much a local mixture composition at a convex or concave region is changed.

- In the current research, the initial temperature at the start of ignition was calculated by using pressure data, which is shown in Sec. 3.3. Since the initial temperature affects flame propagation speed, unburned gas velocity, and burning velocity in many ways, it is more desirable to measure it directly. PLIF, planar laser induced fluorescence, can be used for the measurement.

- LUSIEDA, Leeds University spark ignition engine data analysis, is a reverse thermodynamic code and was developed by the Leeds combustion group. The code calculates burning rates and other properties and has been used for the high-speed LUPOE-2D, which was faster than 750 rpm. To compare the results of simulation and experiment, it is necessary to modify LUSIEDA considering a low speed including 50 rpm.

- In the current work, the image resolution was 1024 x 1024 pixels and the repetition rates of the laser and high speed camera were 2.5 kHz. If image resolution were improved, unburned gas velocity near a flame front could be measured more accurately.

- The current experimental equipment is convenient in replacing fuel. This is because three kinds of gaseous fuels can be provided separately by each compressed cylinder. Hence, it is recommended to conduct experiment with a different kind of gaseous fuel or blended one.

Appendix

A. Turbulent premixed flame

Although turbulent fluid motion can be observed easily in our everyday life just as flowing water in a bathtub and its existence can be perceived intuitively by ordinary people, it is very difficult to define the flow precisely as a concise sentence. Especially, in classical physics, the relevant researches for prescribing turbulence have been carried out over many years though, the problem is still challenging and is not clearly solved yet. Although defining turbulence is difficult, it is certain that turbulence is one of the most critical factors in understanding turbulent combustion.

Briefly mentioning some of its characteristics, turbulent flows are random and diffusive, which makes it possible to mix fluid itself and to increase mass and heat transfer rapidly. Large Reynolds number, which is the ratio of the inertia force to the viscous force in a flow (Marquand and Croft 1994), is also one of the characteristics: it is common that turbulence in a fluid flow occurs as the laminar flow becomes unstable. The range in which turbulent quantities such as velocity or pressure vary with respect to time and space is wide. The magnitude of the vorticity fluctuations in turbulent flows is mostly large, and its range is also wide. In addition, after turbulent flows occur, they eventually dissipate as time goes by because of the viscosity of the fluid where any energy to sustain the turbulent motion is not provided (Tennekes et al. 1972, Lipatnikov 2012).

For these complicated characteristics, turbulent flows have been mainly investigated and analysed through statistical methods such as average velocity in time or spatial quantity, root-mean-square turbulent velocity, and length and time scale of turbulent eddies. In this section, the statistical methods are first introduced. The methods were used to make the judgment on whether a laminar condition was made in the research engine: the results of the statistical methods are presented in Sec. 3.4.3, and, the characteristics of cellular flame were investigated under the laminar condition. And the different types of premixed flame is illustrated with the use of the combustion regime diagram. Lastly, the combustion regime of the current research is described.

In a turbulent flow, an instantaneous velocity at a point x can be decomposed into its mean velocity and fluctuating velocity in time domain, which is known

as the Reynolds decomposition: the decomposition can be also carried out in spatial domain (Lipatnikov 2012).

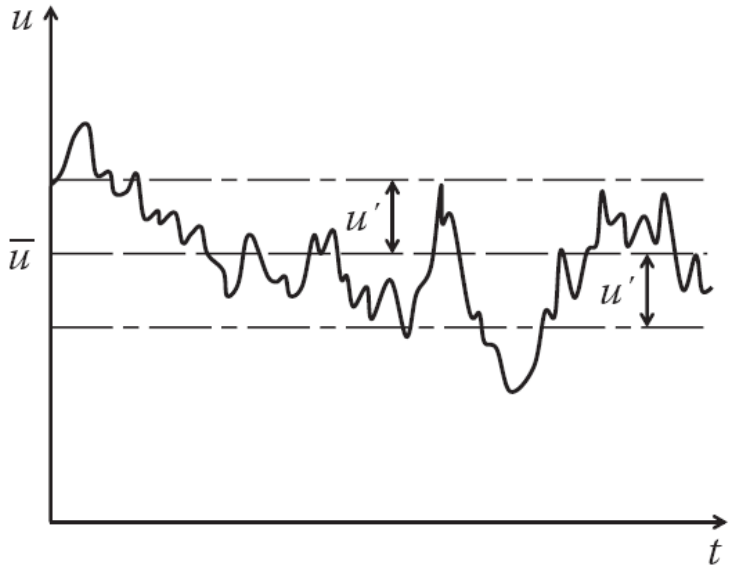

Figure A.1 A sketch of velocity variations at a point in a flow (Lipatnikov 2012)

Figure A.1 shows the velocity variations at a point in a turbulent flow. An instantaneous velocity can be expressed in Eq. (A.1).

$$\mathrm{u}(\mathrm{x},t) = \bar{\mathrm{u}}(\mathrm{x},t) + \mathrm{u}'(\mathrm{x},t) \qquad \textbf{Eq.}\ (\mathrm{A.1})$$

where the instantaneous velocity is u, mean velocity $\bar{\mathrm{u}}$, and fluctuating velocity u'. In order to calculate the mean velocity, the instantaneous velocities are integrated during time τ, which is shown in Eq.(A.2).

$$\bar{\mathrm{u}}(\mathrm{x},t) = \lim_{\tau\to\infty} \frac{1}{\tau} \int_0^{\tau} \mathrm{u}(\mathrm{x},t)dt \qquad \textbf{Eq.}\ (\mathrm{A.2})$$

The mean fluctuating velocity can be calculated simply by subtracting the mean velocity $\bar{\mathrm{u}}$ from the instantaneous velocity u and averaging the value. However, since the mean fluctuating velocity become zero, the value itself cannot show any information on turbulence. Therefore, the root-mean-square

velocity $\overline{u'}$ has to be calculated to characterize turbulence, and its definition can be expressed as follows.

$$\bar{\mathrm{u}}' = \lim_{\tau\to\infty}\left[\frac{1}{\tau}\int_0^{\tau}\left(\mathrm{u}(\mathrm{x},t)-\bar{\mathrm{u}}(\mathrm{x},t)\right)^2 dt\right]^{\frac{1}{2}} \qquad \textbf{Eq.}\ (A.3)$$

The root-mean-square velocity means the level of fluctuating velocity during a given time τ in a turbulent flow, that is, the larger the value becomes the more the fluid motion oscillates. In order to perceive the strength of turbulence intuitively, it is needed to mention the concept of turbulence intensity. The definition of turbulence intensity is the ratio of the root-mean-square velocity $\bar{\mathrm{u}}'$ to mean velocity $\bar{\mathrm{u}}$ (Burluka 2014), the equation is as follows:

$$Turbulence\ intensity = \frac{\bar{\mathrm{u}}'}{\bar{\mathrm{u}}} \qquad \textbf{Eq.}\ (A.4)$$

The similar derivations that are shown in Eq. (A.1) to Eq. (A.4) can be obtained by using the spatial averaging technique: the variable has to be changed from time t to space x. However, because of the nature of turbulence, the time averaging technique is appropriate for a statistically steady flow, whereas the spatial average technique should be mainly used in the case of a homogeneous and isotropic flow (Lipatnikov 2012).

In a reciprocating engine that was used in the current work, the flow of a fuel-air mixture in the cylinder was not steady, homogeneous and isotropic because of the periodic movement of the piston and the geometry of the combustion chamber. Especially, cycle-to-cycle variations can take place, and their effect also vary depending on the speed of an engine. In order to represent such fluctuating motion, a separate technique has been employed, which is the ensemble averaging technique (Heywood 1988). The ensemble-averaged mean velocity $\bar{\mathrm{u}}_{ensemble}$ can be calculated as follows:

$$\bar{\mathrm{u}}_{ensemble}(\mathrm{x},\theta_i) = \lim_{N\to\infty}\frac{1}{N}\sum_{i=1}^{N}\mathrm{u}(\mathrm{x},\theta_i) \qquad \textbf{Eq.}\ (A.5)$$

where i is i-th cycle and N is the total number of cycles that is observed in experiment. In the ensemble averaging technique, crank angle θ is substituted for time t and the instantaneous velocity u at a given point x in the cylinder of an engine at a given cycle is normalized by the number of cycles. The fluctuating velocity $\mathrm{u}'(\mathrm{x}, \theta_i)$ can be derived as follows:

$$\overline{\mathrm{u}'}(\mathrm{x}, \theta_i) = \lim_{N\to\infty}\left[\frac{1}{N}\sum_{i=1}^{N}\left(\mathrm{u}(\mathrm{x}, \theta_i) - \bar{\mathrm{u}}_{ensemble}(\mathrm{x}, \theta_i)\right)^2\right]^{\frac{1}{2}} \qquad \textbf{Eq.} \text{ (A.6)}$$

When carrying out engineering studies, it is commonly assumed that a turbulent flow is statistically steady, homogeneous and isotropic because of the randomness or irregularity of turbulence (Burluka 2014). Hence, the results of these three statistic methods are the same under this assumption.

Using the root-mean-square fluctuating velocity, the turbulent Reynolds number Re_t, which is the ratio of the turbulence force to the laminar viscous force in a turbulent flow, is defined as (Burluka 2014):

$$Re_t = \frac{\mathrm{u}' L_t}{\nu} \qquad \textbf{Eq.} \text{ (A.7)}$$

where u' is the root-mean-square velocity, L_t is the length scale, and ν is the kinematic viscosity of the fluid.

In relation to the length scale L_t, three kinds of length scales are mainly employed to calculate the sizes of turbulent eddies in a turbulent flow. And the result of the calculation represents magnitude or intensity, not an accurate number. When the length scales are calculated, the time scales are usually dealt with together and mean how long turbulent eddies sustain in time. The aforementioned length and time scales are integral length and time scales, L_i and τ_i, Taylor length and time scale, L_λ and τ_λ,, and Kolmogorov length and time scale, L_η and τ_η (Mathieu and Scott 2000).

The definition of the integral length scale L_i is that the spatial correlation function $R(r)$ of the velocities at the two adjacent points is integrated in time t. Eq. (A.8) and Eq. (A.9) show the equations of the integral length scale and the spatial correlation function respectively.

$$L_i = \int_0^{\infty} R(r,t)dt$$ **Eq.** (A.8)

$$R(r,t) = \frac{\bar{\mathrm{u}}(x,\ t)\bar{\mathrm{u}}(x+dr,\ t)}{\mathrm{u}'(x,t)\mathrm{u}'(x+dr,t)}$$ **Eq.** (A.9)

In Eq. (A.9), u' indicates the fluctuating velocities at two longitudinal or transversal points at a given time, and dr is the minute displacement between the two adjacent points: refer to Figure A.2. The relationship between longitudinal length scale L_{il} and transversal length scale L_{it} can be expressed as Eq. (A.10).

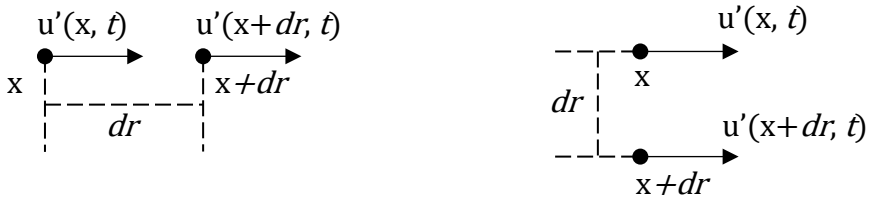

Longitudinal L_{il} Transversal L_{it}

Figure A.2 A sketch of longitudinal and transversal spatial velocity correlations (Ling 2014)

$$L_{il} = 2L_{it}$$ **Eq.** (A.10)

The integral time scale τ_i can be calculated by dividing the integral length scale L_i by the fluctuating velocity u'.

$$\tau_i = \frac{L_i}{\mathrm{u}'}$$ **Eq.** (A.11)

When dealing with the relatively medium sizes of eddies in a turbulent flow, the Taylor length scale is adopted (Mathieu and Scott 2000). Using Taylor series, the spatial correlation $R(r)$ at zero separation r=0 can be defined as:

$$R(r) = 1 + r\frac{dR(r)}{dr}\Big|_{r=0} + \frac{r^2}{2!}\frac{d^2R(r)}{dr^2}\Big|_{r=0} + \cdots$$ **Eq.** (A.12)

Neglecting the higher order terms and conducting parabolic curve fitting about the spatial correlation function *R(r)* again, the Taylor length scale L_λ can be obtained as Eq. (A.13) (Tennekes et al. 1972).

$$L_\lambda = -\frac{1}{2}\frac{d^2R(r)}{dr^2}\Big|_{t=0}$$ **Eq.** (A.13)

Similar to the derivation of Eq. (A.12), the neglecting the higher order terms and plotting a parabolic curve are carried out. Using the temporal correlation *R(t)* at zero separation *t=0*, Taylor time scale can be also derived (Hinze 1975).

$$\frac{1}{{\tau_\lambda}^2} = -\frac{1}{2}\frac{d^2R(t)}{dt^2}\Big|_{t=0}$$ **Eq.** (A.14)

The Kolmogorov length scale is used to characterize the smallest size of eddies of which the kinetic energy eventually changes into heat. The definition of the Kolmogorov length scale is as follow:

$$L_\eta = \left(\frac{\nu^3}{\epsilon}\right)^{\frac{1}{4}}$$ **Eq.** (A.15)

where ν is the kinematic viscosity, and ε is the rate of the kinetic energy dissipation per unit mass in a turbulent flow. And the Kolmogorov time scale is defined as:

$$\eta = \left(\frac{\nu}{\epsilon}\right)^{\frac{1}{2}}$$ **Eq.** (A.16)

As mentioned in Law's research (2006b), where the integral length scale L_i is used in the calculation of the turbulent Reynolds number Re_t in Eq.(A.7). And the relationship between the integral length scale L_i, Taylor length scale L_λ, and Kolmogorov length scale L_η can be represented, with the use of the turbulent Reynolds number: see Eq. (A.17) and Eq. (A.18).

$$L_\lambda = \frac{L_i}{Re_t^{\frac{1}{2}}} \qquad \textbf{Eq.} \text{ (A.17)}$$

$$L_\eta = \frac{L_i}{Re_t^{\frac{3}{4}}} \qquad \textbf{Eq.} \text{ (A.18)}$$

The characteristics of turbulence and the various equations that are mentioned so far are fundamental notions and knowledge in understanding turbulent premixed flame. Especially, the characteristics of turbulent premixed flame depend on the magnitude of turbulent intensity, the morphology of the flames, and these characteristics vary continuously as flames developing.

The significant efforts have been made for the past decades to prescribe the types of the turbulent premixed flame. The diagram showing the different types of turbulent premixed flame was first presented by Borghi et al. (1998). The Borghi combustion regime diagram was plotted with the two dimensionless numbers, which are the velocity ratio and length scale ratio. Two dimensionless numbers, Damköhler number and Karlovitz number, are used in classifying the different types of turbulent premixed flame.

The Damköhler number Da is defined as the ratio of the characteristic time during which a large eddy sustains in turbulent premixed flame to the chemical characteristic time which is related to the unperturbed laminar premixed flame u_n.

$$Da = \frac{\tau_i}{\tau_c} = \frac{L_i}{\delta_l}\frac{u_n}{u'} \qquad \textbf{Eq.} \text{ (A.19)}$$

$$\tau_i = \frac{L_i}{u'} \qquad \textbf{Eq.} \text{ (A.20)}$$

$$\tau_c = \frac{\delta_l}{u_n}$$ **Eq.** (A.21)

Where Eq. (A.19), Eq.(A.20), and Eq. (A.21), τ_i indicates the characteristic time while a large eddy maintains in turbulent premixed flame, which is related to the integral length scale L_i. u' is the fluctuating velocity. τ_c means the chemical characteristic time, and δ_l is the thickness of the unperturbed laminar premixed flame u_n.

In relation to the thickness δ_l, the calculation of the unperturbed laminar premixed flame speed is made possible because the laminar premixed flame depends only on the thermal or molecular diffusivity of a combustible mixture under the aforementioned assumption in Sec. 2.1. And the thickness and the position of the flame would keep the same if the unburned gas proceeds towards the flame front at the same speed as the laminar flame speed.

Karlovitz number is defined as the ratio of the chemical characteristic time in the laminar premixed flame to the characteristic time of the smallest eddy which is dealt with in the definition of Kolmogorov length time scale. This number is a kind of the reciprocal number of Damköhler number, and the focus is put on the effect of the smallest size of eddy in turbulent premixed flame.

$$Ka = \frac{\tau_c}{\tau_\eta} = \frac{\delta_l}{L_\eta}\frac{u'}{u_n}$$ **Eq.** (A.22)

$$\tau_\eta = \frac{L_\eta}{u'}$$ **Eq.** (A.23)

Where Eq. (A.22) and Eq. (A.23), τ_η is the characteristic time while the smallest eddy in turbulent premixed flame sustains, and L_η is Kolmogorov length scale.

Figure A.3 illustrates the different types of premixed flame. The x-axis represents the ratio of a length scale L_t to the thickness of the unperturbed laminar premixed flame δ_l. And the y-axis indicates the ratio of the fluctuating velocity in turbulent flame u' to the laminar premixed flame speed u_n. Describing the types of flame in the figure:

- $Re_t \leq 1$: In this regime, laminar flame or weak turbulent flame are observed. The surface of the flame is smooth, or a small size of wrinkles can be found on it.

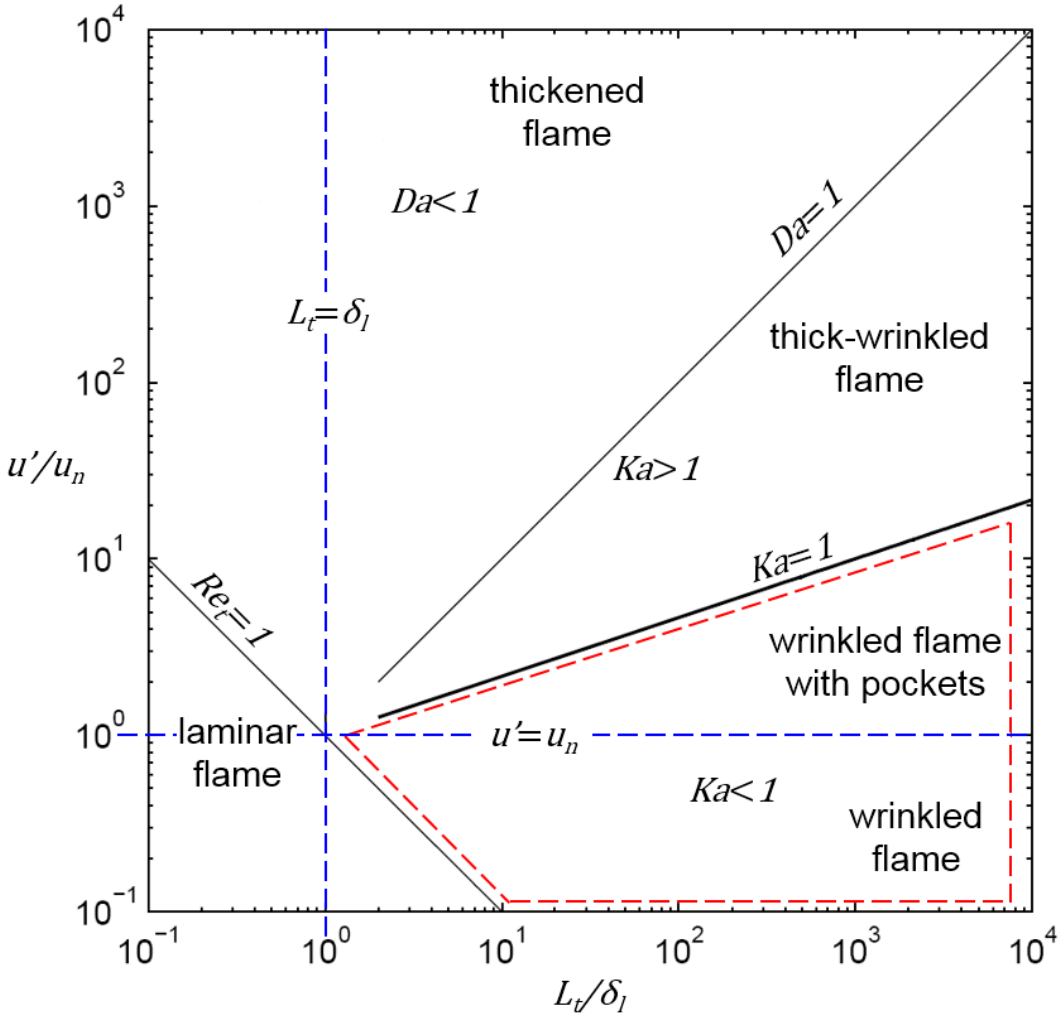

Figure A.3 Laminar and turbulent premixed combustion regime diagram (Borghi et al. 1998, Abdel-Gayed et al. 1989)

- $Ka < 1$: wrinkled or corrugated flamelet regime. Depending on the ratio of the fluctuating velocity u' to the laminar premixed flame speed u_n in the y-axis, the regime can be subdivided.

    - Where $u'/u_n < 1$, a small size of turbulent eddies make the flame surface wrinkled though, the magnitude is not much and the laminar burning velocity is dominant over the turbulent fluctuation.

- Where $u'/u_n > 1$, a relatively larger size of turbulent eddies make the flame surface wrinkled and curved than those at $u'/u_n < 1$. In the areas of the unburned gas or combustion product near the flamelet, some pockets can be observed.

- $1 < Ka < 100$: thick-wrinkled regime. Compared with the thickness of the laminar flame, the size of the smallest turbulent eddies is small. Although the turbulent eddies are enough to penetrate into the flame zone, it is hard for them to infiltrate into the reaction zone.

- $Ka > 100$: thickened flame regime. In this regime. Since the size of the smallest turbulent eddies is smaller than the thickness of the reaction zone, the chemical reaction is affected. It is difficult for the flame structure to sustain, and the extinction in a local area can take place.

The red-dotted area in Figure A.3 is the combustion regime where cellular flame can be observed. The experimental equipment of the current research was configured to make the desirable combustion condition. In order to minimize the occurrence of a turbulence flow inside the cylinder of the research engine, the undesirable components of the cylinder head were removed. On top of it, the directions of the intake ports were diametrically opposite to each other, and the shape of the piston crown was flat. The detailed description is presented in Chapter 3.

B. Calibration of flowmeters in the fuel and air supply system

In order to make sure that an accurate amount of fuel was supplied for the combustion chamber, the calibration for the flowmeters was done before experiment. Brooks thermal mass flowmeter, of which the type is 5863E, was adopted as a reference flowmeter.

$$Q_{ref2} = Q_{ref1} \times \frac{conversion\ factor\ of\ fuel}{conversion\ factor\ of\ reference\ gas}\ [ml/min] \quad \textbf{Eq.}\ (B.1)$$

$$Q_{ref3} = Q_{ref2} \times \frac{P_{ref2}T_{ref3}}{P_{ref3}T_{ref2}}\ [ml/min] \quad \textbf{Eq.}\ (B.2)$$

$$Q_{rtm2} = Q_{rtm1} \times correction\ factor\ [ml/min] \quad \textbf{Eq.}\ (B.3)$$

$$Q_{rtm3} = Q_{rtm2} \times \frac{P_{rtm2}T_{rtm3}}{P_{rtm3}T_{rtm2}}\ [ml/min] \quad \textbf{Eq.}\ (B.4)$$

Q: flow rate P: pressure T: temperature
ref: reference rtm: rotameter

Eq. (B.2) and Eq. (B.4) show the way of calculating the flow rates of the reference flowmeter and rotameters in the calibration condition of this research respectively. In the case of the reference flowmeter, the flow rate Q_{ref1} and gas conversion factor data in the standard condition, i.e. 101325 Pa and 273.15 K, were provided by the manufacturer: refer to Table B.2 and Table B.3. Considering the calibration condition of this research, which is 294.15 K and 201325 Pa, the flow rate of the reference flowmeter Q_{ref3} was calculated applying Boyle's and Charles's law: the relevant equation is Eq. (B.2).

As seen in Eq. (B.3) and Eq. (B.4), the calculation of the flow rate of the rotameter in the calibration condition of this research is similar to that of the reference flowmeter. The air flow rate data of the rotameter Q_{rtm1} in the calibration condition, 101325 Pa and 294.15 K, were provided by the manufacturer, and then the correction factors of hydrogen, methane, and propane were calculated.

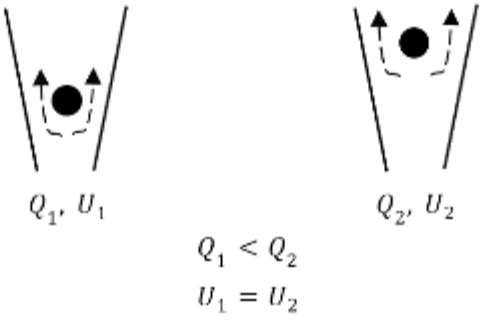

Figure B.1 A schematic diagram of the taper tube inside a rotameter

Figure B.1 shows a schematic diagram of a float and tapered tube in a rotameter. Assuming the velocity of the fluid passing through the area between the float and the wall of the tapered tube is constant, the annular area increases as the float rises (Wilson, Elias et al. 1980, Furness 1989). The force balance on the float between the downward force by the float weight and the force of the upwardly flowing fluid is represented in Eq. (B.5).

$$Float\ weight = Drag + Buoyancy$$

$$V_s\rho_s g = k_d\rho_f U^2 + V_s\rho_f g \qquad \textbf{Eq.}\ (B.5)$$

$$U = \frac{Q}{A} \qquad \textbf{Eq.}\ (B.6)$$

$$U = \frac{Q}{kh} = k_1\frac{Q}{h} \qquad \textbf{Eq.}\ (B.7)$$

V_s: float volume | ρ_s: float density | g: gravity of acceleration
k_d: drag coefficient | ρ_f: fluid density | U: velocity
Q: flow rate | A: area | k: proportional constant
k_1: proportional constant 1/ k | h: height of float

If the volumetric flow rate rises and the float keeps its vertical position, the linear velocity in Eq. (B.6), U, also rise. However, since the terms of the float weight and buoyancy do not change and the force balance in Eq. (B.5) must maintain at the new flow rate, the float position rises. This means that the

annular cross section area between the float and the wall in the tapered tube becomes larger which is why this flowmeter is a variable area meter. Hence, the linear velocity U is equal to the one at the previous flow rate (Wilson, Elias et al. 1980, Baker 2005). The relationship between the annular cross section area A and the vertical position of the float is proportional and can be represented as Eq. (B.7).

Substituting Eq. (B.7) into Eq. (B.5) yields

$$V_s \rho_s g = k_d \rho_f \left(k_1 \frac{Q}{h} \right)^2 + V_s \rho_f g \qquad \textbf{Eq.} \text{ (B.8)}$$

V_s: float volume ρ_s: float density g: gravity of acceleration
k_d: drag coefficient ρ_f: fluid density U: velocity
k_1: proportional constant 1/ k Q: flow rate
h: height of float

Solving Eq. (B.8) for Q, the volumetric flow rate is represented as Eq. (B.9)

$$Q = k_3 \sqrt{\frac{(\rho_s - \rho_f)}{\rho_s}} h \qquad \textbf{Eq.} \text{ (B.9)}$$

$$k_3 = \sqrt{\frac{V_s g}{k_2}}, new\ constant \qquad k_2 = k_d {k_1}^2, new\ constant$$

Q: flow rate ρ_s: float density ρ_f: fluid density
h: height of float V_s: float volume g: gravity of acceleration
k_d: drag coefficient k_1: proportional constant 1/ k

The volumetric flow rate is proportional to the float height, and the constant k_3, the float density ρ_s and the fluid density ρ_f are determined by a rotameter type and the kind of flowing fluid.

Substituting Eq. (B.9) into Eq. (B.3) and then solving for the correction factor yields

$$correction\ factor = \frac{Q_{rtm2}}{Q_{rtm1}} = \frac{\left(k_3\sqrt{\frac{(\rho_s - \rho_{arbitrary\ gas})}{\rho_{arbitrary\ gas}}}h\right)_{rtm2}}{\left(k_3\sqrt{\frac{(\rho_s - \rho_{calibrated\ gas})}{\rho_{calibrated\ gas}}}h\right)_{rtm1}}$$ **Eq.** (B.10)

Q: flow rate k_3: new constant ρ_s: float density
$\rho_{arbitrary\ gas}$: arbitrary gas density h: height of float
$\rho_{calibrated\ gas}$: calibrated gas density

The arbitrary gas in Eq. (B.10) is one of three gaseous fuels that were used in this experiment, and the calibrated gas was air. As shown in Table 3.2 and Table B.1, since the densities of three gaseous fuels and air are too small compared with the float density, Eq. (B.10) can be rearranged.

$$correction\ factor = \frac{\left(k_3\sqrt{\frac{\rho_s}{\rho_{arbitrary\ gas}}}h\right)_{rtm2}}{\left(k_3\sqrt{\frac{\rho_s}{\rho_{calibrated\ gas}}}h\right)_{rtm1}} = \sqrt{\frac{\rho_{calibrated\ gas}}{\rho_{arbitrary\ gas}}}$$ **Eq.** (B.11)

$\rho_{arbitrary\ gas}$: arbitrary gas density h: height of float
$\rho_{calibrated\ gas}$: calibrated gas density

It is assumed that the gases obey the ideal gas law, and substituting Eq. (B.12) into Eq. (B.11) yields Eq. (B.13).

$$\rho = \frac{PM}{RT} \qquad \because PV = nRT, M = \frac{m}{n}$$ **Eq.** (B.12)

$$correction\ factor = \sqrt{\frac{P_{calibrated\ gas}M_{calibrated\ gas}T_{arbitrary\ gas}}{P_{arbitrary\ gas}M_{arbitrary\ gas}T_{calibrated\ gas}}}$$ **Eq.** (B.13)

ρ: density P: pressure T: temperature
M: molecular weight per mole n: amount of gas
R: universal gas constant m: molecular weight

Table B.4 shows the correction factors of three gaseous fuels that were applied to the current research. Considering the pressure and temperature condition when the calibration was done, which was 201325 Pa and 294.15 K, the flow rate of the rotameter Q_{rtm3} was achieved, applying Boyle's and Charles's law.

From Figure B.2 to Figure B.4 shows the result of the calibration. As seen in the figures, the overall performance of the rotameter were in good condition. Especially, the rotameter curves are linear in the range where the experiment was carried out. However, the accuracy is somewhat low in the range where the flow rate is small or reaches their maximum capacities. The difference between the diameters of the inlet and outlet of the rotameter tube and the diameters of the pipes connected to it can cause this error. In this research, the experiment was not carried out in the range.

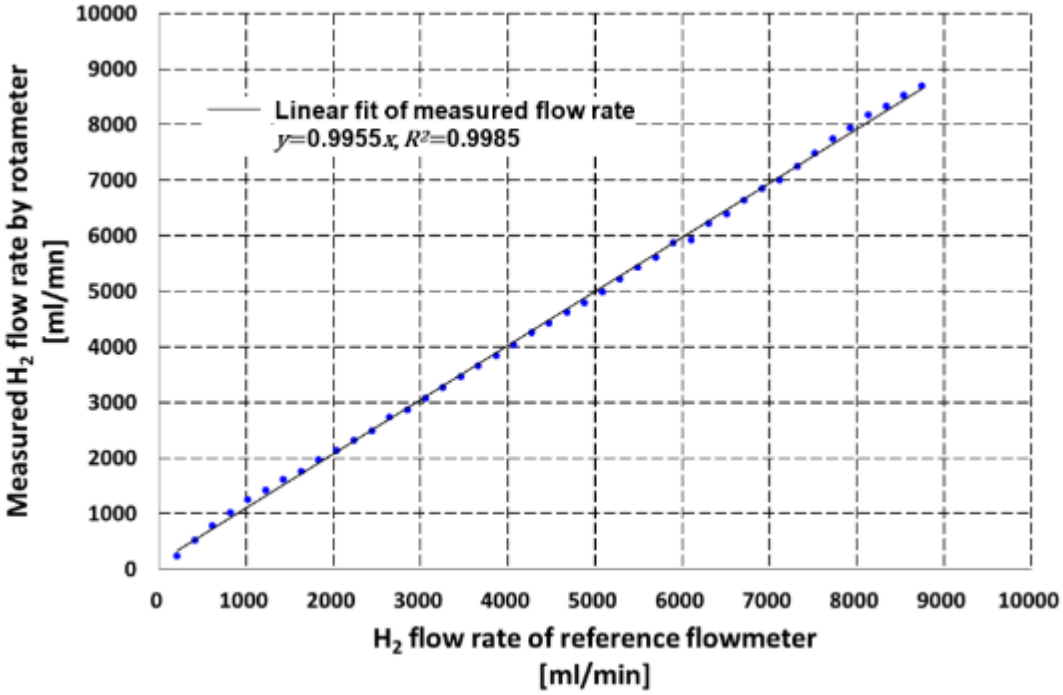

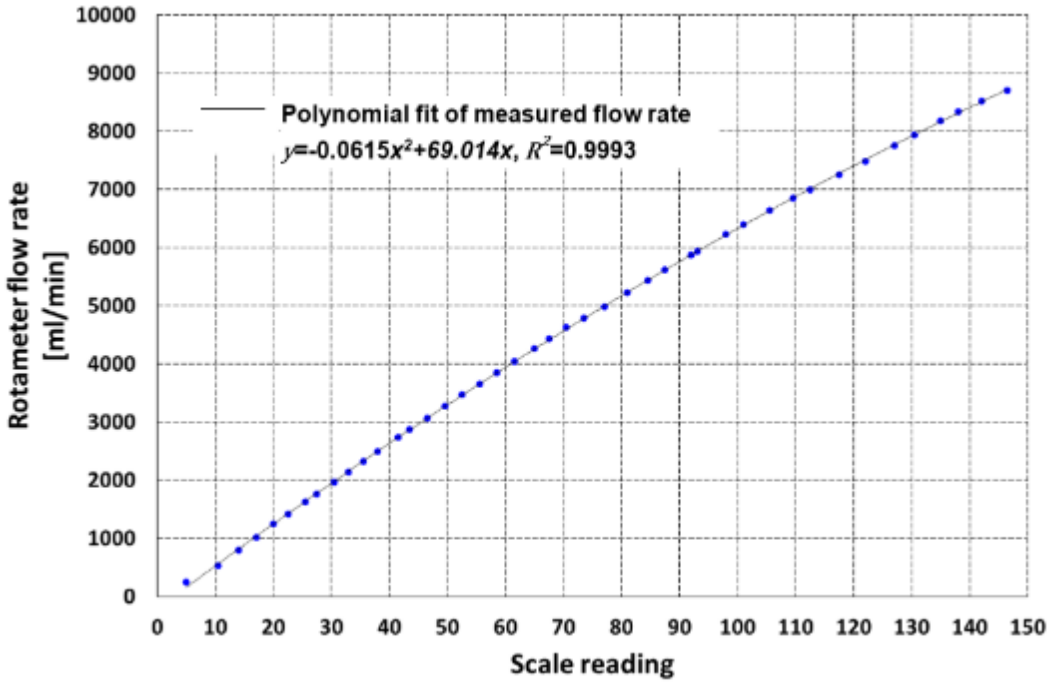

Figure B.2 Rotameter calibration result of H_2

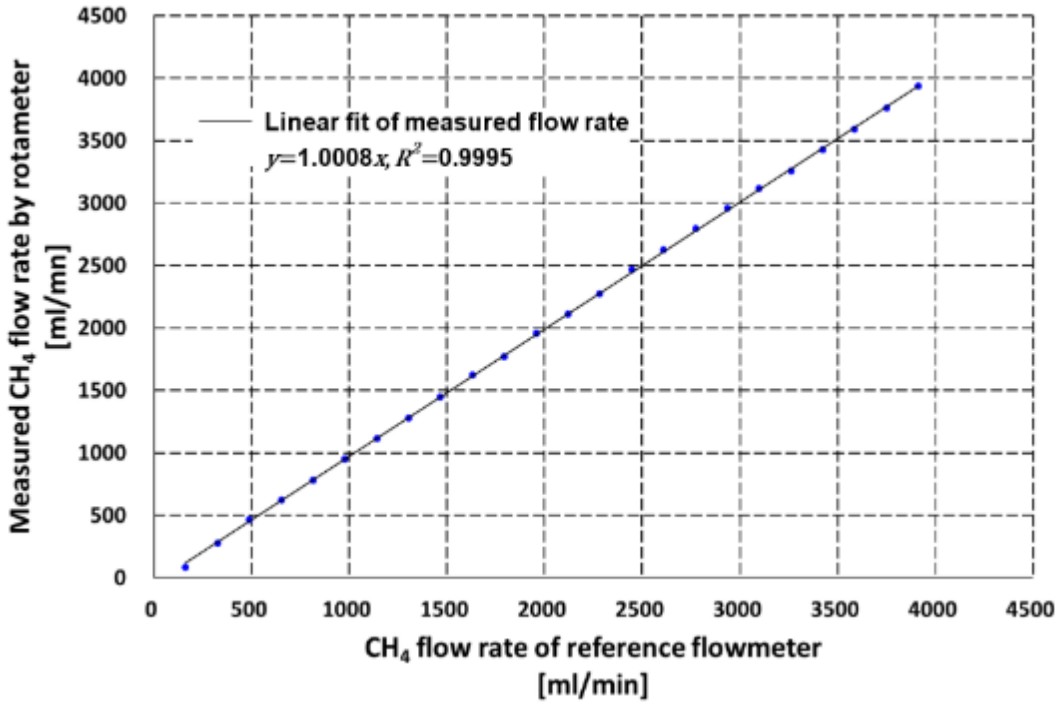

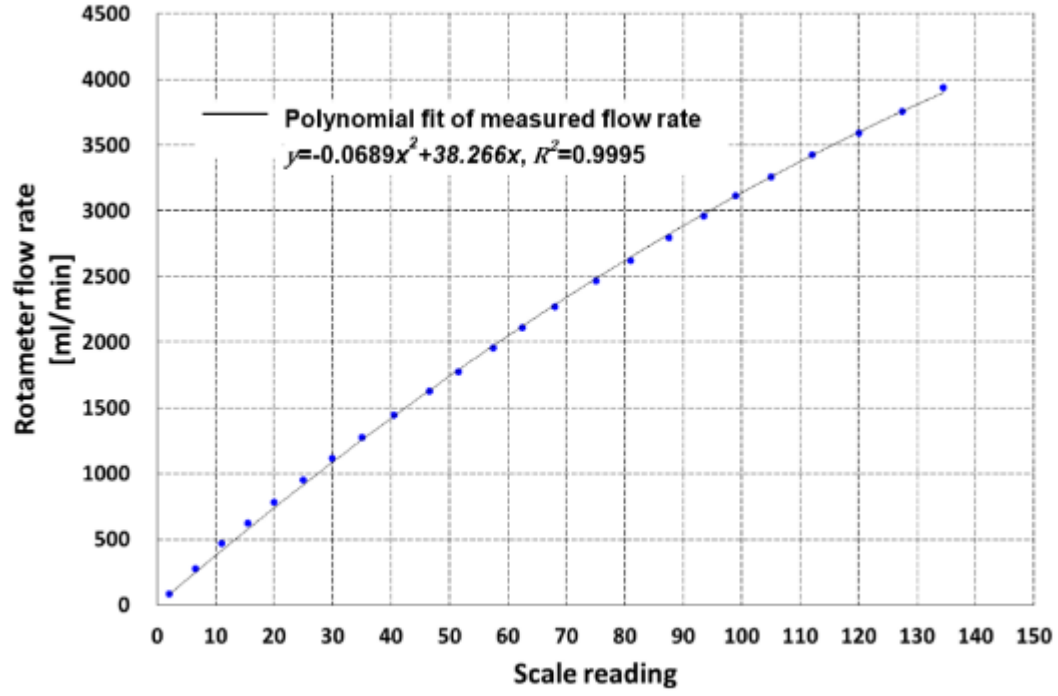

Figure B.3 Rotameter calibration result for CH_4

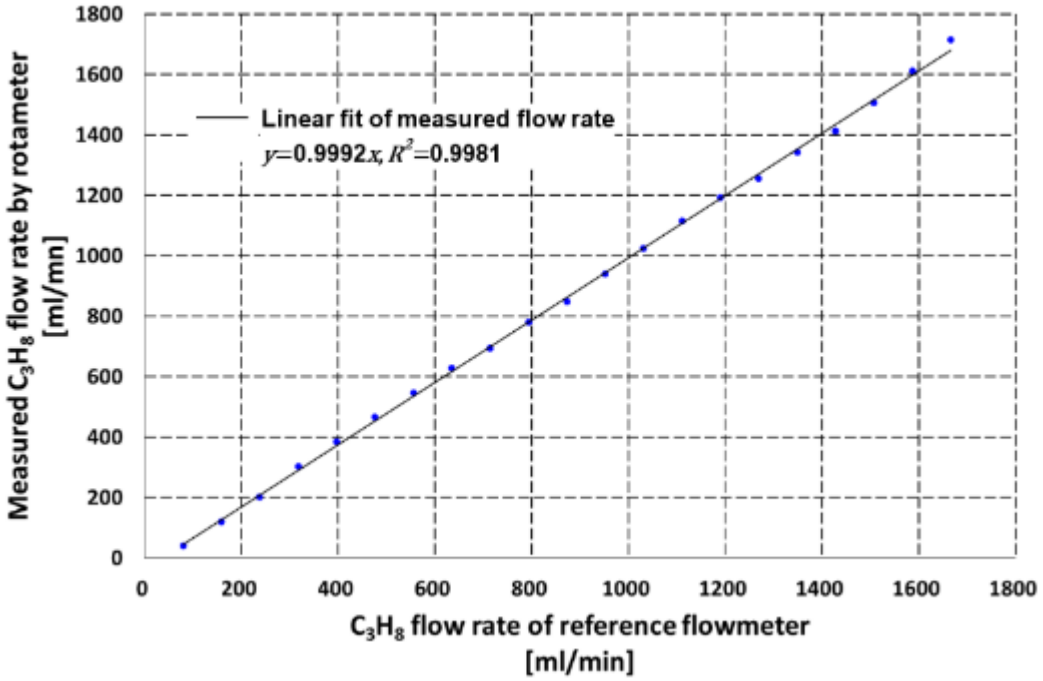

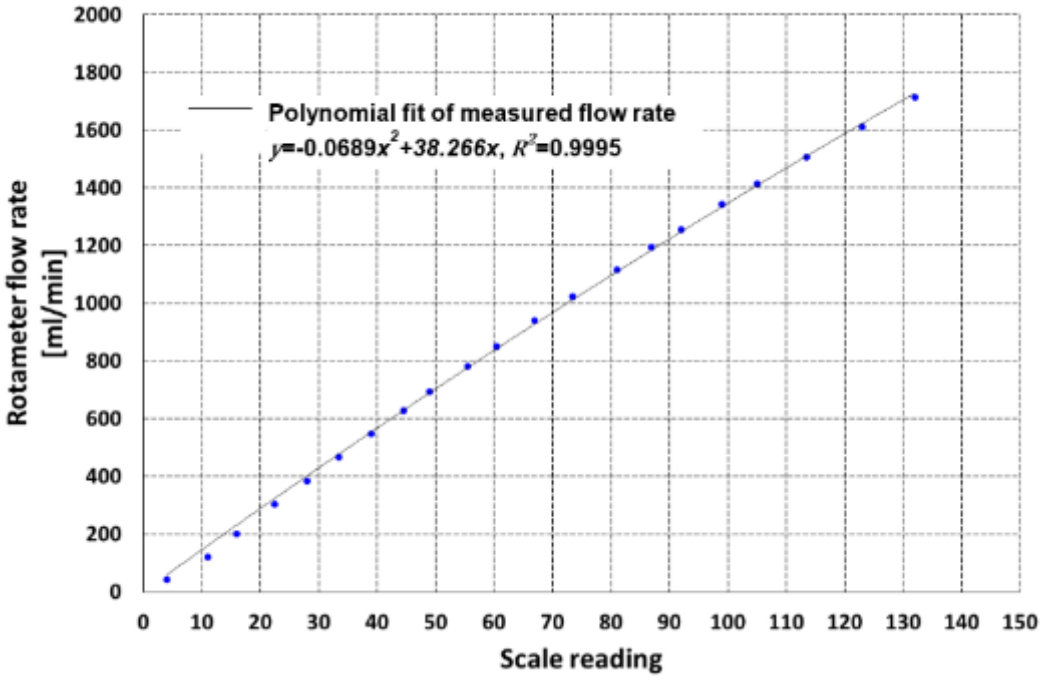

Figure B.4 Rotameter calibration result for C_3H_8

Table B.1 Specification of rotameters (OMEGA 2016)

Type	Capacity at air [ml/min]	Tube length [mm]	Float material	Float density [kg/m^3]
FL-3804G	2313	150	Glass	2530
FL-3804ST	4562	150	Stainless steel	8040

Table B.2 Temperature and pressure conditions with regard to the flow rates of the reference flowmeter and rotameter used in this research

Reference flowmeter flow rate	Pressure temperature condition		Rotameter flow rate	Pressure temperature condition	
[ml/min]	[Pa]	[K]	[ml/min]	[Pa]	[K]
Q_{ref1}	101325	273.15	Q_{rtm1}	101325	294.15
Q_{ref2}	101325	273.15	Q_{rtm2}	101325	294.15
Q_{ref3}	201325	294.15	Q_{rtm3}	201325	294.15

Table B.3 Conversion factors of fuel gases in the reference flowmeter (Brooks Instrument 1992)

Fuel gas	Conversion factor
H_2	1.010
CH_4	0.810
C_3H_8	0.394
Air	1.000

Reference condition: 101325 Pa, 273.15 K

Table B.4 Correction factors of hydrogen, methane, and propane in the rotameter

Fuel gas	Correction factor
H_2	0.264
CH_4	0.744
C_3H_8	1.234

Reference condition: 101325 Pa, 294.15 K

The calibrations of three thermal mass flowmeters that were installed in the main air supply pipeline and seeding system were also carried out. The reference flowmeter was Brooks 5863E thermal mass flowmeter, which is the same as the one that was used for the calibration of the rotameters in the fuel supply system. Unlike the case of the rotameter calibration, since the fluid to be calibrated was air and all the flowmeters were displayed in SLPM, the use of conversion factors and the calculation of correction factors were not required.

Figure B.5 and Figure B.6 show the calibration results of the flowmeters that were used in the sub-pipelines. The difference between the flow rates of the reference flowmeter and the target flowmeters were very small, and it was confirmed that the HFM-301 flowmeters were accurate enough to measure the air flow rate. Figure B.7 shows the calibration result of the flowmeter that was employed in the seeding system. It was also confirmed that the flow rate was in very good agreement with that of the reference flowmeter.

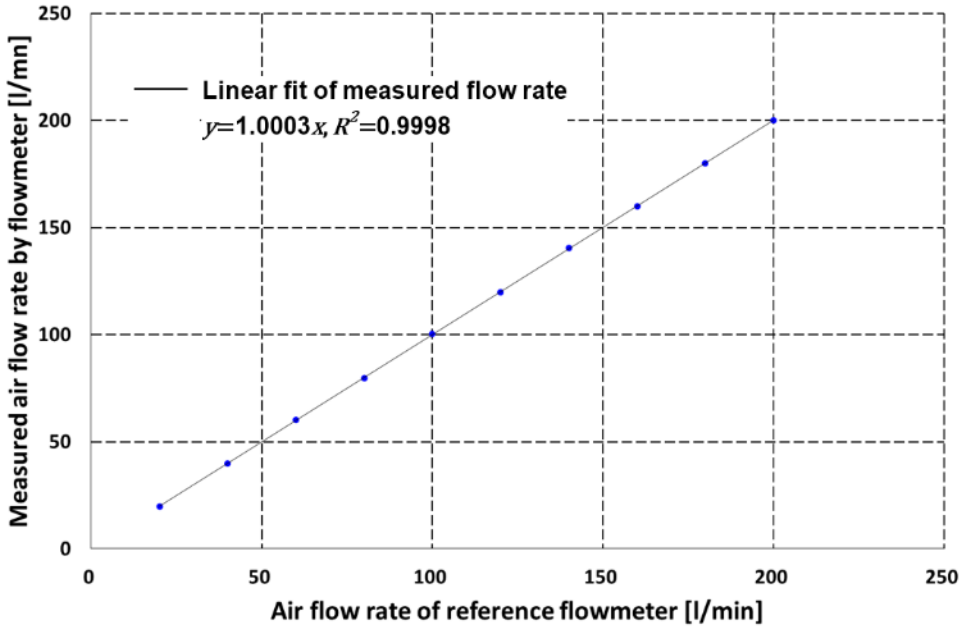

Figure B.5 Calibration result of the first HFM-301 flowmeter used in the air supply line

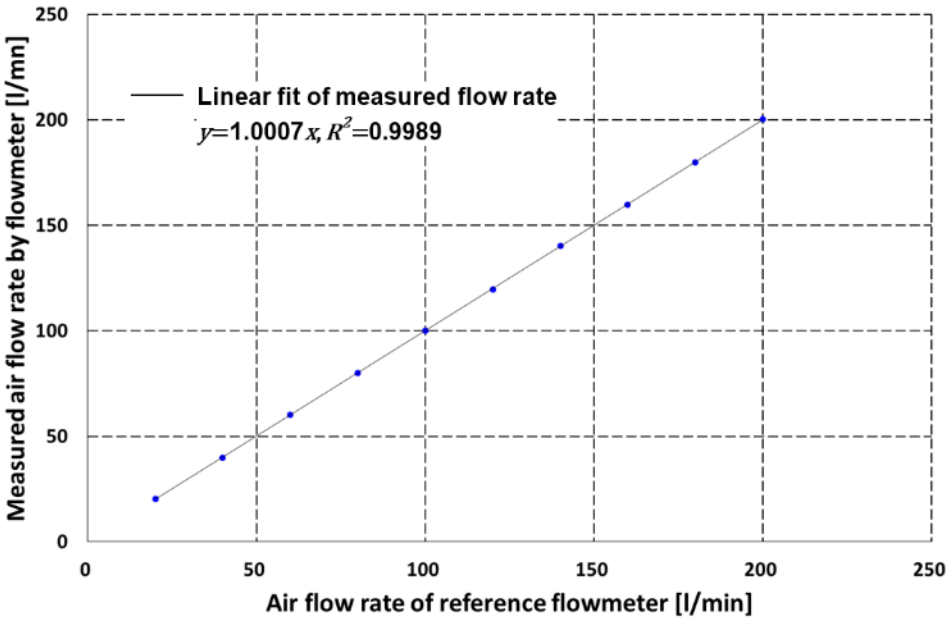

Figure B.6 Calibration result of the second HFM-301 flowmeter used in the air supply line

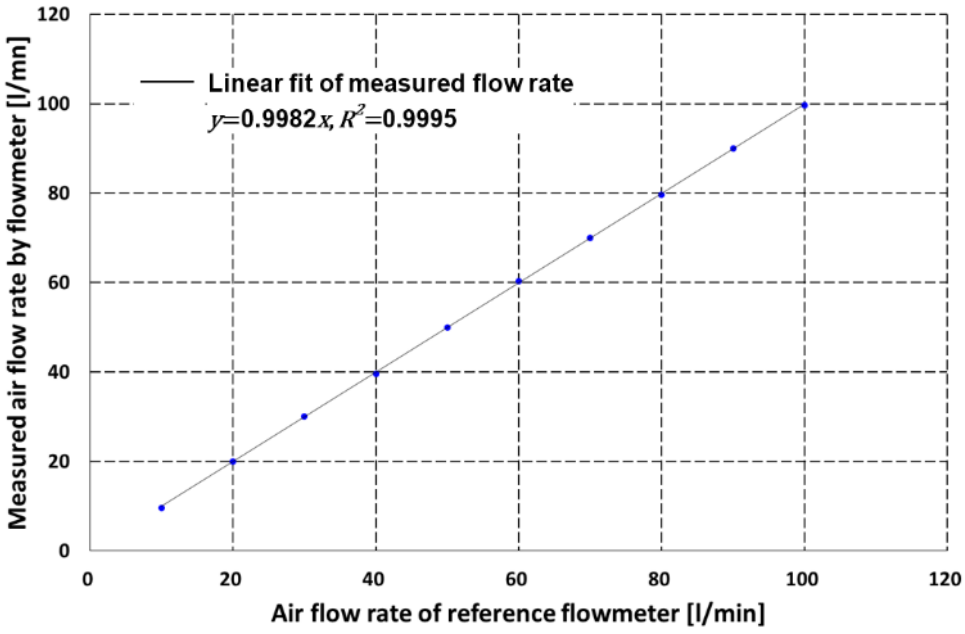

Figure B.7 Calibration result of the Brooks 5863S flowmeter used in seeding system

C. Calibration of pressure transducers

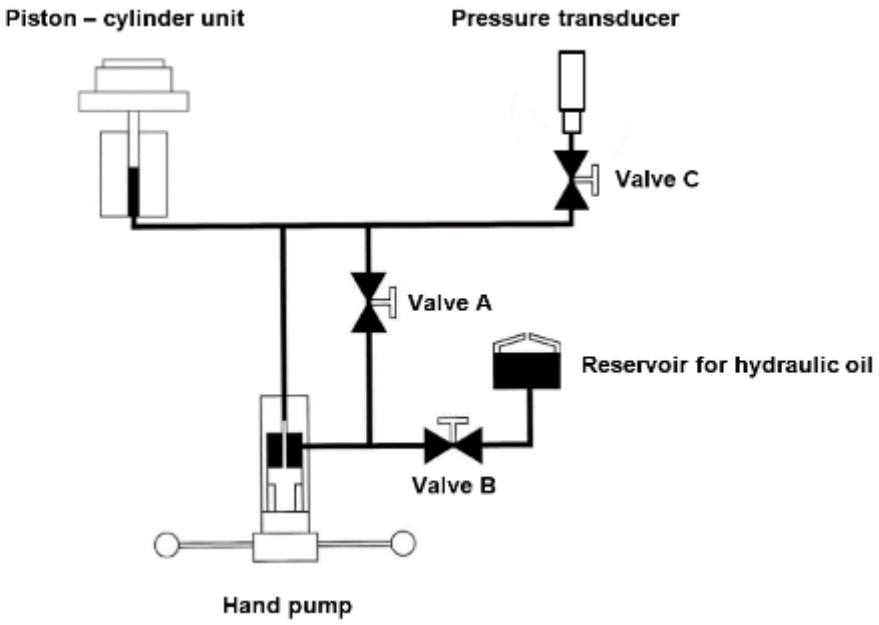

Figure C.1 A schematic diagram of the Budenberg dead weight tester: the figure is modified from the instruction manual (Budenberg 2010)

Figure C.1 shows a schematic diagram of the dead weight tester. The working fluid which is used in the dead weight tester was a typical hydraulic oil. After air that may be trapped in the hydraulic pipeline is removed by opening Valve A, B, and C, a desirable weight is put on the piston-cylinder unit after closing Valve C, and then the hand pump is operated to give pressure to the hydraulic oil until the piston-cylinder unit with the desirable weight is lifted up. By opening Valve C, the hydraulic oil pressure is supplied to pressure the transducer, and then the pressure is released opening Valve A and B. The more detailed information on how to operate the dead weight tester can be read in the manufacturer instruction manual (Budenberg 2010).

In order to display and store an electrical signal which a pressure transducer provides, the LabVIEW script was developed by the author, using a National Instruments 6110 analogue PCI card. An analogue signal that is generated by a pressure transducer with an amplifier is transmitted to a port of the analogue PCI card, and then is converted in a digital form. Through the script, the electrical signals that the absolute and dynamic pressure transducers generated during the calibration could be displayed: refer to Figure C.2

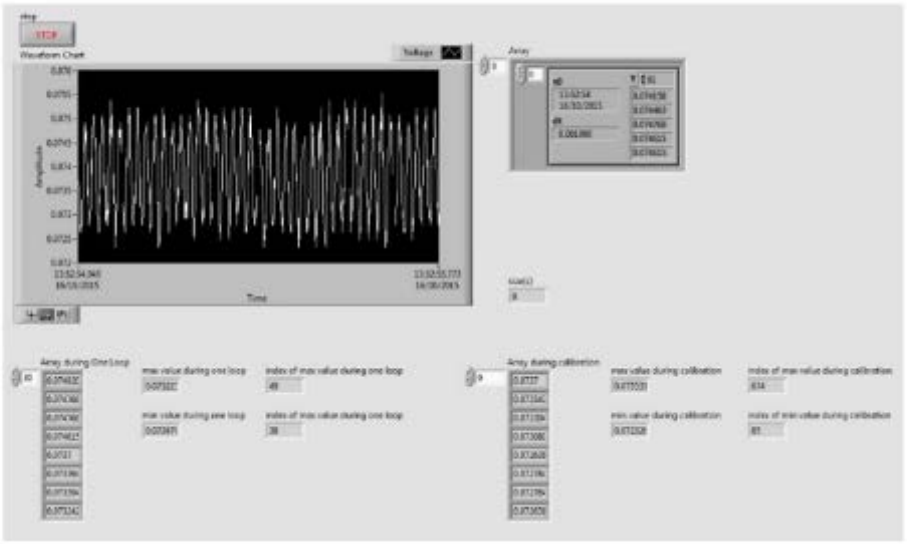

(A) Front Panel of the script

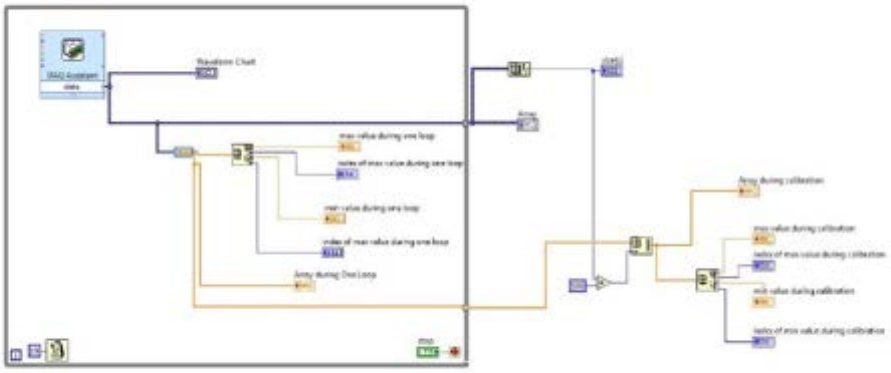

(B) Block diagram of the script

Figure C.2 LabVIEW script for the calibration of the absolute and dynamic transducers

Using the dead weight tester and the LabVIEW script above, the calibration of both transducers were carried out regularly. According to the studies carried out by Kuratle and Marki, and Rosseel, Sierens et al. (1992, 1999), pressure transducers can drift from their initial performance curve as they are exposed to high pressure and temperature continuously. Hence, it was essential to check the performance of the absolute and dynamic pressure transducer before experiment.

Figure C.3 and Figure C.4 show the results of the calibration. Through the calibration, the performances of both pressure transducers such as their linearity and hysteresis could be checked. It was confirmed that both of them were in good condition. The accuracy of the absolute and dynamic pressure

transducer in their operation ranges in the experiment, 0-5 and 0-100 bar, was ±1.5 and 2% respectively.

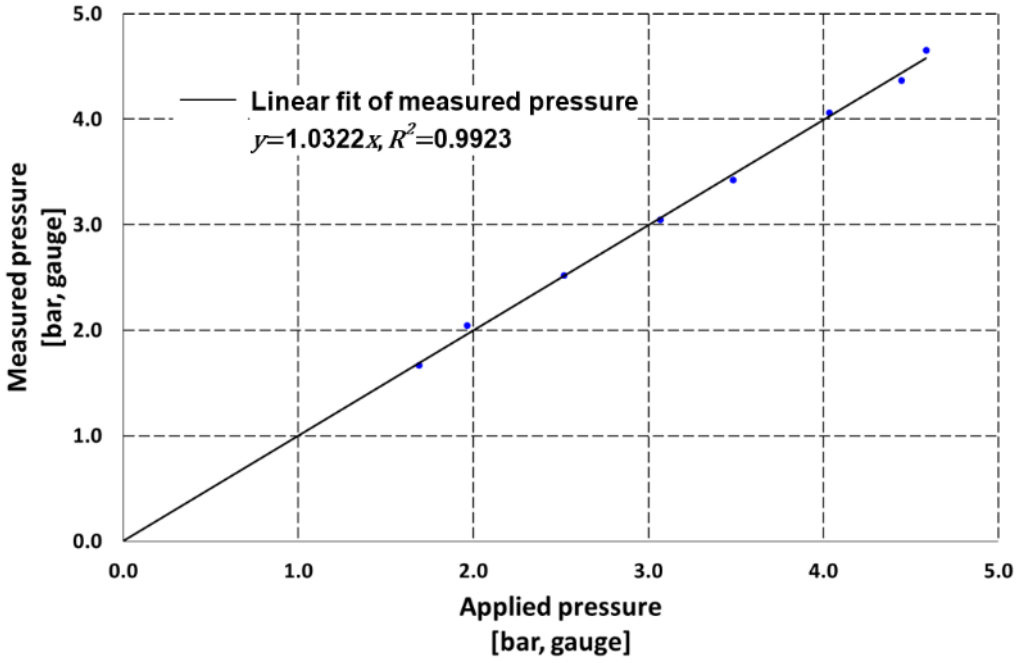

Figure C.3 Result of the calibration of the absolute pressure transducer

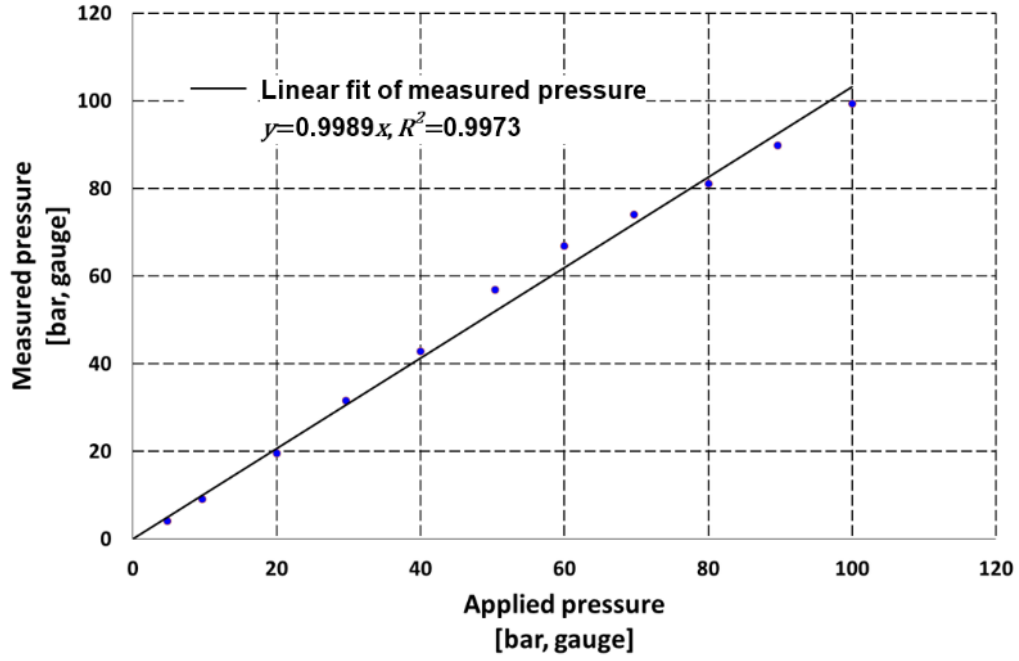

Figure C.4 Result of the calibration of the dynamic pressure transducer

D. Derivation of curvature

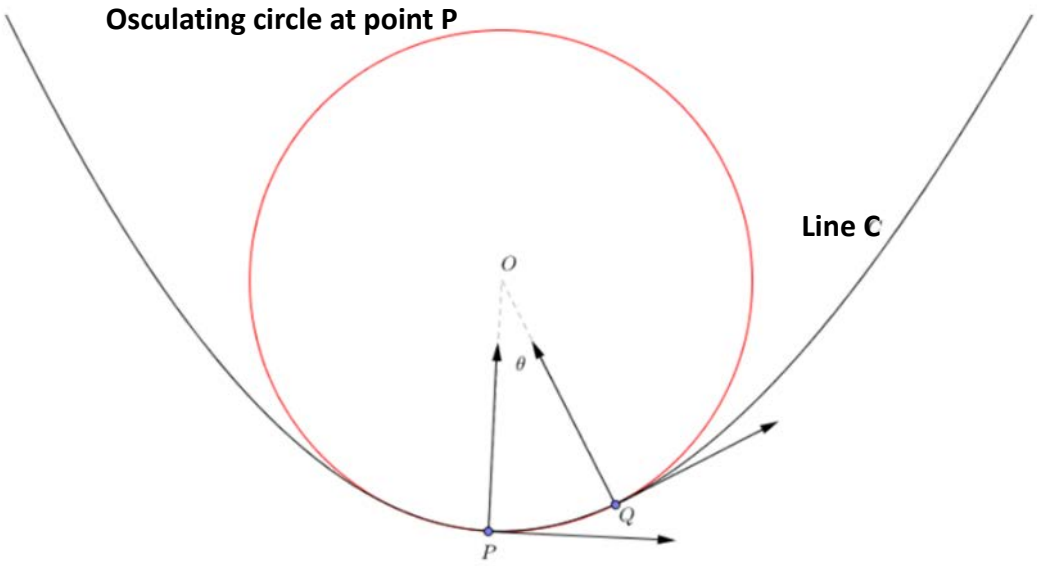

Figure D.1 A schematic diagram for the derivation of curvature

Assuming that the line C is dependent on time t, that is, $C(x,y)$, $x=x(t)$, $y=y(t)$, the following derivation can be done.

$$\overline{OP} = r$$

$$Curvature = \frac{1}{r}$$

$$r = \left|\lim_{P\to Q}\frac{\Delta PQ}{\Delta\theta}\right| = \left|\lim_{\theta\to 0}\frac{s}{\theta}\right| = \left|\frac{ds}{d\theta}\right|$$

$$r = \left|\frac{ds}{d\theta}\right| = \left|\frac{ds}{dt}\frac{dt}{d\theta}\right|$$

$$\frac{ds}{dt}\frac{dt}{d\theta} = \sqrt{\left(\frac{dx}{dt}\right)^2 + \left(\frac{dy}{dt}\right)^2} \times \frac{\left(\frac{dx}{dt}\right)^2 + \left(\frac{dy}{dt}\right)^2}{\frac{d^2y}{dt^2}\frac{dx}{dt} - \frac{d^2x}{dt^2}\frac{dy}{dt}}$$

$$\frac{1}{r} = \frac{\frac{d^2y}{dt^2}\frac{dx}{dt} - \frac{d^2x}{dt^2}\frac{dy}{dt}}{\left\{\left(\frac{dx}{dt}\right)^2 + \left(\frac{dy}{dt}\right)^2\right\}^{\frac{3}{2}}}$$

Reference

ABDEL-GAYED, R. G., BRADLEY, D. & LUNG, F. K. K. 1989. Combustion regimes and the straining of turbulent premixed flames. Combustion and Flame, 76, 213-218.

ABDI AGHDAM, E. 2003. Improvement and validation of a thermodynamic SI engine simulation code. University of Leeds.

ADRIAN, R. J. 2005. Twenty years of particle image velocimetry. Experiments in fluids, 39, 159-169.

ADRIAN, R. J. & WESTERWEEL, J. 2011. Particle image velocimetry, Cambridge University Press.

ANDREWS, G. & BRADLEY, D. 1972. Determination of burning velocities: a critical review. Combustion and Flame, 18, 133-153.

BAKER, R. C. 2005. Flow measurement handbook: industrial designs, operating principles, performance, and applications, Cambridge University Press.

BALUSAMY, S., CESSOU, A. & LECORDIER, B. 2011. Direct measurement of local instantaneous laminar burning velocity by a new PIV algorithm. Experiments in fluids, 50, 1109-1121.

BIROL, F. 2010. World energy outlook 2010. International Energy Agency, 1.

BOBICKI, E. R., LIU, Q., XU, Z. & ZENG, H. 2012. Carbon capture and storage using alkaline industrial wastes. Progress in Energy and Combustion Science, 38, 302-320.

BORGHI, R., DESTRIAU, M. & DE SOETE, G. 1998. Combustion and flames: chemical and physical principles : Roland Borghi, Michel Destriau, Paris, Editions Technip.

BOTHA, J. & SPALDING, D. The laminar flame speed of propane/air mixtures with heat extraction from the flame. Proceedings of the Royal Society of London A: Mathematical, Physical and Engineering Sciences, 1954. The Royal Society, 71-96.

BRADLEY, D., GASKELL, P. & GU, X. 1996. Burning velocities, Markstein lengths, and flame quenching for spherical methane-air flames: a computational study. Combustion and flame, 104, 176-198.

BRADLEY, D. & ROTH, G. 2007. Adaptive thresholding using the integral image. Journal of Graphics Tools, 12, 13-21.

BRIGHAM, E. O. 1988. The fast Fourier transform and its applications, Englewood Cliffs, N.J, Prentice-Hall.

BROOKS INSTRUMENT 1992. Installation and operation manual.

BRUUN, H. H. 1995. Hot-wire anemometry-principles and signal analysis.

BUDENBERG 2010. Budenberg BGH Series Hydraulic Dead-Weight Testers Operating and Maintenance Instructions.

BURLUKA, A., GAUGHAN, R., GRIFFITHS, J., MANDILAS, C., SHEPPARD, C. & WOOLLEY, R. Effects of Hydrocarbon Fuel Structure on Experimental Laminar & Turbulent Burn Rates. 7th European Combustion Meeting, Budapest, 2015.

BURLUKA, A. A. 2014. Combustion in Engines, Lecture notes, School of Mech. Eng., Univ. of Leeds, Leeds.

BURLUKA, A. A., HUSSIN, A. M. E.-D., SHEPPARD, C. G., LIU, K. & SANDERSON, V. 2011. Turbulent combustion of hydrogen–CO mixtures. Flow, turbulence and combustion, 86, 735-749.

BUTLER, G. R. 1999. The effects of swirl on combustion in spark ignition engines. University of Leeds.

CANNY, J. 1986. A computational approach to edge detection. IEEE Transactions on pattern analysis and machine intelligence, 679-698.

CHEN, N. 2014. Reciprocating combustion vessel for laminar flame studies. Institute of Thermofluids, School of Mechanical Engineering, Faculty of Engineering, University of Leeds.

CHEN, N. 2016. Premixed combustion of high calorific value gases. University of Leeds.

DAWOOD, A. E. E. S. 2011. Combustion and flow characteristics in a disc-shaped spark ignition engine. University of Leeds.

DESCHAMPS, B., SMALLWOOD, G., PRIEUR, J., SNELLING, D. & GÜLDER, Ö. Surface density measurements of turbulent premixed flames in a spark-ignition engine and a Bunsen-type burner using planar laser-induced fluorescence. Symposium (International) on Combustion, 1996. Elsevier, 427-435.

DUGGER, G. L. & GRAAB, D. D. 1953. Flame velocities of propane-and ethylene-oxygen-nitrogen mixtures.

EEA 2008. Energy and Environment Report. European Environment Agency.

EGOLFOPOULOS, F. & LAW, C. 1990. Chain mechanisms in the overall reaction orders in laminar flame propagation. Combustion and Flame, 80, 7-16.

EVENING, M. 2013. Adobe Photoshop CS5 for Photographers: a professional image editor's guide to the creative use of Photoshop for the Macintosh and PC, Focal Press.

FAR, K. E., PARSINEJAD, F. & METGHALCHI, H. 2010. Flame structure and laminar burning speeds of JP-8/air premixed mixtures at high temperatures and pressures. Fuel, 89, 1041-1049.

FINNEMORE, J. E. & FRANZINI, J. B. 2002. Fluid mechanics: with engineering applications, McGraw-Hill.

FURNESS, R. A. 1989. Fluid flow measurement, Longman in association with the Institute of Measurement and Control.

GATOWSKI, J. A., HEYWOOD, J. B. & DELEPLACE, C. 1984. Flame photographs in a spark-ignition engine. Combustion and Flame, 56, 71-81.

GIUNTA, C. J. 2016. What's in a Name? Amount of Substance, Chemical Amount, and Stoichiometric Amount. Journal of Chemical Education, 93, 583-586.

GROFF, E. G. 1982. The cellular nature of confined spherical propane-air flames. Combustion and Flame, 48, 51-62.

GU, X. J., HAQ, M. Z., LAWES, M. & WOOLLEY, R. 2000. Laminar burning velocity and Markstein lengths of methane–air mixtures. Combustion and flame, 121, 41-58.

HALL, M. J. & BRACCO, F. 1987. A study of velocities and turbulence intensities measured in firing and motored engines. SAE transactions, 414-441.

HATTRELL, T. 2007. A computational and experimental study of spark ignition engine combustion. University of Leeds.

HEIDEMAN, M., JOHNSON, D. & BURRUS, C. 1984. Gauss and the history of the fast Fourier transform. IEEE ASSP Magazine, 1, 14-21.

HERTZBERG, M. 1989. Selective diffusional demixing: occurrence and size of cellular flames. Progress in Energy and Combustion Science, 15, 203-239.

HEWITT, G., SHIRES, G., POLEZHAEV, Y. & DEVAHASTIN, S. 1998. International Encyclopedia of Heat and Mass Transfer. Drying Technology, 16, 1521-1522.

HEYWOOD, J. B. 1988. Internal combustion engine fundamentals.

HICKS, R. 1994. Turbulent flame structure and autoignition in spark ignition engines. PhD Thesis, Department of Mechanical Engineering, University of Leeds.

HINZE, J. O. 1975. Turbulence: an introduction to its mechanism and theory, New York, McGraw-Hill.

HOLST, G. C. & LOMHEIM, T. S. 2007. CMOS/CCD sensors and camera systems, JCD publishing USA.

HU, E., HUANG, Z., HE, J., ZHENG, J. & MIAO, H. 2009. Measurements of laminar burning velocities and onset of cellular instabilities of methane–hydrogen–air flames at elevated pressures and temperatures. international journal of hydrogen energy, 34, 5574-5584.

HULT, J., RICHTER, M., NYGREN, J., ALDÉN, M., HULTQVIST, A., CHRISTENSEN, M. & JOHANSSON, B. 2002. Application of a high-repetition-rate laser diagnostic system for single-cycle-resolved imaging in internal combustion engines. Applied optics, 41, 5002-5014.

HUSSIN, A. M. T. A. E. 2012. New and renewable energy: renewable fuels in internal combustion engines. University of Leeds.

IRVIN, G. & RICHARD, Y. 2008. Combustion. Academic Press.

IZUMIKAWA, M., MITANI, T. & NIIOKA, T. 1988. Experimental study on cellular flame propagation of blend fuels. Combustion and Flame, 73, 207-214.

KARPOV, V. 1982. Cellular flame structure and turbulent combustion. Combustion, Explosion, and Shock Waves, 18, 109-112.

KARPOV, V. & SEVERIN, E. 1980. Effects of molecular-transport coefficients on the rate of turbulent combustion. Combustion, Explosion, and Shock Waves, 16, 41-46.

KEANE, R. D. & ADRIAN, R. J. 1990. Optimization of particle image velocimeters. I. Double pulsed systems. Measurement science and technology, 1, 1202.

KEYS, R. 1981. Cubic convolution interpolation for digital image processing. IEEE Transactions on Acoustics, Speech, and Signal Processing, 29, 1153-1160.

KISTLER 2010. Quartz High-Pressure Sensor, Type 601A, 601H.

KISTLER 2013. Piezoresistive Absolute Pressure Sensor - Universal Precision Pressure Sensors Type 4043A, 4045A, 4073A, 4075A.

KONNOV, A. 2005. Model of cellular instability of flames of ternary mixtures. Combustion, Explosion, and Shock Waves, 41, 496-503.

KONNOV, A. A. The temperature and pressure dependences of the laminar burning velocity: experiments and modelling. Proceedings of the European Combustion Meeting–2015. Budapest, Hungary, 2015.

KURATLE, R. H. & MÄRKI, B. 1992. Influencing parameters and error sources during indication on internal combustion engines. SAE Technical Paper.

LANGRIDGE, S. 1995. Imaging and thermodynamic analysis of autoignition and knock in SI engines. PhD Thesis, Department of Mechanical Engineering, University of Leeds.

LARSSON, G. 2009. Turbulence related cyclic variation in combustion. University of Leeds.

LAVISION 2010a. DaVis 8.0 software, in product manual(Ed.), GmbH, Göttingen, Germany.

LAVISION 2010b. Flow Master In product manual, 1003005_FlowMaster_D80.pdf (Ed.), GmbH, Göttingen, Germany.

LAVISION 2012. Litron LDY series,in product manual(Ed.), GmbH, Göttingen, Germany.

LAVISION 2013. Sheet optics (divergent)_1003034_SheetOpticsDivergent_D82, in product manual(Ed.), GmbH, Göttingen, Germany.

LAVISION 2014. PIV seminar, in product manual(Ed.), GmbH, Göttingen, Germany.

LAVISION 2015. Imaging Tools, in product manual(Ed.), GmbH, Göttingen, Germany.

LAW, C. 2006a. Propagation, structure, and limit phenomena of laminar flames at elevated pressures. Combustion Science and Technology, 178, 335-360.

LAW, C. K. 2006b. Combustion physics, Cambridge university press.

LAW, C. K., JOMAAS, G. & BECHTOLD, J. K. 2005. Cellular instabilities of expanding hydrogen/propane spherical flames at elevated pressures: theory and experiment. Proceedings of the Combustion Institute, 30, 159-167.

LING, Z. 2014. Flame propagation and autoignition in a high pressure optical engine. University of Leeds.

LINSTROMS, P. J. & MALLARD, W. G. 2016. NIST Chemistry Webbook [Online]. National Institute of Standards and Technology, Gaithersburg MD, 20899. 2016].

LIPATNIKOV, A. 2012. Fundamentals of premixed turbulent combustion, CRC Press.

LIPATNIKOV, A. & CHOMIAK, J. 2005. Molecular transport effects on turbulent flame propagation and structure. Progress in energy and combustion science, 31, 1-73.

LITRON LASERS 2010. LDY 300 Series Nd:YLF PIV laser system operation handbook.

LONG, E. J. & HARGRAVE, G. K. 2011. Experimental measurement of local burning velocity within a rotating flow. Flow, turbulence and combustion, 86, 455-476.

MARKSTEIN, G. H. 1951. Experimental and theoretical studies of flame-front stability. Journal of the Aeronautical Sciences, 18, 199-209.

MARKSTEIN, G. H. Instability phenomena in combustion waves. Symposium (international) on Combustion, 1953. Elsevier, 44-59.

MARQUAND, C. & CROFT, D. R. 1994. Thermofluids: an integrated approach to thermodynamics and fluid mechanics principles, John Wiley & Sons.

MATHIEU, J. & SCOTT, J. 2000. An introduction to turbulent flow, Cambridge University Press.

MELLING, A. 1997. Tracer particles and seeding for particle image velocimetry. Measurement Science and Technology, 8, 1406.

MERZKIRCH, W. 1984. Flow Visualization ,(1987). Academic Press inc, 5, 52.

METGHALCHI, M. & KECK, J. C. 1980. Laminar burning velocity of propane-air mixtures at high temperature and pressure. Combustion and flame, 38, 143-154.

MITANI, T. & WILLIAMS, F. 1980. Studies of cellular flames in hydrogen□ oxygen□nitrogen mixtures. Combustion and Flame, 39, 169 -190.

MOBIL, E. 2013. The Outlook for Energy: A view to 2040. Exxon Mobil, 6.

MOESLUND, T. 2009. Canny Edge Detection. Retrieved December, 3, 2014.

MORLEY, C. 2005. Gaseq: a chemical equilibrium program for Windows. Ver. 0.79.

MURAD, A. E. 2006. Flow and combustion in disc and pent-roof SI engines. University of Leeds.

NAGANUMA, S. 1994. 물리수학의 직관적방법, 청음사.

NAKAHARA, M. & KIDO, H. 1998. A study of the premixed turbulent combustion mechanism taking the preferential diffusion effect into consideration. 九州大學工學部紀要, 58, 55-82.

NATIONAL INSTRUMENTS 2016. Motion Synchronization Using RTSI.

NEIJ, H., JOHANSSON, B. & ALDÉN, M. 1994. Development and demonstration of 2D-LIF for studies of mixture preparation in SI engines. Combustion and Flame, 99, 449-457.

NIEUWSTADT, F. T. 2012. Flow visualization and image analysis, Springer Science & Business Media.

NOMURA, T., TAKAHASHI, Y., ISHIMA, T. & OBOKATA, T. LDA and PIV Measurements and Numerical Simulation on In-Cylinder Flow Under Steady State Flow Condition. 12th International Symposium on Applications of Laser Techniques to Fluid Mechanics, Lisbon, Portugal, 2004. 1-17.

OTSU, N. 1975. A threshold selection method from gray-level histograms. Automatica, 11, 23-27.

OTSU, N. 1979. A threshold selection method from gray-level histograms. IEEE transactions on systems, man, and cybernetics, 9, 62-66.

OVERMARS, E., WARNCKE, N., POELMA, C. & WESTERWEEL, J. Bias errors in PIV: the pixel locking effect revisited. 15th international symposium on applications of laser techniques to fluid mechanics, Lisbon, Portugal, 2010. 5-8.

PARK, O., VELOO, P. S., LIU, N. & EGOLFOPOULOS, F. N. 2011. Combustion characteristics of alternative gaseous fuels. Proceedings of the Combustion Institute, 33, 887-894.

PETERSEN, R. E. & EMMONS, H. W. 1961. Stability of laminar flames. Physics of Fluids (1958-1988), 4, 456-464.

RAFFEL, M., WILLERT, C. E. & KOMPENHANS, J. 2007. Particle image velocimetry: a practical guide, Springer Science & Business Media.

RALLIS, C. J. & GARFORTH, A. M. 1980. The determination of laminar burning velocity. Progress in Energy and Combustion Science, 6, 303-329.

ROBERT, P. 2010. Fuel and Exhaust Residual Effects in Spark Ignition and HCCI engines. PhD Thesis, Department of Mechanical Engineering, University of Leeds.

ROSSEEL, E., SIERENS, R. & BAERT, R. 1999. Evaluating piezo-electric transducer response to thermal shock from in-cylinder pressure data. SAE technical paper.

SERWAY, R. A. & VUILLE, C. 2014. College physics, Cengage Learning.

SEZGIN, M. & SANKUR, B. 2004. Survey over image thresholding techniques and quantitative performance evaluation. Journal of Electronic imaging, 13, 146-166.

SPALDING, D. B. & COLE, E. H. 1973. Engineering thermodynamics, Hodder Arnold.

TELEDYNE HASTINGS INSTRUMENT 2010. Instruction manual HFM-301/305/306 Flow meters HFC-303/307 Flow controllers.

TENNEKES, H., LUMLEY, J. L. & LUMLEY, J. 1972. A first course in turbulence, MIT press.

TRIER, Ø. D. & JAIN, A. K. 1995. Goal-directed evaluation of binarization methods. IEEE Transactions on Pattern Analysis & Machine Intelligence, 1191-1201.

TRUFFAUT, J.-M. & SEARBY, G. 1999. Experimental study of the Darrieus-Landau instability on an inverted-'V'flame, and measurement of the Markstein number. Combustion science and technology, 149, 35-52.

TSI 2003. Instruction manual.

TURNER, J. T. & ZHANG, S. 2011. Analysis, presentation, and understanding in experimental fluid flow studies: A colourful evolutionary story. Optics & Laser Technology, 43, 358-374.

VAREA, E., MODICA, V., VANDEL, A. & RENOU, B. 2012. Measurement of laminar burning velocity and Markstein length relative to fresh gases using a new postprocessing procedure: Application to laminar spherical flames for methane, ethanol and isooctane/air mixtures. Combustion and Flame, 159, 577-590.

WESTBROOK, C. K. & DRYER, F. L. 1984. Chemical kinetic modeling of hydrocarbon combustion. Progress in Energy and Combustion Science, 10, 1-57.

WIENEKE[1], B. & PFEIFFER[1], K. 2010. Adaptive PIV with variable interrogation window size and shape.

WILSON, M. L., ELIAS, D., JORDAN, R., DURHAM, O. & JOERGER, K. 1980. APTI course 435, Atmospheric Sampling. Student Manual.

ZARE, R. N. 2012. My life with LIF: a personal account of developing laser-induced fluorescence. Annual Review of analytical chemistry, 5, 1-14.

ZELDOVICH, Y. 1949. Theory of combustion and detonation of gases, Headquarters, Wright-Patterson Air Force Base, Air Materiel Command.

ZHOU, M. & GARNER, C. 1996. Direct measurements of burning velocity of propane-air using particle image velocimetry. Combustion and flame, 106.

ZILL, D. G. & CULLEN, M. R. 2006. Advanced engineering mathematics, Sudbury, MA;London;, Jones and Bartlett Publishers.

長沼伸一郎 2011. 物理数学の直観的方法: 理工系で学ぶ数学「難所突破」の特効薬, 講談社.